Spin Current Induced Control of Magnetization Dynamics

Dissertation

zur Erlangung des Doktorgrades
der Naturwissenschaften (Dr. rer. nat.)
der Fakultät für Physik
der Universität Regensburg

vorgelegt von
Martin Maria Decker
aus München

im Jahr 2017

Promotionsgesuch eingereicht am: 29.10.2017
Die Arbeit wurde angeleitet von: Prof. Dr. Christian Back

Prüfungsausschuss:	Vorsitzender:	Prof. Dr. Karsten Rincke
	1. Gutachter:	Prof. Dr. Christian Back
	2. Gutachter:	Prof. Dr. Jaroslav Fabian
	weiterer Prüfer:	PD Dr. Alfred (Jay) Weymouth

Der Termin des Promotionskolloquiums: 08.02.2018

Contents

Introduction

Over the last 30 years, starting with the discovery of the giant magnetoresistive effect in 1988 [Bai88; Bin89], the idea of using the spin degree of freedom for data processing emerged and developed under the name "spintronics" [Wol01]. One branch of spintronics is dedicated to the development of new data storage devices which allow for high information densities, fast access times, low power consumption and non-volatility. A prominent candidate to fulfill these requirements is magnetic random access memory (MRAM) [Cha07]. Current technology uses direct current induced switching as writing mechanism and the tunneling magneto-resistance as read-out process, the so-called spin transfer torque MRAM (ST-MRAM)[1]. A ST-MRAM device consists of two magnetic layers separated by an oxide tunnel barrier. One of these layers is thick and pinned into a certain direction, thus called fixed layer. The second, free layer can be switched by applying a current pulse from the fixed to the free layer across the tunnel barrier. Since the current is spin polarized with polarization direction given by the fixed layer, angular momentum is transferred from the fixed to the free layer and enables switching of the free layer if the current is large enough [Cha07]. Unfortunately, the writing current across the tunnel barrier leads to its degradation and therefore is the Achilles' heel of this technology [And14]. Thus, a way to efficiently manipulate the magnetization electrically has still to be established.

In recent years, the spin Hall effect (SHE) [Dya71b] in normal metals with strong spin orbit coupling such as Pt and Ta has been discovered and used to control the dynamics of adjacent FM layers [And08; Liu11; Dem11a; Dem11b]. The SHE converts a charge current in the NM into a transverse spin current that is absorbed by the FM and thus angular momentum is transferred from the NM to the FM. The conversion efficiency is described by the so-called spin Hall angle (SHA) θ_{SH} which connects charge current density j^{c} and spin current density j^{s} via $j^{\mathrm{s}} = \frac{\hbar}{2|e|}\theta_{\mathrm{SH}}\, j^{\mathrm{c}}$. With respect to magnetization dynamics, the SHE primarily exerts a torque of the form $\boldsymbol{T}_{\mathrm{FL}} \propto \boldsymbol{m} \times (\boldsymbol{m} \times \boldsymbol{\sigma}_{\mathrm{DL}})$, with the unit vector of the magnetization $\boldsymbol{m}$ and the polarization direction of the injected spin current created by the SHE $\boldsymbol{\sigma}_{\mathrm{DL}}$. This torque, in certain situations, influences the effective damping of the FM and is therefore called "damping-like torque".

While studying magnetization dynamics under the application of in-plane (ip) currents, a second effect has been discovered in metallic bilayers: in experiments concerning current

[1] See the manufacturer homepage: https://www.everspin.com/spin-torque-mram-technology, date: 01.12.2017

driven domain wall movement in Pt/Co wires, a torque of the form $\boldsymbol{T} \propto \boldsymbol{m} \times \boldsymbol{\sigma}_{\mathrm{FL}}$, with the unit vector $\boldsymbol{\sigma}_{\mathrm{FL}}$ perpendicular to both current and Pt/Co interface normal has been detected. Torques of this form are called "field-like" and from symmetry considerations the physical origin has been attributed to the so-called Rashba effect[2] [Mir10a].

In metallic heterostructures with ultrathin ($< 1\,\mathrm{nm}$) FM layers, both damping- and field-like torques have subsequently been found to appear with comparable strength. Due to the fact that the physical origin of current induced torques lies in spin orbit coupling, the term "spin orbit torque" is used as a general name without relating a measured torque to any certain physical effect (like SHE or Rashba effect) [Gar13].

Finally, the possibility of switching the magnetization of microstructured NM/FM elements using ip currents has been demonstrated [Mir11; Liu12a; Liu12b]. These findings promise a transfer of technology in the writing process of MRAM cells from passing the current across a delicate tunneling barrier to passing the current through an underlying NM layer, thereby solving the above-mentioned endurance problem.

However, the physical processes incorporated in SOT induced magnetization reversal are not yet fully understood, hindering an efficient engineering towards applications. The lack of understanding is present at two levels: A) the actual dynamics of the switching process itself is unknown and completely different possible scenarios have been proposed for current induced magnetization reversal. Therefore the magnetization reversal process is hard to model, even if the strength of both field- and damping-like torques are known for a given device. B) the physical origin of the SOTs, and therefore the way to systematically increase the SOT efficiency remains unclear. There is an ongoing debate whether SHE or Rashba effect are the primary cause of the measured torques. In addition, the role of the NM/FM and FM/oxide interfaces is not yet fully understood. Part of the confusion in this field stems from the lack of using a consistent model to evaluate experimental data such that experimental results cannot easily be compared to each other.

This thesis addresses both of the above-mentioned points: One part is dedicated to the comparison of different SOT measurement techniques, focusing on the question whether the measured data can be understood within a common drift diffusion model. The second part deals with the dynamics of current induced magnetization reversal and, for the first time, presents a temporal and spatially resolved study of such a process.

This thesis is therefore separated into three main parts:

Part I provides the framework for understanding current induced SOT experiments in metallic NM/FM bilayers. For this purpose, the basics of micromagnetism and the equation of motion describing the magnetization dynamics are introduced. Subsequentially, a short introduction into the physical origin of spin orbit torques is given and a drift diffusion model used to describe field- and damping-like torques is introduced. As a last step,

[2] regarding the name convention, see footnote 2 on page 26

the well established theoretical concept of ferromagnetic resonance (FMR) and (dynamic) magnetic susceptibility is introduced as it is the basis of many approaches to quantify SOTs in NM/FM hetero structures.
Part II is dedicated to the fundamental question of the origin of the SOTs. A Pt(x)/Py(4 nm) sample series with varying Pt thickness is studied under the assumption that the bulk spin Hall effect is the dominant source of the damping-like torque. In this scenario, a consistent drift diffusion model exist for two complementary experimental techniques: the SHE induced spin transfer torque (STT) experiment on the one hand and the so-called inverse spin Hall effect (ISHE) experiment on the other hand. In the STT experiment, an ip charge current induces a measurable torque on the magnetization via the SHE generated spin current flow from the NM into the FM. There exist many different experimental techniques of this type, of which the so-called "modulation of damping" (MOD) is chosen in this work due to its experimental clarity. In the ISHE experiment, by contrast, magnetization dynamics induces a spin current flow from the FM into the NM, which is converted into a measurable charge current in the NM again via the SHE. From the reciprocity of the two experiments it is expected that measurements of the conversion efficiency (i.e. the spin Hall angle) of spin and charge currents should result in the same outcome if conducted by current induced SOT measurements on the one hand, as well as ISHE measurements on the other hand [Tse14]. It is shown in part II how such a comparable measurement must be set up in order to obtain clear experimental results and it is found that the STT/ISHE experiments deliver comparable results. However, indications are found for the appearance of effects that go beyond the bulk SHE model. A detailed description of the organization of part II is given on pages 47 ff.
Part III finally presents a time and space resolved study of the magnetization reversal in perpendicularly magnetized Pt/Co elements. By using 1 ns wide current pulses it is shown that deterministic magnetization reversal is possible for a wide range of applied fields and that the switching process itself is driven by complex domain nucleation and propagation.

Part I.

Micromagnetism and Spin Orbit Torques: Theoretical Framework

1. Magnetization Dynamics I: Energy Terms and Equation of Motion

This chapter is intended to introduce the terms and concepts in the description of magnetization dynamics needed throughout this work. It basically follows [Ber09; Kob13; Her09; Wol04]. At first, the coordinate system used within this thesis is introduced. The ferromagnetic film always lies within the x, y plane with a thickness $d \ll L, w$. The angle between the magnetization and the z axis is θ and the angle of the in-plane component of $\boldsymbol{M}$ with respect to the x axis is defined as φ.

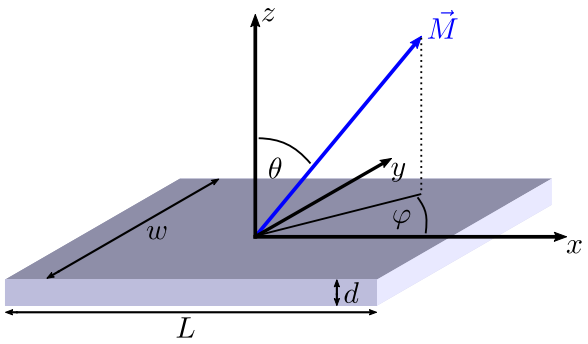

Figure 1.1.: *Coordinate system used in this work.*

1.1. Micromagnetism

In general, magnetism is purely a quantum mechanical phenomenon. To describe, for example a metallic ferromagnet, (FM) such as Ni or Co one needs to treat a many-body problem taking into account the electronic structure of the respective crystal and additionally the spin of the electrons. This can be done using e.g. density functional theory. However, if one wants to describe the magnetization dynamics of a macroscopic sample it, is impossible to use these methods due to the large number of atoms involved. It is therefore convenient to transfer the microscopic properties to a continuum theory describing the time evolution of the sample's magnetization under the influence of different torques [Kob13; Coe10; Sto06; Ber09]. This continuum theory is called micromagnetic theory. It describes the magnetization at every point in the ferromagnet as a vector function of space and time, $\boldsymbol{M}(\boldsymbol{r}, t)$. Using this formalism, analytic solutions can be derived for uniform

and nonuniform, linear and nonlinear magnetization dynamics as e.g. spin waves in thin magnetic films [Ber09; Gur96]. The same formalism, however, can be discretized onto a grid to carry out micromagnetic simulations, which allows to study magnetization dynamics that cannot be described analytically due to the complex magnetic interactions in real ferromagnetic devices. The key advantage of micromagnetic theory is that the size of the grid in these simulations can be chosen much bigger than the lattice constant of the FM crystal treated. The procedure is therefore also called coarse-graining [Gri03] and has to be treated with caution in certain situations.

The key assumption of the theory in general is $|\boldsymbol{M}(\boldsymbol{r},t)| = M_\mathrm{s}$ at every point. The saturation magnetization $M_\mathrm{s} = \frac{\sum \boldsymbol{\mu}}{V}$ is the sum over all microscopic magnetic moments $\boldsymbol{\mu}$ in a given (cell) volume V. This is true if the temperature is much smaller than the Curie temperature such that the exchange dominates over all the other energies at the smallest scale treated [Ber09]. Due to this restriction it is always possible to normalize $\boldsymbol{M}(\boldsymbol{r},t)$ by dividing by M_s and to use $\boldsymbol{m}(\boldsymbol{r},t) = \frac{\boldsymbol{M}(\boldsymbol{r},t)}{M_\mathrm{s}}$ to describe a system with the unit vector of the magnetization $\boldsymbol{m}$. In micromagnetic simulations, where the system is discretized into cells with dimensions dx, dy, dz, this constraint means that one cell always has a magnetic moment of $\boldsymbol{\mu}_\mathrm{cell} = M_\mathrm{s} V_\mathrm{cell}$ or, differently spoken, $M_\mathrm{cell} = M_\mathrm{s}$. The dimensions of the cells must then be chosen such that the magnetization direction varies only slightly between two neighboring cells, leading to cell sizes in the nm range, for short ranged problems such as e.g. domain walls, up to several µm, for long ranged problems as e.g. magnetostatic spin waves with wavelengths of tens of µm. In this work, micromagnetic simulations were carried out using the mumax^3 package which is documented in [Van14].

1.2. Energy Contributions

In a FM the spatial distribution of $\boldsymbol{m}(\boldsymbol{r},t)$ is given by the minimum of the free energy of the FM, E, that contains contributions from different origins. The total energy $E = \int_\mathrm{FM} dV (\sum \varepsilon)$ is evaluated as an integral over the whole FM volume, where the integrand is a sum of the different local energy densities ε that will be discussed in the following. What makes ferromagnetism such a rich field, is the fact that the energies at play do have very different scales both in strength as well as in their interaction range. A good example for this is the domain structure in perpendicular magnetized, ultrathin Co layers which arises due to the counterplay of the strong but short-ranged exchange interaction and the weaker but long ranged dipolar interaction. A broken symmetry at interfaces in combination with spin orbit coupling in such a system can give rise to a second, antisymmetric exchange called Dzyaloshinskii-Moriya interaction, which will have additional impact on the domain pattern. Since micromagnetism is a continuum theory, all energies need to be derived in continuous form.

1.2.1. Exchange interaction

The fundamental energy contribution in a FM is the exchange interaction between electrons which enables ferromagnetic ordering. The origin of exchange is purely quantum mechanical and results from the coulomb interaction between electrons in combination with the Pauli exclusion principle. It is directly proportional to the overlap of the spatial wavefunctions of the respective electrons and therefore is a short ranged interaction [Sto06, chapter 6]. For electrons with spin $\boldsymbol{S}$ that are localized at lattice points i the exchange interaction can be expressed by the so-called Heisenberg Hamiltonian [Coe10]

$$H_{\text{exch}} = -2\sum_{i>j} J_{ij}\boldsymbol{S}_i \cdot \boldsymbol{S}_j \tag{1.1}$$

where J_{ij} represents the exchange constant between electrons on site i and j. If only nearest neighbors are taken into account, J_{ij} can be simplified to a single exchange constant J for the whole lattice. In micromagnetics this Hamiltonian is expanded into a Taylor series [Chi10; Kit49; Kob13] and results in a continuous form such that the energy density reads [Ber09]

$$\varepsilon_{\text{ex}} = A\left((\nabla m_x)^2 + (\nabla m_y)^2 + (\nabla m_z)^2\right). \tag{1.2}$$

Here, V is the volume of the ferromagnet and A is the exchange stiffness constant which can, for a cubic lattice, be related to the exchange constant J by $A = \frac{nJS^2}{a}$ [Kit49; Chi10]. Here n is the number of atoms in a unit cell, S is the eigenvalue of the spin operator and a is the lattice parameter. Values for A are 13 pJ/m for Py [Van14] and (10-16) pJ/m for ultra-thin Co [Mik15; Thi12].

1.2.2. Dzyaloshinskii-Moriya interaction

In systems with reduced symmetry and strong spin orbit coupling an additional, antisymmetric exchange interaction has been found in the 1960s by Dzyaloshinskii and Moriya [Dzy58; Mor60a; Mor60b] in crystals without inversion center. It has the general form

$$H_{\text{DMI}} = -\sum_{i>j} \boldsymbol{D}_{ij} \cdot (\boldsymbol{S}_i \times \boldsymbol{S}_j). \tag{1.3}$$

Here, $\boldsymbol{D}_{ij}$ is the DM vector that is constructed from the symmetry of the crystal [Mor60a]. In contrast to the usual exchange interaction, the DMI tends to align spins perpendicular to each other and thereby favors magnetic textures that exhibit large gradients in $\boldsymbol{m}(\boldsymbol{r}, t)$ such as domain walls [Thi12]. In the case of ultrathin magnetic multilayers the inversion symmetry is broken at the interface which can lead to the emergence of a DMI even for FMs that show no such interaction in the bulk state [Thi12; Cré98]. This form of DMI is therefore called interfacial DMI (iDMI). For the case of a NM/FM/oxide layer structure

the continuous form of the iDMI can be written as [Thi12]

$$\varepsilon_{\mathrm{iDMI}} = D\left[m_z \nabla \boldsymbol{m} - (\boldsymbol{m}\cdot\nabla) m_z\right] \tag{1.4}$$

Here, D is the iDMI constant. The strength of the iDMI in Pt/Co/Al_2O_3(MgO) multilayers has been measured extensively the last years resulting in values from $D\cdot d_{\mathrm{Co}} \sim 0.3\,\mathrm{pJ/m}$ [Lee14b; Ben15] to $2\,\mathrm{pJ/m}$ [Kim15; Pai16; Bel15]. The exact value strongly depends on the interface [Kim17], which itself is strongly influenced by the growth conditions [Kim15].

1.2.3. Magnetostatic energy

The second class of energy densities is based on dipolar interactions between magnetic moments $\boldsymbol{\mu}_i$. It should first be mentioned that the energy of a magnetic moment in an external field $\boldsymbol{H}_{\mathrm{ext}}$, the so-called Zeeman energy is given by

$$E_{\mathrm{Z}} = -\mu_0 \boldsymbol{\mu}\cdot\boldsymbol{H}_{\mathrm{ext}} \quad \Leftrightarrow \quad \varepsilon_{\mathrm{Z}} = -\mu_0 M_{\mathrm{s}}\, \boldsymbol{m}\cdot\boldsymbol{H}_{\mathrm{ext}} \tag{1.5}$$

where the local energy density for the continuous case is given on the right-hand side. In a FM the magnetization at each point is subject to the field generated by the dipolar fields of the magnetic moments of the whole volume of the FM. The dipolar energy of two magnetic moments can be written as [Chi10, chapter 1][1]

$$E_{\mathrm{d}} = -\mu_0 \boldsymbol{\mu_1}\cdot\boldsymbol{H}_{\mathrm{d}} = -\frac{\mu_0}{4\pi|\boldsymbol{r}|^3}\left(3(\boldsymbol{\mu_1}\cdot\hat{\boldsymbol{r}})(\boldsymbol{\mu_2}\cdot\hat{\boldsymbol{r}}) - \boldsymbol{\mu_1}\cdot\boldsymbol{\mu_2}\right) \tag{1.6}$$

where $\boldsymbol{r}$ is the vector connecting the two magnetic moments in space. The first equality of the equation shows that the energy can be written in the form of Eq. (1.5), e.g. the energy of two dipoles is given by the Zeemann energy of $\boldsymbol{\mu}_1$ in the field generated by $\boldsymbol{\mu}_2$, here labeled $\boldsymbol{H}_{\mathrm{d}}$. If the FM is pictured in discretized form the field $\boldsymbol{H}_{\mathrm{d}}$ acting on the moment $\boldsymbol{\mu}_i$ is the sum over the dipole fields generated by all remaining magnetic moments $\boldsymbol{\mu}_{j\neq i}$

$$\boldsymbol{H}_{\mathrm{d},i} = \frac{1}{4\pi}\sum_j \left(\frac{\boldsymbol{\mu}_j}{|\boldsymbol{r}_i - \boldsymbol{r}_j|^3} - 3\frac{(\boldsymbol{\mu}_j\cdot(\boldsymbol{r}_i - \boldsymbol{r}_j))(\boldsymbol{r}_i - \boldsymbol{r}_j)}{|\boldsymbol{r}_i - \boldsymbol{r}_j|^5}\right). \tag{1.7}$$

The field $\boldsymbol{H}_{\mathrm{d}}$ is often called stray field outside the FM and demagnetizing field inside the FM. This sum can be converted into a continuous integral form which reads [Her09]

$$\boldsymbol{H}_{\mathrm{d}}(\boldsymbol{r}) = \frac{M_{\mathrm{s}}}{4\pi}\int dV' \frac{(\boldsymbol{r}-\boldsymbol{r}')\nabla\boldsymbol{m}}{|\boldsymbol{r}-\boldsymbol{r}'|^3} + M_{\mathrm{s}}\int dS' \frac{(\boldsymbol{r}-\boldsymbol{r}')\boldsymbol{m}\cdot\boldsymbol{n}}{|\boldsymbol{r}-\boldsymbol{r}'|^3} \tag{1.8}$$

where the first integral is taken over the volume of the FM and the second integral over its surface and $\boldsymbol{n}$ is the surface normal unit vector. The above equation can be interpreted

[1] note the different definition of magnetic moment in this book: $\boldsymbol{M} = \mu_0\boldsymbol{\mu}$.

as follows: there are two distinct sources of the demagnetizing field, one is $\nabla \boldsymbol{m}$ inside the bulk of the FM, which can therefore be identified as volume charge. On the boundary of the FM, $\boldsymbol{m} \cdot \boldsymbol{n}$ gives the directional derivative of $\boldsymbol{m}$ perpendicular to the surface and hence acts like a surface charge. Both charges build up a demagnetizing field that points into the opposite direction of $\boldsymbol{m}$ inside the FM, hence the name demagnetizing field.

Another approach to obtain $\boldsymbol{H}_\mathrm{d}$ is based on Maxwell's equations in matter. First it should be noted that, without current flow, the magnetic flux is given by $\boldsymbol{B} = \mu_0(\boldsymbol{H}_\mathrm{d} + \boldsymbol{M})$ with $\nabla \boldsymbol{B} = 0$ and $\nabla \times \boldsymbol{H} = 0$. It follows $\nabla \boldsymbol{H}_\mathrm{d} = -\nabla \boldsymbol{M}$ which is formally equal to the electrostatic equation $\nabla \boldsymbol{E} = \frac{\rho}{\varepsilon_0}$ with the charge density ρ. By associating a vector potential such that $\boldsymbol{H}_\mathrm{d} = \nabla U_\mathrm{d}$ the Poisson equation $\Delta \boldsymbol{H}_\mathrm{d} = \nabla \boldsymbol{M}$ has to be solved in order to find the demagnetizing field. It should be stressed that, in absence of other sufficiently strong fields, $\boldsymbol{M}$ is determined by $\boldsymbol{H}_\mathrm{d}$, which again depends on the magnetization such that finding the equilibrium position is highly nontrivial. Both the magnetization and the demagnetizing field are in general non-homogeneous throughout the FM if the form of the FM is not highly symmetric. There are cases, however, where the integration of Eq. (1.8) can be carried out analytically. This is the case for ferromagnetic ellipsoids, in which both the magnetization and the demagnetizing field are homogeneous and are related via a linear equation:

$$\boldsymbol{H}_\mathrm{d}(\boldsymbol{r}) = -M_\mathrm{s}\, \boldsymbol{N} \boldsymbol{m}. \tag{1.9}$$

Here, $\mathbf{N}$ is the so-called demagnetization tensor which can be diagonalized if the coordinate system (x, y, z) is in accordance with the main axes of the ellipsoid which will be labeled a, b, c. Then, only N_{xx}, N_{yy}, N_{zz} are nonzero and $N_{ii} \in [0, 1]$ while the trace is $N_{xx} + N_{yy} + N_{zz} = 1$.

The values for N_{ii} are calculated in [Osb45] for different limiting cases of ellipsoids. One example of a highly symmetric ellipsoid is a sphere, where the tensor elements are $N_{ii} = \frac{1}{3}$. In this thesis, thin films are treated, which can be approximated as infinitely flat oblate spheroids $a \sim b \gg c$ for which only one element of the demagnetizing tensor is nonzero:

$$\boldsymbol{H}_{\mathrm{d,thin\ film}} = -M_\mathrm{s} N_{zz} m_z \hat{z}, \qquad N_{zz} = 1 \tag{1.10}$$

If a structure, for example a (infinitely long) stripe is patterned out of the film which has dimensions $L > w \gg c$, where usually $L, w \sim \mu\mathrm{m}$ (with e.g. $\frac{L}{w} > 10$) and $d \sim \mathrm{nm}$, the demagnetization field is not homogeneous across the width of the stripe. It is possible, however, to define an average demagnetizing field over the whole volume of the FM such that, if the magnetization is saturated e.g. by an external field, $\boldsymbol{H}_{\mathrm{d,average}} := -\boldsymbol{N}_\mathrm{eff} \boldsymbol{M}_\mathrm{saturated}$. Often the approximation of an infinitely long elliptic cylinder is used, for which $N_{xx} \approx 0$, $N_{yy} \approx \frac{d}{w}$ and therefore $N_{zz} \approx 1 - \frac{d}{w}$; even though the geometry has the form of a rectangular prism and not of an ellipsoid due to the ease of the form of N_{yy}. For rectangular prisms such

demagnetizing factors are calculated in [Aha98] and compared to the elliptical case. Such a treatment allows estimating the impact of the demagnetizing field on e.g. the ferromagnetic resonance frequency of a stripe like device in saturated case but fails to predict the effects of the inhomogeneous demagnetization fields, which is most prominent in the case of low externally applied fields.
Finally, the energy density due to the demagnetizing field is given by:

$$\varepsilon_\mathrm{d} = -\frac{\mu_0 M_\mathrm{s}}{2} \boldsymbol{m} \cdot \boldsymbol{H}_\mathrm{d} \tag{1.11}$$

where the factor of two accounts for double counting. For the special case of a thin film/an infinitely long stripe this contribution can be written as

$$\varepsilon_\mathrm{d,film} = \frac{\mu_0 M_\mathrm{s}^2}{2} m_z^2., \quad \varepsilon_\mathrm{d,stripe} = \frac{\mu_0 M_\mathrm{s}^2}{2} \left(N_{yy} m_y^2 + N_{zz} m_z^2 \right). \tag{1.12}$$

It is directly clear from these equations that, in order to minimize the energy, the magnetization must lie in the film plane. To pull the magnetization out of plane, a large energy has to be provided by other sources. The effect of the demagnetizing field is therefore called shape anisotropy. Depending on the geometry of the FM, preferred directions for the magnetization exist resulting in a low demagnetizing energy which, are called easy axes/planes and directions with high demagnetizing energy, which are called hard axes/planes. For a thin film, regarding only the shape anisotropy, the film plane is the easy plane and the normal of the plane is the hard axis. Assuming a saturation magnetization of $\mu_0 M_\mathrm{s} = 1\,\mathrm{T}/1.8\,\mathrm{T}$ for Py/Co this gives an energy difference of $398/1289\,\mathrm{kJ/m^3}$ between an inplane (ip) and out-of-plane (oop) magnetized state.

1.2.4. Crystalline anisotropy

In all of the 3d transition metals Fe, Co and Ni a second type of anisotropy exists, that depends on the symmetry of the crystal lattice and is therefore called magneto-crystalline anisotropy. In these metals the 3d orbitals are partially filled and therefore determine the electronic and magnetic ground state. Due to the crystal structure of these metals, the orbital moment of the 3d states is quenched and the magnetism is carried mainly by the spin moment. The quenching is a result of the strong interaction of the 3d orbits with the crystal field created by the neighboring atoms which reduces the orbital moment to zero. However, via spin orbit coupling, a small part of the orbital moment is recreated. This orbital moment is now linked firmly to the lattice and the spin orbit coupling transfers this dependence on the spin moment. [Sto06; Coe10; Blu01]. This creates an energy density that depends on the symmetry of the crystal and is usually expressed in the coordinate system of the respective crystal by defining direction cosines (projection of $\boldsymbol{m}$ onto a given direction) $\alpha_i = \boldsymbol{m} \cdot \hat{e}_i$. Here, $\hat{e}_i$ is a crystal axis unit vector. For a cubic lattice, the crystal

axes coincide with an appropriate Cartesian coordinate system such that the unit vectors are x, y, z and therefore $\alpha_i = m_i,\ i = x, y, z$. The lowest order energy density has fourfold symmetry and reads [Coe10; Wol04; Mei14]:

$$\varepsilon_{\text{crystal}} = K_4 \left(\alpha_x^2\alpha_y^2 + \alpha_y^2\alpha_z^2 + \alpha_x^2\alpha_z^2\right) = \frac{K_4}{2}\left(1 - \alpha_x^4 - \alpha_y^4 - \alpha_z^4\right). \tag{1.13}$$

In this work two different FM systems are studied. The first FM used is Permalloy (Py) which is a $Ni_{80}Fe_{20}$ alloy designed such that the magneto-crystalline anisotropies of Fe and Ni (both having a cubic lattice) cancel each other and the result is a soft magnetic material with no significant crystalline anisotropy [Yin06].

The other system is a $Pt/Co(0.5\,nm)/Al_2O_3$ multilayer that deserves special attention. The layer structure is chosen such that the FM is magnetized perpendicular to the film plane, i.e. a very high anisotropy is present that overcomes the demagnetizing energy. Bulk Co has a hexagonal lattice structure with one preferred axis, the c-axis. Therefore the corresponding bulk anisotropy is uniaxial instead of cubic, with a very weak six-fold anisotropy. However, when thin Co layers are grown onto a Pt(111) layer, the Co layer adopts to the Pt fcc structure and therefore has cubic symmetry [Wel94; Nak98; Ole00; Wel01]. The volume anisotropy of fcc Co in bulk-like samples (several 1-10 nm thick) has been measured to be in the order of $K_4 = 70\,kJ/m^3$ [Suz94; Fas95], which is two orders of magnitude smaller than the shape anisotropy. Additionally, the fourfold anisotropy constant vanishes for sub-nm thickness [Fas95] and no sizable in-plane anisotropy is present in Pt/Co multilayers [Wel94] such that for a 0.5 nm thick Co film on Pt(111) the magneto-crystalline anisotropy from the bulk can be neglected.

1.2.5. Interface anisotropy

The physical origin for the perpendicular easy axis of the $Pt/Co(0.5\,nm)/Al_2O_3$ is the interaction of Co with Pt and Al_2O_3 at the respective interface. The perpendicular anisotropy induced by this effect is therefore called interfacial anisotropy. A detailed explanation of the physics of this anisotropy term, based on the model of Bruno [Bru89], can be found in [Sto06, chapt. 7.9].

Bruno has shown theoretically that for more than half-filled d-shells the magnetic anisotropy energy is directly linked to the anisotropy of the orbital moment $\varepsilon_{\text{mag}} \propto -(m_{\text{orb}}^{\text{easy}} - m_{\text{orb}}^{\text{hard}})\cos^2(\theta)$ [Bru89; Wel94; Wel95]. This theoretical prediction has been confirmed by measurements of both the anisotropy constant and the orbital momentum in Pt/Co, Pd/Co and Ni/Co multilayers [Wel94] as well as on a Au/Co-wedge/Au sandwich [Wel95]. A $\frac{1}{d_{\text{Co}}}$ dependence is found indicating that indeed the interface plays a dominant role.

To understand the origin of the PMA in $Pt/Co(0.5\,nm)/Al_2O_3$ it must be known how the orbital moments of the interfacial Co atoms are deformed to lead to an imbalance of ip and

oop orbital moment. It appears that both interfaces lead to a deformation of the Co 3d orbitals in a very similar manner. At the Pt(111)/Co interface, the Co 3d band hybridizes with the Pt 5d band which can be viewed as an effective uniaxial crystal field acting on the Co atoms [Nak98; Man08a]. This effect thus acts at the interface only and leads to a $\frac{1}{d_{\mathrm{Co}}}$ dependence of the anisotropy energy. This prediction was confirmed by measurements of the magnetic moment of single Co adatoms and clusters on a Pt(111) substrate [Gam03]. At the Co/Al_2O_3 interface the PMA stems from covalent Co-O bonds between the oxygen 2p orbitals and the Co 3d orbitals [Ole00; Mon02; Man08a]. In an experiment similar to the abovementioned study the orbital moment of Co adatoms on the oxygen site of a MgO single crystal have been studied and a huge PMA has been found which was again attributed to an uniaxial ligand field at the O site as a result of the covalent bond [Rau14]. The energy density from one interface can therefore be written as [Kim17]

$$\varepsilon_{\mathrm{int}} = -\frac{K_{\mathrm{int}}}{d_{\mathrm{Co}}}\cos^2(\theta) = -\frac{K_{\mathrm{int}}}{d_{\mathrm{Co}}}m_z^2. \tag{1.14}$$

Here, the unit of K_{int} is $[\mathrm{J/m^2}]$. Since there are two different interfaces, the respective terms have to be added up. The thickness dependence allows to separate the interface contribution from bulk anisotropies and if either interface can be changed independently, the contributions of both interfaces can be disentangled, see e.g. [Kim17]. In the present work an effective oop anisotropy constant resulting from both interfaces is used as input for calculations and micromagnetic simulations which is given by

$$\varepsilon_{\mathrm{oop}} = -K_{\mathrm{oop}}m_z^2 \tag{1.15}$$

with the effective oop anisotropy constant $K_{oop} = \frac{\left(K_{Pt/Co}+K_{Co/\mathrm{Al_2O_3}}\right)}{d_{\mathrm{Co}}}$. As the thickness of the Co layer in this work is $\sim 0.5\,\mathrm{nm}$, a large enough value for K_{oop} is reached to overcome the demagnetization energy.

Pure Py and NM/Py films grown onto GaAs substrate and capped with an oxide layer in most cases show an oop uniaxial anisotropy of similar origin. However, due to the fact that the Py thickness is in the nm range, the corresponding K_{oop} is much smaller than the demagnetizing energy.

In addition, it is known that Fe, Ni and Fe-Ni alloys grown on GaAs exhibit an additional in-plane uniaxial anisotropy, caused by the GaAs/FM interface [Yin06; Was05]. Such an ip uniaxial anisotropy can be expressed as [Wol04; Was05]:

$$\varepsilon_{\mathrm{ip,u}} = -K_{\mathrm{ip,u}}\left(\hat{\boldsymbol{n}}\cdot\boldsymbol{m}\right)^2 \tag{1.16}$$

with the ip unit vector $\hat{\boldsymbol{n}}$ is pointing along the direction of minimal energy. This anisotropy is very small in the samples measured in this work, the order of magnitude is $400/80/1\,\frac{\mathrm{kJ}}{\mathrm{m^3}}$

for shape/oop/ip anisotropy energy density even for the thinnest (4 nm) measured Py films. However, in the evaluation of ferromagnetic resonance data, even a small ip anisotropy can influence the fitting results for the other parameters and should be included in the analysis.

1.3. Landau-Lifshitz-Gilbert Equation

The knowledge of the energy contributions allows to find the equilibrium position of the magnetization by minimizing the free energy under the restraint $|\boldsymbol{M}| = M_\mathrm{s}$. However, if the magnetization is out of equilibrium, an appropriate equation of motion is needed to describe the dynamics of the system. This requirement is met by the Landau-Lifshitz-Gilbert equation (LLG) that describes the time evolution of a magnetic moment in an effective field $\boldsymbol{H}_\mathrm{eff}$ [Ber09]:

$$\frac{\partial \boldsymbol{m}}{\partial t} = -\gamma\, \boldsymbol{m} \times (\mu_0 \boldsymbol{H}_\mathrm{eff}) + \alpha\, \boldsymbol{m} \times \frac{\partial \boldsymbol{m}}{\partial t} = \boldsymbol{T}_\mathrm{eff} + \boldsymbol{T}_\mathrm{damp}. \tag{1.17}$$

Here γ is the gyromagnetic ratio and α is the Gilbert damping parameter. Since the change in magnetization is always perpendicular to $\boldsymbol{m}$, the LLG is a torque equation such that any terms on the right-hand side are labeled $\boldsymbol{T}_i$.

The first term on the right-hand side is called precessional torque, since a misalignement of $\boldsymbol{M}$ and the effective field $\boldsymbol{H}_\mathrm{eff}$ leads to a precession of the magnetization around $\boldsymbol{H}_\mathrm{eff}$. The precession frequency is determined by the gyromagnetic ratio γ. For a free electron, $\gamma = 176 \times 10^9 \frac{\mathrm{rad}}{\mathrm{Ts}}$ and therefore the precession frequency $f = \frac{\omega}{2\pi} = -\frac{\gamma}{2\pi}\mu_0 H_\mathrm{eff}$ lies in the GHz frequency range for an effective field $\mu_0 H_\mathrm{eff} \sim 100\,\mathrm{mT}$, a typical value for the experiments in this thesis[2].

The second torque, proposed by Gilbert 1955 [Gil55][3] introduces a viscous type damping where α determines the strength of the damping. In most FMs used for dynamic experiments α is small, ~ 0.008 in the Py films studied in this work but it can also be rather large, on the order of 0.5 for the ultra-thin Co grown on a Pt underlayer as will be detailed later.

The effective field introduced in the LLG equation comprises all different energy terms

[2] let θ be the angle between M and H, $H \| z$, and φ the angle describing the movement of M in the x, y plane, neglect the damping term. Then $\frac{\partial M}{\partial t} = M\cos(\theta)\frac{\partial \varphi}{\partial t} = \mu_0\gamma M H\cos(\theta) \quad \Rightarrow \quad \frac{\partial \varphi}{\partial t} = \omega = \gamma\mu_0 H_\mathrm{eff}$. This simple calculation holds only if the effective field does not depend on $\boldsymbol{M}$.

[3] [Sas09] gives a review about the form of the damping term and about this "special" reference which is always cited but cannot be found.

introduced before. Field and energy are connected via[4]

$$H_i = -\frac{1}{\mu_0 M_\mathrm{s}} \frac{\delta \varepsilon_i}{\delta \boldsymbol{m}} \tag{1.18}$$

where the index i stands for the respective energy term [Ber09]. Altogether, the effective field of a thin film is therefore given by [Ber09; Van14]

$$\begin{aligned} H_\mathrm{eff} &= H_\mathrm{exch} + H_\mathrm{DMI} + H_\mathrm{dem} + H_\mathrm{ani} + H_\mathrm{ext} \\ &= \frac{2A}{\mu_0 M_\mathrm{s}} \Delta \boldsymbol{m} + \frac{2D}{\mu_0 M_\mathrm{s}} \left(\frac{\partial m_z}{\partial x}, \frac{\partial m_z}{\partial y}, -\frac{\partial m_x}{\partial x} - \frac{\partial m_y}{\partial y} \right) - M_\mathrm{s} m_z + \frac{2K_\mathrm{oop}}{\mu_0 M_\mathrm{s}} m_z + H_\mathrm{ext}. \end{aligned} \tag{1.19}$$

From the LLG, the equilibrium of $\boldsymbol{m}$ is simply given by the condition $\boldsymbol{m}_\mathrm{eq} \times \boldsymbol{H}_\mathrm{eff} = 0$ and therefore $\boldsymbol{m}_\mathrm{eq} \parallel \boldsymbol{H}_\mathrm{eff}$.

In the last years it has been found that the injection of a charge current into NM/FM heterostructures influences the magnetization dynamics of the FM layer, i.e. additional torques on the magnetization are observed experimentally. These torques are called "spin orbit torques" (SOT) due to their physical origin, the spin orbit coupling [Gar13]. These additional torques must be included in the LLG equation. Due to the fundamental restriction of conservation of $|\boldsymbol{M}|$ any given torque acting on $\boldsymbol{m}$ can be decomposed into two orthogonal torques of the form

$$\begin{aligned} \boldsymbol{T}_\mathrm{FL} &= -\gamma \tau_\mathrm{FL} \boldsymbol{m} \times \boldsymbol{\sigma}_\mathrm{DL} \\ \boldsymbol{T}_\mathrm{DL} &= \gamma \tau_\mathrm{DL} \boldsymbol{m} \times (\boldsymbol{m} \times \boldsymbol{\sigma}_\mathrm{DL}) \end{aligned} \tag{1.20}$$

where $\boldsymbol{\sigma}_\mathrm{DL/FL}$ is a unit vector [Ber09]. Here the torque of $\boldsymbol{T}_\mathrm{FL}$ corresponds to the addition of another field $\boldsymbol{H} \parallel \boldsymbol{\sigma}$ to the effective field and induces a precession of $\boldsymbol{m}$ around $\boldsymbol{\sigma}_\mathrm{DL}$ if no other torque is present. Hence such a torque will be named field-like torque in the following. It can just be added to the effective field torque.

The form of $\boldsymbol{T}_\mathrm{DL}$ is of fundamental difference since this torque directly moves the magnetization to the direction of $\boldsymbol{\sigma}$. The vector component of $\boldsymbol{\sigma}$ that is parallel/antiparallel to $\boldsymbol{H}_\mathrm{eff}$ will counteract/enhance the damping torque $\boldsymbol{T}_\mathrm{damp}$, hence it is called damping-like torque. In the general case where $\boldsymbol{\sigma} \nparallel \boldsymbol{H}_\mathrm{eff}$ the equilibrium position must be calculated from $\boldsymbol{T}_\mathrm{eff} + \boldsymbol{T}_\mathrm{DL} = 0$ and is therefore no longer given by $\boldsymbol{M}_\mathrm{eq} \parallel \boldsymbol{H}_\mathrm{eff}$.

[4] the variation in this equation reduces to a simple derivative for all fields created by non-space dependent energy contributions like the anisotropy fields etc. For the exchange energy, the calculation is more difficult and results in the expression given below [Ber09; Van14]. The derivative with respect to $\boldsymbol{m}$ is, strictly speaking, a directional derivative on the surface of the sphere with radius M_s due to the conservation of the magnetization vector's length. This should be kept in mind when doing calculations in Cartesian coordinates, especially when plotting anisotropy fields etc. However, the effective field can be calculated by applying the full gradient in all 3 Cartesian dimensions, as done e.g. in mumax^3 [Van14] and still be used in the LLG equation because the cross product ignores the components that are not perpendicular to $\boldsymbol{m}$. The author wants to thank Johannes Stigloher and Martin Buchner for a fruitful discussion of this (sometimes) important detail.

Including the additional SOTs, the generalized LLG reads

$$\frac{\partial \boldsymbol{m}}{\partial t} = -\gamma \boldsymbol{m} \times (\mu_0 \boldsymbol{H}_{\text{eff}} + \tau_{\text{FL}} \boldsymbol{\sigma}_{\text{FL}}) + \alpha \boldsymbol{m} \times \frac{\partial \boldsymbol{m}}{\partial t} + \gamma \tau_{\text{DL}} \boldsymbol{m} \times (\boldsymbol{m} \times \boldsymbol{\sigma}_{\text{DL}}) \,. \tag{1.21}$$

To solve the LLG numerically, it is common to transform it into its explicit form[5] which can be handled by standard ODE solvers and reads:

$$\begin{aligned} \frac{\partial \boldsymbol{m}}{\partial t} = \frac{\gamma}{1+\alpha^2} \Big\{ & -\boldsymbol{m} \times (\mu_0 \boldsymbol{H}_{\text{eff}} + \tau_{\text{FL}} \boldsymbol{\sigma}_{\text{FL}}) + \tau_{\text{DL}} \boldsymbol{m} \times (\boldsymbol{m} \times \boldsymbol{\sigma}_{\text{DL}}) \\ & - \alpha \Big[\boldsymbol{m} \times (\boldsymbol{m} \times (\mu_0 \boldsymbol{H}_{\text{eff}} + \tau_{\text{FL}} \boldsymbol{\sigma}_{\text{FL}})) - \tau_{\text{DL}} \boldsymbol{m} \times \boldsymbol{\sigma}_{\text{DL}} \Big] \Big\} \,. \end{aligned} \tag{1.22}$$

This equation is also basis of the micromagnetic simulations package mumax[3] used in this work, see [Van14].

[5] without the additional torques, the transformation converts the LLG into the mathematically equivalent Landau-Lifshitz equation of motion, see [Ber09, p. 27f].

2. Spin Orbit Torques in Metallic Multilayers

The key for an efficient manipulation of NM/FM/oxide elements via electrical currents lies in the so-called spin orbit torques that are created by spin currents and spin accumulations either at the NM/FM or FM/oxide interface and/or in the bulk of the NM. The name spin orbit torque already implies that the origin of theses effects lies in the spin orbit coupling. Measurements of current induced torques in FM/NM/Oxide multilayers have shown that both field-like and damping-like torques are present in general, however, the relative strength and sign differ from multilayer to multilayer, depending on the single layer properties as well as on the interfaces of the NM. It is therefore quite puzzling to find out about the microscopic origins of the torques and to make quantitative predictions in order to engineer the layer structures for a given application.
There are two distinct scenarios that lead to a torque on the magnetization: If a spin accumulation in the FM itself is created by some mechanism and if this spin accumulation is not collinear with the magnetization, the spin accumulation will start to precess around the local magnetization due to exchange coupling. Vice versa, the magnetization precesses around the spin accumulation giving rise to a field-like torque. In the second case, a spin current enters a FM at an interface and is absorbed, thereby transporting angular momentum to the FM. In this case the torque on the magnetization has a damping-like form.
There are two distinct physical effects that have evolved as explanation for the appearance of the experimentally observed torques which will be discussed below, namely the spin Hall effect (SHE) and the Rashba-Edelstein (REE) effect. Thus, in the following the concept of spin accumulation and spin current will be introduced. Afterwards, both SHE and REE will be introduced and it will be shown how these effects can create a torque on the magnetization.

2.1. Spin and Charge Currents

In this section the concept of spin currents and spin accumulations shall be introduced. Phenomenologically, these quantities can be understood well in the context of the drift diffusion formalism. Therefore, in the following the drift diffusion equations for both charge and spin transport will be introduced for NMs first and then be generalized for FMs, following the respective sections in [Fab07; Obs15] in accordance with [Dya12; Han13a].

2.1.1. Drift diffusion equation for charge

In metals, electric transport can be described by a drift diffusion model if the dimensions of the device are much bigger than the mean free path and the system is only distorted little from equilibrium. In this case, the drift diffusion equation for the electron charge density is given by [Fab07]

$$\begin{aligned} -|e|\frac{\partial n}{\partial t} + \nabla \boldsymbol{j}^{\mathrm{c}} &= 0 \\ j_i^{\mathrm{c}} = \sigma E_i + |e| D \frac{\partial n}{\partial x_i} &= \sigma (\nabla \mu)_i. \end{aligned} \tag{2.1}$$

Here, n is the electron particle density, $j_i^{\mathrm{c}} = -|e| j_i^{\mathrm{part}}$ is the charge flow in direction i, where j_i^{part} is the particle current, $\sigma = \frac{e^2 \tau n}{m}$ and $D = \frac{v_{\mathrm{F}}^2 \tau}{2}$ are the electrical conductivity and the diffusion coefficient where τ is the momentum relaxation time, m the electron (effective) mass and v_{F} the Fermi velocity. The first line is a continuity equation for the charge and the second line defines the charge current. The charge density at a given point in space can change only if there is a divergence in the charge current at this point. It is convenient to define an electrical effective potential μ such that the current can be written as $\boldsymbol{j}_{\mathrm{c}} = \sigma \nabla \mu$. The drift diffusion equation is solved for μ and the current can be calculated subsequently.

2.1.2. Drift diffusion equation for spin

Similar equations describe the spin drift and diffusion, however, due to the nature of spin transport two important differences occur. The first difference between charge and spin drift and diffusion is the fact that there is no conservation for the spin and an additional relaxation term is added to the continuity equation for the spin. The second difference is that the spin current has two degrees of freedom. A spin current is therefore described by a second rank tensor $\boldsymbol{j}^{\mathrm{s}}$ with entries j_{ij}^{s} where the first index denotes the spatial coordinate and the second index denotes the spin polarization direction. Consider first a NM where a spin (particle) accumulation can be defined as $s_j = n_{+j} - n_{-j}$ where $n_{\pm j}$ is the number of electrons with spin pointing in $\pm x_j$-direction. The spin momentum accumulation is then $\frac{\hbar}{2}\boldsymbol{s}$. In a NM all parameters, e.g. like σ, are the same for electrons regardless of their spin direction and the drift diffusion equation can be written as [Fab07]

$$\begin{aligned} 0 &= \frac{\hbar}{2}\left[\frac{\partial s_j}{\partial t} + \frac{s_j}{\tau_{\mathrm{s}}}\right] + \frac{\partial j_{ij}^{\mathrm{s}}}{\partial x_i} \\ j_{ij}^{\mathrm{s}} &= \frac{\hbar}{2}\left[-\mu' E_i s_j - D\frac{\partial s_j}{\partial x_i}\right]. \end{aligned} \tag{2.2}$$

In this equation τ_{s} is the (isotropic) spin relaxation time. A characteristic length that coincides with this time is the so-called spin diffusion length $\lambda_{\mathrm{s}} = \sqrt{D\tau_{\mathrm{s}}}$. The origin of

spin relaxation in metals is usually attributed to the Elliot-Yafet relaxation mechanism [Ell54; Yaf63]. The basic idea of this model is that every momentum scattering event has a certain probability to also switch the spin, which implies $\tau_s = P\tau$ with the probability factor P which must be smaller than one. The constant μ' in the definition of the spin current denotes the mobility and should not be confused with the quasichemical potential μ.

The equations can also be expressed in terms of a quasichemical potential for the spin $\boldsymbol{\mu}^s$ which is, in contrast to the charge current case, a vector that points in the direction of the spin polarization. For the steady state $\frac{\partial \boldsymbol{\mu}^s}{\partial t} = 0$ the equations reduce to [Ami16b; Fab07]:

$$\begin{aligned} \nabla^2 \boldsymbol{\mu}^s &= \frac{\boldsymbol{\mu}^s}{\lambda_s^2} \\ j_{ij}^s &= \frac{\hbar}{2|e|}\sigma \frac{\partial \mu_j^s}{\partial x_i} \end{aligned} \tag{2.3}$$

It should be noted that the spin quasichemical potential and the spin particle accumulation are related by $\boldsymbol{s} = g(\epsilon_F)|e|\boldsymbol{\mu}^s$, where g denotes the density of states at the Fermi level. From the definition of the spin current it can be seen that there are two different cases of spin transport: if there is a spin accumulation and an electric field, the electrons will drift due to this field and in addition carry a net spin current. This situation is referred to as a spin polarized current. On the other hand, a non-homogeneous spin accumulation will lead to a diffusion of spin density, i.e. a spin current, without any charge transport. This is what will be called a (pure) spin current in this thesis.

2.1.3. Drift diffusion in ferromagnets

In an itinerant FM, transport is usually split up into two channels for majority and minority electrons. Let $\uparrow$ / $\downarrow$ denote the majority/minority electrons[1]. The total charge current is given by the sum of the currents carried by both channels, $\boldsymbol{j}^c = \boldsymbol{j}^{c,\uparrow} + \boldsymbol{j}^{c,\downarrow}$. The conductivity is different for both spin populations, and is defined as $\sigma_{\uparrow/\downarrow}$. Then $\sigma = \sigma_\uparrow + \sigma_\downarrow$ is the overall conductivity, $\sigma_s = \sigma_\uparrow - \sigma_\downarrow$ is defined as the spin spin conductivity and $P_\sigma = \frac{\sigma_s}{\sigma}$ as the conductivity spin polarization. In a FM, the quantization axis is naturally defined by the magnetization and usually the coordinate system is chosen such that $\uparrow, \downarrow \parallel \boldsymbol{m} \parallel \hat{z}$. If the spin polarization in the FM is allowed to have components in any direction, the charge

[1] It should be kept in mind that the majority electrons carry spin which is antiparallel to the magnetization unit vector $\boldsymbol{m}$.

and spin current in the FM are [Han13a]:

$$\begin{aligned} j_i^c &= \sigma \frac{\partial}{\partial x_i}\mu - P_\sigma \sigma \frac{\partial}{\partial x_i}(\boldsymbol{m}\cdot\boldsymbol{\mu}^{\mathrm{s}}) \\ j_{ij}^{\mathrm{s}} &= \frac{\hbar}{2|e|}\left[P_\sigma \sigma m_j \frac{\partial}{\partial x_i}\mu - \sigma \frac{\partial}{\partial x_i}\mu_j^{\mathrm{s}}\right]. \end{aligned} \tag{2.4}$$

For $P_\sigma = 0$ these equations reduce to the NM case. In an itinerant FM charge transport is usually accompanied by spin currents due to the fact that the total current is spin polarized. The same holds the other way; if there is a spin current due to a non-homogeneous spin density, there will be an additional charge current. There are, however, physical effects that couple even pure spin and charge currents in a NM as well in a FM. These effects will be introduced in the next section.
It should be noted that the drift diffusion equations in the FM need to be extended in order to take into account the (damped) precession of the local, nonequilibrium spin density around $\boldsymbol{m}$ as will be described in detail in sect. I.2.3 [Han13a]:

$$\frac{\hbar}{2}\left[\frac{\partial s_j}{\partial t} + \frac{s_j}{\tau_{\mathrm{s}}} + \frac{1}{\tau_{\mathrm{ex}}}\boldsymbol{s}\times\boldsymbol{m} + \frac{1}{\tau_{\mathrm{dp}}}\boldsymbol{m}\times(\boldsymbol{s}\times\boldsymbol{m})\right] + \frac{\partial j_{ij}^{\mathrm{s}}}{\partial x_i} = 0. \tag{2.5}$$

In this equation, the term $\frac{1}{\tau_{\mathrm{ex}}}\boldsymbol{s}\times\boldsymbol{m}$ describes the precession of a spin accumulation around the local magnetization due to exchange coupling and the term $\frac{1}{\tau_{\mathrm{dp}}}\boldsymbol{m}\times(\boldsymbol{s}\times\boldsymbol{m})$ describes the damping of this precession, i.e. the absorption of the transverse component of $\boldsymbol{s}$ with respect to $\boldsymbol{m}$. This damping process is very fast in the metallic ferromagnets treated in this work. Therefore any noncollinear spin accumulation that is the result of a spin current entering the FM at an interface, is absorbed in the FM within a few lattice constants [Sti02]. It is therefore convenient to drop the two terms in the drift diffusion equation and shift the absorption of a spin current into the boundary conditions instead [Han13a]. However, if there is a source of spin accumulation within the bulk of the FM, the precession has to be taken into account explicitly as shown in sect. I.2.3.

2.2. Spin Hall Effect

The spin Hall effect (SHE) describes the phenomenon of the conversion of a charge current into a transverse pure spin current. The SHE has been proposed in 1971 by Dyakonov and Perel [Dya71a; Dya71b] but was brought to the attention of the spintronic community only by Hirsch in 1999 [Hir99] and subsequently by Zhang (2000) [Zha00]. The first experimental observation has then been realized in 2004 [Kat04; Wun05] in semiconductors. Since then the SHE has been explored as an efficient way to manipulate and even switch the magnetization in NM/FM bilayers by charge current injection [Mir11; Liu12b; Liu12a]. A comprehensive review of the spin Hall effect has recently been published by Sinova et

al. [Sin15] and is followed throughout this section.

Under the influence of spin orbit interaction, spin and charge currents become coupled in such a way that from a charge current a transverse spin current is created and vice versa. In the drift diffusion formalism, the spin orbit interaction connects the equations for spin and charge currents via a constant θ_{SH} that is called the spin Hall angle $0 < \theta_{\mathrm{SH}} < 1$ [Dya12]:

$$\begin{aligned} j_i^{\mathrm{c}} &= j_i^{\mathrm{c},0} + \frac{2|e|}{\hbar}\theta_{\mathrm{SH}}\,\epsilon_{ijk}\,j_{jk}^{\mathrm{s},0} \\ j_{ij}^{\mathrm{s}} &= j_{ij}^{\mathrm{s},0} - \frac{\hbar}{2|e|}\theta_{\mathrm{SH}}\,\epsilon_{ijk}\,j_k^{\mathrm{c},0}. \end{aligned} \tag{2.6}$$

Here ϵ_{ijk} is the Levi-Civita symbol, and $\boldsymbol{j}_i^{\mathrm{c},0}/j_{ij}^{\mathrm{s},0}$ are the charge/spin currents without spin orbit coupling. The polarization of the spin current is always perpendicular to both charge current and spin current flow direction. For a positive θ_{SH} the polarization unit vector $\boldsymbol{\sigma} = \boldsymbol{n} \times \hat{\boldsymbol{j}}^{\mathrm{c}}$ with the spin current flow direction $\boldsymbol{n}$ [Dec12]. The modified expressions for charge and spin current then read explicitly [Sin15; Dya07; Obs15]:

$$\boldsymbol{j}_i^{\mathrm{c}} = \sigma E_i + |e| D \frac{\partial n}{\partial x_i} - |e|\theta_{\mathrm{SH}}\epsilon_{ijk}\left[\mu' E_j s_k + D\frac{\partial s_k}{\partial x_j}\right] \tag{2.7}$$

$$\boldsymbol{j}_{ij}^{\mathrm{s}} = \frac{\hbar}{2}\left\{-\mu' E_i s_j - D\frac{\partial s_j}{\partial x_i} - \frac{\theta_{\mathrm{SH}}}{|e|}\epsilon_{ijk}\left[\sigma E_k + |e| D\frac{\partial n}{\partial x_k}\right]\right\}. \tag{2.8}$$

The third term in Eq. (2.7) corresponds to the anomalous Hall effect (AHE) and describes the creation of a transverse charge current if a spin polarized current flows in a material. This effect is known in the context of transport in FMs. The fourth term is the inverse spin Hall effect (ISHE), here a transverse charge current is created by a pure spin current. The distinction between these two terms has only arisen historically because the AHE was experimentally found already in 1881 by E. H. Hall (in FM), in contrast to the ISHE which was discovered only recently. The reason for this discrepancy is that in a FM a spin-polarized current can be created easily by applying a dc current. The AHE can be measured easily by picking up the transverse voltage. By contrast to this, the creation of a pure spin current and a subsequent measurement of the resulting spin accumulation has become possible only recently. For the reciprocal effect, such a distinction is not existent: the third and fourth term in Eq. (2.8) together are called spin Hall effect and describe the creation of a pure spin current from a charge current.

The physical origin of the conversion is the same in all cases and has provided a puzzle for theoretical physicists for a long time. The theory of AHE has evolved since the first discovery over 100 years ago finally providing a framework for the understanding of the AHE and the SHE. A detailed description of the AHE and its history can be found in [Nag10]. There are three semiclassical origins of the SHE and AHE, related to different microscopic origins: i) skew scattering, ii) side jump and iii) intrinsic SHE. The first two of

these mechanisms involve scattering on impurities that include spin orbit interaction. The last mechanism leads to a transverse velocity of electrons in a perfect crystal depending only on the band structure, hence its name. A detailed description of these mechanisms, both historically and physically, can be found in recent reviews [Sin15; Nag10]. Here, the important implications for experiments defined in [Sin15] shall be recaptured shortly.

The contributions of different microscopic effects can be grouped by different scaling behavior regarding the dependence on the Bloch state transport lifetime τ. Skew scattering as well as the extrinsic side jump both scale linear with τ, whereas the intrinsic side jump and the intrinsic contribution both scale with τ^0, i.e. they are independent of τ. Here, intrinsic side jump means that the SOC is present in the electrons that scatter at a potential with no SOC term and extrinsic side jump means that electrons without SOC scatter at a potential that has an additional SOC term. Different contributions have to be distinguished by comparison of fully microscopic linear response theory calculations and semiclassical theory.

In experiments, the different contributions can thus be addressed by the different scaling as e.g. possible by tuning the conductivity of the SH material and therefore by tuning τ as published recently for Pt [Sag16].

The pure spin current within the NM does not lead to a spin accumulation within the bulk but only at the borders of the NM structure due to the boundary. The size of the spin accumulation region depends on the spin diffusion length, which leads to different possible measurements and applications depending on the value of λ_s, as will be discussed below.

In a thin film stripe where the current flow is in-plane, there are two nonzero components of the spin current (directions) given by the symmetry of the system. Let $\vec{j}^\mathrm{c} = j\hat{x}$ without loss of generality. Then there is, on the one hand, the in-plane spin current, transverse to j which is polarized perpendicular to the film, j^s_{yz} and, on the other hand, a spin current flowing in z-direction with a polarization in y-direction, j^s_{zy}. In the first experimental observation of the SHE the oop spin accumulation due to the in-plane spin current could be measured due to a long spin diffusion length in the micrometer range in a semiconductor system.

It is instructive to write down the spin drift diffusion equation for this case in the steady state using Eq. (2.2) and Eq. (2.8). The assumption $\vec{j}^\mathrm{c} = j^c\hat{x}$ is introduced via $\boldsymbol{E} = E_x\hat{x}$. Then the equation for s_z across the y direction is:

$$\left.\begin{aligned} \frac{\hbar}{2}\frac{s_z}{\lambda_\mathrm{s}^2} + \frac{\partial j^\mathrm{s}_{yz}}{\partial y} &= 0 \\ j^\mathrm{s}_{yz} &= \frac{\hbar}{2}\left[-D\frac{\partial s_z}{\partial y} - \frac{\theta_\mathrm{SH} j^\mathrm{c}_x}{|e|}\right] \end{aligned}\right\} \quad \frac{s_z}{\tau_\mathrm{s}} - D\frac{\partial^2 s_z}{\partial y^2} = 0. \tag{2.9}$$

The total spin current must vanish at the edge of the film such that the boundary condition

is

$$j_{yz}^{s}\left(y = \pm\frac{w}{2}\right) = 0. \tag{2.10}$$

The solution of the problem is then given by [Kat04]:

$$s_z(y) = -\frac{\lambda_s \theta_{SH} j_x^c}{|e|D} \frac{\sinh\left(\frac{y}{\lambda_s}\right)}{\cosh\left(\frac{w}{2\lambda_s}\right)} \tag{2.11}$$

Due to the SHE induced spin current, there is an oop spin accumulation at the edges of the film; the width of the spin accumulation region is given by the spin diffusion length. In semiconductors, this length can be as big as several µm, such that the oop spin accumulation can be measured directly, as done in the experiment of Kato et al. [Kat04], where λ_s ~3.5 µm was found. In Fig. I.2.1, the spin accumulation and spin current according to Eq. (2.11) are shown in comparison to the experimental result of Kato et al.

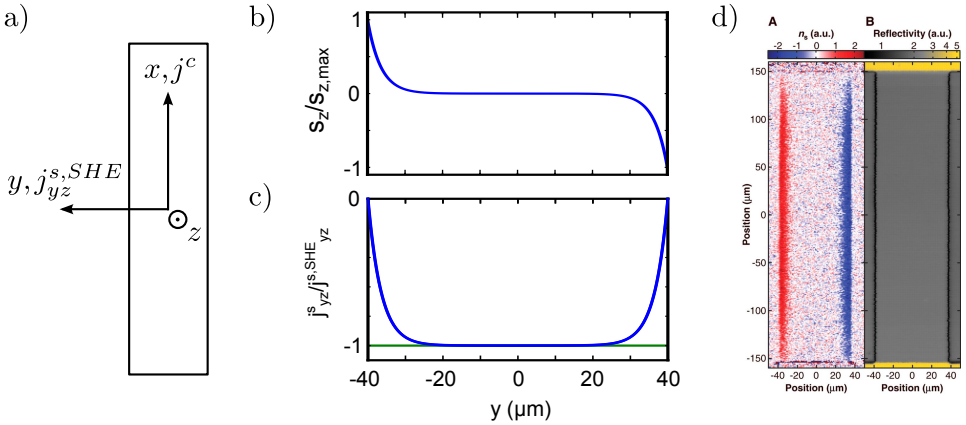

Figure 2.1.: *Spin accumulation and current due to the SHE. a): coordinate system used. A charge current flows through a stripe of width $w = 6\,\mu m$ and the resulting spin Hall spin current flows in $-y$ direction, carrying spin polarization in $+z$. b) shows the spin accumulation for $\lambda_s = 3.5\,\mu m$ and c) shows the spin Hall spin current in green and the total spin current in blue. d) first measurement of the SHE in a GaAs stripe. Preprinted with permission from [Kat04].*

In metals like Pt by contrast, the spin diffusion length is only of the order of a few nm such that the oop spin accumulation at the edge of a microstripe cannot be visualized directly and - thinking of a NM/FM bilayer - will not influence the magnetization dynamics due to the negligible area on which it acts. However, the short spin diffusion length leads to the possibility of using the spin current that flows perpendicular to the NM/FM interface in a bilayer structure.

The spin current leads to a spin accumulation at the NM/FM boundary and part of this spin accumulation diffuses into the FM, where the component transverse to the magnetization is absorbed. In this case, angular momentum is transferred from the NM to the FM thereby creating a possibility to influence the magnetization dynamics of the FM. The

torque exerted on the FM by this mechanism depends on the bulk properties of the NM (such as the strength of the SHE and λ_S) as well as on the NM/FM interface. A drift diffusion model describing these effects is introduced in section I.2.4.

2.3. Rashba-Edelstein Effect

The Rashba-Edelstein effect[2] leads to a spin polarization (spin accumulation) due to an electric current. The Rashba effect is the primary source of the field-like torque as will be shown in this section. It is fundamentally different from the SHE, where there is no spin accumulation in the bulk, only at the interface. The Rashba effect has first been discovered in semiconductors with broken bulk inversion symmetry and/or structure inversion asymmetry (SIA). Bulk inversion asymmetry (BIA) means that the crystal itself has no inversion center; SIA denotes the symmetry breaking resulting from (unequal) interfaces. A review about this effect in semiconductors is given by [Gan16][3] and [Gan14]. The transfer to metallic multilayer systems is described in [Gam11; Mir10b]. A review concentrating on the latest developments is given by [Man15].

The broken symmetry in combination with SOC leads to additional terms in the Hamiltonian of the conduction electrons that depend on the type of symmetry breaking (i.e. the point group of the system, see [Gan14]) and on the strength of SOC. Generally, the absence of inversion symmetry is found to lead to a $\boldsymbol{k}$ dependent spin splitting of the bands. This spin splitting is expressed by a Hamiltonian that contains the product of $\boldsymbol{k}$ and $\boldsymbol{\sigma}$ where the former is the electron wave vector and the latter is the vector of Pauli spin matrices of the electron [Gan14]. There are two names that are associated with two cases of broken symmetry leading to different splitting Hamiltonians. The first one is called Dresselhaus spin splitting, which applies for BIA in bulk crystals, leading to cubic terms in k [Dre55]; and for BIA in 2D semiconductor quantum wells, where it leads to k-linear terms [Gan14]. The second one is called Rashba spin splitting and has been predicted for crystals with one single high-symmetry axis [Ras60] and for SIA in heterostructures and multilayers with unequal interfaces [Byc84]. The Pt/Co/Al_2O_3 and Pt/Py/Al_2O_3 layers used in this work do not show BIA; therefore only the Rashba type effect can be observed. Most of the theory concerning Rashba and Edelstein effects has been developed for 2D systems due to the fact that these effects have mostly been studied in semiconductor heterostructures. In such a structure, electron motion is confined to the x, y plane and the symmetry breaking at interfaces happens in z-direction. In such a 2D system, the so-called Rashba

[2] There are many different names that are used for this effect, see e.g. [Gan16] but in the context of metallic multilayers the effect is mostly labeled Rashba/or Edelstein effect such that this name shall be used in this work.

[3] this paper corresponds to chapter 24 from [Tsy12]

Hamiltonian is written as [Gam11; Byc84]

$$\mathcal{H}_{\mathrm{SO,R}} = \alpha_{\mathrm{R}} \left(\boldsymbol{k} \times \hat{\mathbf{z}} \right) \cdot \boldsymbol{\sigma} \tag{2.12}$$

with the Rashba constant α_{R} describing the strength of the SOC. The z-axis is parallel to the film normal. This Hamiltonian is constructed by symmetry arguments and is the basis for all calculations regardless of the microscopic origin of the splitting. It can be seen that this form of the Hamiltonian formally corresponds to the interaction of the electron spin with a k-dependent magnetic field by writing

$$\mathcal{H}_{\mathrm{SO,R}} = \boldsymbol{\sigma} \cdot \boldsymbol{B}_{\mathrm{SO,R}}, \qquad \boldsymbol{B}_{\mathrm{SO,R}} = \alpha_{\mathrm{R}} \left(\boldsymbol{k} \times \hat{\mathbf{z}} \right) \tag{2.13}$$

It should be noted that this field does not break the time reversal symmetry and only acts on the electron‘s spin, not on the charge such that the term “field” should therefore be used with care [Gan14].

The microscopic origin of the Rashba Hamiltonian and/or the Rashba field is discussed controversely in the literature, a recent review is given in [Kra15] and the references on page 1 therein. One explanation that occurs in literature is to treat the Rashba effect in analogy to the spin orbit coupling of an electron with orbital momentum $\boldsymbol{l}$ that moves in the electric potential of a nucleus. Due to relativistic effects, the electric field transforms into an effective magnetic field acting on the spin of the electron, thus coupling orbital and spin moment [Sto06, chap. 6.4]. If now the electric fields in a crystal have a broken symmetry, e.g. at an interface where the ligand fields for example may have a preferred axis oop, the conduction electrons experience a net electric field perpendicular to the interface. The Rashba field is then related to the asymmetric crystal field potential (V) of either an interface (SIA) or the crystal itself (BIA) [Gam11]. An electron moving in the electric field of the potential $\boldsymbol{E} = -\nabla V$ in this picture feels a magnetic field $\boldsymbol{B}_{\mathrm{SO}} = -\frac{\hbar}{2m_e c^2} \boldsymbol{k} \times \boldsymbol{E}$, which is exactly the form of $\boldsymbol{B}_{\mathrm{SO,R}}$ [Gam11; Sto06, chap. 6.4]. Unfortunately, the simple assumption of a field gradient at the interface is an oversimplification, see [Pfe99; Kra15].

The occurrence of the k-dependent Rashba field directly gives a hand-waving argument how a current can create a spin accumulation in a system where it acts on the carrier electrons: if spin relaxation is taken into account, the electrons will (partly) align with the average Rashba field. The average Rashba field again is given by the nonzero averaged k-vector due to an applied in-plane current [Ede90].

Indeed it has been shown by Vas'ko & Prima [Vas79], Aronov & Lyanda-Geller [Aro89], and Edelstein [Ede90] that a charge current in the presence of the Rashba Hamiltonian Eq. (2.12) leads to a spin polarization of the conduction electrons in semiconductors [Gan16]. A key ingredient to observe the spin polarization is indeed spin relaxation, as worked out nicely for different relaxation mechanisms in [Aro91].

In contrast to the SHE, the spin accumulation is built up directly within the FM which immediately leads to a coupling of spin accumulation and magnetization which, in turn, generates a torque on $\boldsymbol{m}$ as described below.
In a ferromagnetic transition metal, the spin accumulation of the conduction electrons couples to the local magnetic moments via exchange coupling. For the 3d ferromagnets Fe, Co and Ni the more localized d-electrons and the delocalized s electrons can be separated and the system is treated as if the d-electrons carry the magnetization, the s electrons carry the current and the two electron populations are coupled via exchange [Man08b; Man09; MA09; Gam11]. Then, the Hamiltonian for the s-electrons reads [Man09]

$$\mathcal{H} = \frac{\boldsymbol{p}^2}{2m_\mathrm{e}} - \Delta_\mathrm{ex}\boldsymbol{m}\cdot\boldsymbol{\sigma} + \frac{\hbar}{2m_\mathrm{e}c^2}\left(\nabla V \times \boldsymbol{p}\right)\cdot\boldsymbol{\sigma}. \tag{2.14}$$

The first term is the free electron energy, the second term describes the exchange energy between the itinerant electrons ($\Delta_\mathrm{ex} = \frac{J_\mathrm{ex}\hbar M_\mathrm{s}}{2\gamma}$ [MA09]) and the magnetization $\boldsymbol{m}$ and the third term is the spin orbit term that reduces to the Rashba interaction form for a metallic multilayer without BIA. Due to the coupling of carrier spins and magnetization, the spin accumulation created by the current will induce a torque on $\boldsymbol{m}$. In the case in which the exchange coupling is much stronger than the SOC, the torque is calculated to be [Man09; MA09; Gam11][4]

$$\boldsymbol{T}_\mathrm{SO,R} = \frac{m\Delta_\mathrm{ex}}{e\hbar E_\mathrm{F}}\alpha_\mathrm{R}\left(\boldsymbol{m}\times\left(\hat{\boldsymbol{z}}\times\boldsymbol{j}^\mathrm{c}\right)\right). \tag{2.15}$$

This form again allows to define a field that produces this torque when inserted into the LLG equation and reads

$$\mu_0\boldsymbol{H}_\mathrm{R} = \frac{\alpha_\mathrm{R}}{2\mu_\mathrm{B}M_\mathrm{s}}P\left(\hat{\boldsymbol{z}}\times\boldsymbol{j}^\mathrm{c}\right) \tag{2.16}$$

where μ_B is the Bohr magneton and $P = \frac{\Delta_\mathrm{ex}}{\epsilon_\mathrm{F}}$ is the spin polarization of the current [Gam11; Han13a]. This field is often labeled "Rashba field" in the literature whenever there is a field-like torque that supposedly has its origin in the Rashba effect and shall not be confused with the k-dependent "field" discussed above. In the presented form, $\boldsymbol{H}_\mathrm{R}$ as calculated for a 2D system is not directly applicable to a metallic multilayer which has a full 3D character. It is possible to transform the above calculations to the 3D case [Hel17], however one thereby assumes a homogeneous Rashba interaction over the film thickness, which is presumably not the case. From first principles calculations it has been found that the field-like torque mostly stems from the FM/NM interface (e.g. Pt/Co) [Han13b; Fre14] and FM/Oxide interfaces [Kru05] and the averaged field-like torque should therefore scale with $\frac{1}{d_\mathrm{FM}}$. The dependence on the FM thickness is validated experimentally for NM/FM/oxide systems [Ski14; Fan13; Pai15; Ou16]. A recent publication even reports the presence of a field-like torque in a FM/Oxide system without NM that shows scaling

[4] in [Man09], in eq. 50 there is an erroneous factor of 2, as pointed out in [MA09; Gam11]

with the inverse FM thickness [Emo16].
In conclusion, the Rashba effect leads to a torque that can be described by an additional field which scales with the strength of the ip current and is found to be of great importance in very thin FMs only. Given by the form of Eq. (2.16) the corresponding field-like torque (as defined in Eq. (1.20)) is written as

$$\boldsymbol{T}_{\mathrm{FL,R}} = -\gamma\tau_{\mathrm{FL,R}}\boldsymbol{m}\times\boldsymbol{\sigma}_{\mathrm{FL,R}} \tag{2.17}$$

with $\tau_{\mathrm{FL,R}} = -\frac{\alpha_{\mathrm{R}}P}{2\mu_{\mathrm{B}}M_{\mathrm{s}}}j^{\mathrm{c}}$ and $\boldsymbol{\sigma}_{\mathrm{FL,R}} = \boldsymbol{y}$ for a charge current that flows in x-direction.

2.4. Spin Transport Across a Normal Metal/Ferromagnet Interface

As already discussed above, the SHE does not directly exert a torque on the magnetization in a NM/FM bilayer. Instead, the SHE is the source of a spin current that flows along the layer normal and the torque on $\boldsymbol{m}$ is the result of the absorption of (parts) of the spin current at the NM/FM interface.
Given by the geometry of the sample and the short spin diffusion length, the important component of the spin current in the NM flows in z direction only and hits the substrate/NM interface at $z = -d_{\mathrm{NM}}$ and and the NM/FM interface at $z = 0$. The tensor spin current j^{s}_{ij} can thus be reduced to a vector j^{s}_{zj} with $j = x, y, z$ indicating the spin current polarization only or, short, $\boldsymbol{j}^{\mathrm{s}}$.
Drift diffusion equations describe well the transport in systems where the Fermi wavelength is of the order of the interatomic distance such that size quantization effects do not play a role, even though the thickness of the layers is in the nm region. It is therefore possible to describe spin and charge transport in the NM and FM layer, respectively, using this formalism. At the interface between different layers the electronic band structure changes abruptly and leads to discontinuities that cannot be treated within the drift diffusion approach. However, it is possible to take these discontinuities into account within a drift diffusion model by introducing boundary conditions between different layers that are justified by a full quantum mechanical model [Bra06]. This task has been performed under the name of "magnetoelectronic circuit theory" (MCT), which provides a framework to describe transport across FM/NM multilayers. The MCT is reviewed in [Bra06; Bra01] which are the basis of the following discussion. The basic idea of this theory follows the electronic circuit theory founded by Kirchhoff's laws to describe networks of different electric elements if a voltage is applied at well defined points in the lattice. In MCT, the concept of charge transport is widened to include the spin degree of freedom. In the case of a NM/FM interface the bulk of the NM is seen as a node, the interface itself plays the role of a resistor and in the bulk of the FM, another node is set. The nodes are characterized

by a distribution function and the interface is characterized by a scattering matrix that connects different states n of the distribution function in the NM to the states m in the FM. This scattering matrix is computed using a quantum mechanical model and/or first principles calculations for given materials. If the limits of the drift diffusion formalism are met, the boundary conditions are reduced to simple numbers for a given spin direction.
In the FM the quantization axis is given by the magnetization direction, labeled $\uparrow$ / $\downarrow$ for majority/minority spins. In the NM, however, no preferred axis exists and spin accumulations/currents can have any polarization direction. Therefore, if one has a NM/FM interface, spin accumulations/currents have to be split into parts parallel and transverse to $\boldsymbol{m}$.
In the following, the boundary condition for the spin current across a NM/FM interface is treated with the interface being the x, y plane at $z = 0$. The magnetization points in y direction and the polarization of the incoming spin current is characterized by two angles θ_s and φ_s where the former gives the angle between spin polarization and $\boldsymbol{m}$ and the latter describes the position of the transverse part within the x, z-plane, following [Sti02; Ami16a].
The parallel part is well described by the two current model and the interface is characterized by a finite conductance for both majority and minority (charge) currents

$$\boldsymbol{j}^{\mathrm{c},\uparrow} = G^{\uparrow}\Delta\mu^{\uparrow} \qquad \boldsymbol{j}^{\mathrm{c},\downarrow} = G^{\downarrow}\Delta\mu^{\downarrow} \tag{2.18}$$

with the spin dependent interface conductivities $G^{\uparrow}/G^{\downarrow}$ and the drop in the quasichemical potential $\mu'^{\uparrow}/\mu'^{\downarrow}$ for majority/minority spins, respectively [Ami16a]. The difference between the two currents results in a spin current across the interface. The interface conductivities $G^{\uparrow}/G^{\downarrow}$ are given by [Bra06]

$$G^{\uparrow(\downarrow)} = \frac{e^2}{h}\left[M - \sum_{nm}^{M}\left|r_{nm}^{\uparrow(\downarrow)}\right|^2\right] = \frac{e^2}{h}\sum_{nm}^{M}\left|t_{nm}^{\uparrow(\downarrow)}\right|^2. \tag{2.19}$$

Here, $t^{\uparrow(\downarrow)}$, $r^{\uparrow(\downarrow)}$ are the transimission and reflection probabilities for majority/minority spins at the interface which depend on the difference of the Fermi surface for both populations and M is the number of conducting channels in the NM.
The transverse part deserves more attention[5]. A scheme of the scattering process of an incoming spin state is given in Fig. I.2.2. It must be noted first that a spin state transverse to the quantization axis is given by the superposition of up and down states $a\,|\uparrow\rangle + b\,|\downarrow\rangle$ with complex amplitude factors a, b. Without loss of generality it is assumed that the incoming transverse spin current is polarized in z direction such that $\varphi := 0°$. The transverse part of the spin state is given by $\overline{a}\,b$ with $\mathfrak{Re}\{\overline{a}\,b\}$ describing the $\varphi = 0°$ component and

[5] the following explanation follows a private communication with M. D. Stiles in May 2017 resembling the findings of [Sti02] and [Bra06, sect. 5.3]

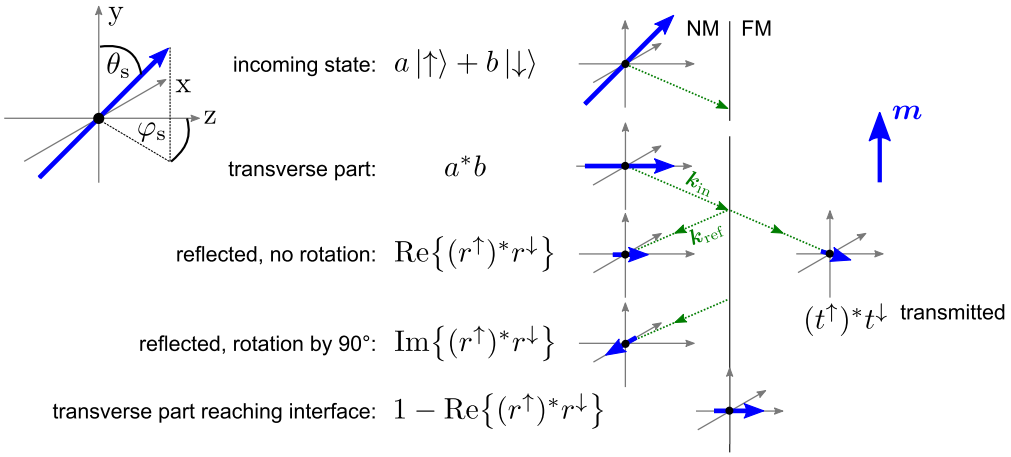

Figure 2.2.: *Scattering of an incoming spin state at an NM/FM interface. The blue arrows represent the spin polarization and the magnetization in the NM/FM, respectively. The incoming/outgoing k-vectors are represented by the green dashed lines.*

$\mathfrak{Im}\{\overline{a}\,b\}$ describing the part with $\varphi = 90°$. The transport across the interface is then again determined by the transmission and reflection amplitudes $t^{\uparrow(\downarrow)}/r^{\uparrow(\downarrow)}$ for majority/minority states. To understand the difference of collinear and noncollinear transport it is instructive to have a look at a few limiting cases. Consider first full reflection for one spin population and full transmission for the other. In this case the transverse component is completely absorbed at the interface and only collinear components are left, both in the reflected and the transmitted part; this effect is therefore called spin filtering [Sti02]. It is a purely quantum mechanical phenomenon and has no classical analogy. On the other hand, if both components are fully transmitted, the whole transverse part enters the FM without any loss at the interface and the spin current is continuous at the interface. The last limiting case is full reflection for both components, then no transverse part is lost; however, since the scattering is complex, it can induce a rotation of the transverse reflected part. This again is a fully quantum mechanical phenomenon. To find the boundary condition for the spin current in the NM, one needs to take into account only incoming and reflected part; the reflected spin polarization is given by $r^\uparrow a\,|\uparrow\rangle + r^\downarrow b\,|\uparrow\rangle$ such that the reflected transverse component is given by $\overline{(r^\uparrow a)}\, r^\downarrow b$. The change in the transverse part of the reflected v.s. the incoming spin state is thus given by $\overline{(r^\uparrow)}\, r^\downarrow$ and $\mathfrak{Re}\left\{\overline{(r^\uparrow)}\, r^\downarrow\right\}$ gives the part of the reflected spin that is still in the same direction as the incoming one, whereas $\mathfrak{Im}\left\{\overline{(r^\uparrow)}\, r^\downarrow\right\}$ gives the part that has rotated by 90°. The transverse spin current at the interface is computed by summing up $1 - \overline{(r^\uparrow)}\, r^\downarrow$ for every incoming state. The quantity $\sum_{\text{states}}[1 - \overline{(r^\uparrow)}\, r^\downarrow]$ is then called spin mixing conductance (SMC). It gives a boundary condition for the spin current in the NM arriving at the interface at $x = -0$.
The real part, corresponding to $1 - \mathfrak{Re}\left\{\overline{(r^\uparrow)}\, r^\downarrow\right\}$ is the transverse incoming spin that actually reaches the interface and the imaginary part is the transverse, rotated spin that flows back

from the interface. In the same notation as used above the SMC reads [Bra01; Bra06, eqns. 98, 144]

$$G^{\uparrow\downarrow} = \frac{e^2}{h}\left[M - \sum_{nm}^{M} \overline{(r_{nm}^{\uparrow})}\, r_{nm}^{\downarrow}\right] \tag{2.20}$$

It should be noted that in the literature different forms of the SMC are used in parallel, which may be normalized to the area of the NM/FM interface A_{int} and or by the conductance quantum. The conversion is given by

$$\begin{aligned} g^{\uparrow\downarrow} &= \frac{h}{e^2} G^{\uparrow\downarrow}, \quad [G^{\uparrow\downarrow}] = \frac{1}{\Omega}, \quad [g^{\uparrow\downarrow}] = 1 \\ \tilde{g}^{\uparrow\downarrow} &= \frac{g^{\uparrow\downarrow}}{A_{\mathrm{int}}}, \quad [\tilde{g}^{\uparrow\downarrow}] = \frac{1}{\mathrm{m}^2}, \quad \tilde{G}^{\uparrow\downarrow} = \frac{G^{\uparrow\downarrow}}{A_{\mathrm{int}}}, \quad [\tilde{G}^{\uparrow\downarrow}] = \frac{1}{\Omega\,\mathrm{m}^2} \end{aligned} \tag{2.21}$$

The full boundary condition for the spin current at the NM/FM interface is finally given by

$$\begin{aligned} \boldsymbol{j}^{\mathrm{s}} = &\left[-\left(G^{\uparrow} + G^{\downarrow}\right)\Delta\boldsymbol{\mu}_{\mathrm{s}} \cdot \boldsymbol{m} + \left(G^{\uparrow} - G^{\downarrow}\right)\Delta\mu\right]\boldsymbol{m} \\ &+ \mathfrak{Re}\left\{G^{\uparrow\downarrow}\right\}(2\Delta\boldsymbol{\mu}_{\mathrm{s}} \times \boldsymbol{m}) \times \boldsymbol{m} - \mathfrak{Im}\left\{G^{\uparrow\downarrow}\right\}(2\Delta\boldsymbol{\mu}_{\mathrm{s}} \times \boldsymbol{m})\,. \end{aligned} \tag{2.22}$$

The first two terms on the right side describe the collinear part of the spin current with the drops in the quasichemical potentials for the spin $\Delta\boldsymbol{\mu}_{\mathrm{s}}$ and for the charge $\Delta\mu$. The second two terms correspond to the transverse part, where the double cross product gives the part of $\boldsymbol{\mu}_{\mathrm{s}}$ that is transverse to $\boldsymbol{m}$ and lies in the plane spanned by $\boldsymbol{m}$ and $\boldsymbol{\mu}_{\mathrm{s}}$, i.e. the incoming transverse part. The incoming transverse part is reduced by the amount of backscattered transverse spins without rotation, parametrized by the real part of the SMC. The reflected, rotated part is then perpendicular to both $\boldsymbol{m}$ and the incoming transverse part and parametrized by the imaginary part of the SMC.
In the context of these interface conductivities, $G_{\mathrm{SH}} = \frac{e^2}{h}M$ is the so-called Sharvin conductivity, which is given by the number of conducting channels and indicates the interface resistance for perfectly transparent contacts. In the free electron gas model this value can be calculated by counting the k-vectors involved in the transport across the interface such that

$$\tilde{G}_{\mathrm{SH}} = \frac{e^2}{h}\frac{k_{\mathrm{F}}^2}{4\pi} \tag{2.23}$$

with the Fermi wave vector k_{F} [Han13a, eq. (14) with $r_{\uparrow(\downarrow)} = 0$]. Obviously, the Sharvin conductivity is the upper limit for all spin dependent conductivities.

2.5. SHE Induced Torques

In the following section, the torques that result due to the spin transport across the NM/FM interface are shown as derived from a drift diffusion model [Han13a]. This model is in accordance with the model widely used to describe spin pumping and inverse SHE

experiments (see the respective parts of this thesis). It is therefore used to test the reciprocity of these different experiments within one framework.
The fact that the torque on $\boldsymbol{m}$ is caused by the transfer of angular momentum (by a spin current) the term "spin transfer torque" (STT) is used to denote experiments in which this mechanism is used to determine the SOTs in metallic bilayers.

2.5.1. Drift diffusion model for SHE induced SOTs

Generally, the torque on the magnetization due to a spin accumulation in a FM is given by the torque between the spin accumulation within the FM and the magnetization [Han13a], in a reciprocal way as in Eq. (2.5):

$$\boldsymbol{T} = \frac{\gamma}{\tau_{\mathrm{ex}} M_{\mathrm{s}}} \boldsymbol{m} \times \boldsymbol{s} + \frac{\gamma}{\tau_{\mathrm{dp}} M_{\mathrm{s}}} \boldsymbol{m} \times (\boldsymbol{m} \times \boldsymbol{s}) \,. \tag{2.24}$$

If this equation is combined with Eq. (2.5), the torque is related to the divergence of the spin current. As discussed before, it is convenient to assume an instantaneous relaxation of the transverse spin current at the interface of the FM due to the fact that τ_{dp} is very short. This means that the spin current is absorbed directly at the interface and results in a torque. To understand this simplification, again a look is taken at the different possibilities for an incoming spin state at the interface. First, it is clear that the collinear part does not produce any torque, simply because the cross product is zero and therefore can be neglected. The second important fact is that the relaxation of the collinear spin accumulation happens via transfer of angular momentum to the lattice. In contrast to this, the absorption of the transverse part of the spin current in the FM is dominated by the transfer of angular momentum from the spin accumulation to the magnetization simply because $\tau_{\mathrm{ex}} \ll \tau_{\mathrm{s}}$. The reason for the fast relaxation is that the spin of electrons entering the FM starts to precess in the exchange field of the FM. Taking the sum over all possible k vectors, it is found that that the precession of different electrons dephases quickly. After a few lattice spacings the transverse part of the spin current is fully absorbed [Sti02]. If the FM is thicker than this decay length, it doesn't matter if the incident spin current is absorbed at the interface due to spin filtering, as described above, or if it gets transmitted and absorbed within the FM. For the reflected part a similar argument holds: if there is some reflected component that has rotated upon reflection, this rotation has to exert a torque on the magnetization due to angular momentum conservation.
In order to find explicit expressions for the current created torques the drift diffusion equation in the NM is solved under the boundary condition given above for the NM/FM interface and vanishing spin current at the NM and FM outer interfaces as well as charge current restriction to be in plane. As a result both damping- and field-like torque [Han13a][6]

[6] note that eq. 10 in [Han13a] must be normalized in order to be added to the LLG as an interfacial

are given by

$$\begin{aligned} \boldsymbol{T}_{\mathrm{DL}} &= \gamma\tau_{DL}\boldsymbol{m}\times(\boldsymbol{m}\times\boldsymbol{\sigma}), \quad \tau_{\mathrm{DL}} = \frac{\hbar}{2|e|M_{\mathrm{s}}d_{\mathrm{F}}}\eta_{\mathrm{DL}}\theta_{\mathrm{SH}}j^{\mathrm{c}} \\ \boldsymbol{T}_{\mathrm{FL}} &= -\gamma\tau_{FL}\boldsymbol{m}\times\boldsymbol{\sigma}, \quad \tau_{\mathrm{FL}} = -\frac{\hbar}{2|e|M_{\mathrm{s}}d_{\mathrm{F}}}\eta_{\mathrm{FL}}\theta_{\mathrm{SH}}j^{\mathrm{c}} \end{aligned} \tag{2.25}$$

where the torque strength $\tau_{\mathrm{DL,FL}}$ has units of Tesla and the so-called spin injection efficiencies $0 \leq \eta_{\mathrm{DL,FL}} \leq 1$ contain the physics resulting from drift diffusion in the NM under the applied boundary conditions. In general, this form of the equations is generic to an interfacial torque and the factor $\theta^{\mathrm{eff}} = \eta_{\mathrm{DL}}\theta_{\mathrm{SH}}$ is an effective conversion factor, often called "effective spin Hall angle". The spin injection efficiencies are given by [Han13a]:

$$\begin{aligned} \eta_{\mathrm{DL}} &= \left(1-\frac{1}{\cosh\left(\frac{d_{\mathrm{NM}}}{\lambda_{\mathrm{s}}}\right)}\right)\frac{\left|\tilde{G}_{\mathrm{r}}^{\uparrow\downarrow}\right|^2+\mathfrak{Re}\left\{\tilde{G}_{\mathrm{r}}^{\uparrow\downarrow}\right\}\tanh\left(\frac{d_{\mathrm{NM}}}{\lambda_{\mathrm{s}}}\right)^2}{\left|\tilde{G}_{\mathrm{r}}^{\uparrow\downarrow}\right|^2+2\mathfrak{Re}\left\{\tilde{G}_{\mathrm{r}}^{\uparrow\downarrow}\right\}\tanh\left(\frac{d_{\mathrm{NM}}}{\lambda_{\mathrm{s}}}\right)^2+\tanh\left(\frac{d_{\mathrm{NM}}}{\lambda_{\mathrm{s}}}\right)^4} \\ \eta_{\mathrm{FL}} &= \left(1-\frac{1}{\cosh\left(\frac{d_{\mathrm{NM}}}{\lambda_{\mathrm{s}}}\right)}\right)\frac{\mathfrak{Im}\left\{\tilde{G}_{\mathrm{r}}^{\uparrow\downarrow}\right\}\tanh\left(\frac{d_{\mathrm{NM}}}{\lambda_{\mathrm{s}}}\right)^2}{\left|\tilde{G}_{\mathrm{r}}^{\uparrow\downarrow}\right|^2+2\mathfrak{Re}\left\{\tilde{G}_{\mathrm{r}}^{\uparrow\downarrow}\right\}\tanh\left(\frac{d_{\mathrm{NM}}}{\lambda_{\mathrm{s}}}\right)^2+\tanh\left(\frac{d_{\mathrm{NM}}}{\lambda_{\mathrm{s}}}\right)^4}. \end{aligned} \tag{2.26}$$

The prefactor $1-\mathrm{sech}$ in these equations is a result of the NM bulk drift diffusion and the fraction represents the transparency of the interface. In the above equation a rescaled SMC is introduced as

$$\tilde{G}_{\mathrm{r}}^{\uparrow\downarrow} = \tilde{G}^{\uparrow\downarrow}\frac{2\lambda_{\mathrm{s}}\tanh\left(\frac{d_{\mathrm{NM}}}{\lambda_{\mathrm{s}}}\right)}{\sigma_{\mathrm{N}}^{0}} \tag{2.27}$$

with the electrical bulk conductivity σ_{N}^{0} of the NM.

For a charge current that flows in x-direction $\boldsymbol{\sigma} = \boldsymbol{y}$ for the case of a positive spin Hall angle. By comparing Eq. (2.25) and Eq. (2.17) it becomes clear that the field-like torques originating from SHE and Rashba effect show the same symmetry and cannot be easily separated in the experiment. However, an upper bound can be set to the SHE contribution by the knowledge of the SMC.

In early publications concerning the spin Hall effect, the interface resistance has not been taken into account in the data evaluation. Instead, a transparent interface has been assumed such that the transverse spin current reaching the NM/FM interface is absorbed completely and gives a pure damping-like torque. The boundary condition that belongs to this picture is a vanishing transverse spin accumulation at the NM/FM interface. Using this boundary condition and the drift diffusion equation Eq. (2.2) the spin injection

torque by substituting $\delta(z) \to \frac{1}{M_{\mathrm{s}}d_{\mathrm{F}}}$

efficiency η_{trans} evaluates to [Liu11]:

$$\eta_{\text{trans}} = \left(1 - \frac{1}{\cosh\left(\frac{d_{\text{NM}}}{\lambda_{\text{s}}}\right)}\right) \tag{2.28}$$

which is exactly the first part of the full model including the interface resistance. The spin current across the interface, determining the torque on $\boldsymbol{m}$, falls off if the thickness of the NM layer comes close to λ_{s} due to the backflow of spin current from the substrate/NM interface. A comparison of the full model and the transparent interface simplification is shown in Fig. I.2.3. Using a transparent interface results in the largest torque, therefore a

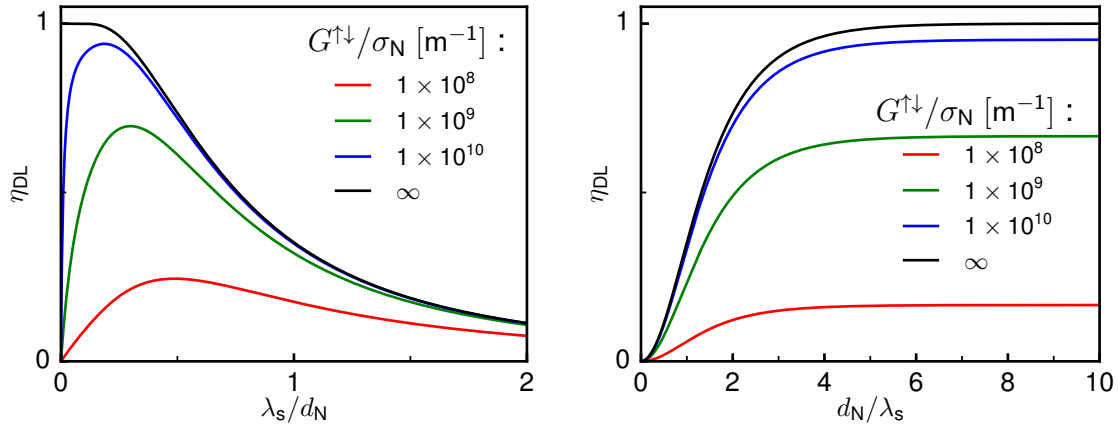

Figure 2.3.: *Spin injection efficiency of the damping-like torque for different ratios of* SCM *to conductivity, for simplicity a purely real* SMC *is assumed. The case of an infinite ratio corresponds to a transparent interface. Realistic values are* $\mathfrak{Re}\{G\}^{\uparrow\downarrow} \sim 1 \times 10^{14} \frac{1}{\Omega\,\text{m}^2}$ *and* $\sigma_N \sim 1 \times 10^6 \frac{1}{\Omega\,\text{m}}$ *such that the ratio varies between* $1 \times 10^8 - 1 \times 10^9 \frac{1}{\text{m}}$

calculation of θ_{SH} using this simplification always leads to a lower bound of the SH angle.

2.5.2. Data evaluation of direct SHE experiments

The evaluation of η as defined above, including the interface resistance, requires the knowledge of $G^{\uparrow\downarrow}$ and σ_{N}^0. Fortunately, both quantities can be determined experimentally. This allows to fit the measured $\eta\theta_{\text{SH}}$ to obtain both the spin diffusion length and the SH angle for a series of samples with varying NM thickness.

For this purpose Eq. (2.26) is simplified using the approximation $\left|\tilde{G}^{\uparrow\downarrow}\right|^2 \approx \mathfrak{Re}\left\{\tilde{G}^{\uparrow\downarrow}\right\}^2$. This approximation is justified as $\mathfrak{Im}\left\{\tilde{G}\right\}$ is approximately one order of magnitude smaller than the real part of the SMC in metal/metal interfaces [Zwi05]. The absolute value of $\tilde{G}^{\uparrow\downarrow}$ is therefore dominated by the real part. Note that this argument does not imply $\mathfrak{Im}\left\{\tilde{G}^{\uparrow\downarrow}\right\} = 0$. Using the above approximation and after some algebra the simplified injection efficiency

can be written as [Pai15]:

$$\eta_{\mathrm{DL}} \approx \frac{2\mathfrak{Re}\left\{\tilde{G}\right\}^{\uparrow\downarrow} \tanh\left(\frac{d_{\mathrm{NM}}}{2\lambda_{\mathrm{S}}}\right)}{\frac{\sigma_{\mathrm{N}}}{\lambda} + 2\mathfrak{Re}\left\{\tilde{G}\right\}^{\uparrow\downarrow} \frac{1}{\tanh\left(\frac{d_{\mathrm{NM}}}{\lambda}\right)}}. \tag{2.29}$$

As shown in section II.5.1 the SMC cannot be measured directly for a given sample but must be determined from a sample series of different NM thickness. It is therefore advantageous to express the spin injection efficiency in form of the so-called effective SMC, which can be determined experimentally for every given layer structure via Eq. (5.7) and Eq. (5.8):

$$\eta_{\mathrm{DL}} = 2\frac{e^2}{h}\mathfrak{Re}\left\{\tilde{g}_{\mathrm{eff}}^{\uparrow\downarrow}\right\} \frac{\lambda_{\mathrm{S}}}{\sigma_N} \tanh\left(\frac{d_{\mathrm{NM}}}{2\lambda_{\mathrm{S}}}\right) \tag{2.30}$$

This equation can be used to obtain both the SHA and the spin diffusion length from a fit to the normalized effective SH angle via

$$\left(\eta_{\mathrm{DL}}\theta_{\mathrm{SH}}\right)^{\mathrm{norm}} := \eta_{\mathrm{DL}}\theta_{\mathrm{SH}} \frac{h}{2e^2} \frac{\sigma_{\mathrm{N}}^0}{\mathfrak{Re}\left\{\tilde{g}_{\mathrm{eff}}^{\uparrow\downarrow}\right\}} = \theta_{\mathrm{SH}}\lambda_{\mathrm{S}} \tanh\left(\frac{d_{\mathrm{NM}}}{2\lambda_{\mathrm{S}}}\right) \tag{2.31}$$

3. Magnetization Dynamics II: Theory of Ferromagnetic Resonance

Ferromagnetic resonance (FMR) is the name of resonantly driven magnetization precession around a stable equilibrium position. It can be understood mathematically in analogy to a driven damped harmonic oscillator. The system, initially in its equilibrium, is driven via a periodic excitation $\propto \cos(\omega t)$. If the driving torque is small enough, the response of the system is linear, i.e. the precession amplitude is directly proportional to the driving torque strength. If the frequency of the driving torque is chosen such that is coincides with the resonance frequency of the system, FMR occurs and the precession amplitude is at maximum. Hereby, the resonance frequency of the system depends on the internal field, i.e. the energy landscape of the magnetization. In an FMR measurement usually an external field is applied to sweep the internal energy and at every external field value the amplitude of precession is measured. The field value at which FMR occurs is called resonance field. As in every damped system there is a characteristic linewidth of the resonance curve that depends on the damping of the system. The measured linewidth consists of an intrinsic part, given by the Gilbert damping parameter and extrinsic parts. The extrinsic contributions depend on the particular FM studied. In general, extrinsic intrinsic contributions have to be carefully disentangled in measurements in order to find the Gilbert damping parameter. Measurements of the FMR thus allows to determine some key parameters of a magnetic system. In this section, the linearized LLG is solved and it is shown that, in addition to the internal parameters, the SOTs entering the LLG equation can be quantified from FMR measurements. Solutions of the LLG equation have been presented many times and the following part sticks with the general approach used in [Wol04; Här16, see the appendix]. The inclusion of the DL term was performed by the author in [Dec12] and checked against the results of [And08; Pet07; Liu11][1]. The explicit calculation of the results presented in the following is done in a "bruteforce" approach using the computer algebra system Maple and is shown in more detail in the appendix.
In the following part, it is assumed that the magnetization of the whole sample can be represented as one single magnetic moment, the so-called macrospin. This simplification is strictly true only if a) the equilibrium magnetization, the internal field and the driving torque are homogeneous across the whole sample and if b) there are no standing spin

[1]The author wants to thank K. Ando for sharing details of his calculation results

waves excited in the sample. Condition b) is not fulfilled in confined systems but - as will be shown in section II.6 - the macrospin approximation can still be used to evaluate the experiments if care is taken to minimize the impact of the mode structure. Within the macrospin approximation the exchange energy does not play any role as it is implicitly included by setting all magnetic moments parallel.

The starting point for solving the LLG is to separate the torques acting on $\boldsymbol{m}$ into static and dynamic ones. The static torque is simply written as

$$\boldsymbol{T}_\mathrm{s} = -\gamma \boldsymbol{m} \times \mu_0 \boldsymbol{H}_\mathrm{eff} + \gamma \tau_\mathrm{DL,s} \boldsymbol{m} \times (\boldsymbol{m} \times \boldsymbol{\sigma}), \tag{3.1}$$

where the field-like torques are substituted into the effective field for clearness during the calculation. The magnetization is excited by a high frequency driving torque:

$$\boldsymbol{T}_\mathrm{d} = -\gamma \boldsymbol{m} \times \mu_0 \boldsymbol{h}_\mathrm{d} \mathrm{e}^{i\omega t} + \gamma \tau_\mathrm{DL,d} \boldsymbol{m} \times (\boldsymbol{m} \times \boldsymbol{\sigma}) \, \mathrm{e}^{i\omega t} \tag{3.2}$$

The calculation of the dynamic response follows the general idea of small angle oszillations around the equilibrium position. This means that the equilibrium magnetization $\boldsymbol{m}_\mathrm{eq}$ must be found first, which can be done in two ways: a) minimize the total energy density or b) use the condition

$$\frac{\partial \boldsymbol{m}_\mathrm{eq}}{\partial t} = \boldsymbol{T}_\mathrm{s} = 0. \tag{3.3}$$

In the laboratory coordinate system $\boldsymbol{m}_\mathrm{eq} = m_x \hat{x} + m_y \hat{y} + m_z \hat{z}$ is usually expressed by the two angles θ and φ:

$$\boldsymbol{m}_\mathrm{eq,lab} = \begin{pmatrix} \sin(\theta)\cos(\varphi) \\ \sin(\theta)\sin(\varphi) \\ \cos(\theta) \end{pmatrix}. \tag{3.4}$$

Once the equilibrium position is found and therefore θ and φ are known, it is advantageous to define a local coordinate system (x', y', z') which is aligned with the equilibrium magnetization such that $\boldsymbol{m}_\mathrm{eq} = \hat{x}'$. In this coordinate system the LLG can easily be linearized for small angle precession. In general, it holds that $\boldsymbol{m}(t) = \boldsymbol{m}_\mathrm{eq} + \Delta\boldsymbol{m}(t)$ with $\boldsymbol{m}_\mathrm{eq}(t) \cdot \Delta\boldsymbol{m}(t) = 0$ where the last condition follows from the fact that the magnetization moves on a sphere and, for a small enough change in position, this change is always perpendicular to $\boldsymbol{m}$ itself. In the local coordinate system this translates to

$$\boldsymbol{m}(t) = \boldsymbol{m}_\mathrm{eq} + \Delta\boldsymbol{m}(t) = \begin{pmatrix} 1 \\ \Delta m_{y'}(t) \\ \Delta m_{z'}(t) \end{pmatrix} \tag{3.5}$$

thereby reducing the calculation to a two-dimensional problem. All terms entering the LLG are subsequently transformed into the local coordinate system, using a set of two

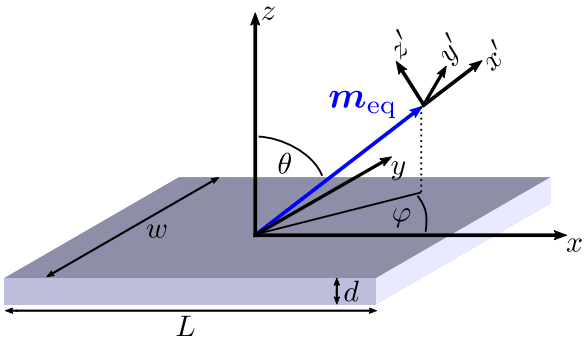

Figure 3.1.: *Laboratory coordinate system* (x, y, z) *and local coordinate system* (x', y', z') *defined by the equilibrium position* $\boldsymbol{m}_{eq}$*. The transformation is performed by first rotating by* φ *around* $z = z'$ *and then rotating by* $\frac{\pi}{2} - \theta$ *around the new* y'*-axis. In this coordinate system the small angle precession takes place in the* (y', z') *plane only.*

angles φ_i, θ_i for each quantity. In order to solve the resulting set of equations, a complex exponential ansatz $\Delta\boldsymbol{m}(t) = \Delta\boldsymbol{m}\, e^{i\omega t}$ is chosen, of which the real solution is:

$$\boldsymbol{m}_r(t) = \mathfrak{Re}\left\{\begin{pmatrix} 1 \\ \Delta m_{y'} e^{i\omega t} \\ \Delta m_{z'} e^{i\omega t} \end{pmatrix}\right\} = \begin{pmatrix} 1 \\ \mathfrak{Re}\{\Delta m_{y'}\}\cos(\omega t) - \mathfrak{Im}\{\Delta m_{y'}\}\sin(\omega t) \\ \mathfrak{Re}\{\Delta m_{z'}\}\cos(\omega t) - \mathfrak{Im}\{\Delta m_{z'}\}\sin(\omega t) \end{pmatrix}. \tag{3.6}$$

Here, Δm_i is a complex number, constant in time, which gives the amplitude and phase of the motion of $\Delta m_i(t) = \Delta m_i e^{i\omega t}$ and $\mathfrak{Re}\{\Delta m_i(t)\} = |\Delta m_i|\cos(\omega t + \varphi_i)$. This ansatz is inserted into the equation and the result is linearized by keeping only terms that are linear in $\Delta m_{y'}, \Delta m_{z'}$ and the driving torque strength, leading to a set of linear equations that can be solved by standard algebra. The solution of this problem can be written in terms of a dynamical susceptibility defined by:

$$\begin{pmatrix} \Delta m_{y'}(t) \\ \Delta m_{z'}(t) \end{pmatrix} = \begin{pmatrix} \chi_{y'y'} & \chi_{y'z'} \\ \chi_{z'y'} & \chi_{z'z'} \end{pmatrix} \begin{pmatrix} d_{y'}(t) \\ d_{z'}(t) \end{pmatrix}. \tag{3.7}$$

Here, $d_{y'}(t) = (h_{y'} - \frac{\tau_{\mathrm{DL,d}}}{\mu_0}\sigma_{z'})e^{i\omega t}$ and $d_{z'}(t) = (h_{z'} - \frac{\tau_{\mathrm{DL,d}}}{\mu_0}\sigma_{y'})e^{i\omega t}$ stand for the driving torques comprising of both driving fields (and field-like SOT) and damping-like SOT. Hereby, $\tau_{\mathrm{DL,d}}$ is the strength of the driving, damping-like torque, in contrast to $\tau_{\mathrm{DL,s}}$ which denotes a static damping-like torque. Due to the double cross product in the damping-like SOT term, the $h_{y'}$ and $\sigma_{z'}$ as well as the $h_{z'}$ and $\sigma_{y'}$-components act on the magnetization in the same way. Therefore, it is possible to substitute a small rf damping-like torque (with in plane spin polarization) into an oop driving field as done e.g. in [Che16]. Note that, in order to allow different phases between different driving torques, all h_i, σ_i are complex numbers. To simplify the notation, a complex quantity is written as $a = a' + i\,a''$ in the following. Each entry of the susceptibility itself again is a complex number, $\chi_{ii} = \chi'_{ii} + i\chi''_{ii}$.

The general form of the susceptibility reads:

$$\boldsymbol{\chi}_\mathrm{f} = \frac{1}{N_\mathrm{f}} \begin{pmatrix} \mathfrak{H}_0 + i\dfrac{\alpha\omega}{\mu_0\gamma} & -\mathfrak{H}_2 + \mathfrak{s} + i\dfrac{\omega}{\mu_0\gamma} \\ -\mathfrak{H}_2 - \mathfrak{s} - i\dfrac{\omega}{\mu_0\gamma} & \mathfrak{H}_1 + i\dfrac{\alpha\omega}{\mu_0\gamma} \end{pmatrix}, \tag{3.8}$$
$$N_\mathrm{f} = \mathfrak{H}_0\mathfrak{H}_1 + \mathfrak{s}^2 - \mathfrak{H}_2^2 - (1+\alpha^2)\left(\frac{\omega}{\mu_0\gamma}\right)^2 + i\left(\mathfrak{H}_0 + \mathfrak{H}_1\right)\frac{\omega}{\mu_0\gamma}\left(\alpha + \frac{2\,\mathfrak{s}}{\mathfrak{H}_0 + \mathfrak{H}_1}\right).$$

Here, $\mathfrak{H}_0$, $\mathfrak{H}_1$ and $\mathfrak{H}_2$ are (mathematically complex) terms that depend on the different energy contributions entering the effective field and the static, field-like SOT. These terms are evaluated at the equilibrium position and fully determine the dynamics of the magnetization. Explicit expressions for the general case are given in the appendix, section IV.B. The static damping-like torque is contained in $\mathfrak{s}$.

In the following, explicit expressions are given for the simplest case that captures the main features of FMR in a thin Py film without damping-like SOT. In such a film there are three main energy contributions: the Zeeman energy for the external field, the demagnetizing energy and an uniaxial oop anisotropy that is relatively weak, as discussed in section I.1.2.5. This results in an internal field $H_\mathrm{eff} = H + H_\mathrm{dem} + H_\mathrm{ani,oop}$ with the external field of strength H. The natural equilibrium position of such a system lies ip and a strong field of the order of $\mu_0 M_\mathrm{s} \sim 1\,\mathrm{T}$ is needed to saturate the magnetization oop. Therefore, the external field is applied ip such that the oop angles $\theta = \theta_H = 90°$. This configuration is used for all measurements performed in this thesis.

Due to the fact that the demagnetization field and the oop anisotropy have the same form and oppose each other, it is convenient to introduce the so-called effective magnetization

$$M_\mathrm{eff} = M_\mathrm{s} - \frac{2K_\mathrm{oop}}{\mu_0 M_\mathrm{s}} \tag{3.9}$$

which describes the strength of the effective demagnetization field. The equilibrium position is determined by $\boldsymbol{T}_{\mathrm{s},y'} \propto \left(2H\cos(\theta) + M_\mathrm{eff}\sin(2\theta)\right) = 0 \;\Rightarrow\; \theta = \theta_H = 90°$ and $\boldsymbol{T}_{\mathrm{s},z'} \propto \sin(\varphi - \varphi_H) = 0 \;\Rightarrow\; \varphi = \varphi_H$. As there are no ip anisotropies, the equilibrium is simply given by the direction of the external field. In this case the terms used in the susceptibility reduce to

$$\mathfrak{H}_0 = H + M_\mathrm{eff}, \quad \mathfrak{H}_1 = H, \quad \mathfrak{H}_2 = 0, \quad \mathfrak{s} = 0. \tag{3.10}$$

If ip anisotropies and a static damping-like SOT are considered, additional terms appear in the equilibrium condition and in the introduced abbreviations. This can lead to the situation that the equilibrium condition cannot be solved analytically to result in explicit expressions for (θ, φ). In this case the equations have to be solved numerically in order to

fit measured data at all fields and frequencies. These problems arise if the external field is not parallel to the equilibrium position e.g. when the external field is not applied along the easy/hard axis for a non-negligibly small ip anisotropy. In this case the equilibrium position depends on the strength of H and changes during a field scan which is usually referred to as dragging effect. However, at high symmetry positions (H parallel to easy/hard axis) explicit equations exist if H is strong enough to saturate the magnetization. The static damping-like torque also changes the equilibrium position, however, if this effect is small enough it can be neglected, see also sections IV.C and II.4.1.

When evaluating FMR the important quantities are the precession amplitude A at the resonance field/frequency and the form of the $A(H/f)$-curve close to resonance which is given by the susceptibility tensor. It is found that the entries of this tensor can be approximated to simple expressions allowing to evaluate data very elegantly. In the measurements performed in this work, the frequency is always kept constant while the field is swept through FMR. It is therefore convenient to expand the susceptibility around the resonance field and to take into account only terms of first order of H. The dominant term in the above susceptibility tensor is $\mathfrak{H}_0$ because it contains M_{eff} which is usually of the order of $\mu_0 M_{\mathrm{eff}}$ 1 T for ip magnetized Py samples. The damping parameter is usually small, 1×10^{-2} or smaller, as is the static damping-like SOT term. Terms containing these quantities are therefore neglected.

As a first step, the resonance condition can be found by minimizing the denominator N_{f}. In a first order approximation this is done by neglecting terms containing α and the static SOT and results in what is called the general Kittel formula[2]

$$\mathfrak{H}_0\mathfrak{H}_1 - \mathfrak{H}_2^2 = \left(\frac{\omega}{\mu_0\gamma}\right)^2. \tag{3.11}$$

Subsequently it is noted that $\mathfrak{H}_0$ and $\mathfrak{H}_1$ both contain the external field H. The resonance field at a fixed frequency f is called H_{r}. It is possible to expand the susceptibility around H_{r}, i.e. $\mathfrak{H}_0 = \mathfrak{H}_{0\mathrm{r}} + (H - H_{\mathrm{r}})$, $\mathfrak{H}_1 = \mathfrak{H}_{1\mathrm{r}} + (H - H_{\mathrm{r}})$ where $\mathfrak{H}_{0\mathrm{r}}$ and $\mathfrak{H}_{1\mathrm{r}}$ are the previously defined terms evaluated at the resonance field. Additionally, terms that are quadratic in α and $\frac{\mathfrak{s}}{\mathfrak{H}_0+\mathfrak{H}_1}$ are neglected and the resonance condition is used to eliminate part of the appearing terms. For the denominator of the susceptibility this leads to

$$N_{\mathrm{f}} \approx N = (\mathfrak{H}_{0\mathrm{r}} + \mathfrak{H}_{1\mathrm{r}})\left[(H - H_{\mathrm{r}}) + i\frac{\alpha_{\mathrm{eff}}\omega}{\mu_0\gamma}\right]. \tag{3.12}$$

In this step, an effective damping constant is introduced that contains the damping-like

[2] Kittel first derived this equation for the above discussed case of external plus demagnetization field [Kit48]. The resonance condition can also be derived in an absolute general case using a Lagrangian approach [Suh55], see the appendix of [Här16].

SOT:

$$\alpha_{\mathrm{eff}} = \alpha + \frac{2\mathfrak{s}}{\mathfrak{H}_{0\mathrm{r}} + \mathfrak{H}_{1\mathrm{r}}}. \tag{3.13}$$

It is then convenient to define a linewidth in field via

$$\Delta H = \frac{\alpha_{\mathrm{eff}}\omega}{\mu_0\gamma}. \tag{3.14}$$

This term, for zero damping-like SOT, is called intrinsic linewidth due to the fact that it results from the Gilbert damping parameter only. The intrinsic linewidth therefore shows a linear frequency dependence with zero intercept. For nonzero SOT this is not true anymore such that, strictly speaking, the substitution $\alpha \to \alpha + \delta\alpha_{\mathrm{DL}}$ is misleading, since $\delta\alpha_{\mathrm{DL}}$ is frequency dependent and therefore not a damping *constant*.

The denominator is subsequentially brought to the pure real form and the nominator is expanded around H_{r} by application of the same rules as mentioned before. This results in an approximated susceptibility with the following entries:

$$\begin{aligned}
\chi_{y'y'} &= \frac{\mathfrak{H}_{0\mathrm{r}}}{\Delta H\,(\mathfrak{H}_{0\mathrm{r}} + \mathfrak{H}_{1\mathrm{r}})} \frac{\Delta H\,(H - H_{\mathrm{r}}) - i(\Delta H)^2}{(H - H_{\mathrm{r}})^2 + (\Delta H)^2} = A_{y'y'}\left[F_{\mathrm{A}}(H) - iF_{\mathrm{S}}(H)\right] \\
\chi_{y'z'} = -\chi_{z'y'} &= \frac{\frac{\omega}{\mu_0\gamma}}{\Delta H\,(\mathfrak{H}_{0\mathrm{r}} + \mathfrak{H}_{1\mathrm{r}})} \frac{(\Delta H)^2 + i\Delta H\,(H - H_{\mathrm{r}})}{(H - H_{\mathrm{r}})^2 + (\Delta H)^2} = A_{y'z'}\left[F_{\mathrm{S}}(H) + iF_{\mathrm{A}}(H))\right] \\
\chi_{z'z'} &= \frac{\mathfrak{H}_{1\mathrm{r}}}{\Delta H\,(\mathfrak{H}_{0\mathrm{r}} + \mathfrak{H}_{1\mathrm{r}})} \frac{\Delta H\,(H - H_{\mathrm{r}}) - i(\Delta H)^2}{(H - H_{\mathrm{r}})^2 + (\Delta H)^2} = A_{zz}\left[F_{\mathrm{A}}(H) - iF_{\mathrm{S}}(H)\right].
\end{aligned} \tag{3.15}$$

All entries can be expressed as an amplitude factor A_{ij} multiplied by a combination of a symmetric Lorentzian lineshape $F_{\mathrm{S}}(H)$ and an antisymmetric Lorentzian lineshape $F_{\mathrm{A}}(H)$ defined as

$$F_{\mathrm{S}}(H) = \frac{(\Delta H)^2}{(H - H_{\mathrm{r}})^2 + (\Delta H)^2}, \quad F_{\mathrm{A}}(H) = \frac{\Delta H(H - H_{\mathrm{r}})}{(H - H_{\mathrm{r}})^2 + (\Delta H)^2}. \tag{3.16}$$

In this form it hold that $F_{\mathrm{S}}(H_{\mathrm{r}}) = 1$, $F_{\mathrm{A}}(H_{\mathrm{r}} \pm \Delta H) = \pm\frac{1}{2}$ and $F_{\mathrm{S}}(H)^2 + F_{\mathrm{A}}(H)^2 = F_{\mathrm{S}}(H)$. It should be noted that in this form, the linewidth ΔH is the half width at half maximum of the symmetric Lorentzian curve.

This formulation allows to fit experimental data using analytical expressions and gives insight into the physical processes at work due to simple lineshape analysis as will be pointed out in the section dealing with the inverse spin Hall effect. When calculating relevant physical quantities from the solution of the magnetization as a function of time it must be remembered that the expressions given for $m(t)$ are usually the complex ones. Using the equation defining $\boldsymbol{m}_{\mathrm{r}}(t)$, Eq. (3.6), it is observed that the real magnetization moves on an elliptic trajectory in the y', z' plane. The ellipticity of the movement has its roots in the demagnetization field that suppresses large oop precession angles. The

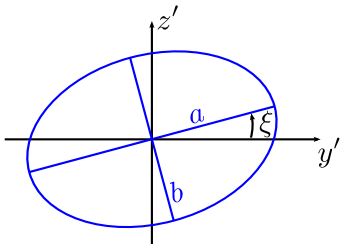

Figure 3.2.: *Elliptical precession curve of $\boldsymbol{m}_r(t)$ in the y', z' plane with main axes a and b and tilt angle ξ. Adapted from [Hen16].*

ellipse is described by the two main axes a, b, a tilt angle ξ between the principal main axis and the y' axis and a phase factor of the precessional motion. Explicit expression for these parameters as a function the complex factors Δm_i are given in [Hen16, appendix A]. The parameters can then be calculated using the susceptibility and the driving torques. It should be noted that, for a general set of driving fields/torques, all four parameters are nonzero and especially $\xi \neq 0$. Using the approximated susceptibility Eq. (3.15) it can be shown, however, that if either $d_{y'} = 0$ or $d_{z'} = 0$ it follows $\xi = 0$ and that $\xi = 0$ at FMR for all combinations of driving fields.

Part II.

Experimental Quantification of Spin Orbit Torques: Comparison of Direct (SHE) and Inverse (ISHE) Spin Hall Measurements in Pt/Py Bilayers

Part II of this thesis is dedicated to the experimental quantification of SOTs in metallic normal metal (NM)/ferromagnet (FM) bilayers. For this purpose, in the last years a variety of different techniques has been established. Despite the effort put into experimental work, the physical origin of current induced SOT is not yet theoretically understood. As already mentioned in the general introduction, in particular, there is a long lasting debate of whether SHE or Rashba effect play the dominant role. Additionally, in NM/FM/oxide elements the question arises whether bulk effects or contributions arising at the NM/FM and/or FM/oxide interface are the primary cause for the observed torques. The disentanglement of different contributions is aggravated by the fact that different models are used for data evaluation of different experiments, hindering a clear comparison of the outcome.

In this thesis, measurements of the spin Hall angle are performed by using two complementary experimental techniques: the so-called spin transfer torque (STT) experiment and the so-called inverse spin Hall (ISHE) experiment. In a STT experiment, an ip charge current flow in a NM/FM/oxide multilayer causes a torque on the magnetization that can be measured. In an ISHE experiment, on the other hand, externally driven magnetization dynamics induces a measurable charge current, such that ISHE and STT can be generally treated as reciprocal effects [Tse14]. The system studied in this work comprises of Pt(x)/Py(4 nm)/Al_2O_3 multilayers with varying Pt thickness. Due to the fact that the FM layer is relatively thick, the detected damping-like torque in STT experiments and the measured ISHE voltage are believed to stem mostly from the spin Hall effect (SHE) in the NM [Liu11; Fan13; Ski14; Pai15; Ou16]. Recently, it has been shown that in this case both experiments can be described within the same drift diffusion formalism based on spin and charge currents connected via the bulk SHE [Han13a; Tse02a; Tse02b; Mos10b]. This enables the comparison of the results of both STT and ISHE measurements in a consistent way.

Within this model, the SHE induced STT experiment can be understood as follows: an ip charge current flowing in the NM is converted into a transverse spin current via the SHE. The spin current eventually reaches the NM/FM interface and is partially absorbed in the FM. The resulting transfer of angular momentum from the NM to the FM leads to a torque on the magnetization[3]. The spin transport across the NM/FM is determined by the spin mixing conductance introduced in section I.2.4. Due to experimental clarity, as STT experiment in this work the method of "modulation of damping" (MOD) is used, as introduced by [And08]. In MOD, the influence of the current induced torques on the magnetization dynamics is measured by using ferromagnetic resonance (FMR). The damping-like torque produced by the SHE in this context is seen as a change of the FMR linewidth, i.e. a change of the measured damping. From section I.2.5 it is clear that the three key quantities describing the MOD experiment are the spin Hall angle θ_{SH}, the spin

[3] the flow of spin current across the NM/FM interface motivates the name "spin transfer torque"

diffusion length λ_S and the spin mixing conductivity $G^{\uparrow\downarrow}$.

ISHE, in contrast, uses the reciprocal effect and is briefly outlined in the following: Motivated by experimental findings of an enhanced Gilbert damping in NM/FM multilayers compared to free standing single FMs [Miz01a], Tserkovnyak et al. developed a model that describes the generation of a pure spin current from the FM into the NM, driven by magnetization dynamics [Tse02a; Tse02b]. This effect is therefore called spin pumping (SP) and consequently the enhanced damping is explained by angular momentum transfer from the FM to the NM. The efficiency of spin current generation is again determined by the spin mixing conductivity. The SP-induced spin current is subsequently converted into an ip charge current via the SHE in the NM. This current can be measured by simple voltage measurements in an open-circuit geometry [Mos10b]. The efficiency of spin current generation and subsequent conversion is governed by the same parameters $G^{\uparrow\downarrow}$, θ_{SH} and λ_S as used to describe MOD in the same system.

The main focus of this part is put on answering the question whether the SHE induced torque on the magnetization and the ISHE voltage generated by magnetization dynamics are reciprocal in the sense that a measurement of spin Hall angle and spin diffusion length in both cases (SHE and ISHE) leads to the same result.

The outline of this part is as follows: The first chapter II.1 gives a short review of current techniques closely related to the ones used in this work, in order to elucidate the different strengths and weaknesses of different approaches (without any claim to completeness) and to motivate the choice of MOD for the measurements performed in this work. Chapters II.2 to II.5 describe the corresponding theoretical models as well as the experimental realization of the measurement techniques (FMR, MOD and SP induced ISHE) used in this part of the thesis as follows: Both experimental methods for determining the SHE/ISHE, as well as the magnetic characterization of the bilayers are based on ferromagnetic resonance (FMR). The SHE/ISHE measurements are conducted on NM/FM micro-stripes, whereas the characterization can be performed on full film samples. Thus, in chapter II.2 the concept of coplanar waveguide based FMR is introduced. Subsequently, II.3 describes both theory and experimental realization of full film FMR.

Chapter II.4 introduces the MOD experiment as performed in this work: magnetization dynamics is measured locally by using time and space resolved magneto-optical Kerr effect. The current induced shift in FMR linewidth in such an experiment gives direct access to the damping-like torque and thus can be used to quantify θ_{SH} and λ_S.

In the following chapter II.5, the concepts of spin pumping (SP) and SP driven ISHE are introduced. It is shown how the spin current in the NM, created by the SP effect, can be quantified by the knowledge of the NM/FM interface parameters and the magnetization dynamics. Subsequently, it is shown how the ISHE leads to a measurable voltage in a NM/FM microstrip and how the ISHE signal can be separated from the inevitable voltage

signal generated by the anisotropic magnetoresistance in such a stripe.
In the above-mentioned chapters, the validity of both the macrospin approximation for the magnetization dynamics as well as the drift diffusion model (in particular the assumption of a homogeneous current density within the single layers) for the charge and spin current transport is assumed. Within the evaluation of measured data, however, it is found that these assumptions do not strictly hold in arbitrary cases and therefore chapters II.6 and II.7 both introduce an extension to the commonly used models.
Due to the fact that both ISHE and MOD experiments are performed on microstripes, the macrospin approximation and therefore the formalism used to describe the magnetization dynamics start to break down if the stripe width is reduced. This is caused by the appearance of standing spin waves (SSWs) in the confined direction, across the stripe width. Chapter II.6 therefore gives a short introduction into magnetization dynamics in thin FM stripes and discusses the implication of the SSWs for SOT measurements.
Chapter II.7 introduces electrical transport in thin metallic layers which goes beyond the Drude model. The section is motivated by the results of conductivity measurements on Pt layers with varying thickness as presented in section II.9.4. It is shown that for very clean Pt, size effects influence the current density distribution in thin multilayers.
Chapters II.8 to II.13 finally describe the experimental results obtained from thickness-dependent measurements of SHE, SP and ISHE in a Pt(x)/Py(4 nm) sample series.
First, chapter II.8 describes how the layer stacks are grown in order to suite the experimental requirements. Subsequently, the characterization results are presented in chapter II.9. Chapter II.10 treats the experimental ISHE results obtained in the Pt/Py samples. The chapter starts with the confirmation of the data evaluation process by the use of micromagnetic simulations. It is shown that for the particular samples studied, the macrospin approximation can be used to evaluate the experimental data. Subsequentially, the experimental results of the ISHE voltage are presented and the spin diffusion length and the spin Hall angle are extracted from the measured ISHE voltage. The experimental results as obtained by MOD are shown in chapter II.11. It is shown that both field- and damping-like torques are present. From the latter the spin diffusion length and the spin Hall angle are extracted by using the same model as for the ISHE. The results of the SP, ISHE and MOD measurements are compared to each other and discussed within the current literature in chapter II.12. The second part is finally concluded by the summary II.13.

1. Review of Experimental Techniques

Experimental techniques used to quantify the SOTs, and in particular the SHE in metallic NM/FM bilayers, can be divided into two main classes:
In the experiments of the first class, a charge current induced influence on the magnetization is measured by probing the response of the FM layer to the application of either dynamic or static ip currents. These experiments are referred to as spin transfer torque (STT) experiments as the torque is caused by the transfer of spin angular momentum from the NM to the FM.
Within this class of experiments another distinction can be made between static and dynamic approaches to quantify the SOTs.
The idea of measuring the (adiabatic) response of a FM to a static applied current is as follows: In equilibrium, the magnetization lies in the direction of lowest energy, where the total torque on $\boldsymbol{m}$ must be zero. It is therefore clear that the appearance of a small SOT (created via a dc current) will change this equilibrium position and therefore the quantification of this change gives access to the strength of the torque. In such a measurement the exact dynamics is not of interest. There are two static methods that are widely used: the so-called "harmonics measurement" which uses an all electrical method to quantify the changes in the equilibrium position [Gar13] by carefully separating different contributions (field-/damping-like) by their respective symmetry. A similar method based on optical probing has recently been published [Fan14]. The latter method is discussed in detail in the appendix and called "static equilibrium change" in this work. The advantage of these static methods is the clarity of the measurement and the exact knowledge of the currents throughout the device since no high frequency effects come into play. The second big advantage is that these measurements do not depend on the damping of the system, which makes them applicable for highly damped systems, in which FMR based approaches fail. However, the change in equilibrium is small for ip magnetized samples and therefore small torques might not be measurable using a static measurement. Thus, generally speaking, static methods are well suited for oop magnetized layers with high damping $\alpha \sim 0.1$.
An all-dynamic approach to quantify SOTs in the context of FMR is to use the SOTs as driving torques and measure the amplitude of precession that depends linearly on the driving torque strength and can be described by the use of the dynamic susceptibility. This is the basis for the extremely wide used spin transfer torque FMR (STT-FMR) method introduced by Liu et al. [Liu11]. The advantage of this method is that the torque strength

required to excite a measurable FMR signal is very small, corresponding to driving fields of $\mu_0 h_\mathrm{d} \sim 0.01 - 0.1\,\mathrm{mT}$ such that small torques can be measured. However, care has to be taken in order to separate field and damping-like SOTs using this method.
A mixed type of experiment uses the influence of static SOTs on the magnetization dynamics in the case of FMR. In an FMR measurement, the resonance condition depends on the internal fields and field-like torques of the system, while the measured resonance linewidth depends on the total damping and damping-like torques. It is possible to excite FMR in a NM/FM bilayer and simultaneously apply a static ip current in order to measure its influence on the resonance position/linewidth. This method was first used by Ando et al. [And08] to measure the damping-like torque created by the spin Hall effect in a Pt/Py bilayer via a modulation of the FMR linewidth by an electric current. This experiment is therefore called "modulation of damping" (MOD). A field-like torque is seen as a variation of resonance position in such an experiment and therefore, this measurement scheme can be used to quantify both damping-like and field-like SOTs in a single measurement. The big advantage of this technique is that FMR intrinsically separates damping-like and field-like torques and is therefore chosen for the measurements performed in this work.
In the experiment of the second class, in contrast, the magnetization dynamics causes a current in the layer that can be picked up as a voltage. This is the case in an inverse spin Hall effect (ISHE) experiment [Mos10b; Mos10a] where a pure spin current is converted into a charge current in the NM. As will be detailed below, the required spin current is created at the interface of a NM/FM bilayer under the action of FMR in the FM in a process called spin pumping. The strength of this spin current can be quantified if the magnetization dynamics and the interface parameters are known. It is then possible to measure the charge current created by the ISHE and calculate the spin Hall angle from this data.
Within the literature, SOT effects are quantified using different torque to current ratios obtained from STT/ISHE experiments which sometimes leads to confusion when comparing values from different publications. Therefore a few remarks shall be given here:

- In STT experiments a current is sent through a NM/FM bi- or multilayer and the impact of this current on the magnetization is measured. In these experiments the measured quantity therefore is the ratio of torque per current, $\frac{\boldsymbol{T}}{I}$ or, for convenience $\frac{\boldsymbol{\tau}}{I}$ which has units of $[\frac{\mathrm{T}}{\mathrm{A}}]$. In almost all publications, however, ratios of torque per current density $\frac{\boldsymbol{\tau}}{j}$ in $[\frac{\mathrm{T}}{\mathrm{A\,m^2}}]$ are found, especially in bilayers in which $d_\mathrm{F} \leq 1\,\mathrm{nm}$ such that a homogeneous current density across the bilayer is assumed and j is calculated from the measured current I and the geometry of the sample [Gar13].

  If the current density differs between NM and FM, however, assumptions on the origin of the torque have to be made in order to give a meaning to $\frac{\boldsymbol{\tau}}{j}$, as $j = j_{NM/FM}$ must be chosen. This is especially important for the field-like torque as the Rashba

contribution and the SHE contribution are expected to result from different origins. In the present work, the SHE in the NM is assumed to be the only origin of the DL torque, such that the ratio $\frac{\tau_{\mathrm{DL}}}{j_{\mathrm{N}}}$ is used to estimate a strength of the effect in the context of applications, for example for the calculation of critical switching currents etc. Under the assumptions that the torque is created a) by the current flow in the NM or FM only and b) acts on the magnetic layer as an interface effect, the torque ratio can be further normalized to the magnetic moment per area and multiplied by $\frac{2e}{\hbar}$ to result in a conversion efficiency of charge current density to transferred angular momentum per area and time, in analogy to Eq. (2.25). These ratios are (in the context of the SHE) called effective SH angle $\theta_{\mathrm{SH}}^{\mathrm{eff}} = \eta_{\mathrm{DL}}\theta_{\mathrm{SH}}$, see Eq. (2.25). Such a normalization is again helpful to make results comparable. As no distinct model must be chosen up to this point, the effective SHA (or better: conversion efficiency) is independent of spin diffusion length and conductivity etc. but is only valid for a certain layer stack. The bulk SH angle of the NM can then be computed from the effective SH angle using a model for interface transparency and transport under certain assumptions. If values for the bulk SHA are compared to each other, care must be taken which input parameters and models are used.

- The second class of experiments are ISHE measurements (see section II.5.2), sometimes also called "spin pumping experiments". The evaluation of an ISHE measurement always involves the use of a particular model of the spin current generation/flow/conversion and therefore always results in the bulk SHA of the NM. Due to this fact, effective SHAs from experiments of the first class cannot be compared to SHAs measured in ISHE measurements.

2. Coplanar Waveguide Based FMR: Creation of Static and Dynamic Fields

All experiments presented in this work are conducted using the phenomenon of FMR to study the magnetic properties as well as the SOTs in Pt/Py bilayers. To perform such a measurement, three basic components are needed in all cases:

- a controllable (static) magnetic field that can be rotated in the sample plane of the magnetic films
- a rf (magnetic) driving field in the GHz range to excite the magnetization
- a way to measure the magnetization dynamics

The first two tasks are solved similarly for all three experiments and are described in the following two sections.

2.1. Static Field

In this work, the FMR measurements are performed with a fixed frequency $f = (0-20)\,\mathrm{GHz}$ and a variable external field H as already discussed previously. The required field range to reach the resonance fields for such frequencies lies between $(0-400)\,\mathrm{mT}$ for the used Py films. These requirements are well fulfilled by electromagnets with a soft-iron core. With such a magnet, fields up to $\sim 2\,\mathrm{T}$ can be created relatively easily, depending on the exact geometry of the magnet. The sample is mounted in the gap of the pole shoe in order to reach the maximum and most homogeneous field. The field is set by controlling the current through the coil using a controllable power supply that can be set via a PC. The field at the position of the sample is measured by a Hall probe. In the full film FMR and ISHE setup a commercially available, calibrated Hall probe is used to measure the field. The probe head is placed in the gap directly above the sample to ensure a correct reading of the field acting on the sample. In the TRMOKE setup, due to limited space, a Hall probe is usually fixed to one of the pole shoes. The field at the sample position is calibrated using the commercial Hall probe that is placed at the position of the sample during the calibration.

To be able to rotate the field in the sample plane, the choice is to either a) rotate the magnet and keep the sample position fixed or b) rotate the sample and keep the magnet steady. For the ISHE and absorption FMR measurements the sample holder with the sample is rotated in the gap via a rotary stage that is controlled by a stepper motor. This allows a fine control over the field angle especially needed in the ISHE measurements. In the TRMOKE setup, the sample must be fixed under the beam, such that it cannot be rotated easily. Therefore the magnet is built such that it can be rotated around the sample holder.

2.2. Creation of the Driving Field

The precession of the magnetization is driven by a small, oscillating magnetic field in the microwave range of frequencies. In the presented work this field is created by the use of a coplanar waveguide (CPW) as described in great detail in [Obs15] and [Här16] and followed in this work. Additional driving fields are created by the current induced in the NM/FM bilayer itself and have to be taken into account in the evaluation of experimental data as will be shown in the following.

2.2.1. Coplanar waveguides

The advantage of CPWs is the fact that they can be designed for a wide bandwidth in frequency and allow for the creation of fields up to the order of 1 mT with relatively low output power (< 500 mW) as delivered by standard microwave generators/amplifiers. In addition, a CPW-based design is very flexible and can be adjusted to all experimental needs. A sketch of the basic geometry of a CPW is shown in Fig. II.2.1. The CPW consists of three current carrying lines separated by a gap. The inner line (signal line) carries a positive current. The outer lines (ground lines) each carry half of this current in the opposite direction thereby closing the circuit. The current that flows through the lines creates an Oersted field which can be calculated from the well known Biot-Savart law for infinitely long conducting wires if the CPW is much longer than its cross section. The ip and oop components of this field are plotted in the lower right of Fig. II.2.1. The field is calculated at the substrate height (represented by the white dotted line) for a 150 nm thick CPW and a homogeneous current density of $\pm 3 \times 10^9 \frac{\mathrm{A}}{\mathrm{m}^2}$. The image in the background shows the crossection of the CPW geometry in the (y, z) plane (black rectangles) and the field strength $|B|$. Note the aspect ratio of 100:1 in this plot. The fact that usually the CPW thickness is much smaller than the ip dimensions allows to calculate the needed fields using a 2D model.
Given by the geometry of the CPW, there are two basic types of excitation geometries for microstructured samples: the FM layer can be placed on top of signal or ground line, such

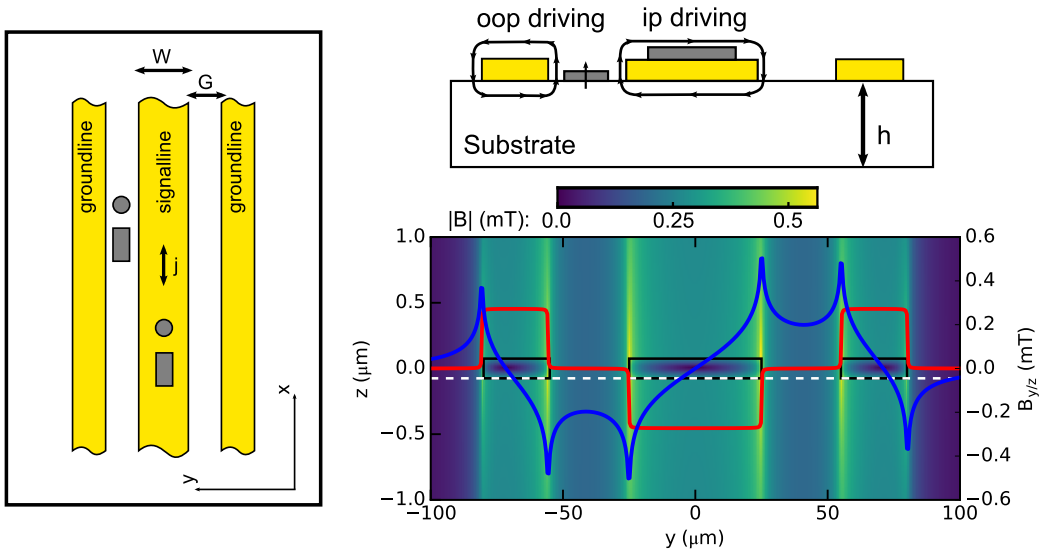

Figure 2.1.: *Geometry of a CPW (left): on an insulating substrate, three (infinitely long) wires are used to carry a high frequency signal. The current flow creates an Oersted field which is used to excite the magnetization dynamics. Top right: depending on the placement of the magnetic element, the driving field is oriented in the film plane (ip driving) or perpendicular to it (oop driving). The Oersted field components of a 150 nm thick CPW are plotted for a homogeneous current density distribution of* $\pm 3 \times 10^9 \frac{\mathrm{A}}{\mathrm{m}^2}$ *within the stripes (lower right). The blue line shows the oop field* h_z *and the red line shows the ip field* h_y*. The color image in the background shows the absolute strength of the field within the* (y, z) *plane. Figure adapted from [Dec12].*

that the driving field is mostly ip. For ip magnetized samples, the ip susceptibility ($\chi_{y'y'}$) is much larger than the other components such that ip driving is very effective. However, turning the external field in the sample plane leads to a variation of the driving field strength, as only the component perpendicular to $\boldsymbol{m}$ contributes to the driving torque. In particular, when the external field is turned to lie perpendicular to the CPW, $\boldsymbol{m} \parallel H_{\mathrm{ext}} \parallel h_{y,\mathrm{rf}}$ and the driving torque is zero. This position is therefore not suited for ISHE measurements as one needs to measure exactly at this angle [Obs14].

If the sample is placed in the center of the gap, the driving field is almost perfectly oop and, if the sample is much smaller than the gap width, quite homogeneous in space. In addition, the driving torque does not depend on the external field ip angle, as static and driving field are always perpendicular in this case. This makes the oop configuration suited for both ISHE and MOD experiments.

The assumption of a homogeneous current density distribution breaks down for GHz frequencies due to the skin effect [Wad91]. The current density is therefore enhanced at the edges of the current carrying lines which results in a higher oop field at the center of the gap. As the driving field strength is a crucial parameter in an ISHE measurement, this effect has to be taken into account. In a previous Ph.D. thesis [Obs15], this problem has been tackled by performing numeric simulations using the commercial software SONNET

to obtain the current density distribution at a given microwave frequency and power for a certain CPW geometry. Subsequently, the driving field is calculated from the current density distribution. The present work follows the exact same procedure such that the interested reader is referred to the abovementioned thesis for a detailed description.
In the full film FMR setup the sample holder consists of a CPW circuit board in which the signal line is ~ 1 mm wide and the ground lines are quasi infinitely wide and connected to a ground plate, see Fig. II.2.2. This design ensures a high frequency bandwidth. A full

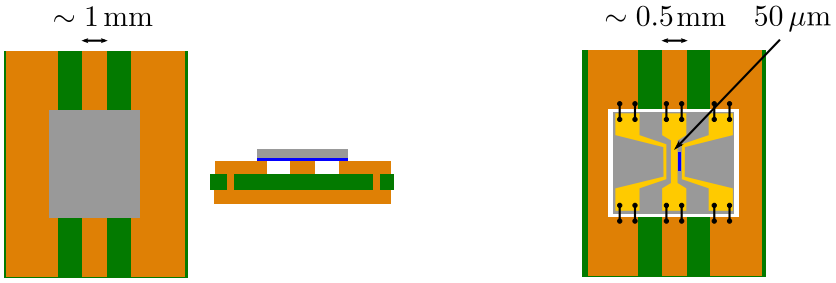

Figure 2.2.: *Full film FMR sample holder and sample placement (left, middle). The holder consists of a circuit board (green) holding a copper CPW with ground plate. The sample is placed face down (magnetic layer drawn in blue) on top of the signal line. In an ISHE/MOD measurement a CPW (gold) is structured on a substrate and the sample is integrated into the circuit board by wire bonding.*

film sample (for example $(3 \times 3)\,\mathrm{mm}^2$) to be measured is then coated with photo resist to protect the surface and placed face down on top of the signal line. The dominant signal then results from the ip driving field directly above the signal line. This is noticed when bringing the external field to the 90° position. Around this angle, the FMR signal decreases strongly down to a tiny signal created by the oop field in the gap. If a full angular dependence shall be taken with good signal to noise ratio it is therefore favorable to measure one full turn, then re-mount the sample with an ip tilt by 90° and measure another full turn. Both data sets can then be combined for analysis.
For measurements on structured samples, the holder itself consists of a specially designed circuit board again in the shape of a CPW. A square is milled out of the circuit board to accommodate the actual sample. The sample consists of an insulating substrate on which the NM/FM bilayers and connector pads according to the needs of the experiments are patterned. As a last step, on every sample a CPW is structured to be connected to the circuit board by wire bonding. The sample holder and CPW are designed symmetrically such that the microwave signal transmitted through the sample can be measured using a powermeter or a fast oscilloscope. Since for high frequencies the impedance of all parts in a circuit must be matched to $50\,\Omega$, care has to be taken to keep all connections like the bonding wires short and to design the CPW on the sample such that it matches the impedance as good as possible. Due to the reduction in size the driving fields in the center of the CPW are much higher than those reachable with the macroscopic structure in the

full film case.

2.2.2. Oersted fields due to induced currents

This section shall introduce the Oersted fields created when a rf/dc current is passed through a metallic bilayer as they excite the magnetization precession (rf) and change the dynamics and equilibrium position (dc). Without loss of generality a (infinitely long) stripe geometry as depicted in Fig. II.2.3 is assumed. For the sake of simplicity a two

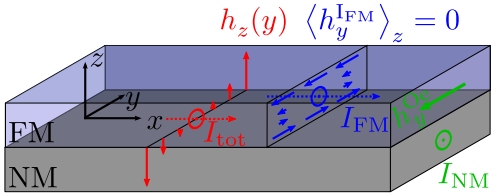

Figure 2.3.: *Current flow and Oersted fields acting on the FM in a NM/FM bilayer.*

current model is used to divide the total current I_{tot} into the parts that flow through the NM/FM,

$$I_{NM/FM} = I_{tot} \frac{\sigma_{NM/FM} d_{NM/FM}}{\sigma_{NM} d_{NM} + \sigma_{FM} d_{FM}}. \tag{2.1}$$

Here, σ denotes the conductivity of the respective layer. From above formula the respective current densities can be computed (by dividing by the cross section), which are assumed to be homogeneous in y and z. This assumption can break down due to two main reasons: on the one hand the homogeneity in y may be broken for ac currents in the GHz regime as the skin effect causes the current density to be concentrated at the stripe edges rather than in the center. However, for thin, low conducting films simulations of the current density distributions show that this effect is small enough to be neglected. On the other hand, the homogeneity in z suffers from interface scattering if the film thickness comes close to the mean free path.

The Oersted field created by I_{tot} can be divided into its y and z component. The y part can then again be split up into the part that is created by the current density in the NM j_{NM}, h_y^{NM}, and the part that is created by j_{FM}, h_y^{FM}. If the thickness of the FM is of the order of the exchange length - i.e. the magnetization is not allowed to vary across the thickness of the FM - the respective fields can be averaged across the thickness of the FM and h_y^{FM} cancels out, leaving only h_y^{NM} [Liu11]. If $w \gg d_{NM}$, the average ip field can be calculated from the current density in the NM via [Liu11]

$$\mu_0 h_y^{Oe} = \frac{\mu_0}{2} j_{NM,x} d_{NM}. \tag{2.2}$$

The z component is position dependent across the width of the stripe and evaluates as

[Fan14]

$$\mu_0 h_z^{\mathrm{ind}}(y) = -\frac{\mu_0}{2}\frac{I_{\mathrm{tot}}}{\pi w}\left[\ln(y) - \ln(w-x)\right]. \tag{2.3}$$

3. Absorption FMR

The measurement of FMR in a full film gives access to the intrinsic magnetic energy landscape and the damping parameter of a given FM layer and therefore is a widely used tool to characterize grown samples prior to structurization.

3.1. Theoretical Considerations

A typical measurement is performed by placing the magnetic layer in a microwave magnetic field and measuring the power that is absorbed in the sample while sweeping the external field. The absorption is thereby given by the change in the transmission of the CPW that creates the driving field. The shape of the absorption curve can be easily derived by the use of the dynamic magnetic susceptibility: The instantaneous power taken from the driving field is given by the derivative of the Zeeman energy of magnetization and generalized driving field, $p(t) = \frac{P(t)}{V} = \frac{\mathrm{d}\varepsilon}{\mathrm{d}t} = -\mu_0 M_\mathrm{s} \frac{\mathrm{d}\boldsymbol{m}(t)}{\mathrm{d}t} \cdot \boldsymbol{d}(t)$. The absorbed power is then calculated by the time average over one period and results in [Gur63, eq. 15.22]

$$\begin{aligned} \langle p(t) \rangle_T &= -\mu_0 M_\mathrm{s} \langle \boldsymbol{m}(t) \cdot \boldsymbol{d}(t) \rangle_T = -\frac{1}{2} \mu_0 M_\mathrm{s} \Re\mathfrak{e} \left\{ \boldsymbol{m}(t) \cdot \overline{\boldsymbol{d}(t)} \right\} \\ &= \frac{1}{2} \mu_0 M_\mathrm{s} \omega \left(\chi''_{y'y'} |d_{y'}|^2 + \chi''_{z'z'} |d_{z'}|^2 + 2\chi'_{y'z'} \left[d'_{y'} d''_{z'} - d''_{y'} d'_{z'} \right] \right). \end{aligned} \tag{3.1}$$

Therefore in an absorption measurement one generally expects a symmetric lineshape [Cel97]. If only one source of driving fields is present, the phase of the driving fields can be set to zero by definition, which means $d'' = 0$. In this case, the imaginary part of the diagonal entries of the susceptibility $\chi''_{y'y'}/\chi''_{z'z'}$ is measured, depending on the chosen driving geometry. Nonzero phases occur if there are secondary currents/fields that are created by inductive or capacitive coupling into the FM layer itself or e.g. into metal capping layers. Such coupling can result in phase lags between the primary driving field and the induced currents directly implying a phase lag in the induced driving field. From Eq. (3.1), however, this situation still leads to a symmetric absorption curve. In real measurements, the line shape sometimes consists of a symmetric and an anti-symmetric part. This effect might be caused by changes of the impedance of the CPW due to the additional load created by the magnetic sample [Bai13b] such that the transmitted power is not only determined by the power dissipation in the sample. To circumvent this problem, the data is modeled using a combination of the symmetric and antisymmetric lineshapes

connected by a mixing angle ϵ via

$$p_{\mathrm{abs}}(H, H_{\mathrm{r}}, \Delta H) = A\left(F_{\mathrm{S}}(H)\cos(\epsilon) + F_{\mathrm{A}}(H)\sin(\epsilon)\right) \tag{3.2}$$

where A is an amplitude factor that contains all proportionality constants and the amplitude factors of the susceptibility [Cel97; Wol04; Här16]. This method is sufficient as long as only the resonance position and the linewidth of the respective curves are of interest.

3.2. Experimental Realization

The FMR setup used to characterize the magnetic layers in this work is based on measuring the absorption dip in the microwave signal transmitted through the CPW by a Schottky diode using a lock-in technique. This method is widely used in the institute and has therefore already been described in great detail previously [Här16; Obs15; Wol04]. The actual setup used within this work has been built up during the thesis of M. Obstbaum [Obs15]. This section thus only gives a very short overview of the experiment. A magnetic layer is placed on top of a CPW based sample holder and brought into the gap of a controllable electromagnet as described in the previous two sections. The microwave frequency and input power is fixed and the external field is swept through FMR while the power transmitted through the CPW is measured. As powermeter, a Schottky diode is used that acts as a rectifier for the rf current such that a dc voltage is picked up when measuring with a low bandwidth device (voltmeter or lock-in amplifier). The absorbed power as a function of the external field is described by Eq. (3.2). As the absorption signal is small compared to the input power it is beneficial to use a lock-in amplifier in order to enhance the S/N ratio. To enable the lock-in technique, the external magnetic field is modulated by a small field H_{mod} at a frequency of 87 Hz. The signal measured by the lock-in amplifier is then proportional to the derivative of Eq. (3.2) with respect to H as long as the modulation field is small (rule of thumb: $H_{\mathrm{mod}} \leq \frac{\Delta H}{5}$). The fitting formula used to extract both resonance field and linewidth is therefore given by:

$$A_{\mathrm{FMR}} = A\frac{-2\left(H - H_{\mathrm{r}}\right)\Delta H\cos(\epsilon) + \left[(\Delta H)^2 - \left(H - H_{\mathrm{r}}\right)^2\right]\sin(\epsilon)}{\left[\left(H - H_{\mathrm{r}}\right)^2 + (\Delta H)^2\right]^2} \tag{3.3}$$

with a proportionality factor A and the mixing angle ϵ discussed in sect. II.3. A typical FMR absorption curve and the respective fit are shown in Fig. II.3.1.

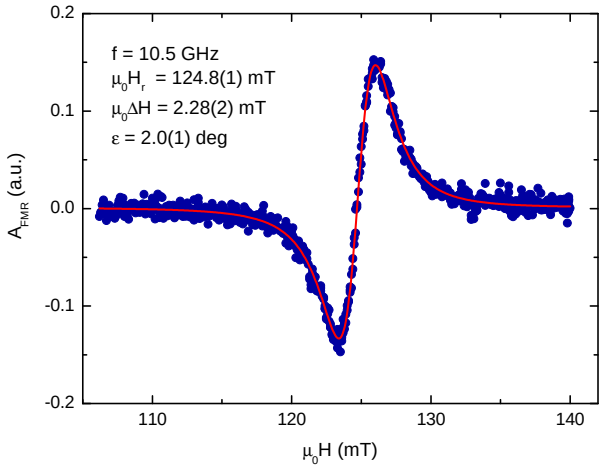

Figure 3.1.: *Typical absorption FMR curve. The plotted data is taken on a 4 nm thick Py film at 10.5 GHz; the dimensions of the sample are* $\approx (3\times4)\,\mathrm{mm}^2$*. From the fit to Eq. (3.3) the resonance field and the linewidth are extracted and further analyzed as a function of the frequency.*

4. Quantification of SOTs by Modulation of Damping

4.1. Theoretical Aspects of MOD

As shown in the previous sections, a static damping-like torque in an FMR measurement appears in the dynamical susceptibility tensor as an additional damping source that adds to the intrinsic damping α, see Eq. (3.13). In addition, the equilibrium condition is shifted away from ip to have a small oop component. However, for an ip-magnetized sample as for a Pt/Py(4 nm) layer, this change is very small such that $\theta \approx 90°$ can be used in all calculations, see section IV.C. This assumption simplifies the mathematical expressions used in the susceptibility and the equilibrium condition drastically as shown in the appendix.

For a quantification of the SOTs, FMR measurements are performed for different applied dc currents which create both field and damping-like torques. These are separated by analyzing the resulting resonance field and linewidth.

The damping-like torque is seen as a shift in the linewidth given by [And08; Liu11]:

$$\mu_0\,\delta\Delta H = \frac{\omega}{\gamma}\frac{2\mathfrak{s}}{\mu_0\left(\mathfrak{H}_{0\mathrm{r}}+\mathfrak{H}_{1\mathrm{r}}\right)} = \frac{\omega}{\gamma}\frac{-\tau_{\mathrm{DL}}\sin(\varphi)}{\mu_0\left(H_{\mathrm{r}}+\frac{M_{\mathrm{eff}}}{2}\right)}. \tag{4.1}$$

In the last step it is assumed that no ip anisotropy and no additional demagnetization field is present. In the studied samples the height to width ratio is $\sim \frac{1}{1000} \approx N_{yy}$ such that corrections to the denominator of $\delta\Delta H$ are of the order of $N_{yy}M_{\mathrm{s}} << M_{\mathrm{eff}}$ and can be neglected. The same argument is valid for a small ip anisotropy of some mT. Due to the fact that the sample is of the shape of a stripe of width w in y and length $L \gg w$ in x-direction, the dc current flows along the x-direction only. This sets the spin current polarization $\boldsymbol{\sigma}$ along y which leads to the $\sin(\varphi)$-like behavior. The spin Hall induced torque is therefore at maximum if the external field is applied perpendicular to the stripe.

The field-like torque and the current created Oersted field are seen as a shift of the resonance field:

$$\mu_0\,\delta H_{\mathrm{r,I}} = h_y^{\mathrm{I,MOD}}\sin(\varphi) = \left(\tau_{\mathrm{FL}}+\mu_0 h_y^{\mathrm{Oe}}\right)\sin(\varphi) \tag{4.2}$$

The calculation of the Oersted field can be performed using Eq. (2.2) but does depend on

the current density distribution within the NM/FM which itself can be nonhomogenous across the height. It is therefore hard to determine the absolute strength of the FL torque resulting from the SOT alone if the magnitude of Oersted field and SOT field are similar. However, lower bounds for the SOT can be found by calculating the maximum possible Oersted field assuming that the whole current flows in the NM. Then, the lower bound for the SOT induced FL torque is the difference in the measured shift and the maximum Oersted field [Emo16].
The modulation of damping method therefore provides a straightforward and very clear way of separating field- and damping-like torques in one single measurement and gives direct values for the strength of both torques as a function of the applied ip current.
Since the MOD technique builds up on the exact determination of the linewidth, effects that parasitically influence this quantity must be avoided carefully. In confined structures one problem that appears lies in the modes structure discussed in section II.6, as the overlap of multiple modes can lead to a deviation in the measured linewidth. This effect, however can be reduced by the use of a sample design that minimizes mode structure effects.

4.2. Time and Space Resolved FMR

In order to perform the MOD measurements and especially to study the mode structure in the microstructured stripes a way to locally measure FMR is needed. This can be achieved by directly probing the magnetization dynamics using a time and space resolved optical technique. In the present work this is done by means of time resolved magneto-optical Kerr effect (TRMOKE) spectroscopy. This technique allows measuring the oop component of the magnetization stroboscopically by probing the magnetization using a pulsed laser system where the probe pulses are much shorter than the precession period. This technique has been developed in the workgroup over a long time, see for example [Neu06; Per07; Hof10] and allows probing the dynamics of microstructured FMs locally, with a spacial resolution limited by diffraction and with picosecond temporal resolution.

4.2.1. Magneto-Optical Kerr effect

The magneto-optical Kerr effect (MOKE) is a widely used technique to probe the magnetization of FM thin films [Bad91]. MOKE describes the change of the polarization axis of linearly polarized light upon reflection from a FM sample depending on the relative orientation of $\boldsymbol{m}$ and the polarization axis of the incident light. The change of polarization depends on the relative orientation of the plane of incidence and the magnetization [Coe10] as depicted in Fig. II.4.1. The magnetization component perpendicular to the plane of incidence (transverse configuration) leads to a small change in the reflected inten-

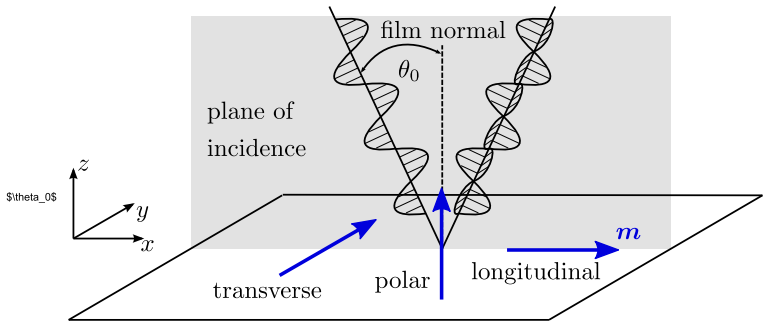

Figure 4.1.: *Definition of the three configurations of MOKE. The sample lies in the (x, y) plane and the incident light vector in the (x, z) plane. Depending on the relative orientation of the magnetization vector (blue arrow) and the incidencent light the configuration is called transverse, polar or longitudinal. Adapted from [Coe10].*

sity, depending on the polarization of the incidence beam. The magnetization component that lies within the plane of incidence is split up into ip (longitudinal configuration) and oop components (polar configuration). Both components lead to a rotation of the polarization direction depending on the relative orientation of the magnetization direction and incident beam. It is important to note that the polar Kerr effect scales with $\cos(\theta_0)$, while the longitudinal effect scales with $\sin(\theta_0)$ [Coe10]. In the presented work the incident light is focused on the sample by an objective lens. Therefore the incidence angles of all wavevectors passing the objective are concentrated around θ_0, such that the polar Kerr effect is dominant. In addition, the two other contributions average to zero due to the radial symmetry of the objective such that [Per07; Neu06; Hof10].
As a result of MOKE the polarization direction of the incident light is rotated by a small angle $\theta_K \propto m_z$ from the incident polarization. The deflection is detected by the use of a Wollaston prism and a balanced photodetector. A Wollaston prism separates an incident beam into two orthogonally polarized components depending on the rotation angle of the prism itself. This allows to mount the prism such that in the case of zero Kerr rotation, both partial beams have the same intensity. A small Kerr rotation then reduces the intensity of one beam and increases the intensity of the other one, leading to a signal at the balanced photodetector that is proportional to $2\theta_K$. When used in combination with a DC laser system, polar MOKE therefore is a widely used tool to record magnetic hysteresis loops.

4.2.2. Time resolved MOKE

The temporal resolution needed to measure FMR using MOKE is achieved by a stroboscopic probing scheme. A pulsed Ti:Sa laser operating at a repetition rate f_{rep} of 80 MHz is used to generate a pulsetrain of ~ 150 fs light pulses at a central wavelength of around 800 nm. The magnetization dynamics is driven by a microwave current in the GHz range. If the driving frequency f is a multiple of the repetition rate and if the phase between laser pulses and microwave signal is constant, the magnetization is always probed at the same distinct position during the precession. In other words, the magnetization is probed at a distinct phase Θ between laser pulses and driving field. Mathematically, this probing scheme is implemented by setting $t = t_n = n\frac{2\pi}{\omega} + \frac{\Theta}{\omega}$ with any positive integer n and the phase angle Θ. For an ip magnetized sample, the result is the measured z-component

$$\begin{aligned} m_z(H, H_{\mathrm{r}}, \Delta H, \Theta) = \; & \mathfrak{Re}\left\{m_z(t_n)\right\} \\ = \; & \Big\{ -\cos(\Theta)\big[A_{yz}d'_y - A_{zz}d''_z\big] + \sin(\Theta)\big[A_{zz}d'_z + A_{yz}d''_y\big]\Big\}F_{\mathrm{S}}(H) \\ & + \Big\{ \sin(\Theta)\big[\underbrace{A_{yz}d'_y - A_{zz}d''_z}_{a_1}\big] + \cos(\Theta)\big[\underbrace{A_{zz}d'_z + A_{yz}d''_y}_{a_2}\big]\Big\}F_{\mathrm{A}}(H) \\ = \; & A\left[\cos\big(\Theta'\big)F_{\mathrm{S}}(H) + \sin\big(\Theta'\big)F_{\mathrm{A}}(H)\right]. \end{aligned} \tag{4.3}$$

In the last step the amplitude prefactor $A = \sqrt{a_1^2 + a_2^2}$ and the effective phase angle $\Theta' = \Theta + \arctan\left(\frac{a_2}{a_1}\right)$ are computed using the appropriate addition theorems (see footnote 4 on page 82). The important point to recognize is that it is possible to set the phase angle Θ such that either the purely symmetric, the purely antisymmetric or a mixture of both lineshapes is measured. A fit to the data using Eq. (4.3) therefore delivers exactly the same information as an absorption measurement: the linewidth and the resonance field. If the phase angle can be determined absolutely, the time resolved method allows to separate different driving field components. A time resolved measurement also allows to directly measure the precession amplitude $|m_z| = \sqrt{m_z(t)^2 + m_z(t + \frac{T}{4})^2} = \sqrt{m_z(\Theta)^2 + m_z(\Theta + \frac{\pi}{2})^2}$ with $T = \frac{2\pi}{\omega}$. This fact directly follows from the periodicity of $m_z(t)$.

To ensure the two abovementioned conditions for stroboscopic probing, all components must be synchronized to one frequency standard and to one fixed phase. A full sketch of the experimental setup used is shown in Fig. II.4.2. The frequency standard is set by a master clock that is part of the laser's control unit, called "synchrolock". It creates a 80 MHz signal and adjusts the laser repetition rate to this frequency by a feedback loop (number I in the figure) by changing the laser cavity length via a stepper motor and piezo actuators holding two of the cavity mirrors.

The synchrolock provides a reference signal (10 MHz) which is used to synchronize the microwave signal generator to the synchrolock both in frequency and in phase. In order

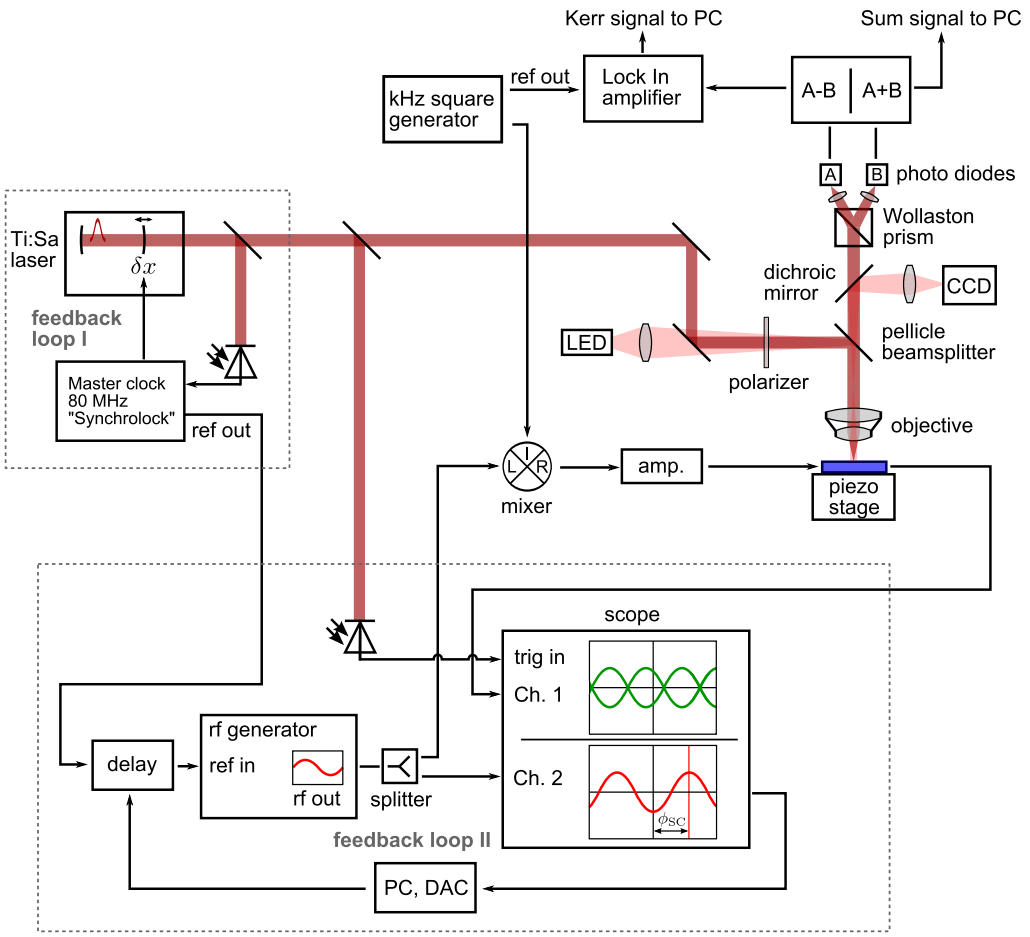

Figure 4.2.: *TRMOKE setup used in this work. For explanation of the components, see the main text.*

to be able to control the phase between microwave signal and laser pulses an electronic phase shifter (delay) is installed between synchrolock and signal generator. In this way the phase can be adjusted by the application of a control voltage at the phase shifter. The actual phase difference between microwave signal and laser pulses is read out by a fast oscilloscope that is triggered from the laser by a biased photodiode. This trigger pulse determines the time zero at the oscilloscope. The phase of the microwave signal at the scope ϕ_{sc} is determined from a cosine fit to the acquired scope signal. It must be noticed that this phase is arbitrary in the sense that it is not the same phase as present at the sample (Θ) due to the fact that all cables etc. contribute to an unknown delay such that $\Theta = \phi_{\mathrm{sc}} + \mathrm{off}$. The absolute time zero at the sample must not be known, however, for the measurements performed in this work[1]. The phase read off from the oscilloscope is actively stabilized to a fixed value by varying the control voltage at the phase shifter (feedback loop II in the figure). This removes long-term phase drifts which are caused by the signal

[1]It can in principle be determined by the use of Eq. (4.3) if the driving field contributions are known.

generator. It is therefore possible to measure over very long times (weeks) with a constant phase.

In order to enhance the signal to noise ratio, a lock-in technique is used to separate the small dynamical Kerr signal from the background. In the current setup, the signal is phase modulated by 180° in order to gain the maximum signal possible. For this purpose, a square signal with a frequency of $f_{\mathrm{mod}} \sim 6.6\,\mathrm{kHz}$ is provided by a second signal generator. This square signal is mixed with the driving signal thereby reversing the sign every half period of the modulation signal. In Fig. II.4.3 the stroboscopic technique with phase

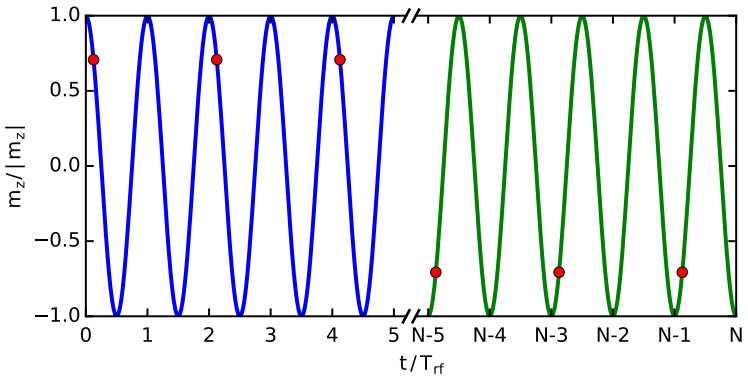

Figure 4.3.: *Stroboscopic probing with phase modulation. Laser pulses (red dots) arrive at a fixed phase every $\frac{f}{f_{rep}}$ period and probe the magnetization at the given instant of time. Due to a (much slower) phase modulation, the Kerr signal is reversed at the modulation frequency, enabling a lock-in measurement.*

modulation is sketched for the case of a ratio $f : f_{\mathrm{rep}} = 2 : 1$ and $f : f_{\mathrm{mod}} = N : 1$, i.e. the magnetization is probed every second driving period and the modulation frequency is much slower than both driving and probing frequency. The oop component of $\boldsymbol{m}$ oscillates at f and the laser pulses arrive at a certain phase resulting in a dc Kerr signal due to the fact that the detector bandwidth is $\ll 80\,\mathrm{MHz}$. Due to the phase modulation, however, the magnetization and thus the Kerr signal switch sign every half period of f_{mod}. If fed into a lock-in amplifier this difference in Kerr signal can be measured with great precision. For this to work the modulation frequency must of course lie within the detector bandwidth.

If the phase is modulated in this way, the signal transmitted through the sample cannot be used for the microwave phase stabilization because both phases are sampled and read at the scope. Therefore, a part of the generator output is directly used instead. The relative phases between transmitted signal and reference signal is found to be stable (by observation of the two channels of the oscilloscope) indicating that mixer and amplifier are phase stable over long times.

The last big part is the optical setup itself, which is based on a Zeiss Axiomat polarization maintaining microscope. The laser passes a linear polarizer and is focused onto the sample by a 100× objective with a numerical aperture of 0.9. The FWHM of the resulting beam

spot is measured to be ~ 500 nm limited by diffraction. The refracted beam again passes the objective and reaches the detector unit. The sample is mounted on a (x, y, z) piezo stage which allows to scan the sample by some tens of micrometers under the beam. In order to locate the sample under the beam and to keep the position of the sample fixed for long-term measurements a bright field image of the sample is generated by a second beam path. The divergent light of a LED with λ = 532 nm is additionally coupled into the microscope and creates an illumination spot on the sample thereby enabling bright field imaging of the sample. The reflected LED light is separated from the laser light by a dicroic lowpass mirror and the image recorded by a CCD camera. By adjusting the focusing optics and CCD camera position it is possible to overlay the laser spot with the center of the LED image and to bring the focal points of both laser and LED image together. Once this is done, a pattern recognition software can be used to actively stabilize both sample position and focus.
The optical probing in combination with the high spatial resolution has important advantages over electrical/absorption measurements in which the averaged magnetization dynamics is measured. These are:

- the optical probing eliminates spurious induced signals
- the signal does not decrease with sample size as long as the dimensions are larger than the probing spot
- the phase information allows for better separation of multiple resonance peaks
- the spatial resolution allows to determinate the spatial structure of the dynamics in confined structures, see section II.6
- if applied properly, resonance position and linewidth in confined structures can be determined correctly, circumventing the problem of edge modes which artificially enhance the measured linewidth

4.2.3. Sample geometry for MOD experiments

In the case of the MOD experiment, a strong dc current needs to be applied to the sample under investigation in order to see a resolvable shift in the linewidth. It is therefore favorable to keep the stripe short, in order to minimize Joule heating problems. In this work, the stripes used for the MOD experiments are chosen to have a dimension of $(16 \times 6)\mu m^2$. In Fig. II.4.4 the MOD sample structure is shown in an overview image (right side) and in detail (left side). The images are taken using an optical microscope with a CCD camera and by scanning electron microscopy, respectively. The sample consists of

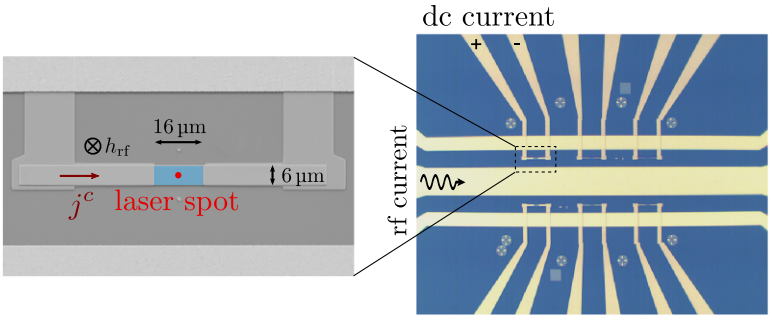

Figure 4.4.: *Image of a MOD sample. On the right, an overview of the center part of the sample is given by an optical image. Six different Pt/Py bilayer stripes are placed in the gap of a CPW. Contact pads allow to apply a dc current through the bilayer stripes. The contact wires and the CPW are separated by a thick Al_2O_3 layer similar to the ISHE samples. The left side shows a detailed SEM image of the stripe used in the MOD measurements to quantify the SHA. The magnetization dynamics is probed at the center of the stripe using the focused beam of a pulsed laser system via TRMOKE.*

a CPW producing an oop driving field in the gap analogously to the ISHE experiment. The bilayer stripes are placed in the gap such that the external field can be rotated ip without changing the driving field efficiency. Different stripe geometries are placed into one CPW in order to be able to vary the geometry for one magnetic multilayer. The final results presented in this work are taken on the stripe shown in detail on the left side of the figure. A measured resonance curve of a pure Py sample of the studied series is shown in Fig. II.4.5.

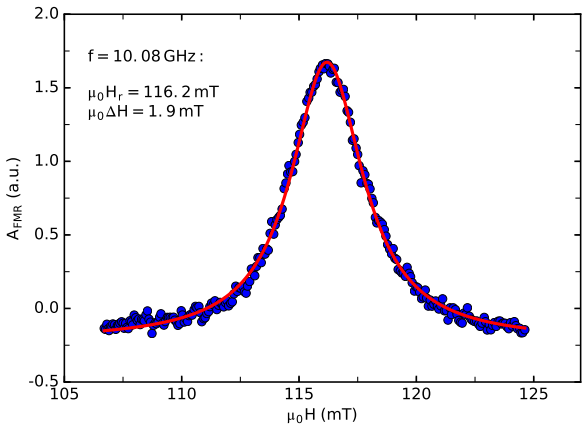

Figure 4.5.: *Raw data of a TRMOKE experiment and fit to Eq. (4.3) in order to extract resonance position and linewidth. The plotted data is taken on a 4 nm thick Py sample without Pt underlayer at 10.08 GHz.*

5. Quantification of the SHE by the Spin Pumping Driven ISHE

5.1. Spin Pumping

In the search for novel materials and functional multilayer systems, it has been noticed in the early 2000s that the FMR linewidth and the determined damping parameter changes if thin FM layers are capped with heavy NM layers [Urb01; Miz01b; Miz01a]. The experimental results have subsequently been explained by the so-called spin pumping (SP) theory [Tse02a; Tse02b]. The theory is based on magnetoelectronic circuit theory and describes the spin current generation at a NM/FM interface driven by the magnetization dynamics in the FM under the assumption that the dynamics is much slower than spin relaxation. Tserkovnyak et al. have shown that in this case the motion of the magnetization vector induces a spin current at the NM/FM interface, flowing from FM into NM direction given by

$$\boldsymbol{j}^{\mathrm{s,pump}} = \frac{\hbar}{4\pi}\left(\mathfrak{Re}\left\{\tilde{g}^{\uparrow\downarrow}\right\}\boldsymbol{m}\times\frac{\mathrm{d}\boldsymbol{m}}{\mathrm{d}t} - \mathfrak{Im}\left\{\tilde{g}^{\uparrow\downarrow}\right\}\frac{\mathrm{d}\boldsymbol{m}}{\mathrm{d}t}\right). \tag{5.1}$$

The pumped spin current density depends on the real and imaginary part of the SMC $\tilde{g}^{\uparrow\downarrow}$; the equation in this form holds for the case that the FM thickness is larger than the spin coherence length [Tse02b]. It therefore depends on the exact same interfacial transport parameter that determines the (dc) spin current transport from NM to FM. Since the spin current is created directly at the NM side of the interface it will generally build up a spin accumulation within the NM that falls off exponentially as a function of the distance from the interface due to spin relaxation in the NM. In the case of very fast spin relaxation, the spin accumulation is approximately zero such that all of the pumped spin current is dissipated immediately. However, for a finite spin flip time, the spin accumulation that builds up will lead to a spin current backflow into the FM, which is described by the same drift diffusion formalism used to describe the transport of a spin current across the interface in section I.2.4. For this reason the net spin pumping current is reduced if a) the NM layer is too thin, such that part of the spin current is reflected back and re-enters the interface and/or b) the ratio of spin scattering time and momentum scattering time $\epsilon = \frac{\tau}{\tau_{\mathrm{s}}}$ is small, such that a high spin accumulation builds up at the NM/FM interface

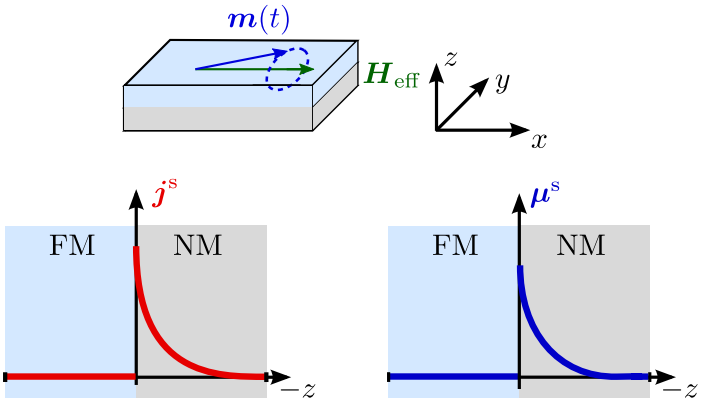

Figure 5.1.: *Spin current and spin accumulation created by SP from FM into NM. Top: In a NM/FM bilayer the FM is brought to FMR. This creates a spin current source at the NM/FM interface by the SP effect. As a result a spin accumulation builds up (right), leading to a partial backflow of the primary spin current into the FM thereby reducing the net spin current dissipated into the NM (left).*

driving a spin current back into the FM. The spin accumulation within the NM can be calculated using the drift diffusion equation with the boundary condition given by the SMC as discussed in section I.2.4 at the NM/FM layer and a source of spin current at the NM side of the NM/FM interface. The exact procedure can be found in [Tse02b][1]. If the precession frequency of the magnetization is much lower than the spin flip rate, the solution of the spin chemical potential (notation of [Tse02b]) and the spin current density are calculated to be[2]

$$\boldsymbol{\mu}^{\mathrm{s}}(z) = \boldsymbol{j}^{\mathrm{s}}(z=0)\frac{4\lambda_{\mathrm{sd}}|e|^2}{\hbar\sigma_{\mathrm{N}}^0}\frac{\cosh\left(\frac{\mathrm{d}_{\mathrm{NM}}-z}{\lambda_{\mathrm{sd}}}\right)}{\sinh\left(\frac{\mathrm{d}_{\mathrm{NM}}}{\lambda_{\mathrm{sd}}}\right)} \quad \Rightarrow \quad \boldsymbol{j}^{\mathrm{s}}(z) = \boldsymbol{j}^{\mathrm{s}}(z=0)\frac{\sinh\left(\frac{\mathrm{d}_{\mathrm{NM}}-z}{\lambda_{\mathrm{sd}}}\right)}{\sinh\left(\frac{\mathrm{d}_{\mathrm{NM}}}{\lambda_{\mathrm{sd}}}\right)} \tag{5.2}$$

The spin accumulation at the interface is therefore proportional to the spin diffusion length of the NM and inversely proportional to its bulk conductivity σ_{N}^0. The higher the spin accumulation at the interface, the higher the backflow current such that the primary, pumped spin current is reduced and the net spin current leaving the interface is $\boldsymbol{j}^{\mathrm{s}}(z=0) = \boldsymbol{j}^{\mathrm{s}}_{\mathrm{pump}} - \boldsymbol{j}^{\mathrm{s}}_{\mathrm{back}}$. The net current is calculated by using the boundary condition Eq. (2.22) to evaluate the backflow current and then solving for $\boldsymbol{j}^{\mathrm{s}}(z=0)$. The final result is

$$\boldsymbol{j}^{\mathrm{s}}(z=0) = \frac{\hbar}{4\pi}\left(\Re\mathfrak{e}\left\{\tilde{g}_{\mathrm{eff}}^{\uparrow\downarrow}\right\}\boldsymbol{m}\times\frac{\mathrm{d}\boldsymbol{m}}{\mathrm{d}t} - \Im\mathfrak{m}\left\{\tilde{g}_{\mathrm{eff}}^{\uparrow\downarrow}\right\}\frac{\mathrm{d}\boldsymbol{m}}{\mathrm{d}t}\right), \tag{5.3}$$

[1] note that the definition of the spin current in eq. 9) of [Tse02b] differs from the definition used in section I.2.1.2. This also affects the boundary condition for the backflow, eq. 13) such that the result (the backflow parameter β) is independent of the exact definition at the very end. Note in addition that $\boldsymbol{j}^{\mathrm{s}} = \frac{\boldsymbol{I}^{\mathrm{s}}}{S}$.

[2] the Einstein relation $\sigma_{\mathrm{N}} = |e|^2 D(2\mathcal{N})$ is used in the expression for $\boldsymbol{\mu}^{\mathrm{s}}$

which corresponds exactly to the primary pumped spin current with a rescaled SMC $\tilde{g}_{\mathrm{eff}}^{\uparrow\downarrow}$ that can be expressed, to the first order of $\mathfrak{Im}\left\{\tilde{g}^{\uparrow\downarrow}\right\}$, as

$$\mathfrak{Re}\left\{\tilde{g}_{\mathrm{eff}}^{\uparrow\downarrow}\right\} = \frac{\mathfrak{Re}\left\{\tilde{g}^{\uparrow\downarrow}\right\}}{1+\beta\mathfrak{Re}\left\{\tilde{g}^{\uparrow\downarrow}\right\}}, \quad \mathfrak{Im}\left\{\tilde{g}_{\mathrm{eff}}^{\uparrow\downarrow}\right\} = \frac{\mathfrak{Im}\left\{\tilde{g}^{\uparrow\downarrow}\right\}}{\left[1+\beta\mathfrak{Re}\left\{\tilde{g}^{\uparrow\downarrow}\right\}\right]^2} \tag{5.4}$$

with the backflow factor

$$\beta = \frac{|e|^2}{h}\frac{2\lambda_{\mathrm{sd}}}{\sigma_{\mathrm{N}}}\frac{1}{\tanh\left(\frac{d_{\mathrm{NM}}}{\lambda_{\mathrm{sd}}}\right)} = \sqrt{\frac{3}{4\epsilon}}\frac{1}{\tanh\left(\frac{d_{\mathrm{NM}}}{\lambda_{\mathrm{sd}}}\right)}\frac{1}{\mathfrak{Re}\left\{\tilde{g}^{\uparrow\downarrow}\right\}}. \tag{5.5}$$

The last equality is true within the free electron model and if $\mathfrak{Re}\left\{g^{\uparrow\downarrow}\right\} \approx g_{\mathrm{Sh}}$ with the number Sharvin conductance g_{Sh} [Tse02b; Jia13, see eq. (62), supplementary material]. This result shows that a precessing FM induces a spin current from the FM into the NM, i.e. it acts as a spin current source. To quantify this spin current, both the magnetization dynamics and the effective SMC need to be known.

The spin current leaving the FM corresponds to a loss of angular momentum which, by angular momentum conservation, manifests itself as an additional torque $\boldsymbol{T} = \frac{\gamma}{M_{\mathrm{s}}d_{\mathrm{F}}}\boldsymbol{j}^{\mathrm{s}}(z=0)$ that has to be added to the LLG equation. The normalization to the magnetic moment per area is the result of the interfacial nature of the torque. This torque can be included into the LLG equation via a renormalization of both gyromagnetic ratio $\gamma \to \gamma_{\mathrm{sp}}$ and damping parameter $\alpha \to \alpha_{\mathrm{sp}}$ [Tse02a; Zwi05][3]:

$$\begin{aligned}\gamma_{\mathrm{sp}} &= \frac{\gamma}{1-\frac{\gamma\hbar}{4\pi M_{\mathrm{s}}d_{\mathrm{F}}}\mathfrak{Im}\left\{\tilde{g}_{\mathrm{eff}}^{\uparrow\downarrow}\right\}} \\ \alpha_{\mathrm{sp}} &= \frac{\gamma_{\mathrm{sp}}}{\gamma}\left(\alpha+\frac{\gamma\hbar}{4\pi M_{\mathrm{s}}d_{\mathrm{F}}}\mathfrak{Re}\left\{\tilde{g}_{\mathrm{eff}}^{\uparrow\downarrow}\right\}\right).\end{aligned} \tag{5.6}$$

A short estimation of the implication of these results can be made using values for $\tilde{G}^{\uparrow\downarrow}$ for metallic bilayers and the Fermi vector k_{F} for Pt from table I) of [Han13a]. The change of the gyromagnetic ratio is calculated to be $\frac{\gamma_{\mathrm{sp}}}{\gamma} = 1.0012$ using Eq. (5.6), $\mathfrak{Im}\left\{\tilde{G}^{\uparrow\downarrow}\right\} = 0.9\times10^{14}\,\frac{1}{\Omega\,\mathrm{m}^2}$, $\mu_0 M_{\mathrm{s}} = 0.9\,\mathrm{T}$ and $\gamma = 185\,\frac{\mathrm{rad}}{\mathrm{T\,s}}$ as typical values for Py. The change is in the range of one over thousand and therefore does not play a significant role in an FMR measurement. A completely different scenario holds for the Gilbert damping parameter: assuming a damping parameter for bare Py of $\alpha = 0.008$, $\alpha_{\mathrm{sp}} = \alpha + \delta\alpha$ can be computed, with $\delta\alpha = 0.0084$ for $\mathfrak{Re}\left\{\tilde{G}^{\uparrow\downarrow}\right\} = 6.0\times10^{14}\,\frac{1}{\Omega\,\mathrm{m}^2}$ and $d_{\mathrm{Py}} = 4\,\mathrm{nm}$; therefore the change is more than 100%. Via FMR measurements it is therefore possible to determine only

[3] Note that $4\pi M_{\mathrm{s}}$ in SI units is $\approx 12.57\times M_{\mathrm{s}}$, with $[M_{\mathrm{s}}]$ =A/m and should not be confused with the sometimes used saturation magnetization $4\pi M_{\mathrm{s}}$ in cgs units with $[4\pi M_{\mathrm{s}}]$=gauss

$\mathfrak{Re}\left\{\tilde{G}_{\mathrm{eff}}^{\uparrow\downarrow}\right\}$. For each NM layer thickness one then calculates the effective SMC via

$$\mathfrak{Re}\left\{\tilde{g}_{\mathrm{eff}}^{\uparrow\downarrow}\right\}(d_{\mathrm{NM}}) = \left[\alpha_{\mathrm{sp}}(d_{\mathrm{NM}}) - \alpha_{\mathrm{F}}\right]\frac{4\pi M_{\mathrm{s}} d_{\mathrm{F}}}{\gamma\hbar}. \tag{5.7}$$

From a thickness-dependent measurement it is possible to deduce both $\mathfrak{Re}\left\{\tilde{g}^{\uparrow\downarrow}\right\}$ and λ_{sd} via

$$\mathfrak{Re}\left\{\tilde{g}^{\uparrow\downarrow}\right\} = \frac{\tilde{g}_{\mathrm{eff}}^{\uparrow\downarrow}(d_{\mathrm{NM}})}{1-\beta\tilde{g}_{\mathrm{eff}}^{\uparrow\downarrow}(d_{\mathrm{NM}})} = \frac{\tilde{g}_{\mathrm{eff}}^{\uparrow\downarrow}(d_{\mathrm{NM}})}{1-\frac{|e|^2}{h}\frac{2\lambda_{\mathrm{sd}}}{\sigma_{\mathrm{N}}^0}\frac{1}{\tanh\left(\frac{d_{\mathrm{NM}}}{\lambda_{\mathrm{sd}}}\right)}\tilde{g}_{\mathrm{eff}}^{\uparrow\downarrow}(d_{\mathrm{NM}})}. \tag{5.8}$$

The additional parameters that must be known for the analysis of the data are therefore the magnetic moment per area, $M_{\mathrm{s}}d_{\mathrm{F}}$ which can be measured using a magnetometer, γ which can be evaluated via FMR and the bulk conductivity of the normal metal, σ_{N}^0.

5.2. SP Driven ISHE

In the last section it has been shown that in a NM/FM bilayer, when the FM undergoes FMR, a spincurrent is injected from the FM into the NM. This spin current is converted into a charge current via the ISHE if there is a sizeable SHE in the NM. The charge current can then be detected by picking up the resulting voltage across the sample. The ISHE can in this way be used for the quantification of the SHA in the NM once all important parameters like the SMC and the magnetization dynamics are known. The technique of measuring the ISHE, as well as a historical overview has been worked out recently in the author's workgroup and can be found as Ph.D. thesis [Obs15] with the key parts of that work published in [Obs14; Wei14]. The same knowledge has subsequently been used in another Ph.D. thesis [Här16]. The ISHE part of the presented work therefore directly follows [Obs15].

5.2.1. Origin and form of the ISHE voltage

As shown in the spin pumping section, the injected spin current itself is time-dependent and can be written down explicitly using Eq. (5.3) and the time-dependent magnetization vector (in its real form), Eq. (3.6) as

$$\boldsymbol{j}^{\mathrm{s}}(z=0) = -\frac{\hbar\omega}{4\pi}\left[\mathfrak{Re}\left\{\tilde{g}_{\mathrm{eff}}^{\uparrow\downarrow}\right\}\begin{pmatrix}\mathfrak{Im}\left\{\overline{\Delta m_{y'}(t)}\, m_{z'}(t)\right\}\\ -\mathfrak{Im}\left\{\Delta m_{z'}(t)\right\}\\ \mathfrak{Im}\left\{\Delta m_{y'}(t)\right\}\end{pmatrix} + \mathfrak{Im}\left\{\tilde{g}_{\mathrm{eff}}^{\uparrow\downarrow}\right\}\begin{pmatrix}0\\ \mathfrak{Im}\left\{\Delta m_{y'}(t)\right\}\\ \mathfrak{Im}\left\{\Delta m_{z'}(t)\right\}\end{pmatrix}\right]. \tag{5.9}$$

In this expression, the x'-component $\mathfrak{Im}\left\{\overline{\Delta m_{y'}(t)}\, m_{z'}(t)\right\} = \mathfrak{Im}\left\{\overline{\Delta m_{y'}}\,\Delta m_{z'}\right\}$ is constant in time, whereas the other components periodically vary in time with period $T = \frac{2\pi}{\omega}$.

Performing the time average results in the dc component of the pumped spin current

$$\boldsymbol{j}^{\mathrm{s}}_{\mathrm{dc}}(z=0) = \langle \boldsymbol{j}^{\mathrm{s}}(z=0)\rangle_T = -\frac{\hbar\omega}{4\pi}\mathfrak{Re}\left\{\tilde{g}^{\uparrow\downarrow}_{\mathrm{eff}}\right\}\mathfrak{Im}\left\{\overline{\Delta m_{y'}}\,\Delta m_{z'}\right\}\hat{x}'. \tag{5.10}$$

In this equation, $\mathfrak{Im}\left\{\overline{\Delta m_{y'}}\,\Delta m_{z'}\right\} = |\Delta m_{y'}||\Delta m_{z'}|\sin(\varphi_z - \varphi_y)$ which is used to evaluate micromagnetic simulations in which the absolute phases of the two magnetization components, φ_z and φ_y are known.

The spin current evolves into the NM following Eq. (5.3) and, at every point in z, acts as a charge current source due to the ISHE according to Eq. (2.6) such that the current density is given, in laboratory coordinates, by

$$\boldsymbol{j}^{\mathrm{c}}_{\mathrm{dc}} = \frac{2|e|}{\hbar}\theta_{\mathrm{SH}}\hat{z}\times\boldsymbol{j}^{\mathrm{s}} \tag{5.11}$$

at every point in the NM. In a measurement, one certain ip component of this current is measured which is given by the geometry of the sample; in this work it the x-component. Thus, the x-component of the charge current density is averaged over the thickness of the sample, where of course the FM region contributes with zero current density but shunts the measured voltage and therefore has to be taken into account:

$$\begin{aligned}\langle j^{\mathrm{c}}_x(z)\rangle_z &= \frac{1}{d_{\mathrm{NM}}+d_{\mathrm{F}}}\int_{-d_{\mathrm{F}}}^{d_{\mathrm{NM}}} dz\, j^{\mathrm{c}}_{\mathrm{dc},x} \\ &= \frac{|e|}{2\pi}\frac{\theta_{\mathrm{SH}}}{d_{\mathrm{BL}}}\mathfrak{Re}\left\{\tilde{g}^{\uparrow\downarrow}_{\mathrm{eff}}\right\}\omega\mathfrak{Im}\left\{\overline{\Delta m_{y'}}\,\Delta m_{z'}\right\}\sin(\varphi)\lambda_{\mathrm{sd}}\tanh\left(\frac{d_{\mathrm{NM}}}{2\lambda_{\mathrm{sd}}}\right).\end{aligned} \tag{5.12}$$

Here, the $\sin(\varphi)$ comes from the transformation of Eq. (5.10) into laboratory coordinates and $d_{\mathrm{BL}} = d_{\mathrm{NM}} + d_{\mathrm{F}}$ is the total thickness of the bilayer. This current, by Ohm's law $V = RI = \frac{1}{\sigma_{\mathrm{BL}}}\frac{L}{d_{\mathrm{BL}}w}\,w d_{\mathrm{BL}}\,\langle j^{\mathrm{c}}_x(z)\rangle_z$, leads to a voltage that can be picked up in x-direction and is given by

$$\begin{aligned}V_{\mathrm{ISHE}} \equiv V_x &= \underbrace{\frac{|e|}{2\pi}\frac{\theta_{\mathrm{SH}}L}{\sigma_{\mathrm{BL}}d_{\mathrm{BL}}}\mathfrak{Re}\left\{\tilde{g}^{\uparrow\downarrow}_{\mathrm{eff}}\right\}\omega\lambda_{\mathrm{sd}}\tanh\left(\frac{d_{\mathrm{NM}}}{2\lambda_{\mathrm{sd}}}\right)}_{V^0_{\mathrm{ISHE}}}\mathfrak{Im}\left\{\overline{\Delta m_{y'}}\,\Delta m_{z'}\right\}\sin(\varphi) \\ &= V^0_{\mathrm{ISHE}}\,\mathfrak{Im}\left\{\overline{\Delta m_{y'}}\,\Delta m_{z'}\right\}\sin(\varphi).\end{aligned} \tag{5.13}$$

The voltage along x is at maximum if the stripe is magnetized along y, which results from the cross product in the ISHE conversion equation Eq. (5.11). The shape of the voltage curve as a function of the external field, $V_x(H)$ is determined by $\mathfrak{Im}\left\{\overline{\Delta m_{y'}}\,\Delta m_{z'}\right\}$ and can be calculated from the susceptibility and the driving fields, allowing to compute the SHA θ_{SH} from the measured voltages. Using the approximated susceptibility Eq. (3.15), it can be shown that $\mathfrak{Im}\left\{\overline{\Delta m_{y'}}\,\Delta m_{z'}\right\} \propto F_{\mathrm{S}}(H)$ such that the measured lineshape is always symmetric with respect to the resonance field for any driving torques and relative

phases. It will be shown in the next section how to set up a measurement in order to exclude parasitic effects from an ISHE measurement. As a result, the ISHE voltage must be recorded at $\varphi = 90°$, i.e. the magnetization must be perpendicular to the stripe. If all magnetic parameters and the dynamics are known, the measured voltage at this angle can be normalized in such a way that, from the result, both the spin diffusion length and the SHA can be obtained by fitting to:

$$V_{\mathrm{ISHE}}^{\mathrm{norm}} = \frac{2\pi}{|e|}\frac{G_{\mathrm{sheet}}}{L}\frac{V_{\mathrm{ISHE}}(\varphi = 90°)}{\mathfrak{Re}\left\{\tilde{g}_{\mathrm{eff}}^{\uparrow\downarrow}\right\}\omega\mathfrak{Im}\left\{\overline{\Delta m_{y'}}\,\Delta m_{z'}\right\}} = \theta_{\mathrm{SH}}\lambda_{\mathrm{sd}}\tanh\left(\frac{d_{\mathrm{NM}}}{2\lambda_{\mathrm{sd}}}\right). \tag{5.14}$$

In the above expression $G_{\mathrm{sheet}} = \sigma_{\mathrm{BL}} d_{\mathrm{BL}}$ is the measured sheet resistance of the bilayer.

5.2.2. Rectified voltage due to anisotropic magnetoresistance

The voltage due to ISHE, unfortunately, is not the only one that is measured when performing a voltage measurement at an arbitrary ip field angle. An additional signal source consists of a rectification signal due to an induced current in the sample stripe and the time varying anisotropic magnetoresistance (AMR). It is known since 1875 that, in a FM, the longitudinal resistance depends on the angle between the magnetization and the current direction. This effect leads to a change in Ohm's law and results in a field created by an electrical current [McG75; Jur60]:

$$\boldsymbol{E} = \rho_{\perp}\boldsymbol{j}^{\mathrm{c}} + \Delta\rho\,\boldsymbol{m}(\boldsymbol{m}\cdot\boldsymbol{j}^{\mathrm{c}}) + \rho_{\mathrm{H}}\boldsymbol{m}\times\boldsymbol{j}^{\mathrm{ind}}. \tag{5.15}$$

Here, $\rho_{\perp}$ and $\rho_{\parallel}$ denote the resistivity for $\boldsymbol{m}\perp\boldsymbol{j}^{\mathrm{c}}$ and $\boldsymbol{m}\parallel\boldsymbol{j}^{\mathrm{c}}$, respectively and $\Delta\rho = \rho_{\parallel} - \rho_{\perp}$. In this equation it is evident that the the multiplication of $\boldsymbol{m}$ and $\boldsymbol{j}^{\mathrm{c}}$ leads to a rectification of the ac current that, in turn, leads to a dc component in the measured voltage. Assuming precessional motion of $\boldsymbol{m}$ and an induced ac current in x-direction j_x^{c}, the rectified field in x-direction is calculated by taking the time average of E_x and by considering only terms linear in Δm_i [Che16]:

$$E_{\mathrm{dc},x} = -\frac{1}{2}\Delta\rho\sin(2\varphi)\left[\mathfrak{Re}\left\{j_x^{\mathrm{c}}\right\}\mathfrak{Re}\left\{\Delta m_{y'}\right\} + \mathfrak{Im}\left\{j_x^{\mathrm{c}}\right\}\mathfrak{Im}\left\{\Delta m_{y'}\right\}\right]. \tag{5.16}$$

Conventionally, in an AMR measurement time zero is defined by the ac current within the sample such that $\mathfrak{Im}\left\{j_x^{\mathrm{ind}}\right\} = 0 \rightarrow j_x^{\mathrm{ind}}(t) = j_x^{\mathrm{ind}}\cos(\omega t)$. In the above equations, $\Delta\rho$ is the change in resistivity of the FM and j_x^{ind} is the current density in the FM. However, the AMR signal can also be expressed in terms of ΔR and I_x^{ind}. The advantage is that ΔR can be measured directly and that I_x^{ind} is the quantity that enters the parasitic driving fields described in the next part. The AMR rectified voltage is than expressed as [Che16;

Obs15]

$$V_{\mathrm{AMR}} \equiv V_{\mathrm{dc},x} = LE_{\mathrm{dc},x} = \underbrace{-\frac{1}{2}\Delta R\, I_x^{\mathrm{ind}}}\ \mathfrak{Re}\left\{\Delta m_{y'}\right\}\sin(2\varphi)$$
$$= \quad V_{\mathrm{AMR}}^{0} \quad \mathfrak{Re}\left\{\Delta m_{y'}\right\}\sin(2\varphi). \tag{5.17}$$

The dependence of the voltage on $\mathfrak{Re}\{\Delta m_{y'}\}$ suggests that, in general, the AMR lineshape contains both symmetric and antisymmetric parts. Therefore, it is not possible to separate the AMR voltage from the ISHE voltage by a simple lineshape analysis. In fact, there has been a long discussion within the community whether the dc-voltage measured in NM/FM bilayers undergoing FMR can be attributed to ISHE [Mos10b; Mos10a] or is polluted by spurious AMR [Har11]. The debate eventually converged into the agreement that both effects are present and have to be disentangled carefully by angular dependent measurements [Aze11; Bai13a; Obs14; Har16].

5.2.3. Angular dependence of AMR and ISHE voltage

To show how the separation works in the case of an ip angular dependence the equations for AMR and ISHE voltage have to be evaluated by taking into account specific driving fields and the use of the susceptibility approach in order to get an expression for $\Delta\boldsymbol{m}$. In the experiment conducted in this thesis, the ISHE is measured in the following way: the NM/FM bilayer is structured into a long stripe, $350\times6\,\mu\mathrm{m}^2$ with the long axis parallel to $\hat{x}$; with the voltage picked up along this length. In Fig. II.5.2 the geometry and the different driving fields are sketched. The primary driving field h_z^{CPW} is created by a coplanar

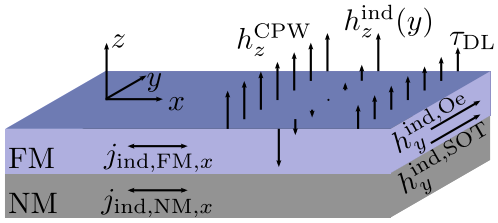

Figure 5.2.: *Driving fields/torques in an ISHE measurement. The primary driving field h_z^{CPW} is out of phase with the other fields created by the induced current I_{ind}.*

waveguide and is nearly homogeneous and solely along $\hat{z}$. Due to electric coupling, a current $I_{\mathrm{ind},x}$ is induced in the bilayer, which leads to the AMR signal discussed before. This current in addition creates driving torques via two effects: the Oersted field created by the current flow as discussed in section II.2.2.2 and the SOTs due to current flow. To the knowledge of the author, the inhomogeneous contribution $h_z^{\mathrm{ind}}(y)$ was never accounted for in the past, probably since it is antisymmetric with respect to the stripe center and supposed to average out. However, the ISHE signal is quadratic in h_z such that this

argument does not hold and $h_z^{\mathrm{ind}}(y)$ needs, in principle, to be included. In addition the SHE will exert a damping-like driving torque on the magnetization which again depends on the induced current density in the NM only. The last effect that contributes to the driving is the field-like SOT, which is denoted by τ_{FL}, acting in the same form as the induced ip Oersted field. Time zero is chosen such that the induced current - and therefore the driving fields/torques created by it - have zero phase; in return the primary field has a phase φ_{CPW} attached to it. Summing up these effects leads to the following driving fields/torques:

- $h_z^{CPW}(t) = h_z^{\mathrm{CPW}}\cos(\omega t + \varphi_{\mathrm{CPW}})$
- $h_z^{\mathrm{ind}}(t,y) = h_z^{\mathrm{ind}}(y)\cos(\omega t)$
- $\tau_{\mathrm{DL}}(t) = -\tau_{\mathrm{DL}}\cos(\omega t)$
- $h_y^{\mathrm{ind,Oe}}(t) = h_y^{\mathrm{ind,Oe}}\cos(\omega t)$
- $\tau_{\mathrm{FL}}(t) = \tau_{\mathrm{FL}}\cos(\omega t)$

In these expressions, all constants are real numbers. The magnetization dynamics is evaluated in the coordinate system of the magnetization such that each component has to be transformed correspondingly. The total ip driving field is then

$$d_{y'}(t) = h_y^{\mathrm{eff}}\cos(\varphi)\cos(\omega t), \quad h_y^{\mathrm{eff}} = h_y^{\mathrm{ind,Oe}} + \frac{\tau_{\mathrm{FL}}}{\mu_0}. \tag{5.18}$$

The total oop driving field is space dependent and involves some trigonometry[4] to evaluate:

$$\begin{aligned} d_{z'}(t,y) &= d_{z'}^{\mathrm{eff}}(y)\cos\left[\omega t + \varphi_{\mathrm{eff}}(y)\right] \\ d_{z'}^{\mathrm{eff}}(y) &= \sqrt{a^2+b^2}, \quad \varphi_{\mathrm{eff}}(y) = \arg\{a + i\,b\} \\ a \equiv h_z^{\mathrm{CPW}}\cos(\varphi_{\mathrm{CPW}}) + h_z^{\mathrm{ind}}(y) - \tfrac{\tau_{\mathrm{DL}}}{\mu_0}\cos(\varphi), &\quad b \equiv h_z^{\mathrm{CPW}}\sin(\varphi_{\mathrm{CPW}}) \end{aligned} \tag{5.19}$$

Here $\arg\{z\}$ denotes the argument of a complex number z. This allows to evaluate the quantities $\mathfrak{Im}\left\{\overline{\Delta m_{y'}}\,\Delta m_{z'}\right\}$ and $\mathfrak{Re}\{\Delta m_{y'}\}$ using Eq. (3.7) together with the the definition of the susceptibility tensor Eq. (3.15) as a function of the symmetric/antisymmetric

4 $a\cos(\omega t+\varphi_a) + b\cos(\omega t+\varphi_b) = c\cos(\omega t+\xi), \quad c=\sqrt{x^2+y^2}, \quad \xi = \arg\{x+i\,y\} \equiv \arctan\left(\frac{y}{x}\right)$
$x \equiv a\cos(\varphi_a) + b\cos(\varphi_b), \quad y \equiv a\sin(\varphi_a) + b\sin(\varphi_b)$
as can be proved by using Euler's identity. The autor wants to thank Richard G. Lyons for posting this fact in: "Sum of two sinusoids" online (12/2017): https://dspguru.com/dsp/tutorials/sum-of-two-sinusoidal-functions/

lineshapes Eq. (3.16). Doing the math leads to:

$$\begin{aligned}\mathfrak{Im}\left\{\overline{\Delta m_{y'}}\,\Delta m_{z'}\right\}(y) &= \Big\{A_{yy}A_{yz}\left(h_y^{\mathrm{eff}}\right)^2\cos^2(\varphi) + A_{zz}A_{yz}\left[d_{z'}^{\mathrm{eff}}(y)\right]^2 \\ &\quad - \left[A_{yz}^2 + A_{yy}A_{zz}\right]h_y^{\mathrm{eff}}\cos(\varphi)d_{z'}^{\mathrm{eff}}(y)\sin\left[\varphi_{\mathrm{eff}}(y)\right]\Big\}F_{\mathrm{S}}(H) \\ \mathfrak{Re}\left\{\Delta m_{y'}\right\}(y) &= A_{yz}d_{z'}^{\mathrm{eff}}(y)\cos\left[\varphi_{\mathrm{eff}}(y)\right]F_{\mathrm{S}}(H) \\ &\quad + \left\{A_{yy}h_y^{\mathrm{eff}}\cos(\varphi) - A_{yz}d_{z'}^{\mathrm{eff}}(y)\sin\left[\varphi_{\mathrm{eff}}(y)\right]\right\}F_{\mathrm{A}}(H)\end{aligned} \tag{5.20}$$

$\mathfrak{Im}\left\{\overline{\Delta m_{y'}}\,\Delta m_{z'}\right\}$ indeed has a purely symmetric lineshape while $\mathfrak{Re}\left\{\Delta m_{y'}\right\}$ has a symmetric as well as an antisymmetric contribution. Due to the oop Oersted field, these quantities are space dependent; however, in an experiment one effectively measures the mean voltage across the stripe width. In a first order approximation this can be taken into account by assuming that the magnetization evolves following the locally present driving field at every point across y. The measured quantities are then given by the average of the above expressions across the stripe width, which, in turn is computed by averaging the respective driving torque contribution. Performing the average leads to

$$\begin{aligned}\left\langle h_y^{\mathrm{eff}}\right\rangle_y &= h_y^{\mathrm{eff}} \\ \left\langle\left[d_z^{\mathrm{eff}}(y)\right]^2\right\rangle_y &= \left(h_z^{\mathrm{CPW}}\right)^2 + \tau_{\mathrm{DL}}^2\cos^2(\varphi) - 2h_z^{\mathrm{CPW}}\cos(\varphi_{\mathrm{CPW}})\tau_{\mathrm{DL}}\cos(\varphi) + \frac{I_{\mathrm{ind}}^2}{12w^2} \\ \left\langle d_{z'}^{\mathrm{eff}}(y)\sin(\varphi_{\mathrm{eff}})\right\rangle_y &= \left\langle h_z^{\mathrm{CPW}}\sin(\varphi_{\mathrm{CPW}})\right\rangle_y = h_z^{\mathrm{CPW}}\sin(\varphi_{\mathrm{CPW}}) \\ \left\langle d_{z'}^{\mathrm{eff}}(y)\cos(\varphi_{\mathrm{eff}})\right\rangle_y &= \left\langle h_z^{\mathrm{CPW}}\cos(\varphi_{\mathrm{eff}}) - \tau_{DL}\cos(\varphi) + h_z(y)\right\rangle_y \\ &= h_z^{\mathrm{CPW}}\cos(\varphi_{\mathrm{CPW}}) - \tau_{DL}\cos(\varphi)\end{aligned} \tag{5.21}$$

These averaged torques are substituted into Eq. (5.20) and the obtained averaged dynamic quantities are used in Eq. (5.13) and Eq. (5.17) to obtain explicit expressions for the measured voltage.

The measured voltage curves $V_{\mathrm{meas}}(H)$ are fit to

$$V_{\mathrm{meas}}(H) = V_{\mathrm{S}}F_{\mathrm{S}}(H) + V_{\mathrm{A}}F_{\mathrm{A}}(H) \tag{5.22}$$

in order to extract the symmetric (V_{S}) and antisymmetric (V_{A}) voltage amplitudes. These amplitudes are then plotted as function of the ip angle $\varphi = \varphi_{\mathrm{H}}$ and are described by the following expressions to fit the measured voltage data:

$$\begin{aligned}V_{\mathrm{S}} &= a\sin(\varphi) + b\sin(2\varphi) + c\cos(\varphi)\sin(2\varphi) \\ V_{\mathrm{A}} &= \qquad\qquad d\sin(2\varphi) + e\cos(\varphi)\sin(2\varphi)\end{aligned} \tag{5.23}$$

with the parameters

$$
\begin{aligned}
a &\equiv V^0_{\mathrm{ISHE}} A_{zz} A_{yz} \left[\left(h_z^{\mathrm{CPW}} \right)^2 + \frac{I_{\mathrm{ind}}^2}{12 w^2} \right] \\
b &\equiv -\frac{1}{2} V^0_{\mathrm{ISHE}} h_z^{\mathrm{CPW}} \left\{ 2 A_{zz} A_{yz} \cos(\varphi_{\mathrm{CPW}}) \tau_{\mathrm{DL}} + \left(A_{yz}^2 + A_{yy} A_{zz} \right) h_y^{\mathrm{eff}} \sin(\varphi_{\mathrm{CPW}}) \right\} \\
&\quad + V^0_{\mathrm{AMR}} A_{yz} h_z^{\mathrm{CPW}} \cos(\varphi_{\mathrm{CPW}}) \\
c &\equiv A_{yz} \left\{ \frac{1}{2} V_{\mathrm{ISHE}} \left[A_{yy} \left(h_y^{\mathrm{eff}} \right)^2 + A_{zz} \tau_{DL}^2 \right] - V^0_{\mathrm{AMR}} \tau_{\mathrm{DL}} \right\} \\
d &\equiv -V^0_{\mathrm{AMR}} A_{yz} h_z^{\mathrm{CPW}} \sin(\varphi_{\mathrm{CPW}}) \\
e &\equiv V^0_{\mathrm{AMR}} A_{yy} h_y^{\mathrm{eff}}
\end{aligned}
\tag{5.24}
$$

What immediately strikes the eye, is the fact that there is only one contribution that has a $\sin(\varphi)$ dependence and delivers the pure ISHE signal from V_{S} at $\varphi = 90°$. All other contributions are zero at this angle. This means that, if the external field angle is carefully adjusted in the experiment by searching for the zero crossing in the antisymmetric voltage signal, the pure ISHE voltage without any parasitic contribution from AMR is measured. However, the amplitude of the symmetric voltage determined at this angle depends - due to the inhomogeneous Oe field - on the strength of the induced current, which is a priory unknown.

In sec. (6.2) of [Obs15] it has already been shown that a full angular measurement allows to determine the additional driving field and phase by a system of equations similar to Eq. (5.23), however both τ_{DL} and $h_z^{\mathrm{ind}}(y)$, as well as the mixing term $\propto h_y^{\mathrm{eff}} d_{z'}^{\mathrm{eff}}$ in the ISHE voltage are not included in the analysis of this work. Nevertheless, from the data of the above-mentioned thesis, a rough estimation of I_{ind} can be obtained for the Pt/Au(12 nm)Py(12 nm) samples studied[5]. At 10 GHz, $\mu_0 h_z^{\mathrm{CPW}} \approx 0.3\,\mathrm{mT}$ and $I_{\mathrm{ind}} \approx 3\,\mathrm{mA}$, in a 5 µm wide stripe. This leads to a total effective driving field of $\mu_0 \sqrt{\left(h_z^{\mathrm{CPW}}\right)^2 + \frac{I_{\mathrm{ind}}^2}{12 w^2}} = 0.37\,\mathrm{mT}$ which is significantly ($\sim 25\%$) higher than the primary driving field and therefore leads to an overestimation of the spin Hall angle. To circumvent this problem, a full angular measurement can be used to determine the strength of the induced current and to use the value in order to correctly evaluate the ISHE signal.

When looking at Eq. (5.23) it is realized that there are more unknown parameters (6) than equations (5) such that additional interconnections of the parameters are needed in order to get a unique set of parameters from a fit to the data. The most natural one is to relate the induced current to the AMR voltage by

$$
V^0_{\mathrm{AMR}} = -\frac{1}{2} \Delta R I_{\mathrm{ind}}. \tag{5.25}
$$

[5] Used: eq. (7.5) on p. 103, fig. (7.3) on p. 100, fig. (4.3) on p. 62 and the results from the discussion in section 6.2 as well as Eq. (2.2) of this work

This is possible due to the fact that ΔR can be determined in a static angular dependent AMR measurement prior to the dynamic ISHE experiment.

5.3. Experimental Access to ISHE

A sketch of an ISHE sample is shown in Fig. II.5.3. The voltage scales linearly with the length L of the stripe such that it must be long enough to give rise to a sufficient signal but short enough to keep the microwave power approximately constant across the full length. Therefore, as a first step in the preparation of an ISHE sample a $(350 \times 6)\mu m^2$ long stripe is patterned from the deposited NM/FM multilayer by Argon ion milling. The stripe is subsequently contacted by bondpads consisting of a few nm Ti as sticking layer followed by 50 nm Au. By pre-sputtering prior to evaporation, the contact resistance is ensured to be negligible compared to the resistance of the bilayer stripe. The magnetization dynamics

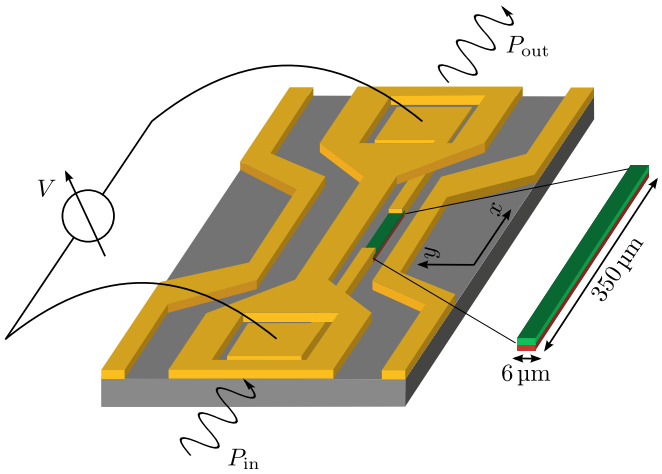

Figure 5.3.: *Schematics of an ISHE sample. The Pt/Py bilayer is patterned into a long stripe and contacted with Au bond pads. A CPW is structured on top such that the stripe lies in the middle of the gap. To separate CPW and stripe electrically, a thick Al_2O_3 layer is grown in between. Holes in the signal line allow for wire bonding on the contact pad. Adapted from [Obs15] with kind permission of M. Obstbaum.*

is excited by an rf magnetic field that must be known as precise as possible. Instead of using an external CPW structure like in the full film FMR setup, the CPW is therefore structured directly on top of the stripe in one liftoff step. The placement is such that the bilayer lies in the gap of the center part of the CPW and holes in the signal line allow for bonding to the electrical contacts of the bilayer as can be seen in the sketch. The total length of the CPW is ~ 2 mm in order to have enough space for the holes and to match the ends of the CPW to the dimensions of the sample holder. The narrower center region of the CPW has the following dimensions: center line width: 50 µm, gap: 30 µm, ground line width: 25 µm. The evaporated layers are again a few nm of Ti and 150 nm of Au. These

dimensions allow for the creation of high enough driving fields using the microwave power available.
To electrically separate the CPW from the bondpads, a 150 nm thick Al_2O_3 layer is grown in between the two layers. The Al_2O_3 is grown in an atomic layer deposition system which ensures a closed layer even at the edges of structures.
The CPW itself is wire bonded to the sample holder's CPW in order to ensure a good transmission through the whole system. In the experiment the power directly before and after the sample holder, P_{in} and P_{out}, are measured using a commercially available and calibrated powermeter. These values are then used to compute the primary driving field acting on the sample from a simulation of the current density distribution. The stripe

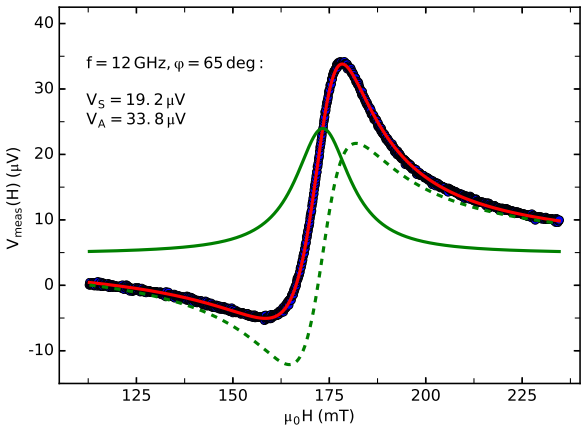

Figure 5.4.: *Fitting of a ISHE voltage curve. The red solid line is a fit to Eq. (5.22), the two green lines represent the symmetric (solid line) and antisymmetric (dashed line) contribution. The curve is taken on a Pt(4 nm)Py(4 nm) sample at 12 GHz and the external field is tilted by 25° from the perpendicular configuration such that the AMR is the dominant source of voltage in this case.*

is connected to a Keithley nanovoltmeter which is precise enough to read the signals of ~ 10 µV obtained in the measurements. The measurement mode is then similar to the previously described FMR: At a fixed frequency the field is swept and the dc voltage is recorded. The resulting curve is fitted to Eq. (5.22) in order to extract the symmetric and antisymmetric voltage components, see Fig. II.5.4. These values are then further evaluated in the experimental results section of the thesis.

6. Standing Spin Waves in Magnetic Microstripes

In some situations, the above-mentioned macrospin approximation breaks down and, instead of a uniform precession, propagating or standing spin waves are exited. Due to the fact that SOT experiments are often conducted on micrometer wide stripes, standing spin waves (SSW) occur in this quantization direction. This fact can, in certain situations, lead to deviations in determined parameters, if the experimental data is evaluated in the macrospin framework. Care must therefore be taken in order to minimize the impact of SSWs on the respective experiments. The following section gives a short introduction into spin waves in thin FM films. Subsequently, the SSW patterns forming in FM stripes are explained and the impact on the SOT measurements is discussed.

One way to excite a spin wave is to use local magnetic fields to non-uniformely drive the magnetization. In this case, spin waves that travel away from the excitation point are created, as would water surface waves do when a stone is dropped into a calm lake. A comprehensive description concerning spin waves can be found in [Sta09; Gur96]. For a short but comprehensive introduction the reader is also referred to the theory part of [Edw12], where a historical overview is given about the topic[1]. In addition, [Sch13; Bau14] cover similar aspects.

There are two main interactions that are key in the understanding of the properties of spin waves: the exchange interaction, which is strong but local, and the dipole-dipole interaction, which is much weaker but long ranged. This leads to two limiting regimes of spin waves: a) short wavelengths, where the spin-spin canting is large such that the energy contribution from exchange dominates and b) long wavelengths, where the spin-spin canting is negligibly small such that the energy contribution results mostly from the dipolar interaction [Edw12]. The latter case is discussed in this thesis due to the geometry of the samples.

In a thin FM film, the dispersion relation can be reduced to k vectors in the film plane due to the fact that a nonhomogeneous magnetization profile along z-direction causes a large exchange energy. An important quantity in this context is the so-called exchange

[1] the cited thesis also points out the difference in nomenclature concerning spin waves

length [Abo13]

$$l_{\mathrm{ex}} = \sqrt{\frac{2A}{\mu_0 M_{\mathrm{s}}^2}}. \tag{6.1}$$

which, for Py, is $l_{\mathrm{ex}} \approx 5\,\mathrm{nm}$ [Abo13]. In a thin film of the order of l_{ex}, there is no variation of the magnetization profile along the z direction[2]. It is therefore sufficient to seek for solutions of plane waves with ip k vector by solving the LLG equation. At the same time, the dynamic nonhomogeneous demagnetizing field, which is created by the nonhomogeneous precession, must obey Maxwell's equations. For a thin FM film and small k vectors ($kd_{\mathrm{F}} \ll 1$) without considering anisotropies, the dispersion relation can then be expressed as [Sti16], adapted from [Kal86]:

$$\left(\frac{\omega}{\mu_0\gamma}\right)^2 = \left(H + M_{\mathrm{s}} l_{\mathrm{ex}}^2 k^2 + M_{\mathrm{s}} - \frac{M_{\mathrm{s}}}{2} k d_{\mathrm{F}}\right)\left(H + M_{\mathrm{s}} l_{\mathrm{ex}}^2 k^2 + \frac{M_{\mathrm{s}}}{2} k d_{\mathrm{F}} \sin(\varphi_k)^2\right). \tag{6.2}$$

Here, H is the magnitude of the external field and φ_k is the angle between the spinwave propagation direction with wavevector k and the static magnetization $\boldsymbol{m}_{\mathrm{eq}}$, which is assumed to be parallel to the external field. Figure II.6.1 shows a plot of the dispersion relation for a 10 nm thick Py film subject to an applied field of 10 mT in y-direction. Two things can be noted immediately from the dispersion relation: For long (micrometer) wavelengths/small k, the dynamics is governed by the dipolar interaction such that the exchange term can be neglected, whereas for large k the opposite holds and the dispersion relation becomes quadratic in k [Kal86]. Second, in the dipolar regime the dispersion relation is, in contrast to e.g. light waves in isotropic media, inherently anisotropic. The two limiting cases are: a) $\varphi_k = 0°$ where the propagation is along the equilibrium magnetization; these waves are called backward volume waves (BV) and b) $\varphi_k = 90°$ where the propagation is transverse to the equilibrium magnetization; these waves are called Demon-Eshbach waves (DE). The DE waves are characterized by a positive slope in the dispersion relation whereas the BV branch of the dispersion relation shows a negative slope around $k = 0$. This difference has a striking impact on the spin wave physics for both field configurations. The physical reason for the different behavior is the fact that DE waves produce both volume and surface demagnetizing fields, while BV waves only produce surface demagnetizing fields [Bau14].

The excitation efficiency ϵ_{SW} of a spin wave depends on the overlap integral of excitation field and mode profile [Sch15], [Gur96, chapt. 6.3]

$$\epsilon_{\mathrm{SW}} \propto \int_0^{\frac{2\pi}{k}} dx\, h(x) q(x,k), \tag{6.3}$$

[2] There exist standing spin waves in z-direction, if the sample is thicker than l_{ex}. These SSW are called perpendicular SSW (PSSW), see e.g. [Sch15]. However, as only very thin films ($d_{\mathrm{F}} < 3l_{\mathrm{ex}}$) are studied in this work, these types of SSW can be neglected as the resonance frequencies/fields lie far outside the available ranges.

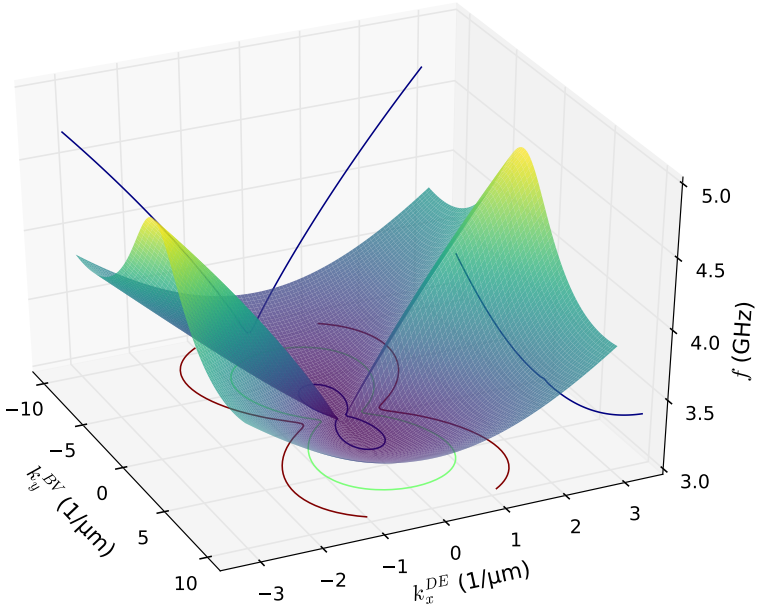

Figure 6.1.: *Dispersion relation for a* 10 nm *thick Py film. The applied field is* $H = 10\,\mathrm{mT}$ *in y-direction. Projections for the DE case* ($k_y^{BV} = 0$) *and the BV case* ($k_z^{DE} = 0$) *are drawn on the walls of the cube. The DE branch has a positive slope, whereas the BV branch starts with a negative slope around* $k = 0$.

with the mode profile $q(x, k) \propto \cos(\omega t - kx)$ for plane waves. If a homogeneous driving field is present at the sample, no propagating spin waves are excited in the bulk because the excitation efficiency is zero[3]; to excite propagating waves therefore antenna structures producing nonhomogeneous driving fields are used [Sti16; Cha14]. However, a homogeneous driving field can excite standing spin waves in confined structures, since these can have even symmetry in space. This topic is covered in a very detailed way in [Bay06]. The book chapter covers a full theoretical description as well as experimental and simulation results and is closely followed in this thesis.

In the following two sections, SSWs across the width of long stripes ($L \gg w$) are treated. The long axis of the stripe is assumed to be in x-direction. There are two limiting cases considering the external field direction which differ in mode structure and resonance position: a) the external field is applied along x, this case is called longitudinally magnetized stripe and b) the external field is applied along y, this case is called transversely magnetized stripe. The intermediate cases where H lies at an angle $0° < \varphi < 90°$ is given by a combination of both cases.

[3] Strictly, at any edge of a FM film, spin waves are excited also for a homogeneous driving field due to the symmetry breaking at the edge.

6.1. Longitudinally Magnetized Stripes

In a longitudinally magnetized stripe, the equilibrium magnetization is fully saturated along $H \parallel \hat{x}$ because there are no static demagnetizing fields in the (infinitely) long direction. The problem then reduces to a one-dimensional one, where the mode profile in y is searched for. The applicable dispersion relation in this case is the DE branch of Eq. (6.2) since the propagation direction is perpendicular to the external field. It is shown in [Bay06] that the confinement leads to a discrete set of eigenmodes that have a symmetric/antisymmetric spatial profile for odd/even indices n

$$\begin{aligned} q_n^{\mathrm{S}}(y) &= A_n^{\mathrm{S}}\cos(\kappa_n y), \quad q_n^{\mathrm{A}}(y) = A_n^{\mathrm{A}}\sin(\kappa_n y) \\ \kappa_n &= \frac{n\pi}{\omega}\frac{d(p)-2}{d(p)}, \quad d(p) = \frac{2\pi}{p\,(1-2\ln(p))}, \quad p = \frac{d_{\mathrm{F}}}{w} \end{aligned} \tag{6.4}$$

and the corresponding eigenfrequencies

$$f_n = \frac{\gamma}{2\pi}\sqrt{\mu_0 H\,(\mu_0 H + \mu_0 M_{\mathrm{s}}) + \frac{\pi}{4}\,(\mu_0 M_{\mathrm{s}})^2\,\frac{d_{\mathrm{F}}}{w}\,(2n-1)}, \quad n = 1, 2, 3, \ldots \tag{6.5}$$

By comparing this equation to the Kittel formula for FMR it is recognized that the frequencies are shifted up by a factor depending on the mode number and the thickness to width ratio $\frac{d_{\mathrm{F}}}{w}$. Therefore, the first mode $n = 1$, which appears as the main peak in a measurement, slightly shifts down in field from what would be expected for full film FMR. It should be noted that shifts in frequency and field are reciprocal, therefore the higher order SSW lie lower in field.
Due to the fact that the spacing in field of the different modes depends on $\frac{d_{\mathrm{F}}}{w}$, there are three different regimes:

- very narrow stripe: the mode spacing is large and much bigger than ΔH such that all peaks can be distinguished in a fit. This allows for separation of the peaks and the correct linewidth is measured.
- intermediate ratio: $\frac{d_{\mathrm{F}}}{w}$ is such that the peaks start to overlap in field and cannot be separated by a fit. This situation can lead to an over/underestimation in linewidth.
- very wide stripe: the mode spacing is much smaller than ΔH such that the effect of the SSWs can be completely neglected.

For a SOT measurement, it is therefore crucial to avoid the intermediate regime.
In order to study the effect of the superposition of SSW on the measurements, a numerical routine is used[4] that solves for eigenfrequencies and -modes for a given external field value.

[4]The author wants to thank Hans Bauer [Bau14] for providing the code of this solver

By solving the problem for a series of fields, a field-swept measurement can be mimicked as shown in Fig. II.6.2 for a 12 nm thick and 4 µm wide Py stripe. At first, the intersects

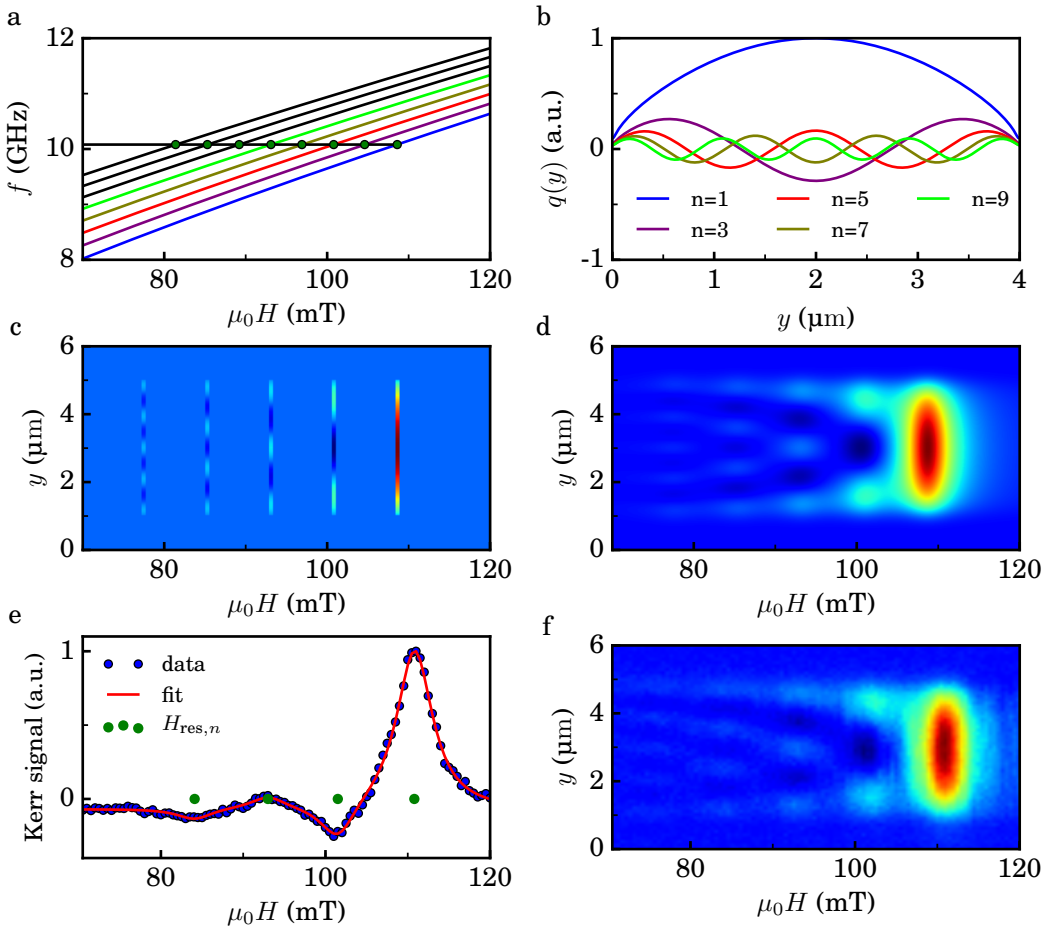

Figure 6.2.: *Numerical calculation of* SSWs *in a* 12 nm *thick,* 4 µm *wide longitudinally magnetized Py stripe and comparison with measured TRMOKE data. a) Dispersion branches of different modes and intersects with a fixed frequency. b) corresponding mode profiles. c) modes are put into array to visualize behavior in a* (H, y) *plane. d) linewidth and probing spot size are added. e),f) measured data; e) shows a cut along the middle of the stripe* ($y = 3$) *together with a fit to extract* $H_{res,n}$ *and* ΔH*. The slight deviation of computed and measured mode profiles is a result of a small oop anisotropy which is neglected in the numerical approach.*

of the dispersion branches with a fixed measurement frequency f are calculated, as shown in panel a); resulting in the respective resonance fields. The corresponding eigenmodes are taken and scaled with their excitation efficiency, see panel b). Due to the homogeneous driving field only the odd modes are excited. In a measurement the SSWs are studied by taking linescans across the width of the stripe for a set of external applied fields H. Panel c) thus shows the eigenmodes in an intensity plot with the x-axis being the field and the y-axis being the space coordinate to see the position of the modes in field. Note the zero padding along y, needed for the next step to follow. The stripe extends from 1 to 5 µm.

In a next step, the modes are given a finite linewidth in field ΔH. For SSWs with small k vector, the quality factor and the frequency linewidth Δf are approximately equal to the one of FMR [Gur96, chapt. 6.3]. These must be converted to a linewidth in field, which depends on the slope of the dispersion relation: $\Delta H = \Delta f \left(\frac{\partial f_n}{\partial H}\right)^{-1}$ [Sha09]. Looking at the dispersion branches, the variation in slope between different modes is very small such that in first order the same ΔH is assumed for all modes. Mathematically this is done by a convolution of the array of c) with a Lorentzian line in H-direction. To take into account the spot size of the laser in a measurement the image is subsequentially convolved with a Gaussian beam profile in y-direction. Panel d) shows the final result of the computation whereas panel f) shows a corresponding TRMOKE measurement taken on a Py stripe at 10.08 GHz. The striking similarity of computed and measured data proves the validity of the numerical methods used. Panel e) shows a linecut of the data f) at the middle of the stripe as a function of field. The knowledge of the properties of the eigenmodes allows for the use of a multipeak fit that assumes a fixed linewidth and one fixed phase for all peaks. Up to 4 peaks are detected, corresponding to mode number $n = 7$.

6.2. Transversely Magnetized Stripes

The case of transversely magnetized stripes ($H \parallel \hat{y}$) differs from the above-mentioned case in two main points:

a) the applicable dispersion relation branch is the BV one. This leads to a much smaller mode spacing in field, due to the fact that the slope of the dispersion relation is much lower compared to the DE case.

b) the internal field is no longer homogeneous across the stripe width (in y-direction) due to the static demagnetization field. An analytic expression for the internal field is given by [Bay06]

$$H_{\text{int}} = H - \frac{M_s}{\pi}\left[\arctan\left(\frac{d_F}{2y+w}\right) - \arctan\left(\frac{d_F}{2y-w}\right)\right]. \tag{6.6}$$

In Fig. II.6.3, the internal field is shown as computed for a 10 nm thick, 1 µm wide Py stripe for different externally applied fields. At low external field values the internal field obtained even goes to zero at the outer regions of the stripe. In reality, this situation corresponds to a magnetization configuration that is no longer saturated along y at the edge region of the stripe but bends by 90° to align with the edge in x-direction. The black solid line represents the value of the internal field calculated by the use of an averaged demagnetizing factor N_{yy} for a rectangular prism as discussed in section I.1.2.3.

The inhomogeneity of the internal field leads to a change in shape of the eigenmodes because of the fact that the dispersion relation has to match the internal field at every point in y. At some point close to the edge there is no possible solution anymore and the precession amplitude must go to zero, leading to a mode profile that is centered at the

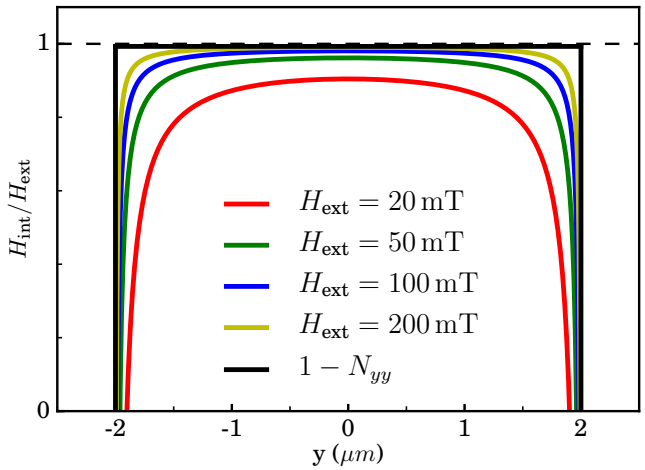

Figure 6.3.: *Internal field in a* 12 nm *thick,* 4 µm *wide Py stripe for different applied fields. The black line represents the value of the averaged demagnetizing factor* N_{yy} *after [Aha98].*

inner part of the stripe. In addition, there exist local solutions for SSW in the potential wells at the edge. These local excitation are therefore called edge modes.

There is no analytic formula for the eigenmodes/frequencies in the transverse case. However, the problem can again be solved numerically in the same fashion as already discussed for longitudinally magnetized stripe[5]. The result of an example computation and a corresponding measurement for comparison are shown in Fig. II.6.4. From panel a) it is clear that the dispersion branches are bundled much closer together compared to the DE case. By comparing the dispersion relation a) and the corresponding modes[6] b) the behavior of mode profile vs. field can be observed: The edge modes (blue colors in panel b)) lie high in field, well separated from each other (the resonance fields are displayed in the lower legend in panel b)). However, when coming to lower fields, the peaks of the modes come closer to the middle region of the stripe and begin to oscillate more and more also in the middle region of the stripe until a band of strongly oscillating modes is reached (not plotted). Within this band, the main $n = 1, 2, 3$ modes are located which are plotted in thick solid and dotted lines in b) and have their resonance fields very close together (upper legend in b)). Due to the fact that the BV dispersion relation has a negative slope for small k, the $n = 2, 3$ modes do lie higher in field compared to the $n = 1$ mode.

A comparison of the shape of the main modes with the cosine like form of the longitudinal case clearly shows the centering at the inner region of the stripe. Panel c) again shows the position of the modes in field and space and d),e) show the computed dataset and

[5] In the numerical approach the magnetization is assumed to be saturated along y for simplicity. In the regions of zero internal field this leads to the appearance of nonphysical solutions that grow exponentially towards the edge and are excluded in the analysis.

[6] Note that the modes are not scaled by the excitation efficiency here for the sake of visibility.

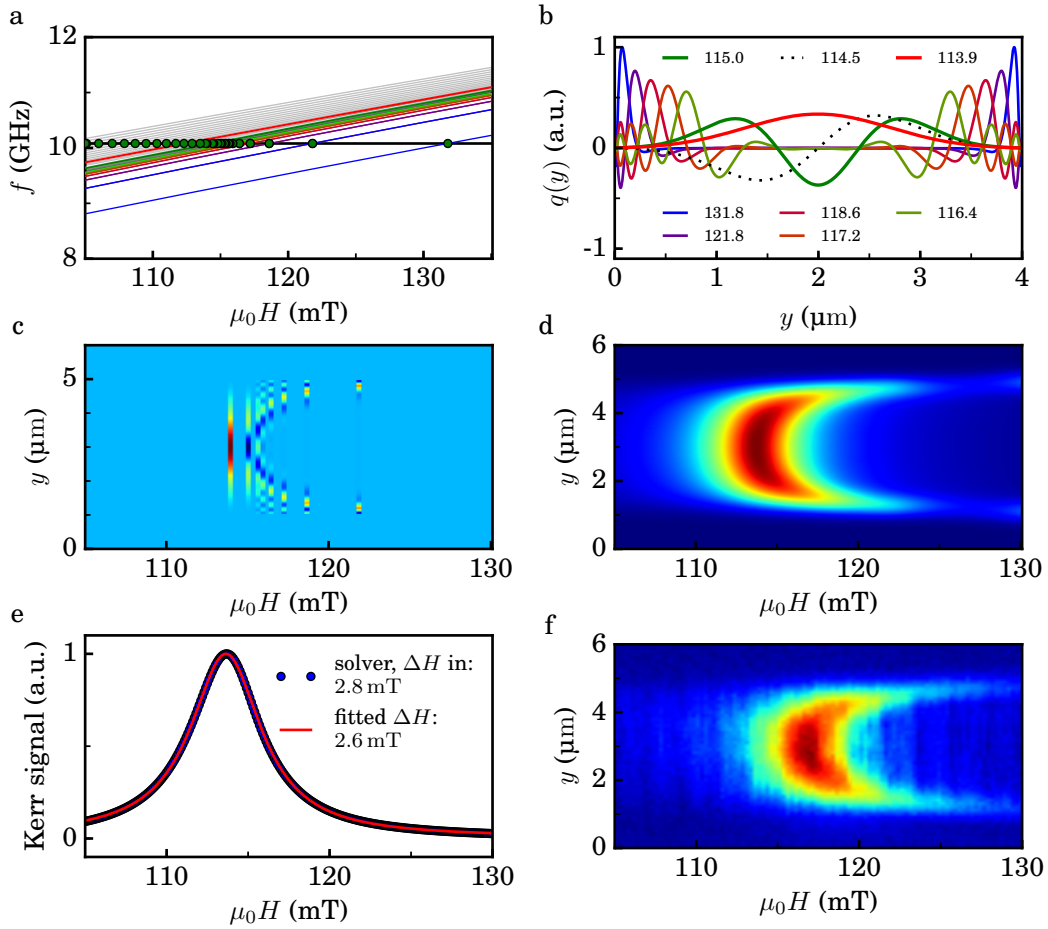

Figure 6.4.: *Numerical calculation of* SSWs *in a* 12 nm *thick,* 4 µm *wide transversely magnetized Py stripe and comparison with measured TRMOKE data. a) Dispersion branches of different modes and intersects with a fixed frequency. b) Corresponding mode profiles. c) The modes are put into an array to visualize the behavior in H and y. d) Linewidth and finite probing spot size are added. f) Measured data. e) shows a scan along the middle of the stripe ($y = 3$) of the computed data d) to compare input and fitted ΔH.*

a corresponding measurement, respectively. The slight shift in resonance position is the result of a small oop anisotropy that is not included in the computation.

Due to the fact that the modes lie close together in this configuration it is not possible to resolve more than one peak from a measurement. This can lead to a wrong fitting result for the linewidth, as displayed in panel e). In contrast to the longitudinal case, the dataset is taken from the computed image rather than from the experimental data. This allows to compare the linewidth used as input during computation and the value obtained from a single peak fit to the simulation data. In the particular case resembling a TRMOKE measurement the linewidth is underestimated by $\delta\Delta H = 0.2\,\mathrm{mT}$ (7 %) which is the result of the overlap of the main modes $n = 1$ and $n = 3$.

6.3. Implication for SOT Measurements

The MOD experiment builds up on the precise determination of the linewidth in the transverse configuration. The influence of the mode structure on the linewidth demonstrated in the last section must therefore be avoided. By using the numerical routine presented here it is found that for the sample geometry used in this thesis ($w = 6\,\mu m$, $d_{Py} = 4\,nm$) a TRMOKE measurement is capable of determining the correct linewidth. The requirement is to place the laser spot at the center of the stripe in order to avoid probing of the edge modes.

For the ISHE experiment the situation is more complex. First, an electric measurement averages the dynamics across the stripe width. This leads to the situation that the edge modes can play a significant role depending on the sample geometry. Second, a full angular dependent measurement involves intermediate cases in which the effects of inhomogeneous internal field and the difference in the dispersion relation branches mix together. The question arises how suitable the data evaluation process of an ISHE measurement - based on the concept of macrospin and magnetic susceptibility in the context of FMR - meets the reality. This question is adressed in the experimental part by full micromagnetic simulations of the dynamics in realistic sample geometries because these allow for arbitrary ip magnetization angles φ. In addition, micromagnetic simulations are not limited by the assumption that the magnetization is saturated at every point across the strip width such that edge effects are included more precisely.

7. Boltzmann Transport in Thin Metallic Layer Systems

In the drift diffusion model used to evaluate the SOT measurements in this thesis, one of the key parameters needed as input is the conductivity of the respective layers, see e.g. Eq. (2.27) and Eq. (5.8). On the basis of the conductivities of both NM and FM, it is possible to compute the current density in a given layer, $j^{\mathrm{c}}_{\mathrm{NM}}$ and $j^{\mathrm{c}}_{\mathrm{FM}}$ from a measured current I. This allows to relate a current induced shift to its physical origin, which rather depends on the current density, in an SOT measurement. Within the drift diffusion model this task is performed by assuming bulk scattering only. This results in a two resistor model in which the current density in each layer is homogeneous and depends on the relative conductivity and cross-section of each layer. In this model, the current density in the NM can be calculated from the total current by the use of Kirchhoff's laws:

$$j_{\mathrm{NM}} = \frac{I}{w} \frac{\sigma_{\mathrm{NM}}}{(\sigma_{\mathrm{NM}} d_{\mathrm{NM}} + \sigma_{\mathrm{FM}} d_{\mathrm{FM}})} \tag{7.1}$$

The assumption of a homogeneous current density within the respective layers, however, breaks down in ultrathin metallic layers: If the dimensions of a conductive specimen are of the same order of magnitude or smaller than the mean free path of the electrons, scattering at the interfaces starts to play an important role. The additional scattering source leads to a) a decrease of the measured conductivity and b) a spatial dependence of the current density within a given layer.

The Pt layers under investigation in this work show a clear reduction of the measured conductivity for decreasing film thickness. In order to understand this behavior, the measured conductivity is fitted to a more complex Boltzmann model of conductivity that shall be introduced within the next sections.

Most of the theoretical work on the subject of thin film conductivity has been done between 1953 (Fuchs' theory [Fuc38]) and the 1980s/90s. The theoretical physicists were first motivated by the experimental observation of a deviation of the conductivity from the bulk value in thin silver films [Sto98, (1898!)] and later by the discovery of the GMR, see e.g. [Bai88; Bin89; Val93; But00]. Despite the fact that the models have been developed many years ago, there is still a debate about the relative strength of different scattering processes. An excellent recent overview of this topic can be found in chapter 5.1 of [Kob13]

and the references therein and [Phi11].

7.1. Drude Theory

The basic assumption of the Drude theory of transport is that electrons move through the material freely between scattering events. There is a specific (mean) time between

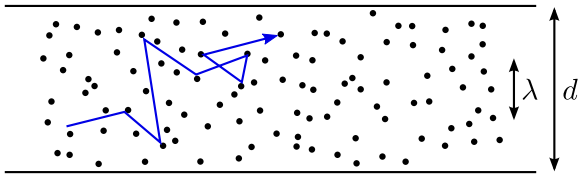

Figure 7.1.: *Drude model of conductivity. In a metallic layer of thickness $d \gg \lambda$ the conduction electrons scatter mostly within the bulk; scatterers are indicated by the black dots.*

scattering events which is called the momentum scattering time τ. Due to the scattering events, the direction of the electron's movement is randomized but the velocity remains constant. Since the conduction electrons lie at the Fermi surface in metals, the velocity at which the electrons move is assumed to be the Fermi velocity v_F. Using a free electron gas approximation the electrical conductivity is given by [Son52; Ash76]:

$$\sigma_0 = \frac{n\mathrm{e}^2\lambda}{mv_\mathrm{F}} \tag{7.2}$$

with the electron density n, the mean free path (MFP) λ, the effective electronic mass m and the Fermi velocity v_F. The momentum scattering time τ can be associated with the momentum mean free path via $\lambda = \tau v_\mathrm{F}$. Together with [Ash76]

$$k_\mathrm{F} = (3\pi^2 n)^{\frac{1}{3}}, \quad v_\mathrm{F} = \frac{\hbar}{m}k_\mathrm{F}, \quad E_\mathrm{F} = \frac{\hbar^2}{2m}k_\mathrm{F}^2 \tag{7.3}$$

this gives

$$\lambda = \sigma\frac{3\pi^2\hbar}{\mathrm{e}^2}(3\pi^2 n)^{-\frac{2}{3}}. \tag{7.4}$$

The bulk conductivity and the bulk MFP are therefore coupled via the (effective) free electron density. It should be pointed out that this relation is valid within the quasi free electron gas and is valid even if the effective mass is not equal to the free electron mass [Son52, p. 6]. The conductivity can be measured via a four point probe measurement if the sample to be measured has bulk properties, a requirement which will be specified in the following chapter. The electron density can be determined via Hall measurements. From the measured Hall coefficient the electron density can be computed via [Ash76; Hur72]

$$n = \frac{1}{eR_H}. \tag{7.5}$$

7.2. Fuchs-Sondheimer Model

If a dimension of a conductor become smaller and smaller, reaching the order of the MFP, the electrons do not solely scatter within the bulk but also at the boundaries. The thin metal films studied in this work have lateral sizes in the micron range, much longer than the MFP. However, the thickness is in the nm range which is well comparable to the MFP of bulk metals at room temperature. In this case electrons additionally scatter at the interfaces substrate/metal and metal/vacuum, which effectively lowers their MFP. This leads to an inhomogeneous current density distribution across the thickness of a film and to a reduced overall conductivity. This problem was first discussed by Fuchs [Fuc38] and

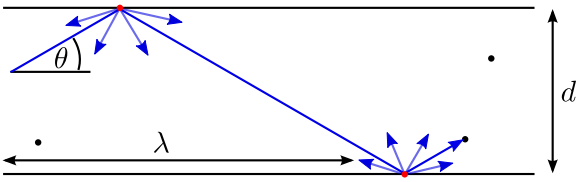

Figure 7.2.: *Fuchs-Sondheimer model of conductivity. If the thickness $d \sim \lambda$, the interface scattering starts to play a role in both the local as well as the overall conductivity. An electron that hits the interface might be a) scattered diffusely i.e. the direction of movement after scattering is randomly distributed or b) scattered specularly, i.e. the k vector is mirrored in z direction.*

later reviewed by Sondheimer [Son52]. To find the current density profile, the Boltzmann equation is used to describe the motion of electrons. A very detailed description of the Fuchs Sondheimer (FS) model, including the step by step analysis can be found in [Son52]. Here, the key assumptions will be discussed, following the above-mentioned paper. The starting point is the Boltzmann equation[1] for a quasi free electron in the presence of an electric field $\vec{E}$

$$-\frac{e}{m}\vec{E}\cdot(\nabla_{\vec{v}}f) + \vec{v}\cdot(\nabla_{\vec{r}}f) = \frac{f - f_0}{\tau} \tag{7.6}$$

where f is the distribution function which gives the number of electrons at a point $\vec{r}$ that move with the velocity $\vec{v}$. The equilibrium distribution is the Fermi Dirac function

$$f_0 = \frac{1}{e^{\frac{E-E_F}{k_B T}} + 1} \tag{7.7}$$

which is a function of the absolute value of the velocity only, since $E = \frac{1}{2}m|\vec{v}|^2$. The assumption of random scattering in the bulk is expressed in the so-called lifetime approxi-

[1] A detailed discussion of the Boltzmann equation and the simplifications made for calculations can be found in [But00].

mation, leading to the relaxation term on the right-hand side of Eq. (7.6). Once a solution of the Boltzmann equation is found and the distribution function is known, the current density can be calculated via

$$\vec{j} = -2\mathrm{e}\left(\frac{m}{h}\right)^3 \int d\vec{v}\, \vec{v} f. \tag{7.8}$$

It can be seen immediately that for $f = f_0$, the integral evaluates to zero due to the fact that f_0 is symmetric in v. Now consider the case of a thin metallic film with thickness d. The film lies in the (x, y) plane such that z is normal to the film plane and $0 < z < d$. The electric field E is assumed to be in the x-direction to drive an ip current. The distribution function can be written as

$$f = f_0 + f_1(\vec{v}, z). \tag{7.9}$$

In linear response, the Boltzmann equation then reduces to a one dimensional equation:

$$\frac{\partial f_1}{\partial z} + \frac{f_1}{\tau v_z} = \frac{\mathrm{e}E}{m v_z} \frac{\partial f_0}{\partial v_z} \tag{7.10}$$

with the general solution

$$f_1(\vec{v}, z) = \frac{\mathrm{e}\tau E}{m} \frac{\partial f_0}{\partial v_x} \left[1 + F(\vec{v}) \mathrm{e}^{-\frac{z}{\tau v_z}}\right]. \tag{7.11}$$

To determine $F(\vec{v})$ the boundary conditions at the interfaces $z = 0$ and $z = d$ have to be taken into account. Generally, a boundary condition can be expressed as a scattering matrix which transfers an incoming electron in the state $\vec{v}$ into an outgoing electron with state $\vec{v}'$ where at every point of the interface particle conservation is required. Since the electrons hitting a surface get reflected, electrons traveling in $+z$-direction satisfy different boundary conditions from those traveling in $-z$ [But00]. The general solution is therefore split into two functions

$$\begin{aligned} f_1^+(\vec{v}, z) \quad & \text{for } v_z > 0 \\ f_1^-(\vec{v}, z) \quad & \text{for } v_z < 0 \end{aligned} \tag{7.12}$$

Within the FS model, the scattering of an electron is assumed to be either totally diffuse, i.e. an electron reaching the interface will be reset to f_0 or totally specular, i.e. the electron will keep v_x, v_y and reverse v_z. Fuchs introduced a factor p which determines the fraction of the electrons that scatter elastically to account for a mixture of both possibilities. The boundary condition then reads

$$\begin{aligned} f_1^+(v_z, z = 0) &= p\, f_1^-(-v_z, z = 0) \\ f_1^-(v_z, z = d) &= p\, f_1^+(-v_z, z = d). \end{aligned} \tag{7.13}$$

By applying the boundary conditions, a solution is found for $F(\vec{v})$ and subsequently the

integration Eq. (7.8) is carried out to end up with a formula for the current density as function of z. The averaged conductivity is given by the z-integrated mean of the current density divided by the electric field and reads

$$\sigma(d) = \sigma_0 \left[1 - \frac{3\lambda(1-p)}{2d} \int_1^\infty dt \left(\frac{1}{t^3} - \frac{1}{t^5} \right) \frac{1 - \mathrm{e}^{-\frac{td}{\lambda}}}{1 - p\mathrm{e}^{-\frac{td}{\lambda}}} \right]. \tag{7.14}$$

The integration over t can be carried out numerically such that the above formula can be used to fit a thickness-dependent conductivity measurement. In doing so, one has to take into account that Eq. (7.4) holds and therefore σ_0 and λ cannot be varied independently. The behavior of the conductivity is shown in Fig. II.7.3. For $p = 1$, which corresponds to purely specular scattering, the conductivity remains unaltered. It is questionable whether

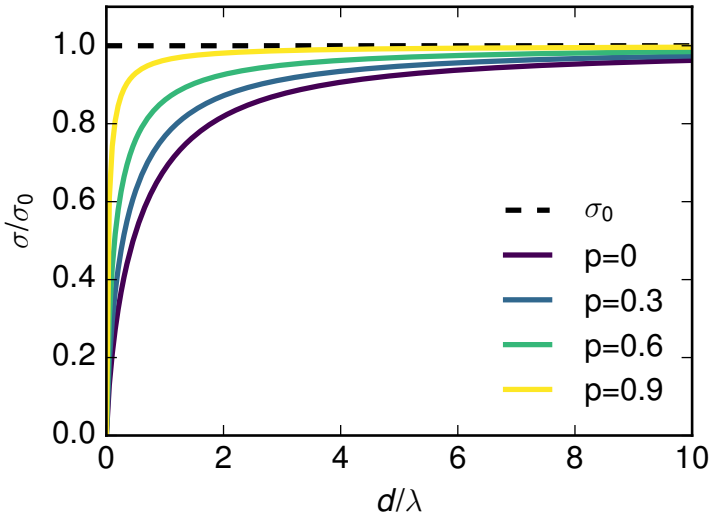

Figure 7.3.: *Reduction of the conductivity calculated using the FS model. The more electrons are scattered diffusely ($p << 1$), the bigger the effect of the interface seen in $\sigma(d)$.*

the very simple picture of partial/specular reflection is physically meaningful. As a result, more sophisticated models have been developed of which the one introduced by Zimann [Zim60] and extended by Soffer [Sof67] based on electro-optical arguments should be discussed here as it allows to estimate p based on the interface roughness. The interface is treated as a plane with a Gaussian variation in z, described by the *rms* deviation from the mean, h. An electron incident on the interface is described by a plane wave with an angle θ between the k vector and the interface normal. If the roughness distribution is uncorrelated, the reflection probability reads

$$p(\theta) = \mathrm{e}^{-\left[\frac{4\pi h}{\lambda}\cos(\theta)\right]^2}. \tag{7.15}$$

This function can be used to replace the constant p in the FS model which results in a similar expression ([Sof67, eq.(21)]) for $\sigma(d)$ to Eq. (7.14). At this point, a quick estimation shows the implication of this scattering model: the Fermi wavelength in metals is in the range of several Å, for Pt $\lambda_F = \frac{2\pi}{k_F} \approx 4\,\text{Å}$ using k_F from [Han13a, Table I]. This value is of the same order of magnitude as the surface roughness of non-epitaxially grown films. The mean over all incident angles for $\frac{h}{\lambda} = 1$ results in $< p(\theta) >_\theta = 0.04 \approx 0$, therefore it is often argued that scattering at the boundary can be treated as purely diffuse [Bra06, S 233]. This argumentation, however, is true only for $\frac{d}{\lambda} \gtrapprox 1$ as discussed in [Sof67]. For the Pt thickness measured in this work the difference between Soffer's and FS's model for $p = 0$ is expected to be small compared to the experimental error such that - for the sake of simplicity - only the FS model is used. For the sake of completeness, it should be mentioned that, for thin films, it may not be true that the two interfaces substrate/film and film/vacuum are equal in roughness. For example one could imagine a single crystalline substrate on which a metal is evaporated that grows in grains such that the substrate/metal interface is very flat but the metal/vacuum interface has a roughness > λ_F. The two interfaces must therefore have two different specularity parameters, which was introduced by Lucas [Luc65]. In this context, another effect known to the thin film community is the growth of islands instead of continuous films for low thicknesses, which leads to a conductivity that gets reduced drastically if the thickness of the film falls beyond the critical thickness of a continuous growth. This effect has been modeled by Namba [Nam70]. All different interface scattering models can be implemented into the fundamental Boltzmann equation and used to extract the key conductivity parameters if the structure of the films is known.

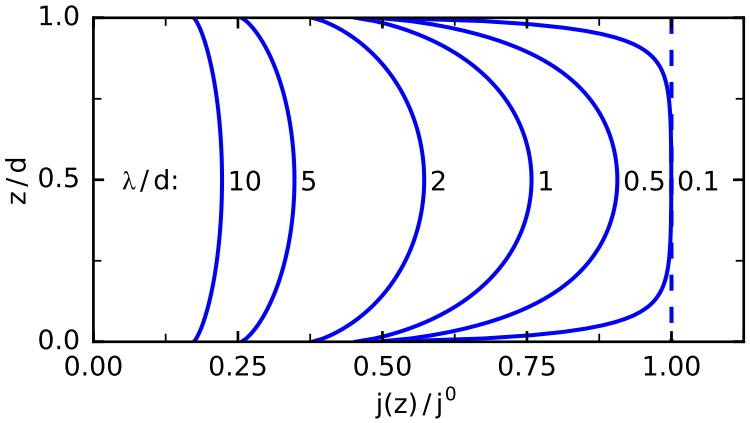

Figure 7.4.: *Current density distribution $j(z)$ across the height of a layer of thickness d for different ratios of mean free path over thickness $\frac{\lambda}{d}$ in the FS model. The current density corresponding to a bulk conductivity σ^0 without surface scattering is j^0 (blue dashed line). The specularity parameter p is set to zero.*

In Fig. II.7.3, the current density distribution within a layer of thickness d is plotted for different ratios of $\frac{\lambda}{d}$ in the case of purely diffuse interface scattering. The non-homogeneity

is pronounced already for the case $d = 2\lambda$.

7.3. Mayadas-Shatzkes Model

Metallic films used in industry are usually deposited via sputtering techniques due to the excellent controllability and the possibility to cover large wafers homogeneously. Therefore, most of the layer stacks are poly-crystalline, which also results from the fact that materials with non-matching lattice constants are combined in multilayer sequences. In 1970, Mayadas and Shaztkes (MS) published a model which describes the consequences of scattering at the grain boundaries and includes this type of scattering into the FS model [May70]. The grain boundaries are modeled as delta potentials of given strength S,

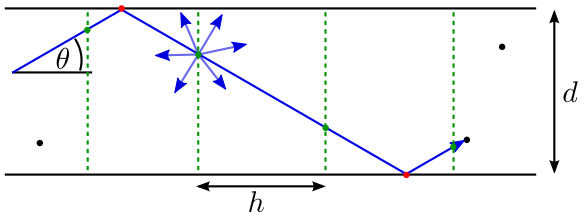

Figure 7.5.: *Mayadas-Shaztkes model of conductivity. In addition to bulk and interface contributions, scattering at grain boundaries is included by artificial δ-potential planes (green dotted lines) representing grain boundaries. An electron passing a grain boundary is reflected with a probability R. The average distance of the planes is h and is identified with the average grain diameter D.*

arranged in parallel planes perpendicular to the electric field E. The planes have an average distance h with a standard deviation of s. An incoming electron will be reflected or transmitted in a specular fashion at every single plane potential. It turns out that this scattering mechanism can be included by substituting the relaxation time in the Boltzmann equation via

$$\frac{1}{\tau^*} = \frac{1}{\tau} + 2F(|k_x|), \qquad F(|k_x|) = \frac{\alpha}{2\tau}\frac{k_\mathrm{F}}{k_x}, \qquad \alpha = \frac{\lambda}{D}\frac{R}{1-R}. \tag{7.16}$$

Here, the strength S of the scattering potential is expressed as a reflection coefficient $0 < R < 1$ for every plane and the mean distance h of the planes has been identified with the average grain diameter, D. The effective conductivity of a thick specimen with bulk conductivity σ_0 is then given by

$$\sigma_\mathrm{g} = \sigma_0\left[1 - \frac{3}{2}\alpha + 3\alpha^2 - 3\alpha^3\ln\left(1 + \frac{1}{\alpha}\right)\right]. \tag{7.17}$$

For a thin film with the FS boundary conditions applied, the overall conductivity then reads

$$\sigma = \sigma_g - \sigma_0 \frac{6(1-p)\lambda}{\pi d} \int_0^{\frac{\pi}{2}} d\varphi \int_1^{\infty} dt \frac{\cos(\varphi)^2}{H(t,\varphi)^2} \left(\frac{1}{t^3} - \frac{1}{t^5}\right) \frac{(1-p)^2 \mathrm{e}^{(-tH(t,\varphi)\frac{d}{\lambda})}}{1-p\,\mathrm{e}^{-tH(t,\varphi)\frac{d}{\lambda}}} \tag{7.18}$$

where

$$H(t,\varphi) = 1 + \frac{\alpha}{\cos(\varphi)\sqrt{1-\frac{1}{t^2}}}. \tag{7.19}$$

Again, this formula can be numerically evaluated and used as a fitting function. The parameters are now σ_0, λ, p and R. The average grain diameter must be fixed, otherwise the use of the model doesn't make sense. For thin metallic films, the grain size is often directly proportional to the film thickness [Sam83; Fis79] up to a maximum thickness from which the grains stay constant in diameter. On the other hand, columnar grains have been reported for some cases which have a thickness independent diameter [Kob16]. In the latter case, the MS model shows the same thickness dependence as the FS model but with a reduced "bulk" conductivity σ_g. In the case of $D_{\mathrm{grain}} \propto d_{\mathrm{layer}}$, the MS model leads to a behavior similar to the FS model. However, the conductivity is reduced far more, depending on the value for R. In Fig. II.7.6 some example curves are plotted. In

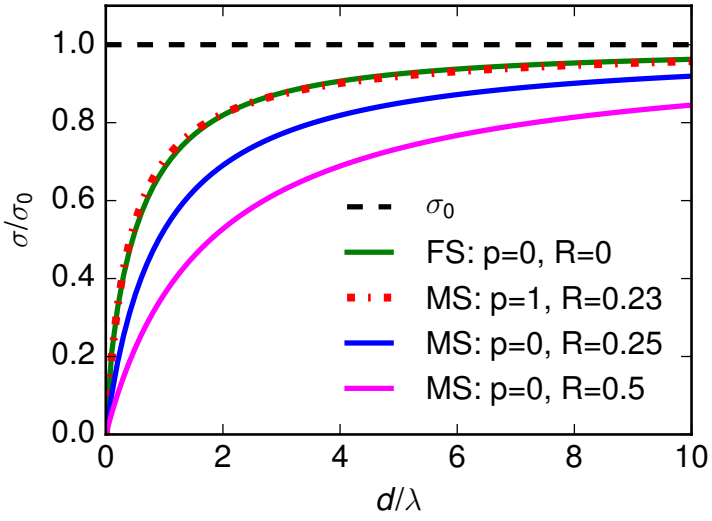

Figure 7.6.: *Reduction of the conductivity calculated using the MS model assuming $D_{grain} = d_{layer}$. The green curve corresponds to the FS model for $p = 0$. The red dotted line is the MS model without interface scattering, the R parameter is chosen such that it overlaps with the FS model. If interface and grain scattering are both active, the conductivity is lowered to values not attainable with the FS model.*

the calculations $D_{\mathrm{grain}} = d_{\mathrm{layer}}$ is assumed. The green and red dotted lines show that the FS curve for $p = 0$ can be reproduced using the MS model without interface scattering

and linearly growing grains. However, using the above-mentioned argument leading to $p = 0$, one parameter is eliminated. In this case, the MS model always results in a reduced conductivity compared to the pure FS model. There is an ongoing debate about the different models and their physical meaning. Simply due to the fact that the MS and FS model predict a similar behavior of σ for thin films it is very hard to distinguish which scattering mechanism is dominant if only data for $\sigma(d)$ is available. In this context, the reader is encouraged to take a look at [Sam83] where the applicability of different models is critically discussed. The effect of grain scattering on the current density distribution is

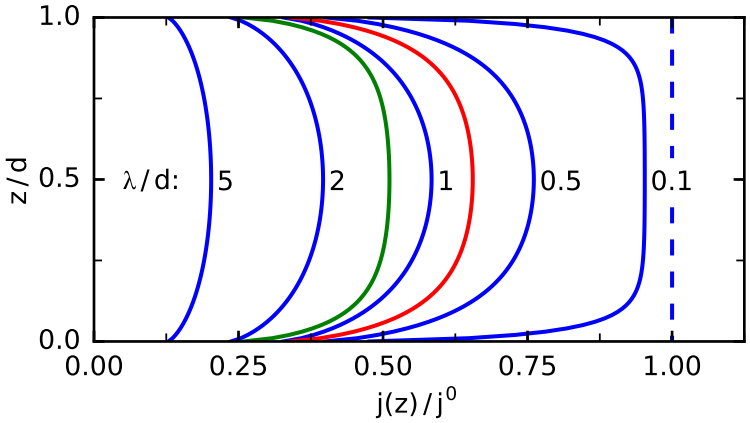

Figure 7.7.: *Current density distribution $j(z)$ across the height of a layer of thickness d for different ratios of mean free path over thickness $\frac{\lambda}{d}$ in the MS model. The average grain diameter is set to be equal to the thickness (blue lines) and to $\frac{d}{2}/\frac{d}{4}$ (red line/green line, both corresponding to $\frac{\lambda}{d} = 0.5$). The current density corresponding to a bulk conductivity σ^0 without surface scattering is j^0 (blue dashed line). The specularity parameter for scattering at the interface p is set to zero and the reflection parameter at grain boundaries is set to $R = 0.25$.*

mainly to further reduce the average value of j as can be seen in Fig. II.7.7 in comparison to the FS case Fig. II.7.4. In addition, the current density distribution becomes more homogeneous if the grain size gets smaller than the thickness due to the reduction of the effective mean free path caused by the grain boundary scattering.

7.4. Current Density Distribution in Bilayers

In the case of a metallic bilayer, the situation gets even more complicated since the electrons initially located in layer one can move through the interface and influence the current density distribution within layer two and vice versa. This effect is shown in the context of SOT computation using the Boltzmann formalism in figure 1 a) of [Han13a] and the discussion in the following part of that paper. In that paper, a Pt/Co bilayer is treated without taking grain scattering into account. In addition, the Fermi surfaces of both metals are assumed to be spherical and of the same size. However, no analytic expression is

given for the current density as a function of z since the mathematical approach is based on a full numerical treatment of the Boltzmann equation.

There is, however, a publication in which an expression for the local conductivity in a bilayer is given [Dim83]. In this publication, the interface between the two layers is characterized by three parameters W, P, Q which determine what happens to an electron hitting the interface approaching from layer a). The parameter $0 \leq W \leq 1$ describes the probability of transmitting the interface (into layer b)). Reflected and transmitted amplitude then are characterized by the specularity parameters P which gives the diffusely scattered part of the reflected amplitude ($0 \leq P \leq 1-W$, 0) and Q which is the diffusely scattered part of the transmitted amplitude ($0 \leq Q \leq W$). This toy model is used here in order to show the influence of different scattering mechanisms on the current density close to the interface between the two metallic layers. The effect of grain scattering is integrated into the formalism used in [Dim83] by following the derivations in [Son52; May70; Dim83] such that its influence can be examined additionally. The influence of different parameter settings

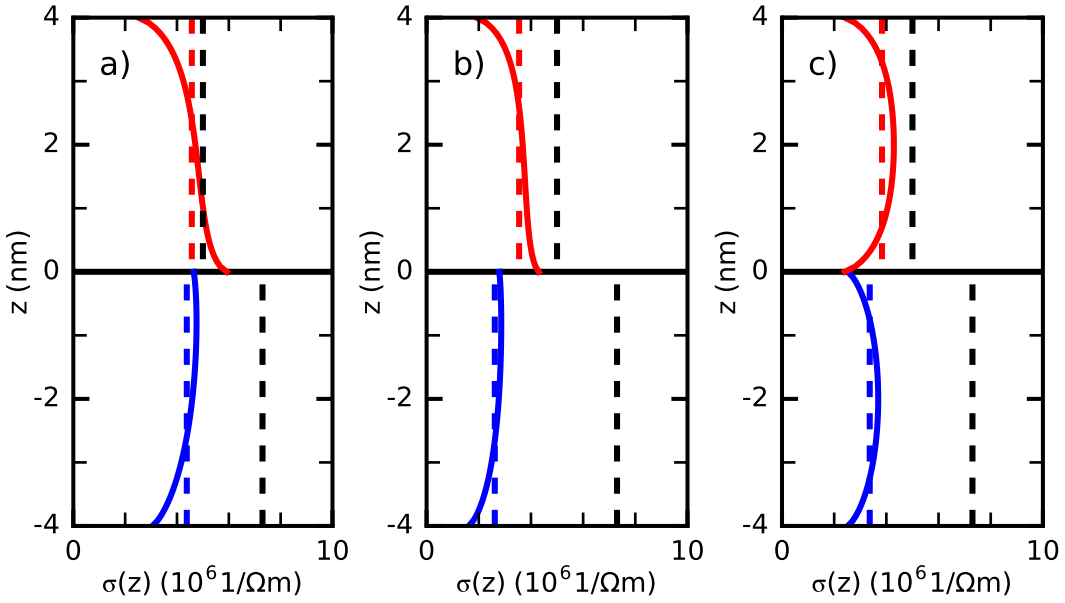

Figure 7.8.: *Local conductivity within a Pt(4 nm)/Py(4 nm) bilayer for different scattering sources and interface parameters. The Pt layer covers negative z values; the Py layer positive z values. The chosen bulk values are indicated by the black dashed lines, the local conductivity is drawn as solid line and the averaged layer conductivity $\sigma(d)$ is drawn as dashed line in blue (Pt) and red (Py) respectively. The outer interfaces are set to specular reflection and the transmission parameter is set to $W = 0.25$ for all cases. a) No grain scattering; interface scattering between Pt and Py is purely specular ($P, Q = 0$). b) grain scattering with $R = 0.25$ in both Pt and Py is assumed; Pt/Py interface scattering again specular. c) No grain scattering but this time the transmitted electrons are diffusely scattered at the Pt/Py interface.*

are shown in Fig. II.7.8 by using the example case of a Pt(4 nm)/Py(4 nm) bilayer. The Pt layer covers negative z values; the Py layer positive z values and the local conductivity

is plotted as function of z in both layers.
The bulk conductivity values $\sigma^0_{\mathrm{Pt}} = 7.3 \times 10^6 \frac{1}{\Omega\,\mathrm{m}}$ and $\sigma^0_{\mathrm{Py}} = 5 \times 10^6 \frac{1}{\Omega\,\mathrm{m}}$ are indicated by the black dashed lines and do not differ much for both meals. The values for the mean free path are $\lambda_{\mathrm{Pt}} = 10.3\,\mathrm{nm}$ and $\lambda_{\mathrm{Py}} = 2.6\,\mathrm{nm}$ [Gur93][2]. Note the difference in the Pt mean free path values determined in this work and [Han13a], which differ by a factor of 2.5[3].
The Pt/Py interface transmission parameters are chosen such that figure 1 a) of [Han13a] can be reproduced (for the Pt/Co layer discussed in that publication). A good agreement is found for $W = 0.25$, $P = 0$, $Q = 0$ which means that 25% of incoming electrons are transmitted without any influence of their momentum and the remaining 75% are reflected specularly. As a result, W is set to this particular value in all panels of Fig. II.7.8.
In panel a), $W = 0.25$, $P = 0$, $Q = 0$ is set and grain scattering is omitted, corresponding to a high-quality, single-crystalline bilayer. The effect of the scattering at the outer interface is visible in both layers. The averaged conductivity in the Pt layer is reduced much more from the bulk value compared to Py due to the much larger MFP. Interestingly, the current density at the Py side of the Pt/Py interface is enhanced significantly due to the electrons entering from the Pt side. In panel b), the same situation is plotted with grain scattering included by setting $R = 0.25$ in both layers. The grain size is assumed to be equal to the thickness of the respective layers. The resulting picture is similar to a) with the difference that the overall conductivity in both layers is further reduced. A big difference in the current density distribution is obtained by changing the Pt/Py interface parameters as can bee seen in panel c). The parameter settings of a) and c) are equal up to the specularity parameters P and Q which are set to diffuse transmission/reflection in c) ($P = 0.25$, $Q = 0.75$). This change leads to an overall reduction of the conductivity and a drastic change of the current density at the Pt/Py interface. This shows that the Pt/Py interface does play an important role in the computation of current density distributions. It must be kept in mind that the determination of the interface parameters via measurements of the bilayer conductivity is a very hard task. In principle, measurements for varying thicknesses of both layers must be performed over a wide range of thicknesses. However, in such a series, problems arise due to the fact that the structural details of the layers depend on the thickness of both layers, e.g. if the Pt roughness changes with d_{Pt} the interface specularity parameters are likely to change with d_{Pt}, which makes fitting to a model virtually impossible.
Nevertheless, a determination of the averaged conductivity by the use of the simple two resistor model can be expected to result in a reasonable approximation for current density distribution calculations due to the fact that the deviation from the averaged conductivity in panels a)-c) and the local conductivity is concentrated most at the interface regions.

[2] The Pt parameters are determined experimentally, see section II.9.4 and the Py values are taken from the cited source.
[3] The low MFP in [Han13a] is caused by a large Fermi wave vector, see the discussion in II.9.3 and II.9.4

The character of this approximation, however, should be kept in mind; especially in the context of interface scattering induced SOTs, see [Han13a].

8. Growth of the Pt/Py Bilayer Series

To study the SOTs in Pt/Py layers, a Pt thickness dependence has to be measured in order to access the two key parameters λ_{SD} and θ_{SH}. As the spin diffusion length is known to be small (< 2 nm), it is important to have enough information in the low thickness regime. From this point of view, a series of Pt(0,1,2,3,4,5,7,10,30)/Py(4) (thickness in nm) is expected to suit the requirements. Since the SOT induced effects saturate for $d_{Pt} > 5$ nm, the two largest thicknesses are used for the conductivity measurements only. The Pt(x)/Py layers are grown in an MBE system dedicated to metals and oxides[1] of the cluster MBE system in the physics department of the University of Regensburg. This system is capable to deposit metal films on two inch wafers at base pressures of mid to high 10^{-11} mbar; the growth pressure of Pt lies in the mid 10^{-10} mbar to low 10^{-9} mbar range (due to the high evaporation temperature), for Py in the low 10^{-10} mbar range. The series of different Pt thicknesses is grown using a wedge shutter. A Pt(x)/Py layer series to measure both λ_{SD} and θ_{SH} using the MOD/ISHE technique has to fulfill certain requirements:

- The substrate must be insulating and must not absorb microwaves in the 4 to 16 GHz range. In addition, the substrate must be flat to support the growth of high-quality, nanometer-thick metal films. Therefore, insulating GaAs epi-ready wafers are chosen as substrate. The rms roughness of such a wafer is around 0.3 nm (measured with a commercial AFM in air).

- The layer structure is intended to be amorphous/polycrystalline in order to show isotropic magnetic behavior. To prepare the substrate before growth, the GaAs wafers are heated to 400 °C for 15 minutes, which removes residual water and organic residues but does not desorb the nm thin natural oxide layer present on the surface (as seen in cross-section TEM measurements of other samples on the same substrate). This oxide layer then serves as isotropic seed for the metal films.

- The Pt film thickness must be known for every layer and is monitored by a quartz microbalance during growth. In the MBE system the main problem is related to the fact that the e-beam evaporator used to deposit the Pt has a relatively small

[1] The author wants to thank Matthias Kronseder, who runs the metal MBE, for all the effort and expertise put into the growth of the Pt/Py layers used in this work

opening angle. This leads to a thickness gradient of 25 % across a 2-inch wafer which is quantified prior to the evaporation of the actual Pt/Py layers. For this purpose, a thickness map of a whole wafer is created by performing AFM measurements of the thickness of the evaporated material at 20 positions across the wafer as shown in Fig. II.8.1. The edges substrate/metal needed for this measurement are created by a lift-off process. The calibration map is then used to calculate the Pt thickness on different positions on the wafer; based on the thickness shown by the quartz microbalance.

- The Py film should be equally thick and of the same quality on all samples. Ideally, the whole series should be grown on one wafer to ensure this requirement. The homogeneity of the films is increased by rotating the sample holder during growth, this has two effects: a) growth induced in-plane anisotropies are suppressed and b) the thickness can only vary radially. The thickness difference from center to edge of the wafers is measured by a calibration wafer and found to be < 10% with a tendency to lower thicknesses at the edges. Therefore, only the center region is used on the wafers, which leads to the situation that not all samples fit onto one wafer. Therefore, two wafers are grown with odd/even Pt thicknesses directly after each other.

- To evaluate the spin mixing conductivity, it is especially important to have a correct reference value of the Gilbert damping parameter for a bare Py film without Pt underlayer. From the growth and characterization of numerous Py films using different deposition systems (both e-beam evaporation and sputtering), it is found that the measured damping in general tends to increase with decreasing Py thickness. Thus, the known "bulk" value measured on thick films cannot be used. A reference Py layer must instead be grown and measured under the same conditions as the Pt/Py films. Additionally, it is found that the increase in damping results from the substrate/Py interface and that especially the GaAs/Py interface leads to enhanced damping. In this case, a Pt "seed" layer removes this interface contribution and enhances the Py quality, thereby reducing the damping. This effect then counteracts the spin pumping such that the spin mixing conductivity is underestimated. On one particular wafer (heated GaAs), the measured damping for $d_{\mathrm{Pt}} = 2\,\mathrm{nm}$ was actually lower than for the bare Py film due to the large damping induced by the GaAs/Py interface. The GaAs/Py interface (or, in general, the substrate/Py interface) is identified as the cause for the increased damping in a series of Py films evaporated on different substrates. To do so, both GaAs and Si substrates (both with natural oxide on top) are mounted in the MBE system together and degased by heating. Subsequently, on one of the GaAs substrates a 5 nm MgO seed layer is grown at low temperature such that the MgO is expected to be polycrystalline. As final step, a 4 nm Py film is evaporated and capped on all samples at once. The pieces are then characterized

	GaAs heated	Si heated	GaAs/MgO	GaAs buffer
α	0.017	0.009	0.006	0.006
$\mu_0 M_{\text{eff}}$ (T)	0.55	0.8	0.96	0.91

Table 8.1.: *Magnetic properties, measured by full film FMR, of Py(3 – 4) nm on different substrates. The first three samples were grown together such that the Py thickness and quality is exactly the same. The last one, "GaAs buffer", depicts a substrate where the oxide layer is removed by repeated sputtering and heating cycles and where a buffer layer of GaAs is grown in the III/V-semiconductor MBE, resulting in a clean GaAs/metal interface.*

by FMR to compare the measured damping. From earlier experiments it is known that the damping is as low as 0.006 on GaAs substrate on which a fresh GaAs buffer is grown in the III/V semiconductor MBE after removing the oxide layer by Ar-ion sputtering and heating. However, this procedure leads to a well-ordered single crystalline GaAs surface which is unwanted for the planned experiments.

The FMR results for all samples are shown in 8.1. The damping is large on oxidized GaAs that is only heated before growth and also on the Si/SiO_x substrate. However, high-quality, polycrystalline Py can be produced on GaAs when evaporating a 5 nm MgO seed layer before the Py growth. The measured damping values of the samples prepared this way resemble those on the clean GaAs buffer surface.

All samples are capped by a combination of < 0.5 nm Al followed by several nm of Al_2O_3 . The very thin Al layer protects the Py film during the Al_2O_3 evaporation (a technique used for example in the growth of high-quality tunnel barriers [Rea07]) and partially/fully oxidizes during Al_2O_3 evaporation. It should be noted that it is possible to replace the Al layer by another MgO layer and still keep the damping low. The measured values of a $GaAs/MgO/Py/MgO/Al_2O_3$ layer stack perfectly agree with the $GaAs/MgO/Py/Al/Al_2O_3$ layer stack discussed above. The choice for Al/Al_2O_3 is motivated mainly by the fact that it can be easily etched wet-chemically using NaOH.

Due to these requirements and technical limitations the sample series is finally grown onto two wafers on two consecutive days in order to keep the growth conditions as constant as possible. In Fig. II.8.1 a sketch of the two wafers, called M150209A (short: wafer A) and M150210 (short: waver B), including the positions of the pieces for different experiments is shown together with the Pt thickness map used to calculate the real d_{Pt} from the respective position on the wafer.
From SQUID, conductivity and full film FMR data it is concluded that the Py thickness on wafer A differs from the intended thickness of $d_{\text{Py}} = 4$ nm. As the effective magnetization and the damping parameter are equal for the bare Py on both wafers, it is concluded that the quality is good for both wafers and the change in saturation magnetization and the

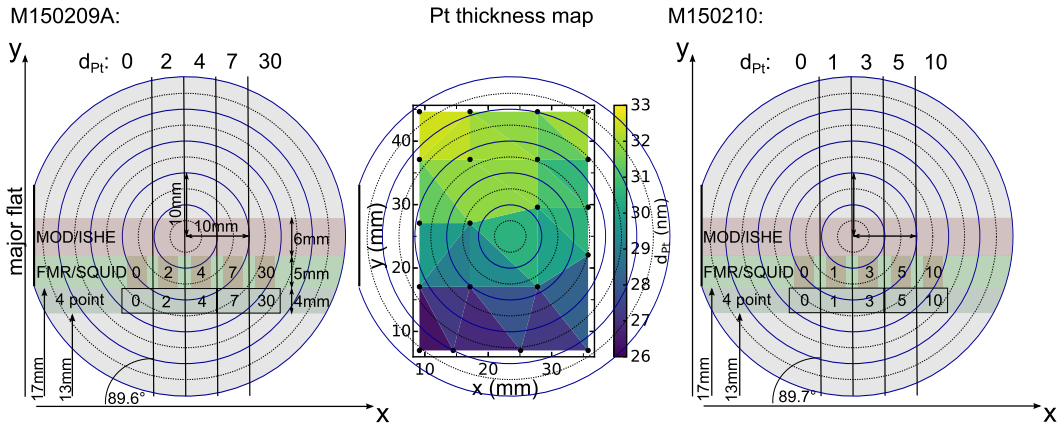

Figure 8.1.: *Sketch of the layers grown for the Pt/Py thickness dependence with the positions of the different samples. In the middle, the Pt thickness calibration map is shown. From this 2D map the exact Pt thickness is calculated depending on the y-coordinate on which the respective sample lies.*

lower conductance shown in the next sections is the result of a reduced thickness only. The Py thickness of wafer A is therefore corrected to $d_{\mathrm{Py,A}} = 3.5\,\mathrm{nm}$ using the results of SQUID and conductance measurements.

9. Experimental Characterization of Magnetic and Electric Properties

9.1. Magnetic Properties I: Saturation Magnetization

As the SOTs in thin metallic bilayers arise from interfacial effects, the torques exerted on the FM layer scale with the magnetic moment per area $\mu_0 M_s d_{Py}$. To measure this quantity, a commercial superconducting quantum interference device (SQUID) is used[1]. In a SQUID measurement, the total magnetic moment of a full film of known dimensions is determined. The area of the sample ($\sim (3 \times 5)\,\mathrm{mm}^2$) is measured using a caliper in order to calculate $\mu_0 M_s d_{Py}$. The result of these measurements is shown in blue dots in Fig. II.9.1. Looking at the graph, the difference of the samples from the two wafers is

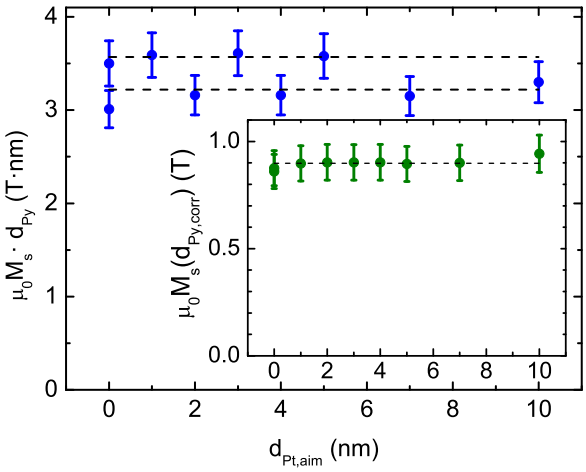

Figure 9.1.: *Magnetic moment per area (blue dots) and calculated saturation magnetization (inset, green dots) for the Pt/Py layers. The saturation magnetization is calculated using the corrected Py thickness for the samples of wafer A. The error bars are estimated from the error in determining the area of the films and represent 90% confidence intervals.*

immediately visible as the points lie on two distinct levels. A similar behavior is found in the electrical conductance and the measured damping. Therefore the thickness of wafer

[1]The SQUID used in the author's workgroup was supervised by Helmut Körner who also kindly helped the author to obtain the results presented here.

A is re-calibrated from both SQUID and conductivity data. The inset of Fig. II.9.1 shows the saturation magnetization calculated for the different layers using the corrected Py thickness values. As a result, all values lie around 0.9 T (dashed line), which is close to the bulk literature value of ~ 1 T [Coe10]. In all calculations, however, the directly measured value of the magnetic moment per area $\mu_0 M_s d_{Py}$ for the respective sample is used as this quantity has the lowest experimental error attached to it.

9.2. Magnetic Properties II: Full Film FMR

After the SQUID measurements, all samples are further characterized by the use of full film FMR. For every layer a frequency dependence of the (ip) resonance field and linewidth is recorded.

From the resonance field data the effective magnetization is determined by fitting the data to the Kittel equation Eq. (3.11), where an oop anisotropy as well as an ip uniaxial anisotropy is taken into account. If the external field lies ip and along the easy axis of the uniaxial anisotropy, $\mathfrak{H}_0 = H_{ext} + M_{eff} + H_{ip}$, $\mathfrak{H}_1 = H_{ext} + M_{eff} + H_{ip}$ and $\mathfrak{H}_2 = 0$ such that the resonance condition simplifies to

$$\left(\frac{\omega}{\gamma}\right)^2 = (\mu_0 H_r + \mu_0 H_{ip} + \mu_0 M_{eff})\,(\mu_0 H_r + \mu_0 H_{ip})\,. \tag{9.1}$$

Here $\mu_0 H_{ip} = \frac{2K_{ip,u}}{M_s}$ is the strength of the ip anisotropy in Tesla such that it can be easily compared to other magnetic fields involved. The above equation is solved for $\mu_0 H_r$ and used to fit the measured data, as shown in the inset of Fig. II.9.2. The value for the

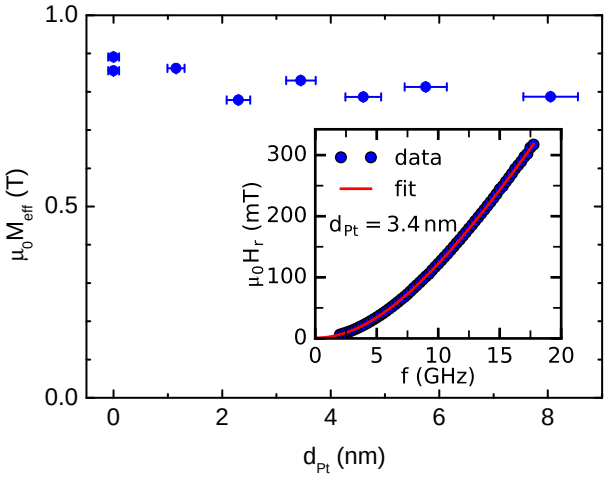

Figure 9.2.: *Effective magnetization of the different samples determined by full film FMR. The inset shows the frequency dependence of the resonance field for a sample with d_{Pt} = 3.4 nm from which M_{eff} is determined by a fit to the Kittel equation.*

gyromagnetic ratio is determined to be $\gamma = 185\,\mathrm{G}\frac{\mathrm{rad}}{\mathrm{Ts}}$ from measurements on thick Py films from the same system and is kept fixed in the evaluation of the thin-film data.
The fit results for M_{eff} are shown in Fig. II.9.2.[2] The measured values of M_{eff} are used to normalize the change in linewidth in the MOD experiments and as input parameter to calculate the magnetization dynamics during the evaluation of the ISHE voltages.

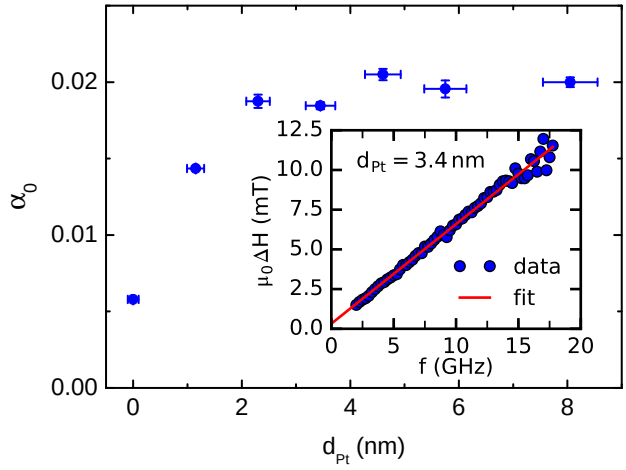

Figure 9.3.: *FMR result for the Gilbert damping parameter of the different Pt/Py bilayers. The inset shows an example curve for the behaviour of the measured linewidth vs. frequency. The slope of the linear fit determines the intrinsic damping. Note that the zero frequency intercept nearly vanishes.*

In order to determine the Gilbert damping parameter of the layers, the measured linewidth is fitted to

$$\mu_0 \Delta H = \frac{\alpha \omega}{\gamma} + \mu_0 \Delta H_0, \tag{9.2}$$

which is Eq. (3.14) with an offset in linewidth. This offset is added to take into account e.g. inhomogneities of the film (such as variation of M_{eff} within different grains) which broaden the FMR linewidth [Wol04; Wol13; Pla98; McM03]. An example curve of the measured linewidth and the results for the damping parameter obtained from the fits for all samples is shown in Fig. II.9.3. Since the offset is small for all samples ($\mu_0 \Delta H_0 \leq 0.6\,\mathrm{mT}$) and the measured linewidth shows a linear behavior with frequency over a wide frequency range, it is concluded that the intrinsic damping is well determined from the slope and other frequency dependent contributions to the linewidth (such as for example two magnon scattering) can be neglected [Wol13; McM03]. The difference between the two wafers can again be seen clearly. The reason lies in the nature of the spin pumping effect that scales

[2] Again, the difference of both wafers is visible. For $d_{\mathrm{Pt}} \geq 2\,\mathrm{nm}$ the values of M_{eff} are slightly lower than for the thinnest Pt sample and the pure Py film. Both features are explained by an oop anisotropy induced at the interfaces, in particular the Pt underlayer. Due to the interfacial nature of this anisotropy, the thinner Py layer from wafer A is influenced more, leading to lower M_{eff} values for this wafer.

with the inverse of the magnetic moment per area.

9.3. Experimental Results of SP

From the measured damping, it is possible to calculate the effective spin mixing conductivity (SMC) $\tilde{g}_{\mathrm{eff}}^{\uparrow\downarrow}$ by the use of Eq. (5.7). Importantly, in the computation the measured magnetic moment is used such that the result, shown in Fig. II.9.4, is independent of the different Py thickness of wafer A and B. The effective SMC is fitted using Eq. (5.8) (solved for $\tilde{g}_{\mathrm{eff}}^{\uparrow\downarrow}$) in order to obtain λ_{SD} and the spin mixing conductivity $\tilde{g}^{\uparrow\downarrow}$. The result of the fit

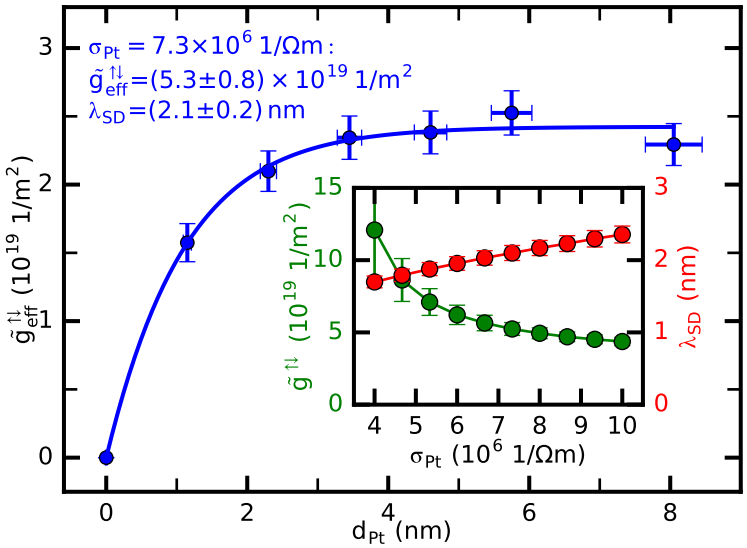

Figure 9.4.: *Effective SMC as function of the Pt thickness. The solid line represents a fit to Eq. (5.8) from which the spin diffusion length and the bare SMC are determined. In the main graph the Pt bulk conductivity* $\sigma_{Pt} = 7.3 \times 10^6 \frac{1}{\Omega\,\mathrm{m}}$ *is used as input value. The inset shows the outcome of the fit for a range of reasonable conductivity values. It is found that the SMC changes drastically with* σ_{Pt} *but the spin diffusion length depends only weakly on* σ_{Pt}.

depends on the value used for the bulk conductivity of Pt σ_{Pt}. In section II.9.4 the bulk conductivity for Pt $\sigma_{\mathrm{Pt}} = 7.3 \times 10^6 \frac{1}{\Omega\,\mathrm{m}}$ is experimentally determined and therefore is used as input for the spin pumping fit. The solid blue line drawn in the main graph belongs to the best fit for this conductivity value. In principle, the conductivity could be determined by the fit as well, however the correlation with the two other parameters is too strong to give reliable results such that a pre-determination is inevitable. In order to quantify the influence of the bulk conductivity, the fit is performed for different fixed values of σ_{Pt}. The results are shown in the inset of Fig. II.9.4. Interestingly, the bare SMC diverges for values $< 4 \frac{1}{\Omega\,\mathrm{m}}$, whereas the spin diffusion length varies only slightly over the range of conductivities used.

The raw values obtained for the effective spin mixing conductivity, saturating at $\tilde{g}_{\mathrm{eff,sat}}^{\uparrow\downarrow}$ ~

$2.4 \times 10^{19}\,\frac{1}{\mathrm{m}^2}$, are in good agreement with literature values for Pt/FM interfaces [Zha15b; Pai15; And11; Obs14; Nan15; Mos10a; Mos10b]. The value for the fitted spin diffusion length also agrees with literature values obtained for NM/FM bilayers as discussed (in comparison with the MOD/ISHE results) in section II.12. The literature values for the SMC scatter from $(2-13) \times 10^{19}\,\frac{1}{\mathrm{m}^2}$ [Zha15b; Aze11; Boo15]. Note that there is a fundamental issue concerning these values: From theory $\tilde{g}_{\mathrm{eff}}^{\uparrow\downarrow} \leq \tilde{g}^{\uparrow\downarrow} \leq \tilde{g}_{\mathrm{Sharvin}}$ must hold. A value of the Sharvin conductivity can be calculated from the free electron model using Eq. (2.23). In [Han13a], the SMC is computed assuming a spherical Fermi surface (FS) of Pt by using a Fermi vector $k_{\mathrm{F}} = 16\,\frac{1}{\mathrm{nm}}$. This k_{F} can be reproduced fairly well by using the Drude model, Eq. (7.3) and Eq. (7.5), and the tabulated (experimental) Hall coefficient of Pt [Hur72]. From $R_{\mathrm{H,exp}} = 2.2 \times 10^{-11}\,\frac{1}{\mathrm{C\,m}^3}$, it follows $n = 28 \times 10^{28}\,\frac{1}{\mathrm{m}^3}$ and $k_{\mathrm{F}} = 21\,\frac{1}{\mathrm{nm}}$. From Fermi vectors of this magnitude one obtains $\tilde{g}_{\mathrm{Sharvin}} = (2.2-3.3) \times 10^{19}\,\frac{1}{\mathrm{m}^2}$, in the range of the measured effective SMC. However, as the Fermi surface of Pt is not spherical, the calculation of n is misleading, because the Hall coefficient must be corrected for band structure effects [Gre72][3].

Indeed, from ab-initio calculations of a realistic Fermi surface of Pt [Zwi05] the obtained $\tilde{g}_{\mathrm{Sharvin,ai}} = 1.75 \times 10^{19}\,\frac{1}{\mathrm{m}^2}$ is smaller than the above values. It is evident that the fitted value for the bare SMC is much too high to be explainable within this model, as recently also pointed out by another group [Pai15]. Since the effective SMC is, from the experimental point of view, a quite solidly determined quantity, it is clear that something is missing in the spin pumping theory used in order to explain the strong enhancement of the measured damping. One reason for this behavior might be the induced magnetic moment of the Pt at the Pt/Py interface as discussed further in section II.12.

9.4. Electrical Conductivity

In order to understand the behavior of the electrical conductivity of the thin Pt layers studied in this work, three series of films are investigated:

- Pt on MgO: It is a very hard task to measure the bulk conductivity from polycrystalline samples due to the fact that the number of unknown parameters, especially the grain size and distribution, introduces too many unknowns. Therefore, a single crystalline sample should be produced if possible to determine this key parameter. It is known that Pt shows single crystalline growth on MgO(100) single crystal substrate [Lai92]. Therefore, a series of (13-190)nm thick Pt films is grown in order to measure the bulk conductivity σ_0 needed for the evaluation of the other, potentially polycrystalline layers. The very large thickness of the last sample is chosen to ensure

[3] the value of $n = 28 \times 10^{28}\,\frac{1}{\mathrm{m}^3}$ cannot be true due to the fact that Pt only has $n = 6.6 \times 10^{28}\,\mathrm{atoms/m}^3$ and, in addition, only $n_{\mathrm{e}} = 0.4\,\frac{\text{conduction electrons}}{\text{atom}}$ [And70; Fis80; Boo15]

a bulk-like behavior even for a mean free path (MFP) λ of the order of 10 nm. Pt is grown in the aforementioned MBE system using an e-gun evaporator at a substrate temperature of 590 °C onto commercially available epi-ready MgO(100) substrates, following ref. [Lai92] for epitaxial growth. The films show a clear RHEED pattern during and after growth. In addition to the main reflexes, a secondary peak is visible, which indicates a surface reconstruction [Has12]. From growth method and RHEED pattern, it is believed that the structure of the films is single crystalline. The layers of this series are then characterized by Georgios Stefanou of the group of Prof. B. J. Hickey in Leeds, UK via X-ray diffraction (XRD) (see e.g. [Few99] for an overview over the technique). This technique allows for a nondestructive determination of the thickness and roughness of the layers. The results of the structural analysis are shown in panel b) of Fig. II.9.6. The roughness of the films is determined to be quite low for the three thickest films, whereas the two thinner films show a substantial roughness which will be discussed together with the conductivity results. The analysis of the FWHM of the XRD Pt-peaks leads to a so-called Scherrer length (as the Scherrer equation is used to evaluate the XRD scans). This length can be associated with the average grain size if all other sources of peak broadening (such as setup resolution etc.) can be excluded by careful calibration. The inset in panel b) shows the Scherrer length values obtained from raw data without corrections for systematic peak broadening. These values are used as input for the grain size in the MS model although it is likely that the peak broadening is caused entirely by the experimental setup.

- thin Pt on GaAs: In order to evaluate the thickness dependence of the conductivity on the substrate used in the final experiment, a series of (1-40)nm Pt[4] is grown onto a GaAs wafer and capped with Al_2O_3 . The growth protocol is: An epi-ready, insulating GaAs waver is transferred into the MBE system and heated to 350 °C in order to evaporate residual water and organic residues. Subsequently, Pt is evaporated at room temperature using the e-gun evaporator. An Al_2O_3 capping layer is used in order to prevent aging of the surface. The thickness of the Pt layer is calculated from the calibration measurement.

- Pt(x)/Py on GaAs: these samples are taken from the wafers on which the actual MOD/ISHE measurements are performed.

In Fig. II.9.5 the measured sheet conductance for the three series is shown. The inset shows the low thickness range data. The dashed lines are linear fits to the data, forced through zero, and point out the clear deviation of the data points from linear scaling. The

[4] Unfortunately, it is not possible to evaporate very large thicknesses (190 nm) frequently due to the limited amount of Pt to be evaporated before a refilling of the crucible is needed.

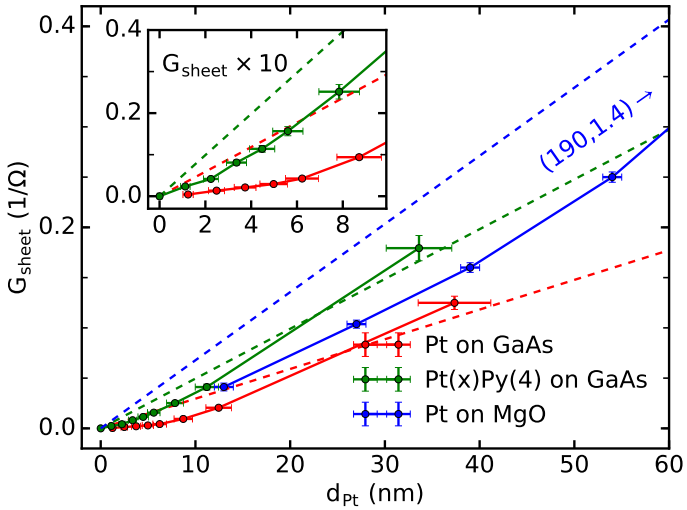

Figure 9.5.: *Pt sheet conductance for the three different sample series discussed in the main text. The inset shows the region of low thickness in detail. The coordinates of the sample with* $d_{Pt} = 190\,nm$ *lie far outside the plotted region and are given in blue text in the main graph. The dashed lines represent the expected linear behavior of* G_{sheet} *for a constant conductivity for the respective samples.*

coordinates of the thickest data point of Pt on MgO are indicated in blue as they are far outside the plotted range. The Pt sheet conductance is computed from the Pt(x)/Py data by subtracting the pure Py conductance, which is a first order approximation but frequently used due to the lack of a better method [Boo15; Ngu16]. There are a few points that are immediately clear from the graph: a) the behavior of the sheet conductance is nonlinear for all three series and b) the values for equal Pt thickness are different for all three series. The nonlinear scaling is an indicator of the presence of interface and/or grain boundary scattering as explained in II.7. The difference in the absolute values for the same Pt thickness can be explained by a different structure of the respective films. i.e. different grain size and/or roughness. In the following evaluation, the measured sheet conductance is converted into a thickness-dependent conductivity and subsequently fitted to both Fuchs-Sondheimer (FS) model and Mayadas-Shatzkes (MS) model described in section II.7. The outcome of the fits is compared and discussed with respect to the particular structural information at hand. In Fig. II.9.6, the conductivity of the three layers is shown in panel a), c) and d) together with fitting results using either the FS or MS model. The results of the fits are listed in table (9.1). In the table, the error determined from the covariance matrix of the fit is displayed in parentheses after the best fit value. If no error is displayed, the values are used as fixed inputs for the fit.

Before performing the evaluation, it is important to note the following constraint: According to Drude theory, the product $\lambda\rho_0 = \frac{\lambda}{\sigma_0}$ is fixed by Eq. (7.4) and only depends on the number of free electrons per volume, n. Realistic values of n can be calculated using the

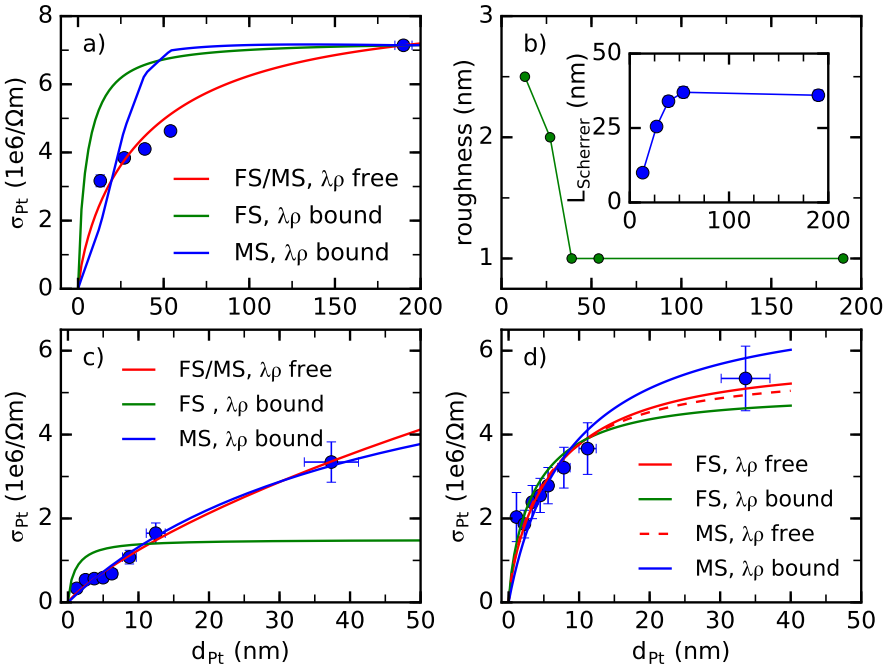

Figure 9.6.: *Pt Conductivities of the three sample series and fits to the FS and MS model. a) conductivity of Pt on MgO substrate. Fits to both FS and MS model do not match the data if the $\lambda\rho$ bound is applied in the fit. From the thickest sample a lower bound for the bulk conductivity is determined to be $\sigma_{Pt} = 7.3 \times 10^6 \frac{1}{\Omega\,\mathrm{m}}$. b) roughness of the Pt layer for the MgO/Pt samples determined by XRD. The inset shows the Scherrer length that is taken as the average grain diameter in the MS model (see text). c) conductivity data and fits for Pt single layers grown on GaAs. d) Pt conductivity of the Pt/Py sample series on GaAs. Compared to c), the conductivity values are significantly higher and show a faster increase of conductivity at low thickness. The difference between c) and d) is attributed to the fact that the Py layer influences the bilayer conductivity beyond the two resistor model.*

atomic density of Pt, $\rho_a = 6.62 \times 10^{28} \frac{\mathrm{atoms}}{m^3}$ [Boo15] and the number of conduction electrons per atom, $n_\mathrm{e} = 0.4 \frac{\mathrm{electrons}}{\mathrm{atom}}$ [And70; Fis80; Boo15] such that $n = 2.7 \times 10^{28} \frac{1}{\mathrm{m}^3}$. This leads to a mean free path of Pt $\lambda = 13\,\mathrm{nm}$ for the literature value $\sigma_0 = 9.1 \times 10^6 \frac{1}{\Omega\,\mathrm{m}}$ [Lid03]. In order to see what kind of implications this bound has, two fits are made: one with fixed $\lambda\rho_0 = \frac{\lambda}{\sigma_0}$ using the literature value for n (called "bound") and one without fixed value (called "no bound"). It has been pointed out recently that the strict validity of the $\lambda\rho_0$ bound might not be valid for grains smaller than the bulk MFP [Zha06], however, there is no model at hand to describe the change quantitatively such that the bound is set using bulk properties. The Pt grown on MgO is evaluated first with the results shown in panel a) of Fig. II.9.6 and the first column of table 9.1. The following assumptions are used for the fits:

- Due to the roughness in the nm range, the reflection at the boundaries is set to be purely diffusive ($p = 0$) in both MS and FS model, see also the discussion after Eq. (7.15).

		Pt on MgO	Pt on GaAs	Pt/Py
FS, no bound	λ (nm)	76(13)	667(479)	12.1(3.0)
	σ_0 $(1\times10^6\,\frac{1}{\Omega\,\mathrm{m}})$	8.4(0.2)	24(13)	5.9(0.6)
FS, bound	λ (nm)	10.3(0.1)	2.1(0.6)	7.1(0.5)
	σ_0	7.3(0.1)	1.5(0.4)	5.0(0.3)
MS, no bound	λ (nm)	73(19)	45(979)	10.5(2.8)
	σ_0 $(1\times10^6\,\frac{1}{\Omega\,\mathrm{m}})$	8.3(1.3)	8.5(2.4)	5.6(0.5)
	R	0(0.1)	0.38(7.87)	0.0(0.1)
MS bound	λ (nm)	769(15)	10.3	10.3
	σ_0 $(1\times10^6\,\frac{1}{\Omega\,\mathrm{m}})$	544(11)	7.3	7.3
	R	0.73(0.1)	0.75(0.01)	0.22(0.03)

Table 9.1.: *Results of the fits of the conductivity data of the different sample series to both FS and MS model. For discussion of the presented values see the main text.*

- The raw conductivity of the thick sample is close to the bulk literature value. If grain scattering is not present and $d_{\mathrm{Pt}} \gg \lambda$ there is no reason why the (bulk) conductivity of the Pt presented here should be much lower than the literature value, as very high grade material is deposited. This reasoning leads to a strong constraint: The fit curves are forced through the point at $d_{\mathrm{Pt}} = 190\,\mathrm{nm}$ because otherwise a $\sigma_0^{\mathrm{Pt}} < \sigma(d_{\mathrm{Pt}})$ is obtained from the fit.

- For the use of the MS model, the grain diameter is set to be the Scherrer length determined by the XRD measurements.

From the unbound FS fit, one gets a very large $\lambda \approx 76\,\mathrm{nm}$ that seems to be not possible within the Drude model as it is seven times larger in magnitude than expected, though the bulk conductivity seems to be quite close to the literature value. Apparently, there is some effect that decreases the conductivity on a different length scale than the MFP. Interestingly, if the MS model is used without bound, one gets the same result and the inter-grain scattering is fitted to be zero. This outcome holds also if the grain size is assumed to be equal to the film thickness for the whole range. This outcome might be another hint that the samples are indeed single-crystalline without grain contribution. If the $\lambda\rho_0 = const(n)$ bound is applied during the fitting, the bulk conductivity (and the corresponding MFP) obtained by the FS model is purely determined by the conductivity of the last point. However, the fit curve does not follow the data at all (up to the last point). The bound MS model diverges as a result of the saturating grain diameter. The conductivity of thin Pt has been studied extensively in [Fis79; Fis80], here the results have been $\sigma_0 = 6\times10^6\,\frac{1}{\Omega\,\mathrm{m}}$, $\lambda = 10\,\mathrm{nm}$ and the computed free electron density has been calculated to be $1.6\times10^{28}\,\frac{1}{\mathrm{m}^3}$; these values are comparable to the ones obtained by the bound FS model. Due to the fact that none of the models seems to give an appropriate

description of the data, the following conclusions are drawn: The quality of the films is determined to be good from all characterization measurements. From the aforementioned reasoning, it is assumed that the bulk conductivity of Pt evaporated in the samples series here is $\sigma_0 = 7.3 \times 10^6 \frac{1}{\Omega\,\mathrm{m}}$ as lower bound. Via the literature value for n, the corresponding MFP is $\lambda = 10.3\,\mathrm{nm}$. This shows that size effects are indeed important in the thin Pt layers used for the MOD/ISHE experiments. It remains unclear, however, what causes the reduction of the conductivity for the thinner Pt samples. From the roughness measurement, it can be guessed that the two thinnest samples might be of lower quality, however, the 40 and 50 nm thick samples are as smooth as the thickest one. In addition, the four thin samples follow a general trend such that the roughness does not seem to be the explanation. In [Cas12] it has been recognized that the conductivity of sputtered Pt increased up to a saturation value of $3 \times 10^6 \frac{1}{\Omega\,\mathrm{m}}$ at a thickness of $\approx 40\,\mathrm{nm}$. In [Ngu16], a similar effect has been seen, however, saturation of the conductivity occurred at $d_{\mathrm{sat}} \sim 15\,\mathrm{nm}$, as well as in [Boo15] where $d_{\mathrm{sat}} \sim 30\,\mathrm{nm}$, both groups reach saturation conducutivities around $5 \times 10^6 \frac{1}{\Omega\,\mathrm{m}}$. In all three experiments, the Pt layer was deposited by DC sputtering onto amorphous substrates such that polycrystalline growth is expected. This possibly leads to a reduction of the saturation conductivity from the bulk value due to grain scattering. Additionally, it might be that the grain size saturates at a certain thickness that is different in these experiments, thereby explaining the difference in the saturation thickness. The difference between sputtered and evaporated layers in terms of conductivity was also clearly observed in [Sag16], however, without any explanation.

Polycrystalline growth is also expected for the Pt layer grown on oxidized GaAs, the evaluation of this set of samples is shown in panel c) of Fig. II.9.6 and the fit values are listed in the second column of 9.1. It is directly visible from the raw data that this series has the lowest overall conductivity. The difference to the series on MgO might be the fact that polycrystalline growth induces grain scattering that is not present in the MgO/Pt layers. In the MS model, the grain size is taken to be equal to the Pt thickness, which provides a best guess for non-annealed samples [Fis79; Sam83; Van84; Zha06] as the thickness does not exceed 40 nm.[5] It should be noted that this assumption is rather strong; in [Zha06], for example, the scaling of D_{Grain} is linear up to 40 nm but the slope is smaller than one.

Both the bounded and the unbounded FS model fits deliver unphysical results. The reason might be that a) the scaling does not follow either FS or MS model or b) the conductivity is dominated by grain scattering and the FS model cannot produce the correct results, see Fig. II.7.6. Due to the lack of a saturation value, the unbounded fit then diverges. The unbounded MS model is apparently overparametrized such that the result of the fit have to be disregarded as well. When using the predetermined σ_0 as fixed input (which then

[5] This must be kept in mind when comparing fit curves from panels a),c) & d). A saturating grain size leads to a kink/a saturation below bulk conductivity in the conductivity curve.

sets the MFP as well), the only free parameter is the grain scattering coefficient $R = 0.75$. Values for R scatter a lot when looking at the literature, a few examples are: $R_{Au} = 0.3$ [Van84] $R_{Cu} = (0.1 - 0.27)$ [Ste05] $R_{Al,Au,Cu} = (0.5 - 0.9)$ [Cam06] $R_{Cu} = 0.38$ [Art92] $R_{Ag} \sim 0.3$ [Art07]. However, values > 0.5 are not often found such that again something not included in the analysis causes an excess lowering of the conductivity. It should be pointed out that even at the lowest film thickness of $\sim 1.2\,\text{nm}$ a finite resistance is measured. This again indicates that excess roughness cannot be the reason as it would prevent a continuous film which would show an infinite resistance (bound by the measurement apparatus and substrate).

It is interesting to realize that the Pt/Py series shows a much higher conductivity at the same thickness compared to the bare Pt on GaAs case. This is probably induced by the Py overlayer because scattering at the Pt/Py interface is likely to be less than scattering at the Pt/Al_2O_3 interface. In addition, due to the (at least) semitransparent interface of Pt/Py, the conduction electrons are not confined to the Pt layer but interchange between layers. This leads to an entanglement of the layers such that the two resistor model is strictly incorrect. In addition, from personal experience it appears that during the growth of metal layers the roughness of the top surface might increase with thickness across a certain range thus leading to a reduced effective thickness. This effect would be shifted to the Py surface removing its visibility in the Pt conductivity. When applying the FS and MS model to the data, one sees that for this series the results do not differ between models as much as the previous ones. However, the resulting bulk conductivity is smaller than the conductivity of the thick Pt on MgO film. This again shows that it is important to fix this parameter before. When using the MS model with fixed σ_0 and MFP, the grain scattering coefficient is $R = 0.22$, which lies much better within the literature values cited above than the very high value obtained for the bare Pt.

From the the conductivity measurements the following statements are summarized:

- There is no set of parameters that can fit all three sets of layers using the FS or the MS model. This leads to the conclusion that the morphology of the films differs, which is caused by the different conditions in growth and/or if the film is a single or bilayer.
- Size effects do play a significant role due to these different scattering mechanisms and the fact that the layer thicknesses used lie in the range of the MFP.
- In order to completely understand the conductivity in terms of bulk, interfaces and grain scattering, a very detailed study of the morphology (grain structure and distribution, bottom and surface roughness etc.) is needed. Layer series should provide many densely lying thicknesses over a wide range; certainly extending the data of this work.

- As input parameter for the drift diffusion model used to evaluate the SOT measurements, a bulk conductivity of $\sigma_0 = 7.3 \times 10^6 \frac{1}{\Omega\,\mathrm{m}}$ is used for the rest of this work.

The implication of these findings are discussed together with the SOT results in section II.12.

10. ISHE: Micromagnetic Simulations and Experimental Results

10.1. Micromagnetic Simulations

It is clear from the theory part, especially from Eq. (5.23) that, in order to quantify the ISHE in a NM/FM bilayer, the ISHE signal has to be disentangled from the AMR signal caused by the induced hf current within the sample stripe. This has been achieved by choosing the ip field angle such that the AMR signal is zero and the ISHE signal is at maximum, which occurs at $\varphi_{ISHE} := \varphi = \varphi_{\mathrm{H}} = \pm 90°$, as can be seen from Eq. (5.23). At these angles, the measured voltage is given by

$$V_{\mathrm{S}}(\varphi_{ISHE}) = V^0_{\mathrm{ISHE}} A_{zz} A_{yz} \left[\left(h_z^{\mathrm{CPW}} \right)^2 + \frac{I^2_{\mathrm{ind}}}{12 w^2} \right]. \tag{10.1}$$

The parameter of interest, V^0_{ISHE}, can be accessed from the measurement if the susceptibility amplitudes A_{ij} can be calculated and the driving terms are known. However, in addition to the similar equation presented in [Obs15], the driving term now contains the induced current which has to be quantified from the experiment. This is, in principle, possible from a full angular measurement of $V_{\mathrm{S}}(\varphi)$ and $V_{\mathrm{A}}(\varphi)$; the new full set of equations to fit this data, derived in this work, is given by Eq. (5.23). Additionally, it has been realized in the progress of this work that in confined structures, for this particular case of long stripes, the mode structure can be of non-negligible influence. Therefore, it shall be clarified whether the macrospin approach in the data evaluation is applicable to the measurements. In order to separate the different effects, micromagnetic simulations are chosen as a tool because the simulation allows to change boundary conditions from macrospin like behavior to realistic samples. The aim of the following section is therefore to

- verify the correctness of Eq. (5.23) via macrospin-like simulations
- clarify the influence of mode structure on ISHE voltage

10.1.1. Implementation of the problem to Mumax

The micromagnetic simulations are performed using the mumax^3 package; for deeper insight see [Van14]. The benefits of this particular software are free availability, speed and ease of use. A sketch of how the geometry is constructed in the code is shown in panel a) of Fig. II.10.1. In mumax^3, there is the possibility to set periodic boundary conditions which are used to mimic a long stripe with dimensions $(75 \times 6)\,\mu\mathrm{m}^2$ by defining a slice of 32×1024 cells with periodic boundary conditions in x. For the calculation of the demagnetizing kernel, mumax^3 uses in total 401 of these slices in one row in x-direction, resulting in the dimensions given above. The cell size is $(5.9 \times 5.9 \times d_\mathrm{F})\,\mathrm{nm}^3$, on the order of the exchange length. The data is taken by averaging the slice in x to obtain one linescan of $\boldsymbol{m}(t, y)$ across the stripe for one period T of the driving frequency. This allows calculating all required dynamic quantities for each position on the stripe and to mimic electrical as well as optical measurements by extracting the dynamic precession amplitudes and phases of the magnetization components. If, for example, a TRMOKE measurement is simulated, the oop magnetization component is recorded at a fixed time step at every position and external field value, leading to color coded images similar to the ones shown in section II.6. To test the fit routine using Eq. (5.23), a first simulation

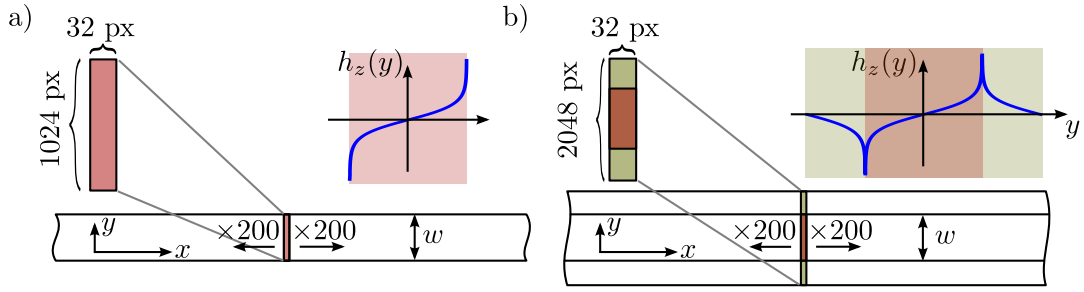

Figure 10.1.: *Sketch of the geometry used in micromagnetic simulations. a): The* 6 µm *wide stripe consists of 401 repetitions of one slice of* 32×1024 *cells. The boundary leads to the evolution of standing spin waves and edge effects. The inset shows the oop inhomogeneous driving field as function of* y*. b): The* 6 µm *wide stripe is mirrored at each side in order to remove the edge effects for "local macrospin" simulations. The calculation is performed on the* 32×2048 *cells slice but the data is only taken from the inner red part. The oop inhomogeneous driving field used is shown as inset.*

is set up to mimic a "local macrospin" behavior, i.e. the magnetization is assumed to be describable by the susceptibility approach but under the action of locally different driving fields. This requires reducing the dynamic dipolar fields and the static demagnetizing field to a negligible amount. The way this toy model is built up in mumax^3 is the following: first, the thickness of the magnetic layer is set to 0.2 nm, thereby greatly reducing the static ip demagnetizing field (see Eq. (6.6)) and reducing the mode spacing to almost zero (see Eq. (6.5)). However, directly at the edge, the internal field is always inhomogeneous,

see e.g. Fig. II.6.3) which leads to distortions close to the edge even for very thin layers. To circumvent this problem, the stripe is "embedded" into two adjacent stripes of half the original width such that the edge problems are simply moved outside, where the magnetization is not probed. Any inhomogeneous driving field is then implemented as shown in panel b) of Fig. II.10.1 by mirroring it along the respective edge. The data is taken across the inner 6 µm only and shows a quite homogeneous dynamics that follows the local driving field up to the very edge where the change of the driving field amplitude in space is too rapid for the magnetization to follow, as can be seen in the third column of Fig. II.10.2. It should be stressed that - due to the fact that the "local macrospin" magnetic boundary condition is unavoidably unrealistic anyway - the choice of the boundary condition for the inhomogeneous driving field does not seem to have a great impact.

10.1.2. Evaluation process of simulation data

An overview of some key results from the simulations is given in Fig. II.10.2. The figure is divided into three columns that show different plots for the case of real boundary condition and two cases of "local macrospin" simulations. The driving field $h_z(t)$ of the first two columns is homogeneous in space, $\mu_0 h_z = 0.1\,\mathrm{mT}$, whereas in column three only the current induced inhomogeneous driving field is used, corresponding to a total induced current of $I_{\mathrm{ind}} = 1\,\mathrm{mA}$. Unless indicated otherwise, the frequency is set to 10 GHz. The stripe dimension is chosen to lie in typical ranges of the experiments performed in [Obs15], especially the thickness is set to 12 nm which leads to pronounced mode structures compared to $d_{\mathrm{F}} = 4\,\mathrm{nm}$ used in the experiments of this work. The topmost image always represents a simulated TRMOKE measurement in which the magnetic signal is recorded in linescans across the stripe width for every field to get an impression of the mode structure. The external field is turned by $\varphi_{\mathrm{H}} = \varphi = 30°$ from the longitudinal axis. In the cases of the local macrospin simulations, no mode structure is visible. In the realistic stripe, higher order even modes being excited at fields lower than FMR can be observed, as expected. The plots in the center row show linescans at the resonance field for both the AMR signal $\propto \mathfrak{Re}\{\Delta m_y\}$ and the ISHE signal $\propto \omega \mathfrak{Im}\left\{\overline{\Delta m_y}\,\Delta m_z\right\}$ calculated at every point in space. The blue lines are taken from the simulated data and the red dashed line represents the value calculated using the susceptibility and the value of the averaged driving field, without the inhomogeneous part. The local macrospin simulation (center) shows a perfect agreement for the homogeneous driving field. As will be discussed later, the result for the inhomogeneous driving field (right) agrees well with Eq. (5.23). For the realisitic sample (left), the deviation from the susceptibility calculation is directly visible. The difference occurs due to the boundary condition that leads to a reduction of the precession amplitude at the edge of the sample. The impact on an electrical measurement is shown in the lowest row, where a real measurement is mimicked by adding up AMR

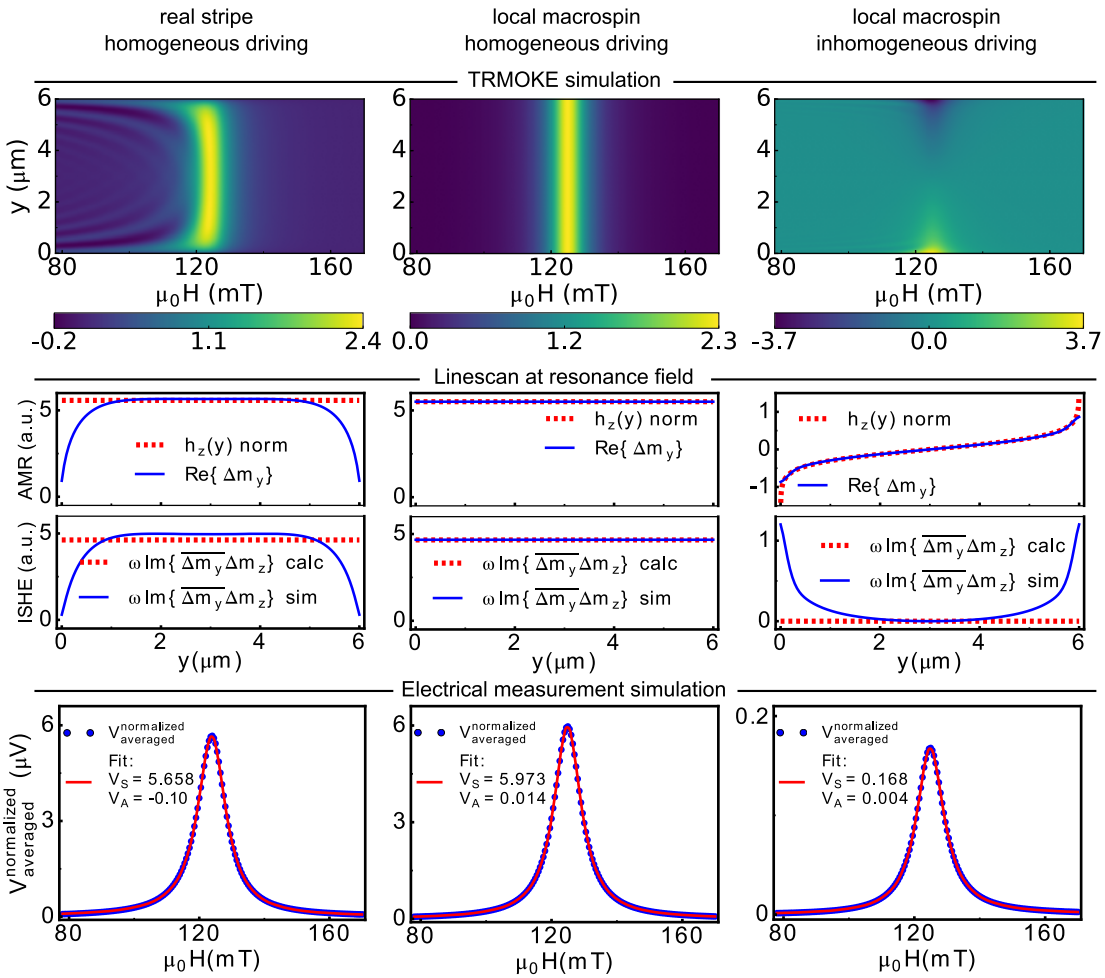

Figure 10.2.: *Simulation results for a realistic stripe of* $w = 6\,\mu\text{m}$ *and* $d_F = 12\,\text{nm}$ *and two "local macrospin" scenarios. In the first two columns only a homogeneous driving field is used to excite the magnetization. In contrast, the third column shows the effect of a purely inhomogeneous oop Oersted field. The upper row shows the mode profile across the stripe width as function of the external field. The middle row shows the spatial distribution of the dynamical quantities needed for the computation of both AMR and ISHE at FMR. In the upper part of this row (AMR), the blue solid line represents* $\mathfrak{Re}\{\Delta m_{y'}\}$ *while the red dashed line represents the spatial profile of the oop driving field. In the lower part (ISHE), the red line represents* $\omega\mathfrak{Im}\{\overline{\Delta m_y}\Delta m_z\}$ *computed by using the homogeneous oop driving field and neglecting the inhomogeneous part. The lowest row shows a simulated electric measurement and a fit to Eq. (5.22) in order to extract symmetric and antisymmetric voltages.*

and ISHE, averaging over the stripe width and fitting it to Eq. (5.22) in order to extract the symmetric and antisymmetric contributions. In the particular examples shown, the antisymmetric amplitude should be zero as predicted by Eq. (5.23). For the two local macrospin cases this is true within a small error, however for the realistic sample the parasitic V_A is one order of magnitude bigger than V_A of the local macrospin case. The cause of this contribution are the higher order modes that add signal to the main peak.

In addition, the determined V_S value is lower for the realistic sample due to the boundary effect. The fitted value from the inhomogenous driving field agrees very well with the value of $V_S = 0.169\,\mu V$ that is calculated from Eq. (5.23) for the used parameters, indicating the validity of the respective fitting routine.

10.1.3. Simulation results

As a second step, the validity of Eq. (5.23) is checked by performing local macrospin simulations as a function of angle for a combination of different driving fields, shown in Fig. II.10.3. Two sets of parameters are chosen, resembling the samples studied in [Obs15] ($d_F = 12\,nm$) and this work ($d_F = 4\,nm$). The input parameters used are listed in table 10.1.

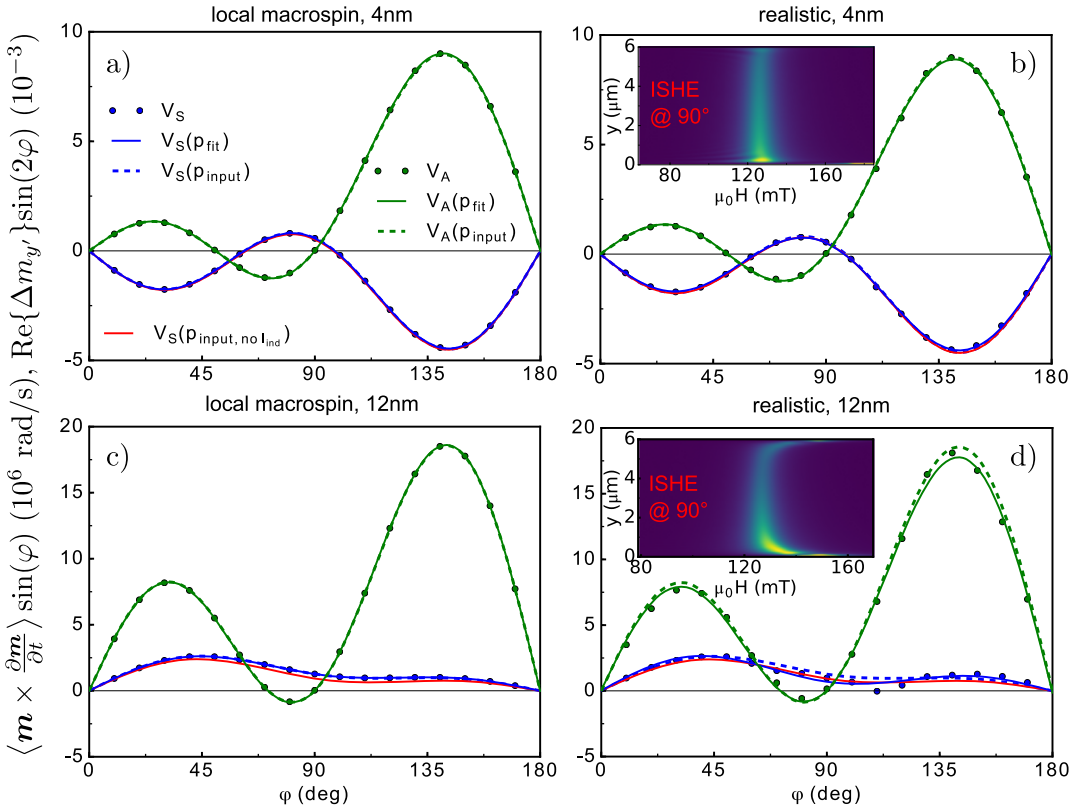

Figure 10.3.: *Angular dependence of the simulated dynamics for a realistic stripe of $w = 6\,\mu m$ and $d_F = 4/12\,nm$ and the corresponding "local macrospin" model. All panels show the simulation data in symbols; blue/green stands for the symmetric/antisymmetric contribution. The blue and green solid lines are fits to the data, the results are listed in table 10.1. The dashed lines are calculated using the fitting function and the input parameters. The red solid line is calculated in the same way but by neglecting the inhomogeneous driving field contribution. Panel a) and c) show the local macrospin model; the respective results for equal input parameters but realistic boundary conditions for a 4/12 nm thick sample are shown in b) and d). The insets of b) and d) show the spatial distribution of $\mathfrak{Im}\left\{\overline{\Delta m_{y'}}\,\Delta m_{z'}\right\}\sin(\varphi)$.*

As the relevant quantities $\mathfrak{Im}\left\{\overline{\Delta m_{y'}}\,\Delta m_{z'}\right\}\sin(\varphi)$ and $\mathfrak{Re}\left\{\Delta m_{y'}\right\}\sin(2\varphi)$ are directly

computed from the magnetization dynamics, the respective prefactors $V^0_{\mathrm{ISHE}}, = V^0_{\mathrm{AMR}} = 1$[1]. In the fitting routine, the induced current is related to the AMR prefector via $V^0_{\mathrm{AMR}} = -\frac{1}{2}\Delta R_{\mathrm{input}} I_{\mathrm{ind}}$ with a fixed $\Delta R_{\mathrm{input}} = -2\frac{V^0_{\mathrm{AMR,input}}}{I_{\mathrm{ind,input}}}$. This corresponds to the experiment in which ΔR is predetermined in a static measurement. The fitting routine reproduces

parameter	12 nm Py			4 nm Py		
	input	fit: "L. M."	fit: realistic	input	fit: "L. M."	fit: realistic
V^0_{ISHE}	1	1	0.58	1	1	0.9
V^0_{AMR}	1	1	0.9	1	1	0.98
h_z^{CPW}	1	-	-	1	-	-
φ_{CPW}	60	60.4	66.8	60	60.2	60.8
h_y^{eff}	0.1	0.1	0.11	0.5	0.5	0.51
τ_{DL}	0.35	0.34	0.69	1.1	1.1	1.1
I_{ind}	1	1	0.9	0.5	0.5	0.498

Table 10.1.: *Parameters used as input in micromagnetic simulations of two different Py layers (columns "input") and the parameters obtained by fitting the data presented in Fig. II.10.3 to Eq. (5.23) (columns "fit: "). The simulations are performed within the local macrospin model ("L. M.") and by using a realistic stripe geometry ("realistic").*

the input parameters for the "local macrospin" case, thereby showing that the procedure works well and the derivation of the equation is valid.

When applied to the realistic simulation data, the outcome does deviate significantly from the input, especially for the thick sample, for which the ISHE voltage is heavily underestimated. If the field is parallel to the stripe, the higher order modes lie lower in field than the main peak (see section II.6.1), such that the signal contains more asymmetric voltage than predicted from macrospin; this effect can be seen in the first column of Fig. II.10.2. When the field angle is turned into the 90° position, edge modes appear due to the demagnetizing field in y-direction as described in section II.6.2. These edge modes lie higher in field than the main peak, shifting the asymmetric contribution to that side, see the inset of panel d) in Fig. II.10.3. In between there must be a smooth transition. For the thin sample, the deviations are not that significant, however the ISHE voltage is off by 10 %. It is therefore clear that the quantification of the ISHE voltage from an angular dependent measurement in a realistic sample does not work perfectly (within the 10% error), even if the thickness of the FM layer is kept low. This results from the fact that the AMR is the dominant signal source in the samples studied in combination with the modulation of the angular dependence of the symmetric/antisymmetric voltages due to the fact that the mode structure changes with the angle of the applied field. As a result,

[1] In order to plot and fit the data, both prefactors are rescaled (see y-axis label in Fig. II.10.3) in order to bring them to the same order of magnitude.

the fit of the angular dependence does not cross the data points of pure ISHE signal at $\varphi_{\mathrm{ISHE}} = \pm 90$ and the ISHE voltage is not reproduced perfectly.

On the other hand, the AMR voltage and therefore the induced current are quite well reproduced from the fits, especially for the thin sample, as they are not so strongly entangled with the other parameters. This allows to predetermine all parameters needed in Eq. (10.1). As the AMR signal vanishes at φ_{ISHE}, the evaluation of the measured voltage at this angle does not suffer from the above-mentioned problem. The only question left is if the averaged signal deviates much from the macrospin case at this angle. The answer to this question is not a general one but depends on the exact geometry of the sample as well as on the driving torque combination. First, the impact of the mode structure depends on the ratio of width and height of the FM, the thinner and wider the better the macrospin approximation is. Therefore, in this work the FM thickness used is 4 nm instead of 12 nm used in [Obs15]. Additionally, the width is increased from 5 to 6 µm. Further increasing the width would lead to problems in the homogeneity of the primary driving field in the experiment. To estimate the deviations in the ISHE voltage for the sample geometry used in the present study, simulations are carried out for some typical values of driving torques. These are obtained by fits of experimental data for the angular dependence of the symmetric/antisymmetric voltages, see section II.10.2. At frequencies $f > 8$ GHz the induced currents are in the range of 0.5 mA at a primary driving field of 0.2 mT. This implies, via Eq. (10.1), an increase of $V_{\mathrm{S}}(\varphi_{\mathrm{ISHE}})$ by only ~ 3%, which is below the detection limit. In Fig. II.10.4 simulation results are shown for an applied field in the 90° position using the parameters for the 4 nm sample from table 10.1. The upper plot shows the spatial dependence of magnetization dynamics at FMR and the lower ones show the simulations of electrical measurements. On the right side the inhomogeneous field due to the current was taken into account, on the left side this term was set to zero. The inset shows the ISHE signal as function of field and space. For homogeneous driving, the dynamics is quite homogeneous across the stripe width, with some small distortion at the edge. The average over the width is close to the value calculated from the susceptibility; the small deviation comes from the fact that the precession goes to zero at the edge. If the current induced field is added, the deviation changes from values below the macrospin value to values larger than the macrospin value, even with the correction for the additional driving strength. In both cases, the deviations are below the experimental detection limit. From the simulations it is therefore concluded that the mode structure does not play a measurable role for the used sample geometry and for low induced currents at magnetic field strength large enough to completely saturate the magnetization.

The measurement procedure to be used therefore is the following: at the $\varphi_{\mathrm{ISHE}} = 90°$ position the AMR signal vanishes. Thus the optimum angle is found where the asymmetric voltage reaches zero. The search for this angle is performed at a high frequency/field. Sub-

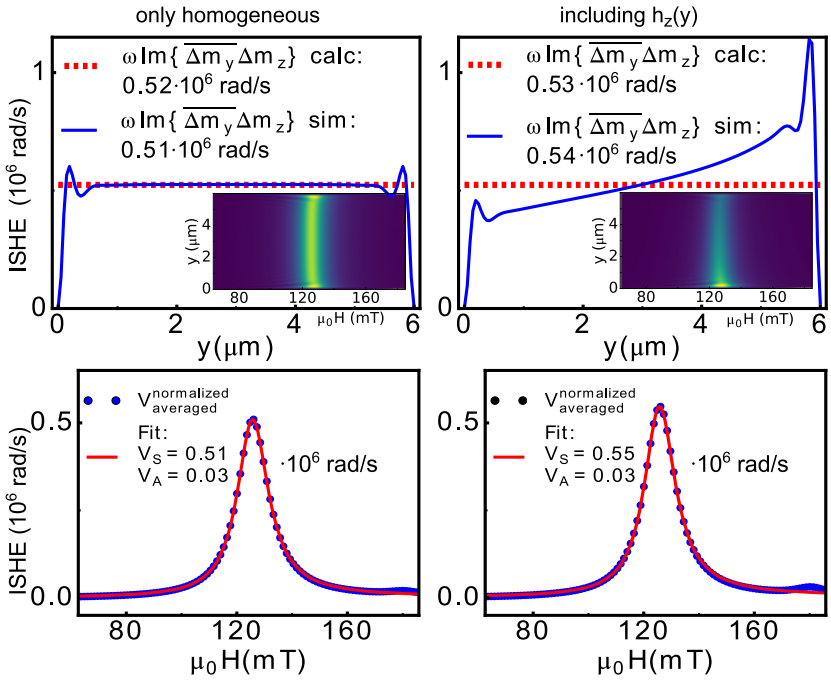

Figure 10.4.: *Impact of mode structure and inhomogeneous driving field on the simulation of an electrical measurement of the ISHE voltage at an applied field angle of* 90° *at 10 GHz. On the left side, a homogeneous driving field is used to drive the magnetization dynamics, whereas on the right side the inhomogeneous Oersted field due to the current flow in the bilayer is added. In both cases, the precession amplitude is averaged across the stripe width and compared to the macrospin calculation. In both cases, the deviation is below the experimental detection limit.*

sequently a frequency dependence of the ISHE signal is recorded. Usually, one finds large antisymmetric contributions at low frequencies that approach zero with higher frequency. In this range, the symmetric signal is used to compute the spin Hall angle. The impact of the induced current is verified to be small by angular dependent measurements.

10.2. Experiment: Angular Dependency

In the experiment, angular dependencies of the symmetric and antisymmetric voltages are measured at four distinct frequencies covering 4 to 16 GHz for every Pt thickness. Data and corresponding fits are shown for the Pt(4 nm)/Py(4 nm) sample in Fig. II.10.5. The fit reproduces the data nicely from 8 to 16 GHz, however, at 4 GHz the fit shows significant deviations from the data. This is the result of the mode structure dominating at low fields. To fit the data, Eq. (5.23) is used in combination with Eq. (5.25). In the fit

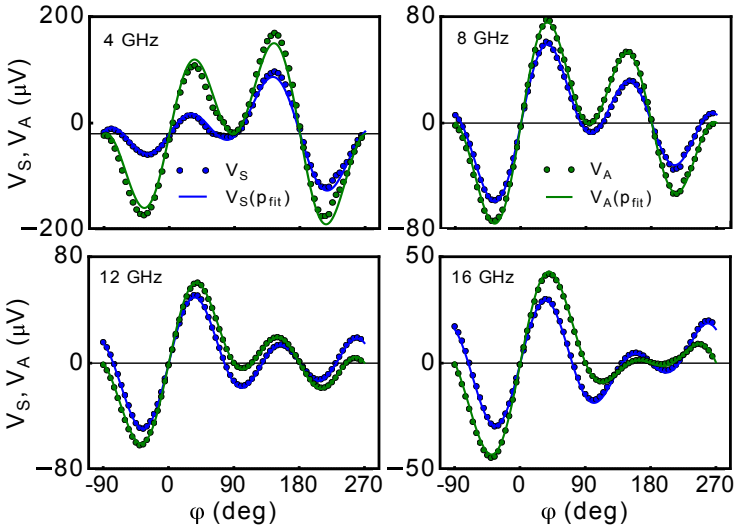

Figure 10.5.: *Angular dependence of symmetric and antisymmetric voltage amplitudes for a Pt(4 nm)/Py(4 nm) sample at different frequencies. The solid lines represent fits to Eq. (5.23). From the fit the amplitude of the induced current can be determined.*

function, I_{ind} is therefore expressed as function of V^0_{AMR} and then calculated back from the fit result for this parameter. The amplitudes A_{ij} are calculated from the susceptibility and the predetermined material parameters. In Fig. II.10.6, the extracted parameters are shown. The error bars in these plots directly represent the goodness of the fit, again showing the deviations at the lowest frequency. Additionally, the correlation coefficients $c_{i,j} = \frac{cov_{i,j}}{\sqrt{cov_{i,i} * cov_{j,j}}}$, $0 \leq |c_{i,j}| \leq 1$ are calculated from the covariance matrix cov of the fit[2]. For all samples, the correlation coefficients between the voltage amplitudes V^0_{AMR} and V^0_{ISHE} and the driving torques h_y^{eff}/I and τ_{DL}/I are quite high, up to 0.9, which indicates a strong entanglement of these four parameters. At high frequencies, the correlation decreases thus making the fit more trustful, whereas for 4 GHz all $c_{i,j} > 0.8$. This analysis indicates that the results of the angular fit should be examined critically. As already described in section II.10.1.3, the main aim of the angular measurement is to determine the strength of the induced current in order to estimate its impact on the driving field at

[2] using scipy.optimize.leastsq from the scipy package (https://www.scipy.org/) which provides the jacobian matrix

φ_{ISHE}. Panel b) shows the fit results for the induced current as a function of frequency for the particular sample. The current does not seem to have a monotonous dependence on the frequency. The inset of the panel shows the averaged values of I_{ind} for $f > 4\,\mathrm{GHz}$; the error bars here span the whole range in which the values lie. The behavior is - up to the last point - quite linear in thickness. This can be attributed to the fact that the sheet conductance scales roughly linear with thickness in this range. All in all, the values of the induced current do not exceed $\sim 0.6\,\mathrm{mA}$. As the primary driving field strength lies around 0.2 mT, the inhomogeneous Oersted field is expected to enhance the ISHE voltage by not more than $\sim 3.5\%$ (calculated by the use of Eq. (10.1)). The three other panels

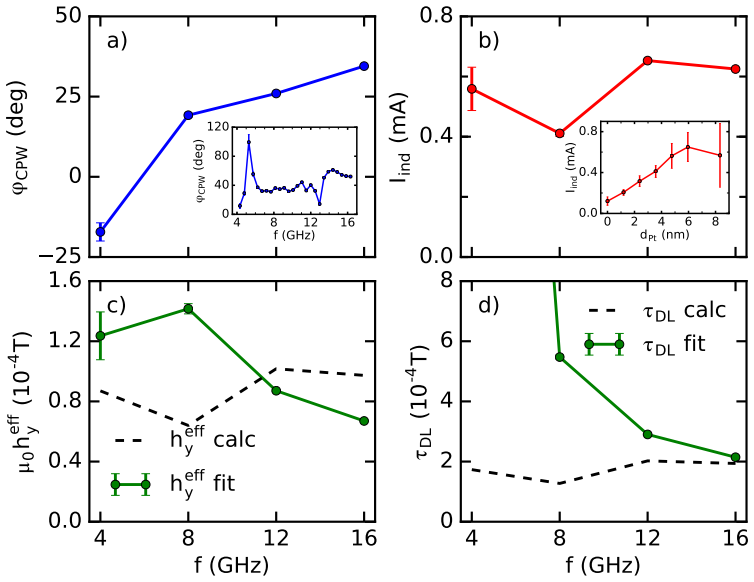

Figure 10.6.: *Parameters of the fit of the angular dependence of V_S and V_A for the Pt(4)/Py(4) sample as function of frequency. Panel a) shows the phase of the primary field with respect to the induced current. The inset shows the same data for the bare Py sample. Panel b) shows the amplitude of the induced current. In the inset, the averaged current is plotted as function of the Pt thickness for all samples. In panel c) and d), the additional driving fields obtained from the fit of the angular dependence is plotted and compared to the torques calculated from the value of the induced current and the MOD results.*

show the phase between primary driving field and induced current (φ_{CPW}) and the two additional homogeneous driving torques. The phase shows a monotonous increase with no big jumps for $f \geq 8\,\mathrm{GHz}$. This is the case for all samples and can be taken as an indicator for the clear hf transmission of the system. The inset in panel a) shows the phase of the induced current for the Py control sample without Pt underlayer. For this sample the frequency resolution is much better; here it is visible that the phase has two pronounced features around 6 and 13 GHz. As shown in the next part of the text, these features can be seen as dips in the microwave transmission in all measured samples. This implies

some kind of resonance in the CPW/ISHE strip system. These regions must therefore be excluded in the quantitative ISHE analysis. As the ratios h_y^{eff}/I and τ_{DL}/I are directly measured (for a dc current) in the MOD measurements, they can be used to check the fitting result for consistency. To do so, the torques corresponding to the fitted value for I_{ind} are calculated and plotted as black dotted lines in panel c) and d). For h_y^{eff}, the fitted and calculated values are reasonably close for the particular sample. The agreement is not that good for all other samples, however, possibly due to the entanglement with the other parameters. The fitted value for τ_{DL} diverges for low frequencies. This happens for all samples, indicating that the low frequency behavior is not well captured by the model. However, for high frequencies the fit routine seems to deliver good overall results despite the entanglement of the parameters.

10.3. Experiment: Pure ISHE

Having determined the induced current by angular dependent measurements, the next step is to perform very careful measurements of the pure ISHE voltage at $\varphi_{\mathrm{ISHE}} = 90°$. As the evaluation of the results depends on the strength of the driving field, it must be calculated and calibrated before the measurements. This is done by calculating the ratio of oop Oersted field vs rf input power h_z/P_{in} of the sample via simulations. This coefficient is then used to calculate the field in the sample from the measured effective power acting on the sample as described in [Obs15, pp. 59-62 and p. 99 ff]. The microwave power is measured directly before the sample holder using a rf powermeter and is plotted exemplary in panel a) of Fig. II.10.7 for the Pt(4 nm)/Py(4 nm) sample. Subsequently, the sample is connected and the transmitted power is measured directly after the sample holder. The difference between both measurements gives the loss across the sample, plotted in panel b). The transmission is good for most frequencies with two dips, one at low frequencies and one at 13 GHz. In the well-behaved region, the loss increases slowly to higher frequencies indicated by the straight line. In this region, it seems appropriate to calculate the power at the center of the CPW P_{eff}, shown in panel c), as the mean of P_{in} and P_{trans} due to the symmetry of the sample. The error of P_{trans} is estimated based on the deviation from the linear loss. This calculation assumes that there is no major impedance mismatch between cables, sample holder and sample such that there is no reflection of power from the sample entrance and the loss across the sample is due to real Ohmic losses along the CPW. As a last step, the effective power is converted to the driving field using the conversion factor for the used CPW. To do so, the CPW is modeled in the software SONNET and the current density distribution is calculated for a set of frequencies at a fixed input power of 10 mW. From the current density, the magnetic field is computed in the gap of the CPW and averaged across the stripe width to obtain $h_z(P_{\mathrm{eff}} = 10\,\mathrm{mW})$. The result of this

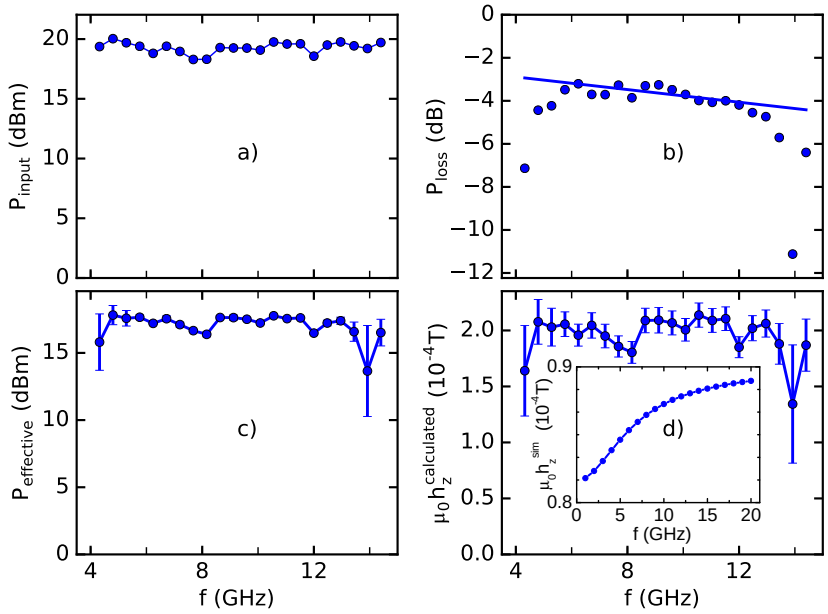

Figure 10.7.: *Power calibration and driving field calculation for a Pt(4)/Py(4) sample. Panel a) and b) show the input power and the power loss over the sample, respectively. From these values, the effective power acting at the center of the sample is calculated (panel c)). The primary driving field is calculated from the effective power by the use of a conversion factor depending on the geometry of the CPW and the frequency. This factor is plotted in the inset; the field per unit power increases slightly for higher frequencies.*

computation is shown in the inset of panel d) which itself shows the primary driving field as function of the frequency.

Having calculated the primary driving field and with the knowledge of the induced current and all required material parameters, it is possible to determine the spin Hall angle and the diffusion length from the pure ISHE voltage. To do so, φ_{ISHE} must be found from the condition $V_{\mathrm{A}}(\varphi_{\mathrm{ISHE}}) = 0$. At this angle, a frequency dependence is recorded in order to judge which frequency range allows for a quantitative evaluation of the ISHE. Due to the mode structure and the inhomogeneous internal field, the antisymmetric voltage is nonzero at low frequencies even at φ_{ISHE} as can be seen from Fig. II.10.8. The antisymmetric voltage component approaches zero (within the scattering of the data) at around 9 GHz for all of the samples. This limits the range of frequencies usable for evaluation to $f > 9\,\mathrm{GHz}$. The inset of the graph shows the behavior of V_{A} as a function of the angle around φ_{ISHE} for a fixed frequency of 12 GHz. One observes a nice monotonous dependency of the voltage on the angle and $\varphi_{\mathrm{ISHE}} = 90.5°$ for this sample. The deviation of the angle from 90° stems from the mounting of the sample and is different for every sample.

After having assured to be at the correct angle, Eq. (5.13) and Eq. (5.20) are used to normalize the ISHE voltage in order to bring it to the form of Eq. (5.14). In Fig. II.10.9 the frequency dependence of the normalized voltage for all samples is shown. Only frequencies

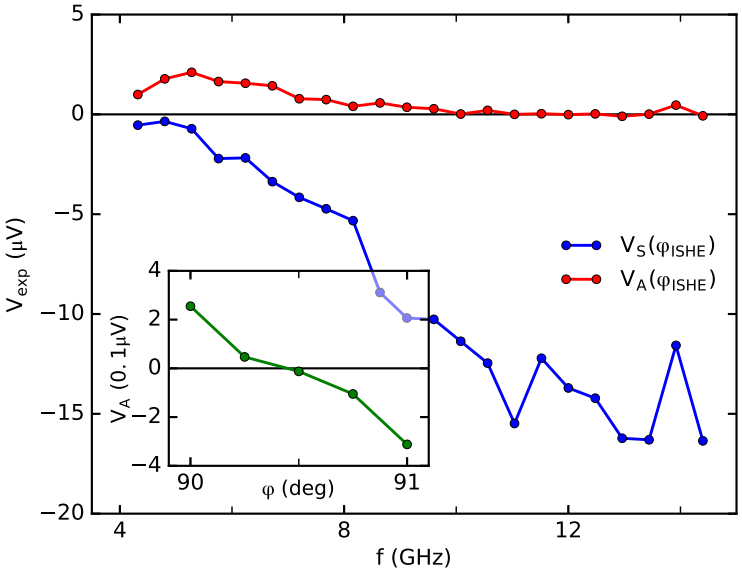

Figure 10.8.: *Measured voltages as function of frequency at φ_{ISHE}. The antisymmetric voltage goes to zero at around 9 GHz. Inset: antisymmetric voltage as function of φ around φ_{ISHE} at a frequency of 12 GHz which shows the zero crossing of V_A around this position.*

where a) the antisymmetric voltage is zero and b) the loss over the sample is smaller than 6 dB are taken into account. The error of the normalized voltages is mostly caused by

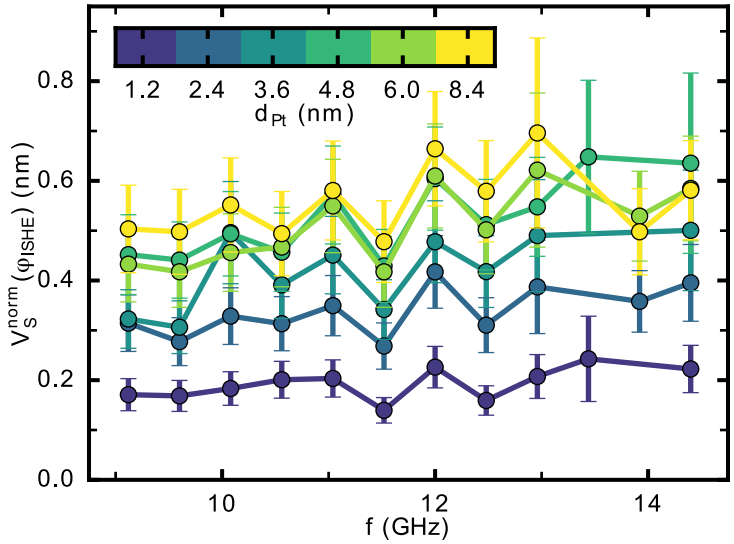

Figure 10.9.: *Fully normalized voltage as function of frequency in the range where the antisymmetric voltage is zero (within errors) and the power loss does not indicate a hf resonance of the CPW/stripe system.*

the error in the primary driving field that determines the precession amplitude of the

magnetization. The normalized voltages are then averaged over the frequency and plotted in Fig. II.10.10. The mean and errors are calculated by a Bootstrap approach[3]. The averaged values are then fitted using Eq. (5.14) in order to extract the SHA and the spin diffusion length, again using the Bootstrap method. The results are $\theta_{\mathrm{SH}} = 31\,\%$ with a

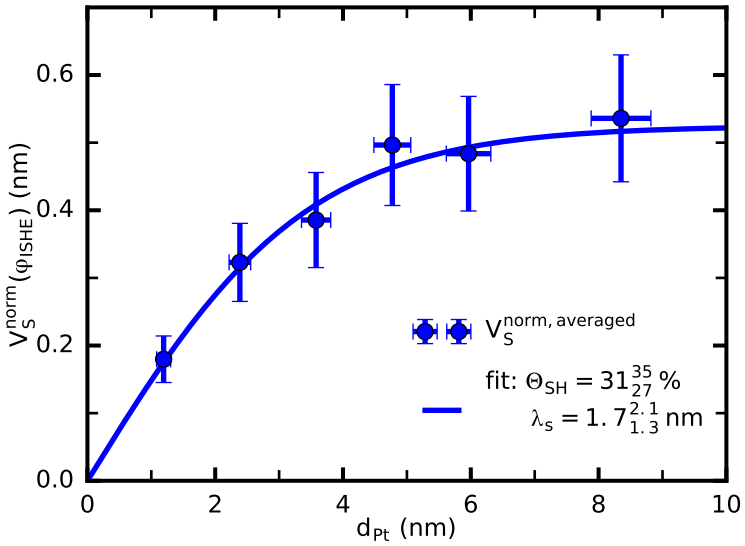

Figure 10.10.: *Fully normalized ISHE voltages averaged over frequency as a function of the Pt thickness. The solid line represents a fit to Eq. (5.14) in order to extract both the spin diffusion length λ_S and the spin Hall angle θ_{SH}. The sub/superscript numbers indicate the lower/upper limit of a 80 % confidence interval.*

80 % confidence interval of $(27-35)\%$ and $\lambda_{\mathrm{SH}} = 1.7\,\mathrm{nm}$ with a 80 % confidence interval of $(1.3-2.1)\,\mathrm{nm}$.

[3] see appendix

11. MOD: Experimental Results

11.1. Experimental Requirements

In a MOD experiment, the strength of DL and FL torque is measured by observing the shift in damping $\delta\Delta H$ and resonance field δH_{r} as a result of an applied ip current. If there are no systematic errors that distort the measurement of resonance field and damping, the strength of the SOTs exerted by the current are directly measured and therefore very well determined, as the separation of DL and FL torques is given by the different form of the respective LLG terms. This natural separation is not present in electrical measurements like ISHE and STT-FMR [Liu11], making MOD an excellent tool for the determination of SOTs.

There is one requirement, however, that is crucial when using MOD to determine the DL torque: the measured linewidth must be caused by the effective damping parameter α_{eff}, defined in Eq. (3.13), only. As the DL torque enters the LLG in the same form as the Gilbert damping, it will enter the linewidth, given by Eq. (9.2) via the replacement $\alpha \to \alpha_{\mathrm{eff}}$. If the linewidth is dominated by extrinsic effects (i.e. the zero frequency offset is large), a change in the effective damping parameter α_{eff} due to the SOT might be suppressed and not fully seen in the change of linewidth, leading to an underestimation of the SOT. This scenario is excluded for the presented Pt/Py samples by the full film FMR characterization which shows only a very small offset in linewidth.

For the special case of the presented work, it is found that there is another possible error that can hinder the measurement of the real linewidth: In narrow stripes, the mode structure can be such that two modes overlap in field and result in an artificially low linewidth, see Fig. II.6.4 and the discussion in the text. The SOT then reduces the single peak linewidth but the spacing in field remains constant which in turn leads to either a too large or too small change of the fitted linewidth. This problem can be excluded by producing a small enough mode spacing via reducing the thickness of the FM layer and by the use of a wide stripe. Micromagnetic simulations - using the sample geometry and material parameters of the real devices - show that the resulting linewidth of a simulated TRMOKE measurement reproduces the input value of the damping constant. In addition, the damping values measured on the stripes and the full film FMR values are in good agreement such that it is concluded that the standing spin waves do not influence the measurements of the SOTs.

11.2. Experimental Results

For the quantification of the SOTs as function of the ip current density, local FMR is measured using TRMOKE for a series of applied currents and the resonance field and linewidth are extracted as described in section II.4.2.3. The external field is always kept perpendicular to the stripe and every measurement is performed for both field polarities in order to verify the symmetry of the SOTs. The resonance field and linewidth as a

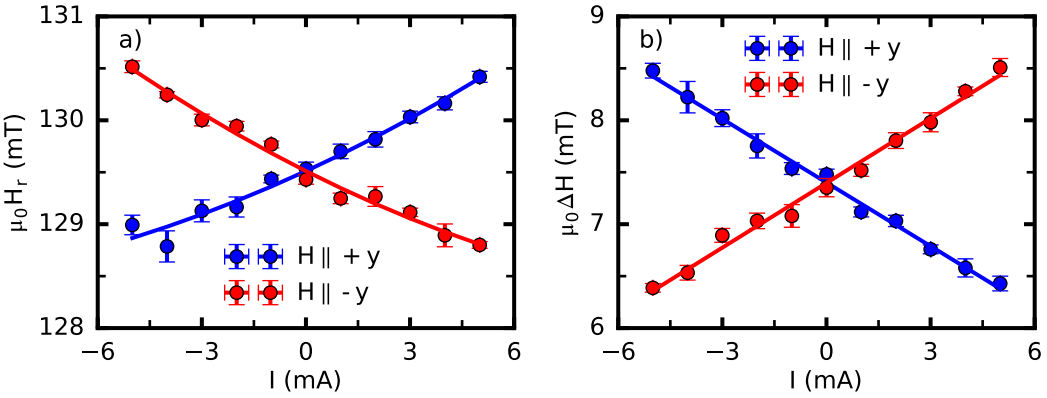

Figure 11.1.: *Current induced changes in a) resonance field and b) linewidth as measured on a Pt(4 nm)/Py(4 nm) stripe at a frequency of 10 GHz. Measurements are conducted for both current polarities and field polarities with field direction being perpendicular to the stripe.*

function of the applied current are exemplarily shown in panel a) and b) of Fig. II.11.1, respectively, for a Pt(4 nm)/Py(4 nm) sample and a frequency of 10 GHz. The two colors represent positive and negative fields, for which the shifts are expected to switch sign. The averaged current density for the largest current applied lies in the range of $\leq 1.2 \times 10^{11} \frac{\mathrm{A}}{\mathrm{m}^2}$ for every sample. At these current densities, thermal contributions are small and do not influence the outcome of the SOT measurements.
From the raw data, some important things can already be observed:

- the shift in resonance position is clearly visible and almost linear, indicating only a small thermal contribution induced by a reduction of M_{eff} .
- the field is shifted about 1.5 mT, which means the measured effect lies in the (sub) percent range compared to the resonance field.
- the change in linewidth is almost perfectly linear
- due to the low starting value for $\mu_0 \Delta H$, the shift of about 2 mT leads to a modulation of the linewidth of $\approx 30\%$

This shows the advantage of experiments where the current generated torques are used to drive the magnetization and the resulting dynamics is measured in order to extract the

SOTs (like SOT-FMR [Liu11] and SOF measurements [Che16]): a driving field/torque of 0.2 mT (one tenth of the fields measured here) already leads to a dynamic signal that can easily be measured. However, the analysis of such measurements is much harder since parasitic effects have to be excluded carefully. In this sense the MOD technique is straightforward and reliable and is only limited by the precision with which the linewidth/resonance field can be measured.

11.2.1. Field-like torque

The resonance position, plotted in panel a) of Fig. II.11.1 is influenced by two factors: the current induced linear shift, described by Eq. (4.2) and a quadratic increase due to Joule heating. To account for the latter, the resonance field is fitted using the following function, derived in [Dec12]:

$$\mu_0 H_r = \underbrace{\frac{1}{2}\left(-\mu_0 M_{\mathrm{eff}}(T_R)\left(1-\beta I^2\right) + \sqrt{\left(\mu_0 M_{\mathrm{eff}}(T_R)\left(1-\beta I^2\right)\right)^2 + 4\left(\frac{\omega}{\gamma}\right)^2}\right)}_{\approx \mu_0 H_r(I=0) + const \cdot I^2} - b_{\mathrm{FL}}\, I. \quad (11.1)$$

This equation is the Kittel equation Eq. (9.1) (without considering the weak ip anisotropy) solved for the resonance field. The temperature dependence is included by assuming a linear change in M_{eff} with temperature (around the effective magnetization at room temperature, $M_{\mathrm{eff}}(T_R)$), whereas $T \propto I^2$ due to Joule heating. The linear slope is given by $b_{\mathrm{FL}} = \frac{\delta\mu_0 H_{r,I}}{I}$. For the current densities used $\beta \approx 0$ and the change in M_{eff} is $\leq 0.1\%$ for all samples. The results for the fitted b_{FL} values are shown in Fig. II.11.2. Panel a) shows

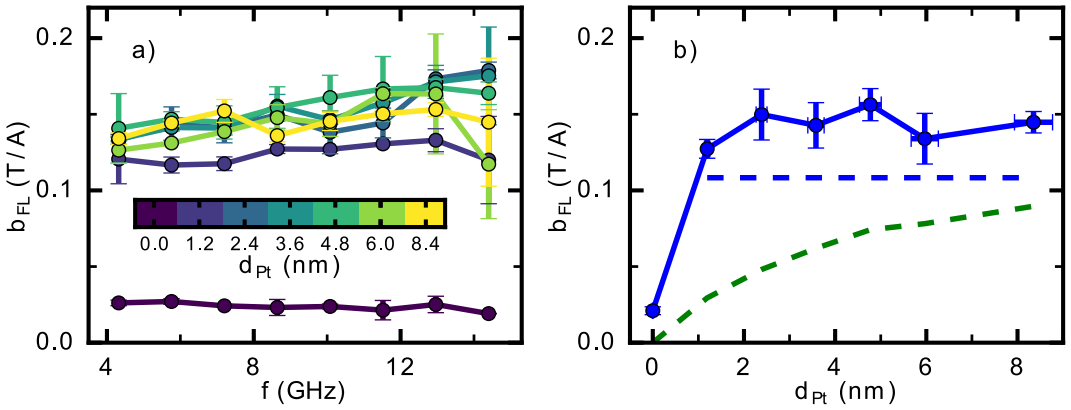

Figure 11.2.: *Field-like torque per unit current as determined by the resonance field shift. a) Frequency dependence of the ratio for different Pt thicknesses. b) Averaged ratio as function of the Pt thickness (blue symbols). The blue dashed line represents an absolute upper bound for an Oersted field that is created by the current flow solely through the Pt layer. The green dashed line shows a more realistic estimation of the Oersted field contribution based on the two resistor model.*

the frequency dependence for all samples. The fitted value can be regarded as constant over a very wide range of frequencies. The averaged values are then plotted as function of d_{Pt} in panel b). In order to check if the measured strength of the field-like torque can be explained by the current induced Oersted field alone, the following estimation is made [Emo16]: the Oersted field is calculated by Eq. (2.2) under the assumption that all of the current flows in the NM such that $b_{\mathrm{Oe,max}} = \frac{\mu_0}{2w} \approx 0.1\,\frac{\mathrm{T}}{\mathrm{A}}$. This value is indicated by the blue dotted line in panel b). It is clear that there must be an additional effect which might be caused by either the SHE via the imaginary part of the SMC, see Eq. (2.25) or a Rashba type effect, see Eq. (2.17). The above estimation, however, is very unrealistic for the Pt samples having a low thickness, therefore the green dotted line shows the current generated Oersted field effect computed by assuming a current density distribution based on the conductivities of Pt and Py.
In either case, the interfacial origin of the effect suggests a scaling with the inverse of the magnetic moment per area such that in the following an effective conversion efficiency $\theta_{\mathrm{FL}}^{\mathrm{eff}} = \frac{\tau_{FL}}{j_{\mathrm{N}}} \frac{2e}{\hbar} M_{\mathrm{s}} d_{\mathrm{F}}$ is introduced in order to compare the strength of field and damping-like torque. The result of this normalization is plotted in Fig. II.11.4 and discussed below. From the raw data the different strength of the effects on the two different wafers is visible. This suggests that part of the torque is indeed of interfacial nature.

11.2.2. Damping-like torque

The change in linewidth is given by Eq. (4.1). Due to the presence of the resonance field in the denominator, the raw slope shows a frequency dependence. By normalizing on the resonance field and M_{eff} the torque per current ratio can be calculated and compared to the field-like torque. Again, the torque is constant over the whole frequency range, as can be seen in panel a) of Fig. II.11.3. The averaged values are shown in panel b) in blue. For comparison, the field-like torque is added in green. Due to the fact that the Oersted field contribution increases with increasing thickness, the field-like torque is expected to saturate, whereas the damping-like torque is expected to go to zero for large thicknesses. The trend seen in the data therefore fulfills the expectation. From the raw torques, the effective conversion efficiencies are calculated via Eq. (2.25) which are valid in the drift diffusion model. The calculation involves the conversion of the measured current into the (homogenous) current density flowing in the NM, $j_{\mathrm{N}}^{\mathrm{c}}(I_{\mathrm{meas}})$. This calculation is performed by the use of the parallel resistor model. In both layers, a homogeneous current density distribution is assumed that is given by the measured conductivity of the respective layer. In Fig. II.11.4, the effective SHA/conversion efficiencies are shown for different assumptions for the conductivity ratios of Pt and Py. The blue symbols show the effective SHA for the case of the thickness-dependent, measured Pt conductivity. The red symbols are calculated assuming a constant conductivity of both Py and Pt for

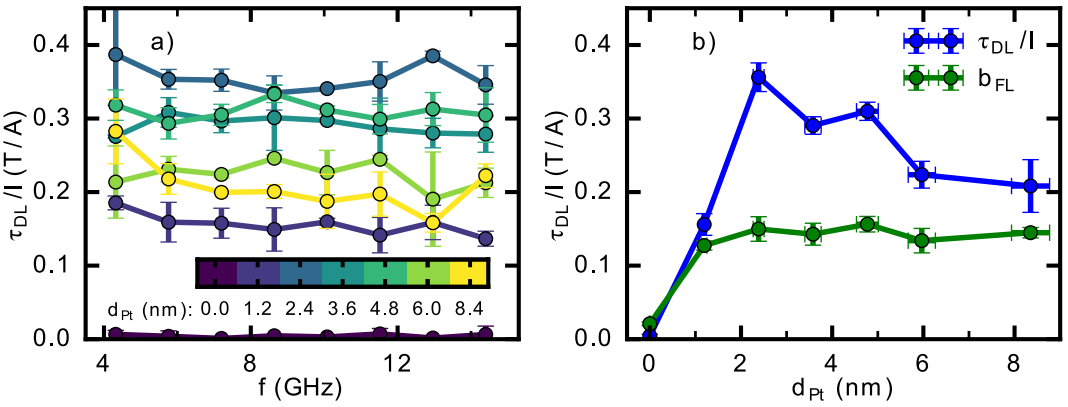

Figure 11.3.: *Damping-like torque as function of applied current. a) The measured torque per current ratio is flat as function of the frequency for all samples. b) Averaged damping-like torque as function of the Pt thickness (blue symbols) in comparison to the field-like torque (green). The DL torque/current ratio has a maximum at 2 nm and then decreases with thickness due to current shunting in the Pt. In contrast, the field-like torque saturates due to the contribution of the Oersted field.*

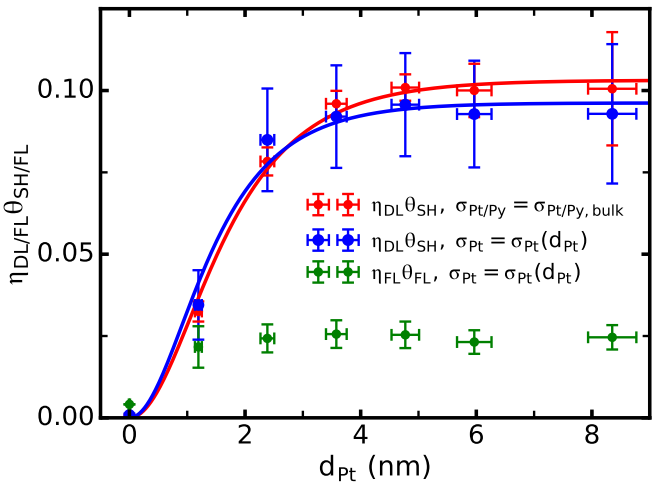

Figure 11.4.: *Effective SHAs obtained from the torque/current ratios. The red symbols represent the damping-like torque and are calculated by taking the bulk values for the respective conductivity. By contrast, the blue symbols are calculated by using the thickness-dependent Pt conductivities. The green symbols are computed by normalization of the field-like torque (Oersted field contribution subtracted) in the same fashion. The red and blue solid lines are a fits of the respective data to Eq. (2.28).*

comparison; the ratio of the conductivities is taken to be the ratio of the bulk values of $\sigma_{\mathrm{Pt}} = 9.1 \times 10^6 \frac{1}{\Omega\,\mathrm{m}}$ and $\sigma_{\mathrm{Pt}} = 6.7 \times 10^6 \frac{1}{\Omega\,\mathrm{m}}$ such that $\frac{\sigma_{\mathrm{Pt}}}{\sigma_{\mathrm{Py}}} \sim 1.36$. The same normalization is applied to the field-like torque in order to show the respective strength of both torques. The field-like, Oersted-field-corrected torque is much smaller than the damping-like one. This is expected when comparing to the literature values for FM layers of $d_{\mathrm{FM}} > 1\,\mathrm{nm}$ [Pai15; Ngu16; Ski14; Liu12a]. The normalization on the Pt current density, however,

makes sense only if the bulk SHE is assumed as the source of the measured FL torque, see section I.2.5. Any Rashba like effect rather scales with the current density at the interface/the current density within the FM itself [Ski14; Fan13; Pai15; Ou16; Emo16]. To make a valuable statement about the origin of the field-like torque therefore requires the measurement of a Py thickness dependence which is beyond the scope of this work.
Under the assumption of a transparent interface, the conversion efficiency $\eta_{\mathrm{DL}}\theta_{\mathrm{SH}}$ can be fitted using Eq. (2.28); the result of the fit belonging to the red/blue symbols is indicated by the red/blue line. By comparing the two fit curves it is clear that there is no big difference between the two methods for current density calculation. The value obtained from the blue curve for the effective SHA is $\theta_{SH}^{\mathrm{eff}} = 0.96 \pm 0.03$ where the error is obtained from the goodness of the fit. Fitting of the red symbols results in a value which is only 7% larger and therefore both results agree within the error bar. A larger difference is found for the spin diffusion length which is $\lambda_{\mathrm{s}} = (1.0 \pm 0.1)\,\mathrm{nm}$ for the blue curve and $\lambda_{\mathrm{s}} = (1.2 \pm 0.1)\,\mathrm{nm}$ for the red curve. These values can be compared to literature values in which the finite interface transparency is not included. In order to take the interface transparency into

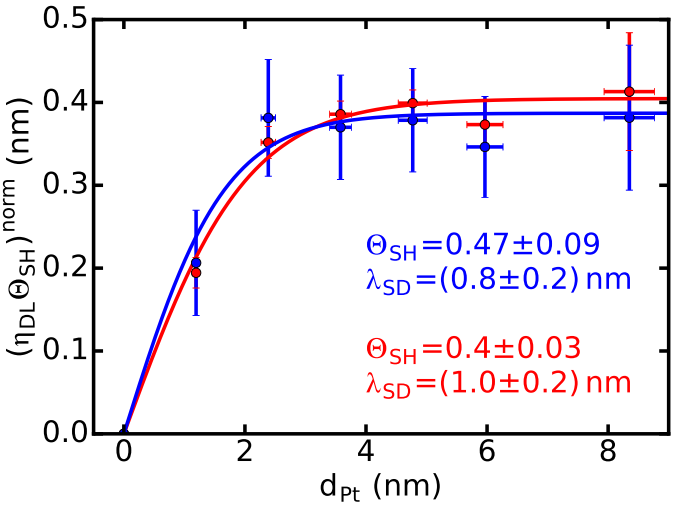

Figure 11.5.: *Normalized conversion efficiencies and spin Hall fits. For the blue symbols, the current density distribution is computed from the varying, measured Pt conductivity. For the red symbols, a constant Pt and Py conductivity, equal to the bulk value, is assumed. The solid lines represent the best fit to Eq. (2.31) for both cases.*

account, the dampling-like conversion efficiency is finally normalized to the effective SMC and fitted using Eq. (2.31) to obtain both the pure SHA and the spin diffusion length. The results of this procedure are shown in Fig. II.11.5. It should be noted here that the conductivity value entering the left side of Eq. (2.31) is the bulk conductivity of Pt and is therefore independent of the thickness. The varying conductivity only affects the current density distribution and therefore the value of $\eta_{\mathrm{DL}}\theta_{\mathrm{SH}}$ as described above. Panel a) shows the normalized conversion efficiency corresponding to the blue symbols in Fig. II.11.4

(current density from measured conducitvities). In panel b) the values correspond to the red symbols in Fig. II.11.4 (current density from constant conducitvities). The errors of the fit parameters given in the graph are obtained from the goodness of the fit as described in IV.A. The bulk conductivity used in the normalization (Eq. (2.31)) is set to $\sigma_{\mathrm{Pt}} = 7.3 \times 10^6 \frac{1}{\Omega\,\mathrm{m}}$ determined in section II.9.4. It is noted that again the data points obtained by the two different computation methods do not differ much and even coincide within the error bars. However, the point at $d_{\mathrm{Pt}} = 2.4\,\mathrm{nm}$ is shifted up by using the thickness-dependent conductivity (blue) compared to the corresponding red point. This particular datapoint dominates the outcome of the fit because it leads to a shorter spin diffusion length. The corresponding SHA in turn goes up due to the fact that the prefactor in Eq. (2.31) contains the product of SHA and spin diffusion length. Consequently, both products $\Theta_{\mathrm{SH}}\lambda_{\mathrm{s}} = (0.38 \pm 0.02)\,\mathrm{nm}$ and $\Theta_{\mathrm{SH}}\lambda_{\mathrm{s}} = (0.40 \pm 0.01)\,\mathrm{nm}$ coincide within the error. If a result for both θ_{SH} and λ_{s} should be given, a confidence interval of $\theta_{\mathrm{SH}} = 0.4 - 0.5$ seems to be adequate and similar, for the spin diffusion length, $\lambda_{\mathrm{S}} = (0.8 - 1.0)\,\mathrm{nm}$. These values are compared to the results of spin pumping and ISHE as well as to literature values in the following section.

It shall be noted that the fit result for the SHA depends linearly on the conductivity σ^0_{Pt} which is again caused by the form of the prefactor of Eq. (2.31).

12. Discussion of SP, ISHE and MOD Results

In this section, the final results obtained within the drift diffusion model are compared to each other and to literature values obtained from similar experimental approaches. When doing so, it has to be differentiated between the methods used to determine the key parameters θ_{SH} and λ_{S} as already discussed in sect. II.1. In spin pumping and ISHE experiments, the finite transparency of the NM/FM interface, described by the SMC, is always included in the analysis. Therefore, SHAs determined via ISHE always correspond to the intrinsic SHA of the NM. In STT experiments which use a current created torque to quantify the above parameters, often the SHA is computed under the assumption of a transparent interface, resulting in $\theta^{\mathrm{eff}} < \theta_{\mathrm{SH}}$.
Table 12.1 shows the confidence intervals for spin diffusion length and SHA obtained by spin pumping, ISHE and MOD as discussed in the respective evaluation part.

	spin pumping	ISHE	MOD
θ_{SH}	–	$0.31^{0.35}_{0.27}$	$0.45^{0.5}_{0.4}$
λ_{S} (nm)	$2.1^{2.3}_{1.9}$	$1.7^{2.1}_{1.4}$	$0.9^{1.0}_{0.8}$
$\theta_{\mathrm{SH}}\lambda_{\mathrm{S}}$ (nm)	–	$0.54^{0.59}_{0.49}$	$0.39^{0.41}_{0.36}$
$\theta^{\mathrm{eff}}_{\mathrm{SH}}$	–	–	$0.1^{0.11}_{0.09}$
$\lambda^{\mathrm{eff}}_{\mathrm{S}}$ (nm)	–	–	$1.1^{1.2}_{1.0}$
$\theta^{\mathrm{eff}}_{\mathrm{SH}}\lambda^{\mathrm{eff}}_{\mathrm{S}}$ (nm)	–	–	$0.12^{0.13}_{0.11}$
$\mathfrak{Re}\left\{\tilde{g}^{\uparrow\downarrow}\right\}$ $(\times 10^{19}\frac{1}{\mathrm{m}^2})$	$5.3^{6.1}_{4.5}$	–	–

Table 12.1.: *Confidence intervals for: bare SHA θ_{SH}, λ_S and $\mathfrak{Re}\left\{\tilde{g}^{\uparrow\downarrow}\right\}$ as obtained from MOD, ISHE and SP within the full drift diffusion model; values obtained for the effective SHA θ^{eff} and the corresponding spin diffusion length λ_S^{eff} obtained from MOD by assuming a transparent interface. Sub and superscript numbers represent the lower and upper limit, respectively.*

The first result that strikes the eye is the very high value for the SHA of 30 to 45%. However, when taking into account the finite interface transparency, similar values of 20–30% have been reported recently [Pai15; Zha15b; Nan15]. It is noted in [Pai15], however, that

these values appear to be quite high compared to theoretical calculations of bulk SHAs, see the values given below. The transparency of the NM/FM interface for a spin current can be defined by $T_{\mathrm{int}} = 2\frac{e^2}{h}\mathfrak{Re}\left\{\tilde{g}^{\uparrow\downarrow}_{\mathrm{eff,sat}}\right\}\frac{\lambda_{\mathrm{S}}}{\sigma_N}$. This result is obtained by setting $d_{\mathrm{NM}} \gg \lambda_{\mathrm{S}}$ in Eq. (2.30). For the Pt/Py layers of this work $T \sim 0.25$, in accordance with similar values obtained recently [Zha15b; Pai15]. This means that previously reported SHAs (under the assumption of a transparent interface) are underestimated by a factor of up to four when compared to intrinsic values and would be corrected up into the same region of the values given above. For the MOD experiment, the large SHA is therefore a direct result of the extended model used for the evaluation of the data.

This argument is corroborated by the fact that the spin Hall angle obtained by the use of the transparent interface model $\theta^{\mathrm{eff}}_{\mathrm{SH}}$ does lie within reported values which, however, scatter a lot (from 0.05 to 0.12 in [Kas14; Liu11; Nan15; Bos17]). In this sense, the (effective) SHA obtained in this work lies well within the expected range.

The same is true for the spin diffusion length, which is short and lies between $(0.9-2.1)\,\mathrm{nm}$ in all three experiments which is in the range of $(0.7-3.7)\,\mathrm{nm}$ as found in [Kas14; Boo15; Zha15b; RS14; Aze11]. The spin diffusion length obtained from SP thereby coincides with the ISHE result (within the error bars) whereas the MOD result is significantly shorter.

In this sense it can be concluded that, within the drift diffusion model, SP, MOD and ISHE experiments result in comparable values of the two main parameters. In [Nan15], MOD and ISHE experiments have been compared in a similar way as presented here, but only one Pt thickness (4 nm) has been studied. By assuming one fixed value for λ_{s} for both cases, the two experiments give comparable results which has been claimed to confirm the reciprocity of MOD and ISHE.[1]. However, in the present work, the Pt thickness dependence allows for a more differentiated evaluation. As a result, the MOD experiment shows a quicker saturation with respect to d_{Pt} and therefore leads to a lower spin diffusion length and a larger SHA compared to the ISHE.

In [RS14] and [Wan14], it is argued that the variation in θ and λ_{SD} comes from the fact that both parameters are correlated in the equation used to compute θ_{SH}. This leads to an error when e.g. taking a literature value of λ_{SD} in order to compute the SHA. Only the product of both quantities should be compared and is believed to lie around $\theta_{\mathrm{SH}}\lambda_{\mathrm{S}} = 0.18\,\mathrm{nm}$ and $0.13\,\mathrm{nm}$, respectively[2]. The value of this product, however, does depend on the transparency of the interface as can be seen from the fact that the value of $\theta^{trans}_{\mathrm{SH}}\lambda^{trans}_{\mathrm{S}} = 0.12\,\mathrm{nm}$ from this work lies well within this range, whereas the $\theta_{\mathrm{SH}}\lambda_{\mathrm{S}} = (0.4-0.5)\,\mathrm{nm}$ is much larger. As described below, the idea of a constant product does also have a physical reason, which is of course only valid for the bare SHA.

[1] interestingly, at $d_{\mathrm{Pt}} = 4\,\mathrm{nm}$ the normalized ISHE/MOD data obtained in this work lie very close together at 0.4 nm such that, by assuming a common λ_{s} and only taking this thickness into account, the same conclusion could be drawn.

[2] This argument, however, does not hold for STT experiments if the transparent interface model is used and if $d_{\mathrm{Pt}} \gg \lambda_{\mathrm{s}}$ because then $\eta \approx 1$ and $\theta^{\mathrm{eff}}_{\mathrm{SH}}$ does not depend on the exact value of λ_{s} used.

Indeed, the product $\theta_{SH}\lambda_S$ is larger in the ISHE experiment compared to MOD, opposite to the behavior of the SHA. This is a result of the fast saturation of the normalized MOD conversion efficiency at $d_{Pt} = 2.4\,\text{nm}$ (see Fig. II.11.5) compared to a saturation thickness of the normalized ISHE voltage around 5 nm, see Fig. II.10.10.

In table III of [Sin15], a collection of values for λ_S and θ for Pt, obtained by different methods, can be looked up. It is found that SHE experiments can be divided into two classes, one in which a FM is directly attached to the Pt layer (MOD, ISHE, SP etc.). Experiments of this class often result in short diffusion lengths between $(1-3)\,\text{nm}$. In the other class of experiments, the spin diffusion in pure Pt stripes is measured using nonlocal measurement schemes (see e.g. [Sin15] for a description). In these experiments, the determined diffusion lengths are much larger, around 10 nm. A recent experiment, in which the spin accumulation is optically probed in the Pt, again without contact to a FM comes to the same conclusion and a spin diffusion length of $\lambda_S = 11\,\text{nm}$ is measured [Sta17]. This fact shows that the NM/FM interface plays an important role in high-quality metallic bilayers.

There are two main effects that are discussed in this context: a) spin memory loss (SML) and b) proximity polarization of the Pt at the interface.

SML has been introduced in the context of SOT measurements in 2014 [RS14] and since then is subject of discussion. In the original publication, SP enhanced damping and ISHE results have been compared to each other. It has been found that the spin diffusion length obtained from SP is much shorter than obtained from ISHE. From this fact it has been concluded that the enhancement of damping saturates quickly not only due to spin relaxation within the bulk of the NM but immediately at the interface. The spin current that passes the interface then relaxes in the NM according to the bulk NM spin diffusion length and therefore the ISHE scales with the bulk λ while SP saturates quicker due to SML at the interface. In the presented study, no significant difference is found in the values for λ_{SD} between SP and ISHE experiments. If so, the observed difference would even be opposite, which suggests that SML might not be very important in the presented case. Mathematically, SML is introduced into the spin drift diffusion equation by a fictitious interface layer that absorbs part of the passing spin current and is characterized by the spin flip parameter $\delta = \frac{d_I}{\lambda_I}$ with the thickness and spin diffusion length of the interface layer. SML at the interface therefore also applies to STT experiments like MOD [RS14] where it influences the spin injection efficiency/interface transparency. A full equation equivalent to Eq. (2.29) including SML can be found in [Pai15]. As a result, a nonzero SML leads to an underestimation of the SHA from such measurements. As the obtained value for the SHA in this work is quite high, a sizeable SML again seems unrealistic.

The second effect often discussed is the fact that Pt has a high paramagnetic susceptibility and therefore exchange coupling leads to an induced magnetic moment in the first few Pt

layers attached to the FM [Wil00; Cam16]. In [Cam16], it has been shown that the form of the increase in damping for $d_{\mathrm{Pt}} < 2\,\mathrm{nm}$ differs for Pt/Py and Pt/Cu/Py layers, which is attributed to the finding that a) Pt in Pt/Py is polarized at the interface and b) the Cu layer suppresses this polarization while not influencing SP in general. This result has been used to call for a generalized model of SP because "In standard SP theory [Tse05] possible induced moments in N are supposed to be *a priori* included in calculations of the spin-mixing conductance $g^{\uparrow\downarrow}$ of a F|N interface [Bra00; Zwi05] which tends to be insensitive to their presence" [Cam16]. It is generally seen that the insertion of a Cu spacer between NM and FM reduces the increase in damping/the measured STT and is ascribed to a reduction of the effective SMC [Nan15; RS14; Zha15b]. In this sense, magnetic proximity supposedly plays a role in the strength of the interfacial effects. However, a Cu insertion layer reduces the effective conversion efficiency and is therefore unfavorable since for any practically usable device a high $\theta_{\mathrm{SH}}^{\mathrm{eff}}$ is needed.

One open question arising during the presented work is how the thickness-dependent conductivity fits into the drift diffusion model.

Recently, some groups also reported varying conductivities in thickness-dependent studies and different models have been used in order to improve the drift diffusion model. In [Cas12], it was first noticed that the resistivity showed a clear nonlinear behaviour in ISHE measurements on Pt/YIG layers but no model was presented to evaluate the data.

In [Ngu16], a strong variation of the Pt resistivity with thickness was found and an extension to the drift diffusion model has been constructed to evaluate STT-FMR data, based on the idea of a simple rescaling of the Pt thickness. The assumption made in this model is a) the Elliot-Yafet mechanism causes the spin relaxation in Pt, which leads to $\lambda_{\mathrm{S}} \propto \sigma_{\mathrm{Pt}}$ and b) the Hall effect is of intrinsic origin, i.e. $\theta_{\mathrm{SH}} = \frac{\sigma_{xy}^{\mathrm{int}}}{\sigma_{\mathrm{Pt}}}$. Therefore, $\lambda_{\mathrm{S}}\theta_{\mathrm{SH}} = const$ and it is possible to rescale the Pt thickness using the respective conductivity for each sample. The intrinsic spin Hall conductivity found is $\sigma_{xy}^{\mathrm{int}} = 2.95 \times 10^5\,\frac{1}{\Omega\,\mathrm{m}}$ and $\frac{\lambda_{\mathrm{S}}}{\sigma_{\mathrm{Pt}}} = 0.8 \times 10^{-15}\,\Omega\,\mathrm{m}^2$. These values convert to $\theta_{\mathrm{SH}} = 0.04$ and $\lambda_{\mathrm{S}} = 5.8\,\mathrm{nm}$ for the bulk conductivity found in this work ($7.3 \times 10^6\,\frac{1}{\Omega\,\mathrm{m}}$). Another study shows how the measured SOT parameters change with varying Pt resistivity by employing different evaporation methods at constant Pt thickness [Sag16] using a nonlocal measurement technique at low temperatures. The findings corroborate the E-Y relaxation mechanism and give $\frac{\lambda_{\mathrm{S}}}{\sigma_{\mathrm{Pt}}} = 0.6 \times 10^{-15}\,\Omega\,\mathrm{m}^2$ ($\rightarrow \lambda_{\mathrm{S}} = 4.4\,\mathrm{nm}$) in good agreement with the above experiment. In addition, the transition from the intrinsic to the extrinsic regime of the SHE can be observed at high conductivities ($\sim 1 \times 10^7\,\frac{1}{\Omega\,\mathrm{m}}$ at 10 K). The intrinsic Hall conductivity found in this study, however, is $\sigma_{xy}^{\mathrm{int}} = 1.6 \times 10^5\,\frac{1}{\Omega\,\mathrm{m}}$ ($\leftrightarrow \theta_{\mathrm{SH}} = 0.04$) and therefore much smaller than the STT-FMR result.

In sharp contrast to these findings, both [Jia13] (ISHE) and later [Boo15] (spin pumping) have recently evaluated data with a drift diffusion model that assumes a constant λ_{S} and a varying conductivity. In [Boo15], it has been pointed out that this is formally equivalent

to the Dyakonov-Perel [Dya71c] spin relaxation mechanism (see for example sec. II of [Mow11] and the references therein). The main implication is that, in contrast to E-Y where $\lambda_s \propto \sigma$, Dyakonov-Perel predicts $\lambda_s \propto \frac{1}{\sigma}$. It has been found that these models fit the data best although the physical meaning of a D-P like relaxation in Pt is questionable as the Dyakonov-Perel mechanism requires broken inversion symmetry [Boo15]. Short values for $\lambda_S < 2\,\mathrm{nm}$ are found in both cases.

In this context, the results obtained in this work are quite interesting: Although it is believed that the bulk conductivity of Pt is quite large, which would give rise to a low bulk SHA from theory, the results of ISHE and MOD including the interface transparency result in very high values for θ_{SH}. This again points towards a non-negligible contribution from a pure interface effect, which becomes more important when treating thin samples with high quality and large mean free path. In none of the above experiments it has been tried to understand the origin of the decrease in conductivity for the thin layers, although it is assumed that it is of interfacial nature.

If interface scattering becomes more important, spin orbit coupling at the interface might dominate over bulk effects as the interface contribution can be much larger than the bulk contribution [Wan16]. Recently, the effect of SML has also been attributed to interface spin orbit coupling [Che15]. The current density directly at the interface thereby strongly depends on the details of the scattering contributions as discussed in section II.7.4.

A recent published work tackles the existence of interfacial SOC by extending the bulk drift diffusion equations [Ami16a; Ami16b] but naturally does not take inhomogeneous current densities into account. In addition, a similar formalism is needed in order to describe the ISHE experiment in order to allow for a comparison of complementary measurements. In that sense, further theoretical and experimental work is required to disentangle the contributions of bulk and interface for both NM and FM. This seems to be especially important regarding the fact that in applications like spin orbit torque switching, the FM layers usually consist of only a few monolayers of material [Gar13; Gar14; Bau17; Dec17], i.e. the FM cannot be described using bulk properties at all.

13. Summary

In conclusion, the spin Hall effect in Pt is studied by using two complementary methods, namely modulation of damping (MOD) and inverse spin Hall effect (ISHE) measurements. Both experimental results are evaluated within a common drift diffusion model under the assumption that the bulk SHE is the source of the damping-like torque in the MOD case and the conversion of spin and charge current in the ISHE case.

Within the thesis, a complete model for the angular dependence of ISHE and AMR voltages is derived, which allows to quantify the induced current and to estimate the impact of this current on the pure ISHE signal. From the measured angular dependent voltage amplitudes, it is verified that the current induced increase of the ISHE signal is negligible.

The effect of standing spin waves on MOD/ISHE measurements in micro stripes is studied by numerical methods and it is shown that, in order to obtain reliable results, the stripe width must be large enough. In particular, it is shown that for the sample geometry used in this work ($w = 6\,\mu\text{m}$ and $d_{\text{FM}} = 4\,\text{nm}$), the effect of the SSWs on the ISHE and MOD is small enough to be neglected.

The measurements are performed on MBE-grown Pt(x)/Py(4 nm)/Al_2O_3 multilayer structures for varying Pt thickness. Careful electrical and magnetic characterization proves the high quality of both Pt and Py films and allows for a consistent normalization of the measured SHE/ISHE data. A bulk conductivity of $\sigma^0_{\text{Pt}} = 7.3 \times 10^6 \frac{1}{\Omega\,\text{m}}$ is found from a thick, single crystalline sample. For thin layers, the Pt conductivity is found to vary with thickness, which is attributed to additional scattering sources such as interface and grain boundary scattering, although a consistent disentanglement of different scattering sources by using the Boltzmann transport equations is not possible.

It is found that, although the general trend of both MOD and ISHE data is similar, the results obtained by the two methods do not show exact reciprocity of SHE/ISHE, indicating the importance of inclusion of interface-generated torques into the drift diffusion model in the future. Nevertheless, a very large SHA of $\theta_{\text{SH}} = 0.3 - 0.45$ is found for Pt in this work.

Part III.

Time Resolved Measurements of the Spin Orbit Torque Induced Magnetization Reversal in Pt/Co Elements

The third part of the presented work is dedicated to the switching of perpendicularly magnetized (PMA, after perpendicular magnetic anisotropy) $Pt/Co/Al_2O_3$ elements via in-plane current induced spin orbit torques. The results presented in this part have been published in [Dec17].

Since the first experimental demonstration of current induced switching in 2011 [Mir11], a lot of work has been done in order to understand the physics of the process and to optimize this switching mechanism towards applicability [Mir11; Liu12a; Avc12; Lee13; Emo13; Gar14; Cub14; Bi14; Lee14b; Lee14a; Tor15; Yu14b; Leg15; Zha15a; Dur16; Fuk16; Li16]. In particular, the application aspects of SOT induced switching have been adressed by improving thermal stability of the device [Wu16] and to investigate the possibility of field-free switching [Yu14b; Tor15; Fuk16; Kon16].

However, to this date, the exact switching mechanism as well as the physical origin of the SOTs that drive the process are still under debate. The possible sources are again the SHE and the Rashba effect which is likely to be strong due to the extremely low thickness of the FM layer. The SOT driven reversal of PMA elements has therefore been extensively studied in order to understand the switching process in the static or quasi-static current limit [Mir11; Liu12a; Emo13; Lee13; Lee14a; Yu14a; Dur16]. These experiments are capable of determining the symmetry of the SOTs and also result in switching phase diagrams but obviously cannot provide a direct description of the dynamics of the switching process itself.

From the theoretical side, there are two different models that are commonly used in order to compute e.g. critical switching currents in the static limit: a macrospin model [Lee13] and a model that incorporates the nucleation and subsequent propagation of domain walls [Liu12a]. These two models result in critical current densities that differ by orders of magnitude simply due to the fact that the energy barrier that has to be overcome is much lower for the latter case. Both models, in addition, require the implementation of a finite temperature in order to describe the statistical nature of switching in a dc limit. The applicability of the two different models depends on the device size: the macrospin model is found to be valid if the lateral dimensions of the sample are in the 10 nm range (in the range of the size of a domain wall) [Zha15a]. If the sample dimensions get bigger, the switching process is believed to follow the domain wall model [Zha15a; Liu12a; Emo13; Lee14b; Dur16]. The question arises, what happens if the current is no longer applied in dc mode (or in long pulses) but if the pulse duration is lowered to reach the ns regime [Avc12; Cub14; Gar14; Zha15a]. It turns out that, although the critical current density rises with decreasing pulse width, switching of a PMA element is possible down to a pulse width of 180 ps [Gar14]. In this experiment, the magnetization has been probed electrically in a dc measurement after current pulse application such that the dynamics can only be accessed indirectly.

A detailed understanding of the process therefore requires temporal and spatial resolution. Both requirements are met by a TRMOKE based pump probe experiment which is for the first time presented in this work. The trajectory of the magnetization of a PMA element is probed as a function of time during the magnetization reversal. By comparing the experimental data and micromagnetic simulations, the importance of the two different SOTs (damping- and field-like) as well as the Dzyaloshinskii-Moriya interaction (DMI) is pointed out.

In order to obtain PMA in NM/FM/oxide structures, the FM layer is kept ultrathin, $\sim 0.5\,\mathrm{nm}$, which may lead to a perpendicular easy axis (see section I.1.2.5) and large damping-like and field-like SOTs due to the dominating influence of interface effects. As a side result, in Pt/FM systems, the effective Gilbert damping parameter α is of the order of $0.1 - 0.5$ for Pt/Co/oxide stacks [Mik15; Miz10]. Recently, it has been found that in such thin FM layers sandwiched between NM and oxide layers, the symmetry breaking leads to the appearance of the (interfacial) DMI which is described in section I.1.2.2. Since DMI favors spiral-like magnetization textures, it leads to a reduced domain wall energy and thus influences the ground state [Mei17] as well as the dynamics of the FM [Mik15].

1. SOT Induced Switching of Perpendicularly Magnetized Elements

The general idea of SOT induced switching of a perpendicularly magnetized element relies on the current created damping-like torque $\boldsymbol{T}_{\mathrm{DL}}$ (as defined in Eq. (1.20)) in combination with a small applied ip field that breaks the symmetry of the magnetic response with respect to the up ($+z$) and down ($-z$) component of $\boldsymbol{m}$.

This can be understood as follows: If no other torques are present, the magnetization is in equilibrium either at $\boldsymbol{m} = \hat{z}$ or $\boldsymbol{m} = -\hat{z}$ due to the effective anisotropy field $\mu_0 H_{\mathrm{oop}} = \left(\frac{2K_{\mathrm{oop}}}{M_{\mathrm{s}}} - \mu_0 M_{\mathrm{s}}\right) > 0$[1]. Without loss of generality, assume $\boldsymbol{m} = \hat{z}$ to begin with. If now an external field $\boldsymbol{H}_{\mathrm{ext}}$ is applied ip (along x-direction), the equilibrium position is given by the vector sum of external field and anisotropy field. The equilibrium position continuously transforms from oop to ip with increasing H and is given by $\boldsymbol{m} \parallel \boldsymbol{H}_{\mathrm{ext}}$ when $H_{\mathrm{ext}} = H_{\mathrm{oop}}$. If released, the magnetization then spontaneously relaxes towards either equilibrium position such that no deterministic switching can be achieved. The same argument is true if only a damping-like torque is applied with $\boldsymbol{\sigma} \parallel \hat{y}$ lying ip. This torque directly pulls the magnetization towards the $-\hat{y}$-direction. If both the damping-like torque and the external field are present, the ip field component perpendicular to $\boldsymbol{\sigma}$ exerts a torque on the magnetization that pushes $\boldsymbol{m}$ towards the negative half sphere for $\boldsymbol{\sigma} \parallel \hat{y}$ and towards the positive half sphere when $\boldsymbol{\sigma} \parallel -\hat{y}$. After the switching event, the external field then stabilizes the final equilibrium position, as shown in panel b) of Fig. III.1.1. This asymmetry leads to bipolar switching if the current direction and therefore $\boldsymbol{\sigma}$ is reversed at a fixed ip field.

The critical strength of the damping-like torque τ_{DL} that needs to be reached in order to switch the magnetization within the macrospin model is given by [Lee13; Gar14]:

$$\tau_{\mathrm{DL,crit}} = \frac{\mu_0}{2}\left(H_{\mathrm{oop}} - \sqrt{2}H_{\mathrm{ext}}\right). \tag{1.1}$$

The limit of zero external field is exactly the torque needed to pull the magnetization ip ($\boldsymbol{m} \parallel -\boldsymbol{\sigma}$). The above equation is valid for pulse widths long enough to allow the magnetization to rotate into the lower half sphere. In the short pulse regime, the switching time and probability therefore depend not only on the strength but also on the rise and

[1] $\mu_0 H_{\mathrm{oop}} \equiv -\mu_0 M_{\mathrm{eff}}$

fall times as well as on the damping [Leg15]. In panel a) of Fig. III.1.1 the m_z trajectory

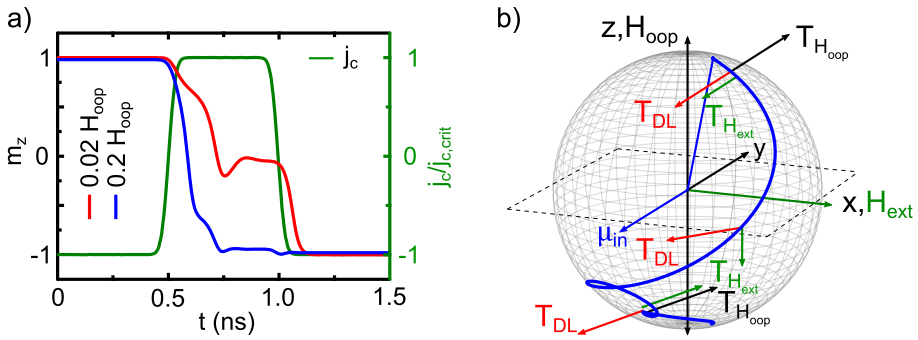

Figure 1.1.: *Numerical evaluation of a current induced switching event within the macrospin model. a) switching trajectories of m_z (blue, red) induced by a 500 ps wide pulse (green line) creating a SOT strong enough to pull the magnetization into the x, y-plane for two different applied ip field strengths $H_x = 0.02 \times H_{oop}$ and $H_x = 0.2 \times H_{oop}$. b) 3D trajectory of the magnetization unit vector for the case of the larger applied field (blue line). The torques resulting from the oop anisotropy field and the external field as well as the damping-like SOT are sketched at three distinct positions in order to elucidate the action of the external field.*

is shown for a fictious 500 ps current pulse (green line) and two different values for the ip field as obtained from a numerical solution of the LLG. In this illustrative case, the damping-like torque is set to be equal to the zero field critical current given by Eq. (1.1). The Gilbert damping parameter is $\alpha = 0.5$. The magnetization is pulled from the upper into the lower half sphere within ≈ 250 ps which is well below the reachable pulse width in the experiment such that the macrospin switching time is not expected to be the limiting factor. The two different $m_z(t)$ curves are obtained for $H_{\mathrm{ext,x}} = 0.02 \times H_{\mathrm{oop}}$ (red curve) and $H_{\mathrm{ext,x}} = 0.2 \times H_{\mathrm{oop}}$ (blue curve). The larger field leads to a decrease in switching time due to the additional torque favoring a down state. For the latter case, the 3D trajectory is shown in panel b) as the solid blue line. In panel b) the torques on $\boldsymbol{m}$ are depicted at different positions in order to clarify the action of the external field. Note that the damping-like torque always acts towards the same direction whereas the torque due to the external field changes sign after the magnetization vector passes the $z = 0$ plane.

If the damping-like torque is smaller than the critical value given by Eq. (1.1), no switching occurs within the macrospin model. However, any combination of ip field and damping-like torques stabilizes one equilibrium in favor of the other one, i.e. the formerly degenerate energy minima at $\pm\hat{z}$ split into a lower and a higher one. Thus switching in reality occurs even for torque values well below the result of Eq. (1.1). This can be understood by the following extension of the model: a) within the macrospin model, thermal assistance must be included, which lowers the critical current [Bed10; Liu14; Lee14a; Led94] and b) for larger samples the macrospin model is invalid and domain wall nucleation and propagation [Liu12a], which can also be thermally assisted [Avc12; Lee14a; Bi14; Gar14; Zha15a], has to be taken into account. This process further reduces the critical switching

current due to the much lower energy cost needed for the formation of the domain wall compared to a coherent rotation of the whole magnetic element. The switching probability in the thermally assisted case follows an Arrhenius law and therefore, for a given current, strongly depends on the pulse width. Vice versa, the critical current depends on the pulse width. It is found that for the particular case of PMA magnetization switching a pulsewidth of ≤ 1 ns is below the thermally assisted regime [Gar14; Bed10; Liu14; Lee14a]. This leads to the expectation of either coherent rotation or deterministic domain wall nucleation/propagation for such short current pulses.

In [Mik15], it has been shown by the use of micromagnetic simulations that for a disk shaped sample the switching process indeed occurs via domain wall nucleation at one side of the disk and subsequent propagation of the domain wall if DMI is included. By using

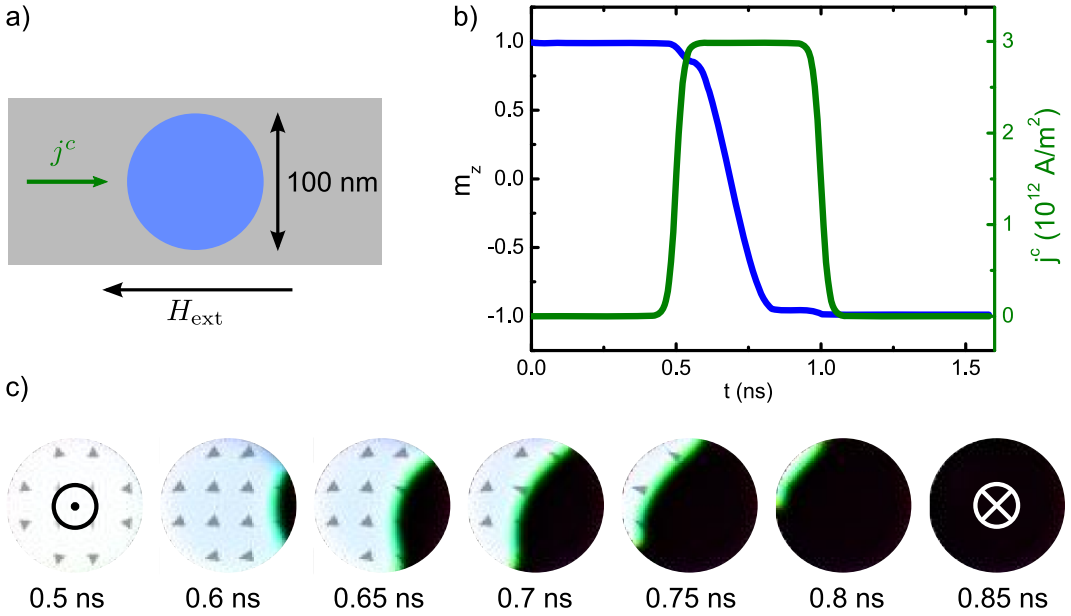

Figure 1.2.: *Micromagnetic simulation of the deterministic domain wall induced reversal of a* 100 nm *disk following [Mik15]. Panel a) shows the design of a sample structure; the grey rectangle represents a Pt strip with a blue Co disk on top. Panel b) shows the averaged z-component of the magnetization (blue line) as a result of a current pulse (green). Panel c) shows snapshots of the magnetization configuration at distinct times. At the right edge of the element, initially pointing in $+z$ direction, a domain nucleates and subsequentially moves to the left until the whole disk is switched into the $-z$ direction.*

the parameters of [Mik15], an exemplary switching event is simulated using mumax^3 and shown in Fig. III.1.2. The magnetic sample in this case consists of a 100 nm diameter Co/Al_2O_3 disk on top of a Pt strip. The current pulse is passed through the strip in x-direction and an external ip field of 0.1 T is applied in the same direction. Panel b) shows the current pulse in green and the averaged z-component of the magnetization in blue. In panel c) the spatial distribution of $\boldsymbol{m}$ is shown. Initially, the whole element is magnetized along $+\hat{z}$ direction. After onset of the pulse, a domain nucleates at the right side of the

disk. The nucleation spot is determined by the combined action of DMI and the external magnetic field. At the edge of the disk, the DMI leads to a tilt of $\boldsymbol{m}$ towards the center of the disk. The external field now counteracts this tilt at the left edge and enhances it at the right edge, setting the nucleation point. This leads to a deterministic behavior of the switching process enabling the use of a stroboscopic probing scheme as given by a pump probe approach.
The aim of the experiment therefore is to clarify whether this kind of mechanism can be observed experimentally.

2. Sample Structure and Experimental Setup

2.1. Layer Sequence and Sample Design

The layer structure of the studied samples consist of four individual layers grown on thermally oxidized highly resistive silicon substrate: $Si/SiO_x|Ta(3nm)/Pt(8.5nm)/Co(0.5nm)/Al_2O_3(5nm)$. Ta is used as a seed layer in order to enhance the perpendicular magnetic anisotropy. After annealing at 270°C for 30 min, the layer shows a perpendicular easy axis as verified by polar MOKE. Using SQUID magnetometry, the saturation magnetization at 300 K is determined to be $\mu_0 M_s$ =1.3 T and the effective anisotropy field is $\mu_0 H_{oop} \approx 0.5$ T, see Fig. III.2.1. The Curie temperature T_C is found to be around 400 K. A temperature

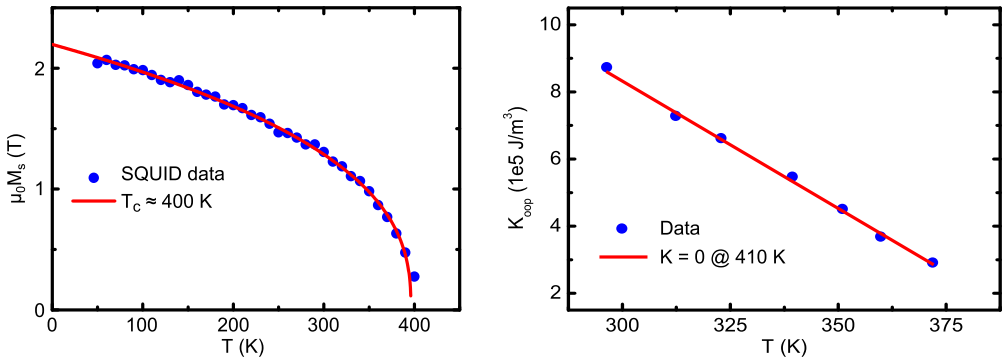

Figure 2.1.: *Characterization results of the $Pt/Co/Al_2O_3$ layer structure. Left panel: temperature dependence of the saturation magnetization as measured by SQUID magnetometry. A Curie temperature of ≈ 400 K is found. Right panel: perpendicular anisotropy constant as a function of temperature. A linear extrapolation of the measured data indicates a vanishing K_{oop} not before the Curie temperature.*

dependent measurement of the oop uniaxial anisotropy constant reveals a vanishing K_{oop} at 410 K such that the sample possesses PMA up to T_C. This fact is of importance since the current pulse injection is expected to generate a non-negligible amount of Joule heating during the switching process.

The layer is subsequentially patterned into two different kinds of samples shown in Fig. III.2.2: $(2 \times 2)\,\mu m^2$ Co squares and 750 nm diameter disks on top of a 2 µm wide Pt strip. The differently shaped magnetic elements allow testing the influence of the shape on the switch-

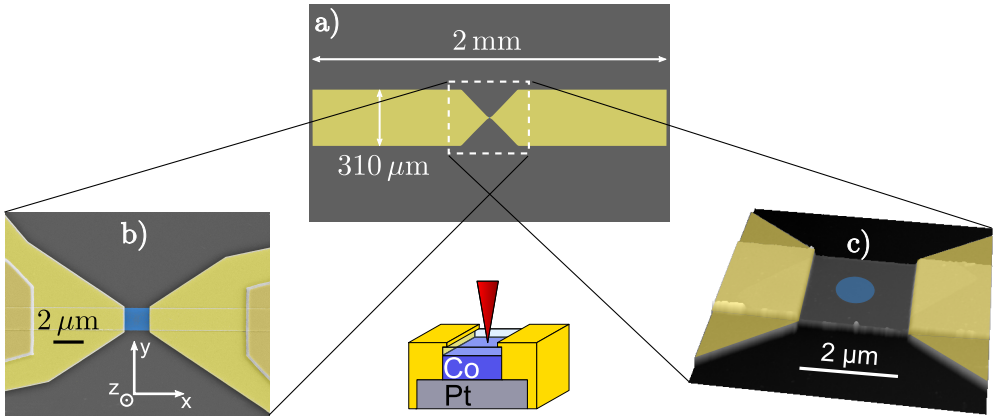

Figure 2.2.: *Sample geometry used in the presented experiment. a) Sketch of a device incorporating a* 310 μm *wide Au microstrip contacting the Pt/Co element. b) Colored SEM pciture of a* $(2 \times 2)\mu m^2$ *Co square sample, colored in blue. c) Colored height profile as obtained by AFM from the second type of sample used: a Co disk (blue) with a diameter of* 750 nm *on top of the* 2 µm *wide Pt strip contacted by the Au contact pad.*

ing process. The fabrication of the magnetic structure (indicated blue) is done by electron beam lithography and wet chemical removal of the protecting Al_2O_3 layer. As a next step the Pt stripe is etched out by Ar^+ ion milling, followed by a lift-off process defining the Au contacts. The contact pads are formed as microstrips matched to 50 Ω impedance in order to enable a good pulse transmission through the device. This is important because the current pulse consists of frequency components up to the GHz range of frequencies. In order to keep the inevitable dc resistance as low as possible the Pt thickness of the active layer is chosen to be relatively thick (8.5 nm) such that the sheet resistance of the multilayer is 60 Ω and the total resistance of a bonded sample lies around 80 Ω. The microstrip design is found to enable lower pulse distortion than a CPW-based design. The finished sample is then bonded into a sample holder that is attached to high-frequency cables in order to connect it to the pulse generation circuit.

After fabrication of the samples, the effective oop field $\mu_0 H_{\mathrm{oop}}$ is measured directly on the element by using the method of static equilibrium change as discussed in the appendix IV.C. This method also allows for a check of degradation of the sample after switching measurements as $\mu_0 H_{\mathrm{oop}}$ is a good indicator of structural changes within the layer due to e.g. excessive joule heating. For all measured samples, no significant changes are found after the time resolved switching measurements. Failure of a device (due to a too large applied current or electric discharge) usually results in an immediate demagnetization of the element.

2.2. Experimental Setup

The general idea of the pump probe experiment is the following: An alternating pulse train switches the magnetization from up to down and back while a pulsed laser is used to probe the magnetization. In Fig. III.2.3, an actual measurement of the z-component

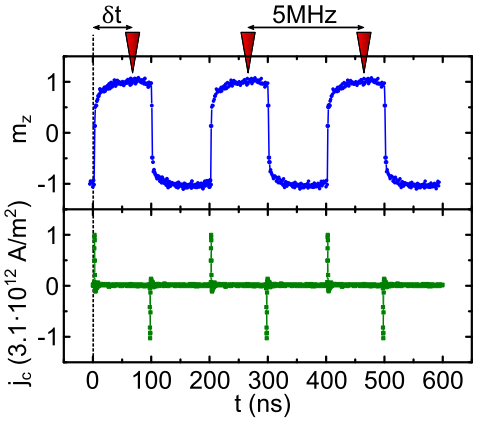

Figure 2.3.: *Time resolved measurement of the bi-polar reversal of a* $(2\times2)\,\mu m^2$ *Co element via injection of 1 ns wide current pulses of alternate polarity. The lower part shows the transmitted current pulses (green symbols) as directly taken from the oscilloscope. Within the period of* 200 ns*, given by the laser repetition rate (*80 MHz*), a positive (set) and a negative (reset) pulse are placed with a spacing of* ≈ 100 ns*. The time trace of the magnetization (blue symbols, upper part) is recorded by scanning the delay* δt *between current pulses and laser probing pulses, indicated by the red cones. The above data is recorded at an applied field of* $\mu_0 H = -50$ mT *over one period and repeatedly plotted in order to clarify the measurement technique. For this measurement, no lock-in technique is used such that both up and down switching event can be recorded.*

of the magnetization (blue symbols) and the transmitted current pulses (green symbols) is shown. The repetition rate of the laser is 5 MHz such that within the 200 ns period one positive and one negative pulse are placed in ≈ 100 ns distance. The delay δt between laser pulses and current pulses is swept and the switching process is measured stroboscopically. In the above figure, one period of 200 ns is recorded and the measured data is repeated in order to clarify the measurement technique. The experiment is performed by using the same laser system and microscope as used for the time resolved FMR measurements (see section II.4.2.2) but changed to the pump probe scheme. A sketch of the setup is shown in Fig. III.2.4. The output of the Ti:Sa laser is divided into two parts. The first part is used to probe the z-component of the magnetization as explained in section II.4.2.2. The second part is used to trigger the pulse train that switches the magnetic element. A train of alternating current (pump) pulses is generated by the use of two pulse generators, A and B. One generator is set to positive and the other one is set to negative pulse amplitudes. The outputs are combined via a resistive power splitter. Two attenuators, directly after the output, suppress crosstalk between the two generators. Subsequently, the pulse train is amplified using a SHF 826H broadband amplifier which enables amplitudes up to ±6 V

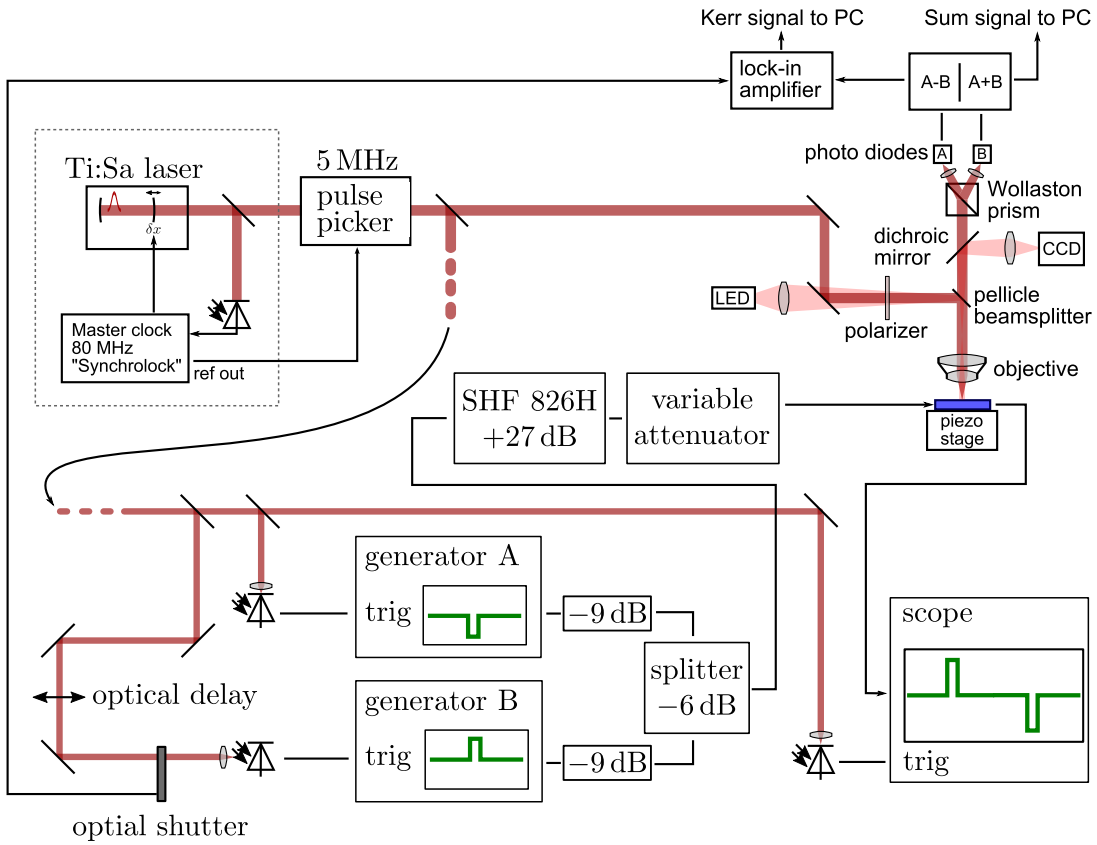

Figure 2.4.: *Time resolved MOKE setup used for the magnetization switching measurements. A detailed explanation of the components is given in the text.*

into 50 Ω impedance. In order to control the peak current density at the sample, a variable attenuator is used that can be set in 1 dB steps. The transmitted current pulses are fed into a fast oscilloscope such that the transmitted amplitude can be read off. From the smearing of the pulse shape at the scope a timing jitter of ≈ 50 ps is found, limiting the time resolution of the measurement.

The repetition rate of the laser is 80 MHz which converts to a period of 12.5 ns. This time window is too small to enable switching and back-switching such that the repetition rate is lowered to 5 MHz by the use of a pulse picker. The delay between current pulses and laser pulses is set by a combination of the electronic delay of the pulse generators and an optical delay line for one generator. The reason for this approach is the following: At each generator, an arbitrarily large electronic delay can be set with a limited step size of 1 ns. This allows to set the delay between both pulses and to find the approximate delay between current and laser pulses. The switching process, however, is to be measured with much finer time resolution, which is achieved by an optical delay line with a nominal resolution of 15 fs. This optical delay is only used for one of the generators and it is this switching event which is recorded in detail (called set pulse in the following), while the second, back

switching (called reset pulse), is usually not measured. The long-time recording shown in Fig. III.2.3 is taken with a time step of 1 ns such that the optical delay is always kept at the same position.

The Kerr signal shown in Fig. III.2.3 is taken by directly reading out the difference voltage at the detector. For the detailed measurements shown below the signal to noise ratio is increased by using a lock-in technique. For this purpose, the beam triggering the set pulse generator is chopped at ≈ 1.6 kHz by an optical shutter. Therefore, half of the measurement time, only the reset pulse acts on the magnetization and therefore determines the magnetization's equilibrium position and the zero signal level. If the set pulse is active, the response of the magnetization is measured in comparison to the zero level by the lock-in amplifier. The reset pulse width is set to be slightly wider than the set pulse in order to guarantee a back switch after each set pulse. In addition, the externally applied ip field is always slightly tilted oop such that one equilibrium position is favored. This equilibrium position is then chosen as the the zero level.

In order to calibrate the Kerr signal on the structured sample, there are two possibilities which are depicted in Fig. III.2.5. First, as mentioned above, the external applied field is slightly tilted (≈ 1.3°) oop. Therefore, when sweeping the external field, the magnetization switches at a certain critical ip field value $H_{\mathrm{crit}} \sim 30\,\mathrm{mT}$. This allows measuring a hysteresis loop and using it to calibrate the Kerr signal from the two distinct levels at zero field. In panel a) such a loop is shown as recorded on a square shaped sample. The ip field value is converted into the effective oop field and a Kerr signal of $\approx \frac{65\,\mathrm{mdeg}}{M_\mathrm{s}}$ is obtained. A second

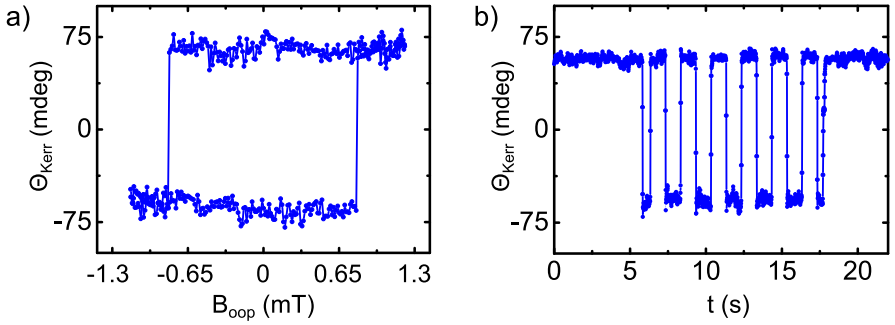

Figure 2.5.: *Static measurements of the equilibrium position of the magnetization on structured samples. a) Static Kerr signal as obtained when sweeping the applied ip field at zero current. Since B_x is tilted oop by ≈ 1.3°, resulting in an oop component B_{oop}, a hysteresis loop is recorded allowing the calibration of the Kerr signal from the zero field levels. b) Kerr signal obtained by the application of a weak quasi-dc current of changing polarity (0.5 Hz square signal) at an applied ip field of $\mu_0 H_x = 20\,\mathrm{mT}$ toggling the equilibrium position between $m_z = \pm 1$.*

possibility is to apply a small ip field $\mu_0 H_x = 20\,\mathrm{mT}$ and to inject a small current with alternating polarity in order to statically switch the magnetization. Panel b) shows such a measurement; the current density at the sample is $\pm 4 \times 10^{10}\,\frac{\mathrm{A}}{\mathrm{m}^2}$. From the two distinct levels, again the Kerr signal for a full reversal ($\approx \frac{60\,\mathrm{mdeg}}{M_\mathrm{s}}$) can be obtained. Using the

same technique allows checking of the symmetries of the switching process. In particular, it is verified that reversing the external field also reverses the switching direction and that an applied field along y-direction does not allow deterministic switching. Note that the measurement results shown in Fig. III.2.5 are obtained on different samples. The possibility of reliably calibrating the Kerr signal allows to convert the lock-in signal into units of M_s (or rather $m_z = \pm 1$) as shown in the figures below.

3. Experimental Results

3.1. Time Traces of Magnetization Reversal

In order to elucidate the mechanism at work, the switching process of the square sample is first studied as a function of time. The laser spot is centered at the middle of the sample and the magnetization is recorded at this fixed position. The resulting time traces are shown in Fig. III.3.1. In the figure, the left side always shows the recorded signal in a time span of 25 ns whereas the right side gives a detailed view of the first 5 ns of the respective left graph. The transmitted current pulse as read from the scope is plotted into the figures as a green solid line. Panel a) shows the switching of the magnetization from down to up under the action of a positive current pulse at negative external ip fields of different strength, as expected for a positive spin Hall angle in Pt. The pulse duration is set to $\tau_p = 1\,\text{ns}$[1] and the peak current density is $j^c_{max} = 3.1 \cdot 10^{12}\,\text{A/m}^2$. This pulse is verified to switch the magnetization by application of single set and reset pulses and recording of the static Kerr signal. For both $\mu_0 H = -50, -100\,\text{mT}$ full saturation towards $m_z = 1$ is reached whereas the magnetization at higher fields relaxes back into the initial position after the pulse has passed. This is a result of the previously mentioned oop tilt of the external field which favors the lower equilibrium position. In the detailed view, it is nicely visible that the switching process is faster for large applied fields as expected from theory. A very interesting finding is that at the lowest field of $\mu_0 H = -50\,\text{mT}$, the switching appears to be very slow and continues even after the maximum of the pulse has passed. In fact, it takes up to $\geq 25\,\text{ns}$ until the magnetization saturates in the upper position.
In panel b), field and current density are fixed to $j^c_{max} = 3.1 \cdot 10^{12}\,\text{A/m}^2$ and $\mu_0 H = -50\,\text{mT}$, respectively, and the pulse width is lowered from a FWHM of 970 ps to 620 ps. For $\tau < 1\,\text{ns}$, the critical current density required for a switching probability ~ 1 can no longer be reached. This leads to a reduced up level as seen in the $\tau_p = 770\,\text{ps}$ case. For even shorter pulses, the magnetization is only canted away from the equilibrium position and relaxes back towards the initial level after the pulse has passed. The reset pulse is not reduced in width and therefore the initial position is well defined in any case.
Panel c) shows a similar result when, instead of lowering the pulse width, the peak amplitude is lowered at a fixed $\tau_p = 1\,\text{ns}$. The same variation of peak current density and pulse width is shown in Fig. III.3.2 for a large applied field of $\mu_0 H = -300\,\text{mT}$. Panel a)

[1] the actual measured FWHM of this pulse is 970 ps as indicated in panel b)

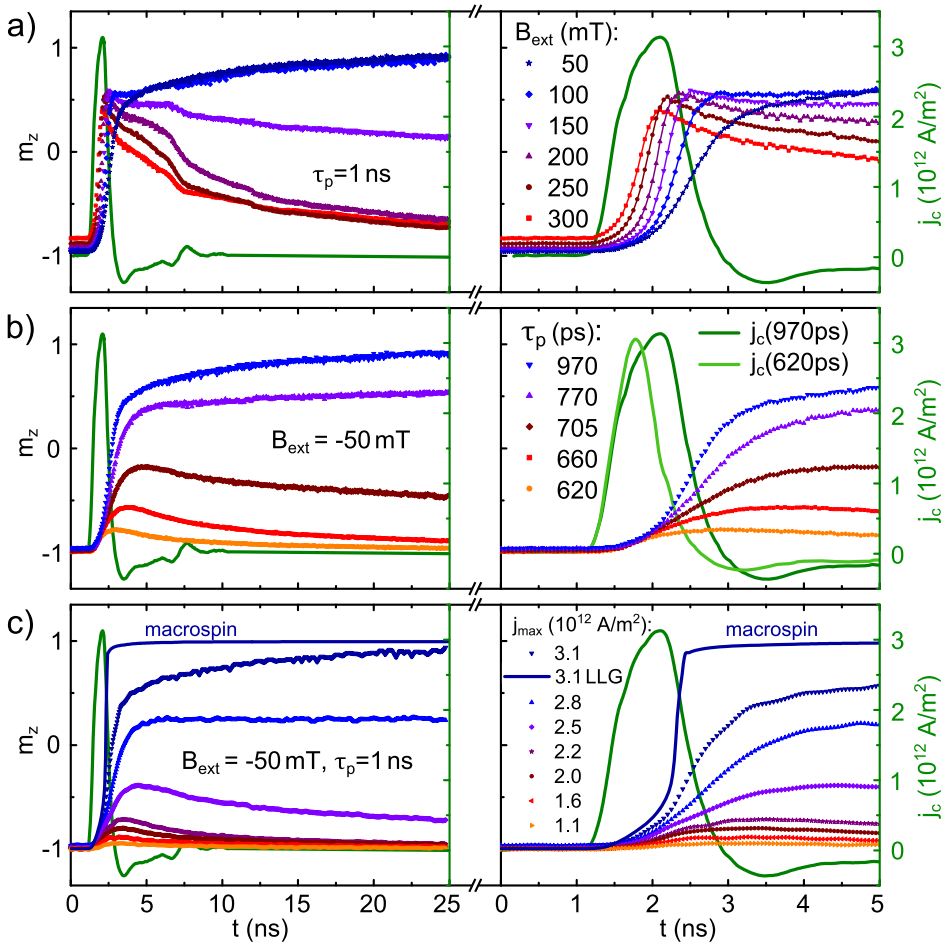

Figure 3.1.: *Time traces $m_z(t)$ (symbols, right axis) and current density $j_c(t)$ (green line, right axis) as a function of time. The right graph of each panel shows the first 5 ns of the respective left graph in detail. a) Measurements for fixed pulse width $\tau_p = 1\,\mathrm{ns}$ and peak current density $j^c_{max} = 3.1 \cdot 10^{12}\,\mathrm{A/m^2}$ at different B_{ext}. b) Pulse width dependence for fixed $B_{ext} = -50\,\mathrm{mT}$ and $j^c_{max} = 3.1{\cdot}10^{12}\,\mathrm{A/m^2}$. c) Power dependence for varying j^c_{max} at fixed $\tau_p = 1\,\mathrm{ns}$ and $B_{ext} = -50\,\mathrm{mT}$. In both graphs the solution of a macrospin calculation is plotted corresponding to the largest current density as discussed in section III.4.1.*

of this figure shows the power dependence at fixed pulse width. The switching process is faster for larger current densities and, in contrast to the low field data, switching occurs down to a current density of $j^c_{\mathrm{max}} = 1.6 \cdot 10^{12}\,\mathrm{A/m^2}$. The magnetization relaxes back into the stable equilibrium directly after the end of the pulse as described previously. For a fixed, large current density the magnetization switches down to the narrowest possible pulse width (limited by the generator), see panel b). Due to the fact that the rise time is relatively constant, the switching speed is quite constant for all pulse widths which is seen in the overlap of the time traces. Interestingly, wider pulses lead to a faster decrease of the magnetic signal after the pulse. This can be understood by considering the stronger Joule heating induced by the wider pulses.

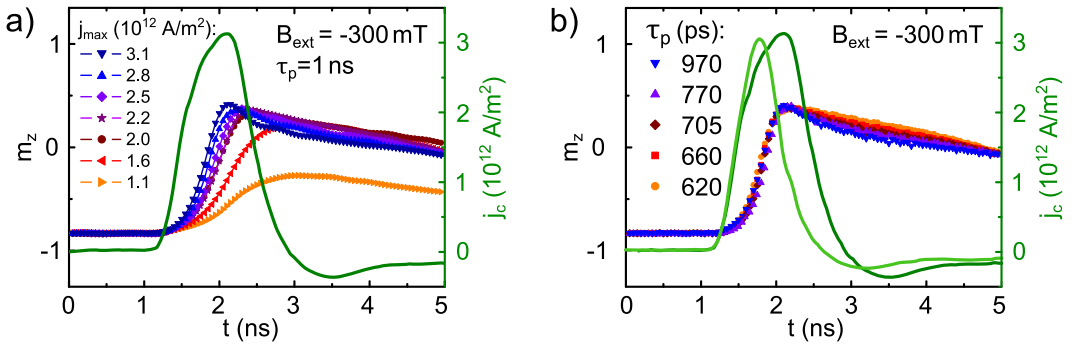

Figure 3.2.: *Time traces $m_z(t)$ (symbols, right axis) and current density $j_c(t)$ (green line, right axis) as a function of time, corresponding to the measurements shown in panel b),c) of Fig. III.3.1 but at large applied field. a) Power dependence for varying j^c_{max} at fixed τ_p = 1 ns and B_{ext} = −300 mT. b) Pulse width dependence for fixed $j^c_{max} = 3.1 \cdot 10^{12}$ A/m^2 and B_{ext} = −300 mT.*

3.2. Time Resolved Imaging of Magnetization Reversal

In addition to the above shown time traces, the switching process is studied as function of both time and space in order to investigate possible spatial inhomgeneities such as domain nucleation and propagation by taking Kerr images of the element at distinct times. In panel b) of Fig. III.3.3, an example of such an image sequence is shown for the $(2 \times 2)\,\mu$m^2 sample and τ_p = 1 ns, $j^c_{max} = 3.1 \cdot 10^{12}$ A/m^2 and $\mu_0 H$ = −50 mT. The images correspond

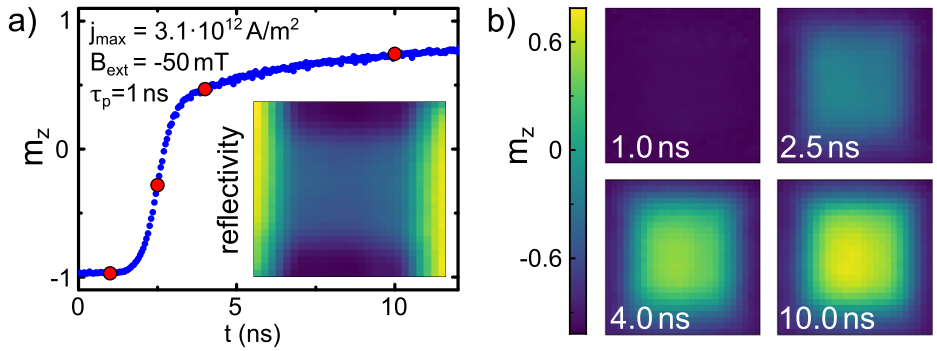

Figure 3.3.: *Images of the magnetization reversal of a $(2 \times 2)\,\mu$m^2 Co square. a) Time trace of the reversal process taken in the middle of the element. The inset shows the reflected intensity when scanning the beam across the sample. The current contact pads can bee seen in yellow at the left- and right-hand side. b) Images of the Co element at distinct times marked by the red dots in panel a).*

to the red dots marked in the time trace of the same switching event shown in panel a) and already discussed in the context of Fig. III.3.1. The inset of panel a) shows the reflected intensity in which the current contacts appear yellow at the left and right side of the quadratic magnetic element. Apparently, the switching process is homogeneous and no propagating domains are seen. This result is found for different peak current densities and pulse widths as well as for any field values within the −300 mT range reachable in the

experiment.

In order to investigate whether the shape of the magnetic element causes the particular outcome found in the quadratic samples, the 750 nm disk shaped sample is studied as a next step. Exemplary time traces and corresponding images are shown in panel a) and b) of Fig. III.3.4, respectively. The time traces obtained are very similar to the ones for the

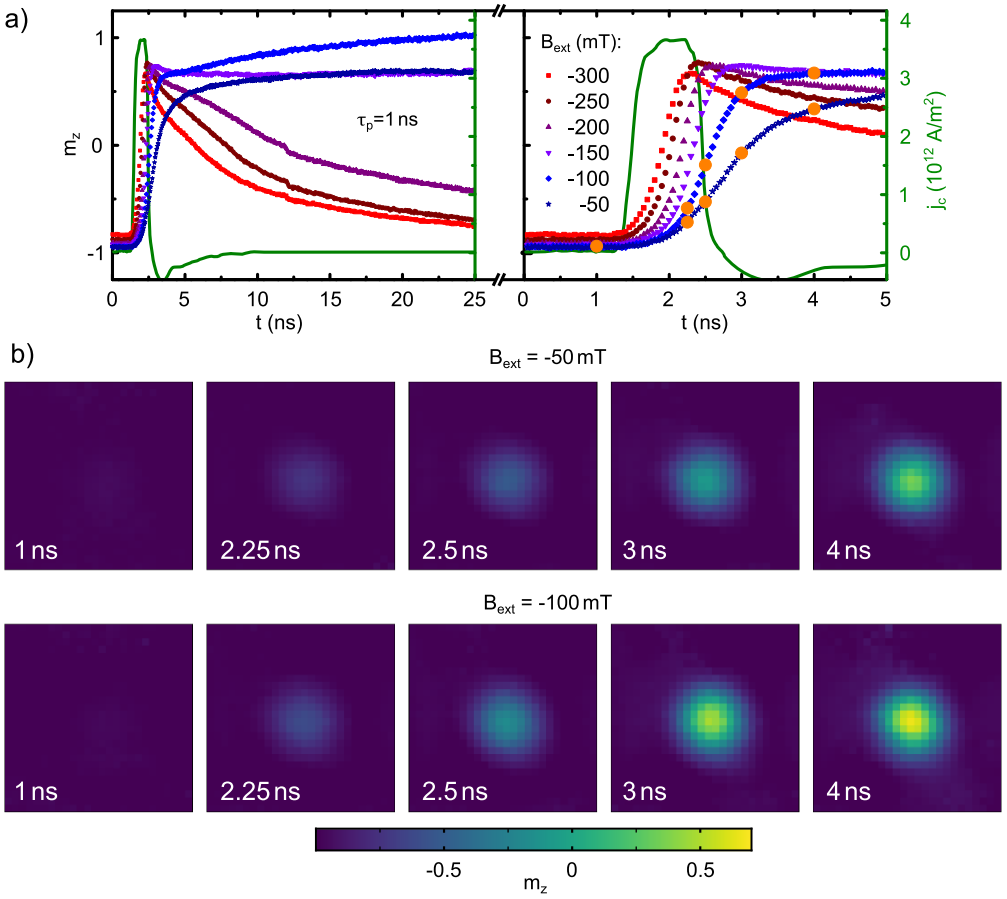

Figure 3.4.: *Time resolved measurements of magnetization reversal of a* 750 nm *disk sample. Panel a) shows the time traces of the switching process in analogy to panel a) of Fig. III.3.1. The right graph shows the first* 5 ns *of the left graph in detail. The orange dots mark the times corresponding to the images shown below in panel b) for two different applied fields.*

square sample. The same slow switching is found for a low external field and the images reveal a homogeneous change in magnetic contrast as found for the square samples before. Therefore, it is concluded that, in the present case, the switching mechanism for both sample geometries has the same origin, to be explored in the following sections.

4. Computational Analysis of the Switching Process

4.1. Numerical Solution of the Macrospin Model

In order to determine whether the measured data can be explained by coherent rotation, the LLG equation (Eq. (1.22)) is solved numerically by using the ODE solver package integrated in Python's SciPy package[1]. As simulation input parameters, the predetermined values for M_s, H_{oop} are used in combination with $\alpha = 0.5$. The SOTs are modeled as a function of time resembling the transmitted pulseshape. As a first test, the switching process at $\mu_0 H = -50\,\mathrm{mT}$ is simulated by using only a damping-like SOT. The critical switching torque found in this scenario corresponds to an effective spin Hall angle (defined by Eq. (2.25) and the explanation in the text below) of $\theta_{eff} = 0.13$, which is close to published values in similar layers structures [Gar14; Zha15b]. This means that the switching current itself could be explained by the macrospin model. However, the time scale of the switching process as found in the experiment and in the macrospin calculations differ significantly. A resulting curve of the macospin model is plotted as a solid blue line into panel c) of Fig. III.3.1. The calculation is performed for $j^c_{max} = 3.1 \cdot 10^{12}\,\mathrm{A/m^2}$, corresponding to the experimental data shown by dark blue triangles. While the switching proccess in the macrospin model occurs within the pulse on-time and saturation is reached immediately after the current reaches its zero level, the relaxation process takes up to $\approx 30\,\mathrm{ns}$ in the experiment. In order to explain this discrepancy, different possibilities are taken into account but cannot explain the long relaxation time. The reason for this is that, within the macrospin model, the switching process must always occur within the current pulse due to the large damping value and the fact that the rise and fall time of the pulse are much longer than the precession frequency (given by the internal field). This statement is true even if additional effects are included: Any additional field-like torque is found to only reduce the critical switching current for the given parameter set and pulse shape. Thermal activation of the switching process can be excluded for two reasons: a) from previous, pulse width dependent studies it has been concluded that for sub-ns pules the thermal activation plays a minor role [Gar14; Bed10; Liu14; Lee14a] and b) any statistical process should lead to a reduction of the switching probability (and therefore saturation

[1] scipy.integrate.odeint()

level) rather than changing the time scale of the switching process itself.
The possibility of Joule heating, however, has to be considered since a current pulse of $j^c_{\max} \sim 3 \cdot 10^{12}\,\mathrm{A/m^2}$ is expected to heat up the microstructure by some tens of Kelvin. Significant heating of the layer close to the Curie temperature is expected to change the material parameters such as the saturation magnetization M_s. This would be seen as a reduction of the Kerr signal and a slow dissipation of the heat might explain the long experimental saturation times. In order to explore this scenario, simulations of the temperature of the element as function of the time are performed using the COMSOL® multiphysics package[2]. It is found that the temperature recovers about $\leq 7\,\mathrm{ns}$ after the end of the pulse. In addition, it is clear that the Curie temperature is not reached in the experiment since this would lead to a plateau around zero in the Kerr signal due to a demagnetization of the Co layer which is not observed in the data. Thus, it is concluded that the macrospin model cannot explain the experimental results.

4.2. Micromagnetic Simulations

It needs to be explained, why the reversal process as probed by TRMOKE appears homogeneous but does not coincide with the results of a macrospin calculation. In order to reveal possible mechanisms, micromagnetic simulations are performed by using mumax[3] [Van14]. The $(2 \times 2)\mu\mathrm{m}^2$ Co element is discretized into a $512 \times 512 \times 1$ cell grid such that the lateral cell size is $\approx 3.9\,\mathrm{nm}$, which is of the order of the exchange length (Eq. (6.1)) of Co for the used saturation magnetization of $\mu_0 M_\mathrm{s} = 1.3\,\mathrm{T}$ (as determined by SQUID) and an exchange constant of $A = 10\,\frac{\mathrm{pJ}}{\mathrm{m}}$ [Mik15]. The uniaxial oop anisotropy constant is $K_\mathrm{oop} = 971\,\frac{\mathrm{kJ}}{\mathrm{m}^3}$ as computed from the measured effective oop field.
In order to reveal the influence of the DMI on the process, a DMI constant of $D \cdot d_\mathrm{Co} = 0.6\,\mathrm{pJ/m}$ is assumed, which lies within reported literature values that range from $D \cdot d_\mathrm{Co} \sim 0.3\,\mathrm{pJ/m}$ [Lee14b; Ben15] to $\sim 2\,\mathrm{pJ/m}$[Kim15; Pai16; Bel15] and values inbetween [Piz14; Mar13; Emo14; Han16; Cho15; Kör15; Pai16]. The DMI constant is chosen such that the ground state of the element is uniform. For a larger value of $D \cdot d_\mathrm{Co}$, the element - in contradiction to the experiment - decays into multiple domains, due to the fact that DMI reduces the energy cost of domain walls.
Like in the experiment, the static field is set along x-direction and is tilted oop by 1° in such a way that for $H < 0 \Rightarrow H_z < 0$. This leads to a relaxation back towards the stable equilibrium position at large field values in accordance with the experimental findings.
It is found that both damping-like and field-like torques as well as a finite temperature (100 K) are needed in order to explain the long switching time at low fields. For torque values of $\tau_\mathrm{FL}/j_\mathrm{c} = 0.045\,\mathrm{pTm^2/A}$ and $\tau_\mathrm{DL}/j_\mathrm{c} = 0.067\,\mathrm{pTm^2/A}$, the measured data is almost

[2] The COMSOL model is kindly provided by Michael Vogel

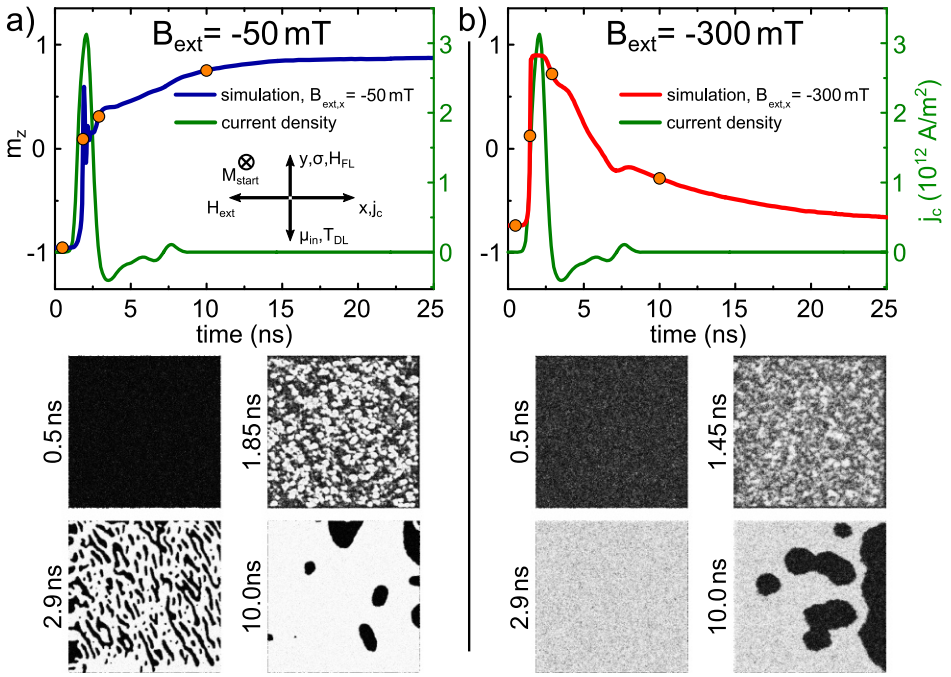

Figure 4.1.: *Micromagnetic simulation of the switching process. Time traces of $m_z(t)$ (blue/red solid line) and current density (green line) are shown in the upper graphs. The orange dots indicate the times for which the corresponding images are shown the lower part. Panel a) and b) show the result for an applied field of $\mu_0 H = -50\,\mathrm{mT}$ and $\mu_0 H = -300\,\mathrm{mT}$, respectively. The simulation results reproduce the experimental data shown in Fig. III.3.1, panel a).*

perfectly reproduced for both low and high fields as shown in Fig. III.4.1. The simulated switching process (images) as well as the corresponding time trace is shown for $\mu_0 H = -50\,\mathrm{mT}$ in panel a) and for $\mu_0 H = -300\,\mathrm{mT}$ in panel b). Interestingly, these torque values closely resemble values published for a similar layer stack [Gar13]. The inset of the time trace graph in panel a) shows the coordinate system and the direction of the fields and torques involved. For a positive applied current, the spin polarization vector σ is parallel to the positive y-direction due to a positive SHA in Pt. Thus, the magnetic moment injected into the Co layer $\boldsymbol{\mu}_{\mathrm{in}}$ points into the negative y-direction and determines the direction of the damping-like torque. A positive field-like torque in this picture corresponds to a field $\boldsymbol{H}_{\mathrm{FL}}$ pointing in the positive y-direction such that the damping-like and field-like torques tend to align the magnetization into opposite directions. Due to the combination of these two opposing contribution and at a finite temperature, small domains are continuously created during the switching event when only a low external field is applied. As long as the pulse is present, these domains are created and annihilated. After the pulse has passed, the remaining domains slowly relax towards the new state and result in a long switching time, see panel a) of Fig. III.4.1. A larger applied field stabilizes the system and results in a fast switching (panel b)). Due to the oop tilting of the external field, the

magnetization starts to relax back into the favored equilibrium position after the end of the pulse as seen experimentally. It must be noticed that the domain nucleation points are

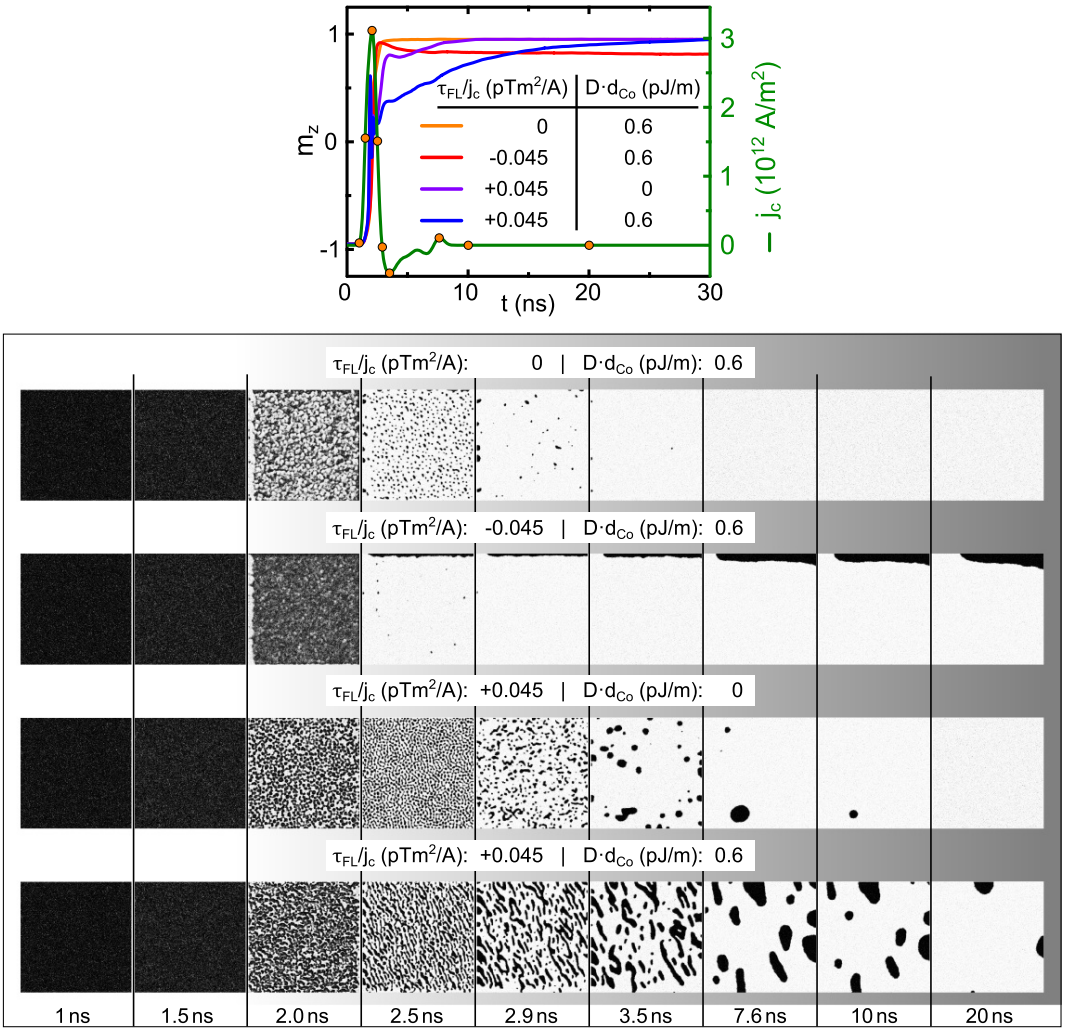

Figure 4.2.: *Micromagnetic simulations of the magnetization reversal at an applied field of* $\mu_0 H = -50\,\mathrm{mT}$ *for different strength and sign of the field-like torque as well as with and without DMI. The upper graph again shows the time traces of magnetization and current density. The very long relaxation time is only found for positive field-like torque and nonzero DMI. The images shown below the graph correspond to the times marked as orange dots along the current pulse.*

given by the random field used in mumax[3] to implement the temperature and therefore the exact domain pattern at a distinct time depends on the seed of the randomize function. Translated into the actual measurement, this means that, if measured with a stroboscopic technique, the statistical average over many switching events results in a homogeneous Kerr signal across the element which corroborates the findings of Fig. III.3.3 and Fig. III.3.4. If conducted at zero temperature, switching always occurs by deterministic domain wall nucleation at one side of the element and subsequent propagation across the sample, in agreement with the simulation results presented in [Mik15] but in sharp contrast to the

measured data. It has to be pointed out that the finite temperature in the simulation is introduced to act as a seed for domain nucleation and does not resemble a realistic temperature increase during the pulse with the related change in magnetic parameters. In order to further elucidate the role of the torque combination and the DMI, Fig. III.4.2 shows the simulated switching events for the above-mentioned parameters with varying field-like torque and with/without DMI. Panel a) again shows the time trace and panel b) shows corresponding snapshots of m_z at distinct time steps marked by orange dots on the current pulse (green line) in panel a). Of particular interest is the image at $t = 2.9\,\mathrm{ns}$ as this marks the zero crossing of the current pulse. At first, the field-like contribution is discussed: without field-like torque (orange line), the switching occurs within the pulse time and the magnetization is saturated shortly after the end of the pulse. For a negative field-like torque (red line), the switching process is even faster and barely any domain is nucleated in the center region of the element. For a positive field-like torque (purple and blue lines), many small domains appear during the pulse on time and stay in the sample even after the pulse is off. The difference between the case with and without DMI is basically only the time it takes for the magnetization to relax. Times up to 20 ns and longer are only found for nonzero DMI.

5. Summary

In conclusion, for the first time, the SOT induced switching process of a perpendicular magnetic element is recorded, delivering microscopic images of the switching process at fine time resolution. It is found that the switching process is strongly deterministic and that the magnetic elements are stable even after up to $> 10^{12}$ consecutive switching events. This proves the applicability of in-plane current induced switching as a promising alternative in ST-MRAM applications. Interestingly, the switching duration is found to be larger than the current pulse length, which is attributed to the combined action of field-like torque and DMI, mediated by a finite temperature. In this case, the switching process incorporates the nucleation of many, statistically distributed domains if the applied external field is small.

The particular values for H_{oop} and H_{crit} of the presented layer system leads to back-relaxation of the magnetization after the switching for larger applied fields, due to a small canting of the ip field in the setup used. This problem is circumvented in samples designed for field-free switching, which allows to engineer towards application in such a way that the fast switching times for larger applied fields can be used.

A recent, independent publication addressing the same topic by the use of time resolved X-ray spectroscopy has reported switching of 500 nm in diameter disks via deterministic domain wall propagation [Bau17]. Although this finding is in contrast to the data presented here, the experimental results have been related to a combination of DMI, damping-like and field-like torque in agreement with the results presented in this work. Especially the relative sign of field- and damping-like torque has been found to play a critical role and is determined in a way that agrees with the findings of this work. It should be noticed that the exact switching process depends critically on the different energy contributions in the FM, which differ between the two experiments. In addition, the Joule heating of the element is expected to depend on the particular layer thickness and choice of substrate. Nevertheless, the fact that both experiments show deterministic switching - despite of the differences in the details of the process - once again shows the robustness of SOT induced magnetization reversal.

Part IV.

Appendix

A. Bootstrap Error Calculation

When fitting data using programs like Origin[1] or self-written codes based on pythons scipy package[2], one usually obtains the parameters for the best fit as well as the standard error of this value. Unfortunately, this error only represents the goodness of the fit, i.e. if the sum of the squared residual is small, the error of the parameters is small. This can lead to a large underestimation of the real errors of the parameters. In addition, it is usually hard to include x-errors in the fit routine. A quick way around these problems is to use a so-called Bootstrap approach to the fitting as described in [Efr93; Efr86]. Assume a dataset of n values (x_i, y_i) with errors $(\Delta x_i, \Delta y_i)$ representing for example the standard deviation that shall be fitted using a function $f(x, y, [p_1, p_2, \ldots])$ with parameters p_k. To obtain the most likely values p_k and their error, one then generates a set of N_B new datasets ($N_\mathrm{B} \sim 10^4$ for the fits used in this work). In each of these datasets every point is shifted around its initial value (x_i, y_i) by adding a random number in both directions. The random numbers added have to follow the distribution of the respective errors $(\Delta x_i, \Delta y_i)$, i.e. for the stated example they have a Gaussian distribution with $\sigma_i = \Delta x_i / \Delta y_i$. Every so generated dataset is then fitted using the fit function and the result of the fit parameters is recorded. From a histogram of the results for a particular parameter p_k, the most likely result and confidence intervals are extracted. The same method can be used for calculating averages of a dataset as this resembles a linear fit with fixed zero slope.

[1] http://www.originlab.de
[2] https://www.scipy.org

B. Derivation of the Dynamic Susceptibility

The LLG equation can be solved for a small excitation around an equilibrium position to find analytic expressions for $\boldsymbol{m}(t)$. This can be done in two distinct ways. The first way is to use a Lagrangian approach. Using this approach, the resonance condition can be calculated from the free energy of the system [Suh55]:

$$\omega_\mathrm{r} = \frac{\gamma}{M_\mathrm{s}\sin(\theta)}\left[\frac{\partial^2\varepsilon}{\partial\theta^2}\frac{\partial^2\varepsilon}{\partial\varphi^2} - \left(\frac{\partial^2\varepsilon}{\partial\theta\partial\varphi}\right)^2\right]^{\frac{1}{2}} \tag{2.1}$$

and the linewidth (full width at half maximum!) is given by

$$\Delta H = \frac{\alpha\gamma}{M_\mathrm{s}}\left|\frac{\mathrm{d}\omega_\mathrm{r}}{\mathrm{d}H}\right|^{-1}\left(\frac{\partial^2\varepsilon}{\partial\theta^2} + \frac{1}{\sin(\theta)^2}\frac{\partial^2\varepsilon}{\partial\varphi^2}\right). \tag{2.2}$$

However, the above equations do not describe the amplitude of the precession as a function of the external field. Therefore, the dynamics of $\boldsymbol{m}(t)$ is derived in the following by explicitly solving the LLG for small excitation/small angle precession around the equilibrium as described in the main text.
Consider the case of a thin (some nm) FM stripe with quasi infinite length L along x and a finite width w in y direction such that there is a nonzero demagnetization field along this direction. In addition, a oop anisotropy as well as an ip uniaxial anisotropy are considered as well as a static and a rf damping-like torque.
The energy contributions in this case are:

- demagnetization energy: Eq. (1.12)
- anisotropy energy: Eq. (1.15) and Eq. (1.16)
- Zeeman energy/external field: Eq. (1.5)

As a first step, all vector quantities are expressed in spherical coordinates. The external field is written in laboratory coordinates as

$$\boldsymbol{H}_\mathrm{L} = H\begin{pmatrix}\sin(\theta_H)\cos(\varphi_H)\\ \sin(\theta_H)\sin(\varphi_H)\\ \cos(\theta_H)\end{pmatrix} \tag{2.3}$$

In similar manner the static damping-like SOT polarization vector is defined as

$$\boldsymbol{\sigma}_{\mathrm{DL,s_L}} = \begin{pmatrix} \cos\left(\varphi_{\mathrm{DL,s}}\right) \\ \sin\left(\varphi_{\mathrm{DL,s}}\right) \\ 0 \end{pmatrix} \tag{2.4}$$

where the spin torque polarization is restricted to the (x, y) plane from the beginning on. The same restriction is made for the ip uniaxial anisotropy which has its easy axix unit vector defined as

$$\boldsymbol{n}_{\mathrm{ip,u_L}} = \begin{pmatrix} \cos(\varphi_{\mathrm{ip,u}}) \\ \sin(\varphi_{\mathrm{ip,u}}) \\ 0 \end{pmatrix} \tag{2.5}$$

In order to transform from laboratory to local coordinates and back, the following rotation matrices are used:

- turn from lab into magnetic coordinates:

$$R_{\mathrm{L}\to\mathrm{M}} = \begin{pmatrix} \sin(\theta)\cos(\varphi) & \sin(\theta)\sin(\varphi) & \cos(\theta) \\ -\sin(\varphi) & \cos(\varphi) & 0 \\ -\cos(\theta)\cos(\varphi) & -\cos(\theta)\sin(\varphi) & \sin(\theta) \end{pmatrix} \tag{2.6}$$

- turn from magnetic coordinates into lab. coordinates:

$$R_{\mathrm{M}\to\mathrm{L}} = \begin{pmatrix} \sin(\theta)\cos(\varphi) & -\sin(\varphi) & -\cos(\theta)\cos(\varphi) \\ \sin(\theta)\sin(\varphi) & \cos(\varphi) & -\cos(\theta)\sin(\varphi) \\ \cos(\theta) & 0 & \sin(\theta) \end{pmatrix} \tag{2.7}$$

The magnetization in its own coordinates is simply given by

$$\boldsymbol{m} = \begin{pmatrix} m_{x'} \\ m_{y'} \\ m_{z'} \end{pmatrix}. \tag{2.8}$$

The total energy is expressed in the local coordinate system by writing the magnetization components $m_i,\ i = (x, y, z)$ as function of the local versions $m_i,\ i = (x', y', z')$ via transforming the magnetization into laboratory coordinates

$$\boldsymbol{m}_{\mathrm{L}} = R_{\mathrm{M}\to\mathrm{L}} \cdot \boldsymbol{m} = \begin{pmatrix} \sin(\theta)\cos(\varphi)m_{x'} - \sin(\varphi)m_{y'} - \cos(\theta)\cos(\varphi)m_{z'} \\ \sin(\theta)\sin(\varphi)m_{x'} + \cos(\varphi)m_{y'} - \cos(\theta)\sin(\varphi)m_{z'} \\ \cos(\theta)m_{x'} + \sin(\theta)m_{z'} \end{pmatrix} \tag{2.9}$$

and inserting this magnetization vector into the expressions for the respective energy. The

resulting energy contributions are given by:

$$\begin{aligned}\varepsilon_{\mathrm{dem}} = \frac{1}{2}\mu_o M_{\mathrm{s}}^2 \big\{ & N_y \left[\sin(\theta)\sin(\varphi)m_{x'} + \cos(\varphi)m_{y'} - \cos(\theta)\sin(\varphi)m_{z'}\right]^2 \\ & + N_z \left[\cos(\theta)m_{x'} + \sin(\theta)m_{z'}\right]^2 \big\}\end{aligned} \tag{2.10}$$

$$\begin{aligned}\varepsilon_{\mathrm{ani}} = & - K_{\mathrm{oop}} \left[\cos(\theta)m_{x'} + \sin(\theta)m_{z'}\right]^2 \\ & - K_{\mathrm{ip,u}} \left[m_{x'}\sin(\theta)\cos(-\varphi+\varphi_u) + m_{y'}\sin(-\varphi+\varphi_u) - m_{z'}\cos(\theta)\cos(-\varphi+\varphi_u)\right]^2\end{aligned} \tag{2.11}$$

From these energy terms, the effective field is calculated via

$$H_{\mathrm{eff},i} = -\frac{1}{\mu_0 M_{\mathrm{s}}}\frac{\partial \varepsilon}{\partial m_i},\ i = (x', y', z'). \tag{2.12}$$

The result of this calculation is not written down explicitly due to the shear length of the expression. The external field is transformed into local coordinates by application of the rotation matrix $R_{\mathrm{L}\to\mathrm{M}}$ defined above.

$$\boldsymbol{H}_{\mathrm{ext}} = H \begin{pmatrix} \sin(\theta)\sin(\theta_H)\cos(\varphi-\varphi_H) + \cos(\theta)\cos(\theta_H) \\ -\sin(\theta_H)\sin(\varphi-\varphi_H) \\ \sin(\theta)\cos(\theta_H) - \cos(\theta)\sin(\theta_H)\cos(\varphi-\varphi_H) \end{pmatrix} \tag{2.13}$$

Subsequently, the expression defining equilibrium position is computed. To do so, the static torque is calculated by inserting the effective field and the equilibrium magnetization, given by

$$\boldsymbol{m}_{\mathrm{eq}} = \begin{pmatrix} 1 \\ 0 \\ 0 \end{pmatrix} \tag{2.14}$$

into the equilibrium condition:

$$\boldsymbol{T}_{\mathrm{eq}} = -\gamma \boldsymbol{H}_{\mathrm{eff}} \times \boldsymbol{m}_{\mathrm{eq}} + \gamma\tau_{\mathrm{DL,s}} \boldsymbol{m}_{\mathrm{eq}} \times \left(\boldsymbol{m}_{\mathrm{eq}} \times \boldsymbol{\sigma}_{\mathrm{DL,s}}\right) \stackrel{!}{=} (0,0,0) \tag{2.15}$$

As a result, two equations are obtained that both have to be fulfilled:

$$\begin{aligned}\boldsymbol{T}_{\mathrm{eq},y'} \propto & \left(-\frac{1}{2}N_z\sin(2\theta) + \sin(\theta)\cos(\theta)\sin(\varphi)^2 N_y\right) M_{\mathrm{s}} \\ & + \left(\sin(\theta)\cos(\theta_H) - \cos(\theta)\sin(\theta_H)\cos(-\varphi+\varphi_H)\right) H \\ & -\sin(2\theta)\cos(\varphi-\varphi_u)^2 \frac{K_{\mathrm{ip,u}}}{\mu_0 M_{\mathrm{s}}} + \sin(2\theta)\frac{K_{\mathrm{oop}}}{\mu_0 M_{\mathrm{s}}} - \frac{\tau_{\mathrm{DL,s}}}{\mu_0}\sin\left(-\varphi+\varphi_{\mathrm{DL,s}}\right) \stackrel{!}{=} 0\end{aligned} \tag{2.16}$$

and

$$\begin{aligned}\boldsymbol{T}_{\mathrm{eq},z'} \propto & \frac{1}{4}\left(\cos(-2\varphi+\theta)-\cos(2\varphi+\theta)\right) N_y M_\mathrm{s} - \sin(\theta_H)\sin(-\varphi+\varphi_H) H \\ & + \cos(\theta)\cos\big(\varphi-\varphi_{\mathrm{DL,s}}\big)\frac{\tau_{\mathrm{DL,s}}}{\mu_0} + \sin(\theta)\sin(2\varphi-2\varphi_u)\frac{K_{\mathrm{ip,u}}}{\mu_0 M_\mathrm{s}} \stackrel{!}{=} 0\end{aligned} \tag{2.17}$$

It is evident that these equations cannot be solved analytically to obtain explicit formulas for θ, φ in general cases.

The driving fields can be defined in the local coordinate system because they have no influence on the equilibrium position. The actual strength of the driving field components in the local system can be calculated for a given equilibrium position and torques given in the laboratory system. Therefore, the driving Oersted field / field-like SOT is defined as

$$\boldsymbol{h}_\mathrm{d}(t) = \begin{pmatrix} h_{x'} \\ h_{y'} \\ h_{z'} \end{pmatrix} \mathrm{e}^{i\omega t} \tag{2.18}$$

and the driving damping-like SOT polarization vector is defined as

$$\boldsymbol{\sigma}_{\mathrm{DL,d}}(t) = \begin{pmatrix} \sigma_{\mathrm{DL,d},x'} \\ \sigma_{\mathrm{DL,d},y'} \\ \sigma_{\mathrm{DL,d},z'} \end{pmatrix} \mathrm{e}^{i\omega t}. \tag{2.19}$$

The ansatz for the magnetization is, as explained in the FMR section,

$$\boldsymbol{m}(t) = \begin{pmatrix} 1 \\ \Delta m_{y'} \\ \Delta m_{z'} \end{pmatrix} \mathrm{e}^{i\omega t}. \tag{2.20}$$

All torques and the ansatz for $\boldsymbol{m}(t)$ are subsequently inserted into the LLG equation Eq. (1.21) and the resulting set of coupled equations is linearized, i.e. only terms linear in $\Delta m_{y'}, \Delta m_{z'}$ and the components of $\boldsymbol{\sigma}_{\mathrm{DL,d}}, \boldsymbol{h}_\mathrm{d}$ are kept. Additionally, the equilibrium conditions are used to eliminate some terms and to reduce the set of equations from three to two. It is possible to define the abbreviations $\mathfrak{H}_0, \mathfrak{H}_1, \mathfrak{H}_2$ and $\mathfrak{s}$ in order to bring the set of equations down to a very simple form:

$$\begin{pmatrix} -\mathfrak{H}_2 - \mathfrak{s} - \frac{i\omega}{\mu_0\gamma} & -\mathfrak{H}_0 - \frac{i\alpha\omega}{\mu_0\gamma} \\ -\mathfrak{H}_1 - \frac{i\alpha\omega}{\mu_0\gamma} & -\mathfrak{H}_2 - \mathfrak{s} - \frac{i\omega}{\mu_0\gamma} \end{pmatrix} \cdot \begin{pmatrix} \Delta m_{y'} \\ \Delta m_{z'} \end{pmatrix} = \begin{pmatrix} h_{z'} - \sigma_{\mathrm{DL,d},y'} \\ h_{y'} - \sigma_{\mathrm{DL,d},z'} \end{pmatrix}. \tag{2.21}$$

From this result, the generalized driving fields are taken. The solution to this system of equations is given by the susceptibility Eq. (3.8) written down in the main text.

The explicit form of the terms are:

$$\begin{aligned}\mathfrak{H}_0 = \quad & M_\mathrm{s}\left[-N_z\cos(2\theta)+\cos(2\theta)\sin(\varphi)^2 N_y\right] \\ & + H\left[\sin(\theta)\sin(\theta_H)\cos(-\varphi+\varphi_H)+\cos(\theta)\cos(\theta_H)\right] \\ & - \frac{2K_{\mathrm{ip,u}}}{\mu_0 M_\mathrm{s}}\cos(2\theta)\cos(\varphi-\varphi_u)^2 \\ & + \frac{2K_{\mathrm{oop}}}{\mu_0 M_\mathrm{s}}\cos(2\theta)\end{aligned} \tag{2.22}$$

$$\begin{aligned}\mathfrak{H}_1 = \; & M_\mathrm{s}\left[-N_z\cos(\theta)^2+(\frac{1}{2}\cos(\theta)^2-\frac{1}{4}(\cos(2\theta)-3)\cos(2\varphi))N_y\right] \\ & + H\left[\sin(\theta)\sin(\theta_H)\cos(-\varphi+\varphi_H)+\cos(\theta)\cos(\theta_H)\right] \\ & + \frac{K_{\mathrm{oop}}}{\mu_0 M_\mathrm{s}}\left[\cos(2\theta)+1\right] \\ & + \frac{K_{\mathrm{ip,u}}}{\mu_0 M_\mathrm{s}}\left[-\frac{1}{2}(\cos(2\theta)-3)\cos(2\varphi-2\varphi_u)-\cos(\theta)^2\right]\end{aligned} \tag{2.23}$$

$$\begin{aligned}\mathfrak{H}_2 = \; & \frac{1}{4}N_y M_\mathrm{s}\left[\sin(-2\varphi+\theta)-\sin(2\varphi+\theta)\right] \\ & - \frac{K_{\mathrm{ip,u}}}{\mu_0 M_\mathrm{s}}\cos(\theta)\sin(2\varphi-2\varphi_u)\end{aligned} \tag{2.24}$$

$$\mathfrak{s} = -\frac{\tau_{\mathrm{DL,s}}}{\mu_0}\sin(\theta)\cos\big(\varphi-\varphi_{\mathrm{DL,s}}\big). \tag{2.25}$$

These expressions are used to justify the approximations made in the derivation of the simpler equations describing the different experiments.
Especially the assumption $\theta = 90°$, which is made since both external field and demagnetization force the magnetization to lie ip, leads to great simplification:

$$\begin{aligned}\mathfrak{H}_0 &= M_{\mathrm{eff}} - N_y M_\mathrm{s}\sin(\varphi)^2 + H\cos(-\varphi+\varphi_H) + \frac{2K_{\mathrm{ip,u}}}{\mu_0 M_\mathrm{s}}\cos(-\varphi+\varphi_u)^2 \\ \mathfrak{H}_1 &= M_\mathrm{s} N_y\cos(2\varphi) + H\cos(-\varphi+\varphi_H) + \frac{2K_{\mathrm{ip,u}}}{\mu_0 M_\mathrm{s}}\cos(2\varphi_u-2\varphi) \\ \mathfrak{H}_2 &= 0 \\ \mathfrak{s} &= -\sin(\varphi)\frac{\tau_{\mathrm{DL,s}}}{\mu_0}\end{aligned} \tag{2.26}$$

C. Static Equilibrium Change

Recently, it has been shown that the strength of SOTs can elegantly be determined by measuring the small shift in the equilibrium condition due to an applied dc current. This technique is mostly used for perpendicular magnetized samples because it does not depend on the value of the damping constant which is usually large in those systems, leading to a huge linewidth that makes FMR measurements extremely challenging. However, the method itself is very generic and can, in principle, be used for ip magnetized samples, too. In this work, the shift in m_z is measured by static MOKE which gives access to the damping-like SOT and the energy landscape of the FM as will be shown in the following. In analogy to the FMR case, the full magnetization vector is written as $\boldsymbol{m} = \boldsymbol{m}_{\mathrm{eq}} + \Delta\boldsymbol{m}$, where the small $\Delta\boldsymbol{m} = \Delta m_{y'} + \Delta m_{z'}$ is static and results from a small torque $\boldsymbol{d}$ created by a field or a SOT in analogy to the FMR case only that the driving torque now is static [Fan14; Fan13; Gar13]. The deviation from the equilibrium position can be described by taking the limit $\omega \to 0$ in the (not approximated) susceptibility tensor Eq. (3.8). In addition, $\mathfrak{s} = 0$ because it is assumed that the equilibrium is given without SOT present. The result is a generally valid formulation of the static susceptibility (with arbitrary θ, φ), which contains off-diagonal elements $\frac{-\mathfrak{H}_2}{\mathfrak{H}_0\mathfrak{H}_1}$.
In an actual measurement, the magnetization component m_z in the laboratory coordinate system is measured such that the equilibrium magnetization must be pulled ip for quantitative analysis (in this case, the z-axes of laboratory and local coordinate system coincide). For perpendicular magnetized samples, this is done by applying an external ip field that is strong enough to saturate $\boldsymbol{m}$ ip, resulting in $\mathfrak{H}_2^2 \approx 0$ and $\frac{\mathfrak{H}_2}{\mathfrak{H}_0\mathfrak{H}_1} \approx 0$. In this case, the static susceptibility reduces to

$$\Delta\boldsymbol{m} = \boldsymbol{\chi}_{\mathrm{static}}\boldsymbol{d} = \begin{pmatrix} \frac{1}{\mathfrak{H}_1} & 0 \\ 0 & \frac{1}{\mathfrak{H}_0} \end{pmatrix} \begin{pmatrix} d_y \\ d_z. \end{pmatrix} \tag{3.1}$$

The small displacement torques are $d_{y'} = (h_{y'} - \frac{\tau_{\mathrm{DL}}}{\mu_0}\sigma_{z'})$ and $d_{z'} = (h_{z'} - \frac{\tau_{\mathrm{DL}}}{\mu_0}\sigma_{y'})$. In this case both torques are real due to the static nature[1]. It is therefore found that an ip field induces a shift of the magnetization ip and that an oop field has the same effect as a damping-like SOT that results from an ip polarized spin current. The change in $m_z = m_{z'}$

[1] This result is in accordance with the deviation given in the supplementary material of [Fan13].

is given by

$$\Delta m_Z = \frac{h_z - \frac{\tau_{\mathrm{DL}}}{\mu_0} cos(\varphi)}{\mathfrak{H}_0} = \frac{h_z - \frac{\tau_{\mathrm{DL}}}{\mu_0} cos(\varphi)}{H + M_{\mathrm{eff}}} \tag{3.2}$$

where the last equality is valid for the case of $H_{\mathrm{eff}} = H_{\mathrm{ext}} + H_{\mathrm{dem,thin\ film}} + H_{\mathrm{oop}}$ as discussed above. This is the first order approximation used for the Pt/Co layers used in this work. The oop shift due to $h_{z'}$ is independent of the ip angle φ whereas the SOT effect scales with $cos(\varphi)$. One very important consequence of this dependence is the fact that the change in m_z changes sign if φ is rotated by 180°, that is, if the external field is reversed. It is therefore possible to separate the contributions resulting from an oop field and from a damping-like SOT by reversing the field. From the symmetry it holds $\Delta m_{z,\mathrm{SOT}} = \frac{\Delta m_z(H) - \Delta m_z(-H)}{2}$ and $\Delta m_{z,h_z} = \frac{\Delta m_z(H) + \Delta m_z(H)}{2}$. If the absolute value of Δm_z can be measured, such a measurement allows to quantify τ_{DL}. Additionally, the method can be used to straight forwardly measure M_{eff} from a field-dependent measurement by fitting to the $\frac{1}{H+M_{\mathrm{eff}}}$ dependence. This is very helpful to measure M_{eff} in structured, perpendicularly magnetized samples where other methods are hard to realize.

The signal strength of this method is governed by $H+M_{\mathrm{eff}}$, which is fundamentally different for ip ($M_{\mathrm{eff}} > 0$) and oop ($M_{\mathrm{eff}} < 0$) magnetized samples. Realizing that for an oop magnetized sample $H + M_{\mathrm{eff}} = 0$ for the H value at which the magnetization is just pulled ip, it is clear that a relatively large Δm_z can be obtained even with a small shifting torque if the external field is varied in the vicinity of the transition.

Assuming a reasonable value for $\frac{\tau_{\mathrm{DL}}}{j_{\mathrm{c}}} = 60\,\frac{\mathrm{fT\,m^2}}{\mathrm{A}}$ and a current density of $j_{\mathrm{c}} = 1 \times 10^{11}\,\frac{\mathrm{A}}{\mathrm{m^2}}$ leads to a $\tau_{\mathrm{DL}} = 6\,\mathrm{mT}$ that has to be detected. For a perpendicular magnetized Pt/Co layer, at a H value such that $\mu_0(H + M_{\mathrm{eff}}) = 100\,\mathrm{mT}$ this results in $\Delta m_{z,\mathrm{SOT}} = 0.06 \rightarrow \delta\theta = 3.4°$. For a Pt/Py(4 nm) layer however, $\mu_0 M_{\mathrm{eff}}\ 1\,\mathrm{T}$, bounding the change in m_z to $\Delta m_{z,\mathrm{SOT,max}} = 0.006 \rightarrow \delta\theta = 0.34°$ even for zero applied field.

Note however, that the susceptibility approach only holds if the equilibrium position is fixed by the external field and the change in the total $\boldsymbol{m}$ (also the ip components) induced by the SOT is small, which only holds if $H \gg \tau_{\mathrm{DL}}$. The strength of this method therefore lies in the application for perpendicular magnetized samples.

The method is also usable for determining the energy landscape of arbitrary oop magnetized samples by the application of a static ip field and a slowly varying oop field of some mT. In this setup, a lock-in technique can be used to detect Δm_z at different ip field angles and use Eq. (3.2) with an appropriate expression for $\mathfrak{H}_0$ to determine e.g. different anisotropy contributions.

Bibliography

[Abo13] G. S. Abo, Y. K. Hong, J. Park, J. Lee, W. Lee, and B. C. Choi. "Definition of Magnetic Exchange Length". In: *IEEE Trans. Magn.* **49** (2013), pp. 4937–4939. DOI: 10.1109/TMAG.2013.2258028.

[Aha98] A Aharoni. "Demagnetizing factors for rectangular ferromagnetic prisms". In: *J. Appl. Phys.* **83** (1998), pp. 3432–3434. DOI: 10.1063/1.367113.

[Ami16a] V. P. Amin and M. D. Stiles. "Spin transport at interfaces with spin-orbit coupling: Formalism". In: *Phys. Rev. B* **94** (2016), p. 104419. DOI: 10.1103/PhysRevB.94.104419.

[Ami16b] V. P. Amin and M. D. Stiles. "Spin transport at interfaces with spin-orbit coupling: Phenomenology". In: *Phys. Rev. B* **94** (2016), p. 104420. DOI: 10.1103/PhysRevB.94.104420.

[And08] K. Ando, S. Takahashi, K. Harii, K. Sasage, J. Ieda, S. Maekawa, and E. Saitoh. "Electric manipulation of spin relaxation using the spin hall effect". In: *Phys. Rev. Lett.* **101** (2008), p. 036601. DOI: 10.1103/PhysRevLett.101.036601.

[And11] K. Ando, S. Takahashi, J. Ieda, Y. Kajiwara, H. Nakayama, T. Yoshino, K. Harii, Y. Fujikawa, M. Matsuo, S. Maekawa, and E. Saitoh. "Inverse spin-Hall effect induced by spin pumping in metallic system". In: *J. Appl. Phys.* **109** (2011), p. 103913. DOI: 10.1063/1.3587173.

[And14] K. Ando, S. Fujita, J. Ito, S. Yuasa, Y. Suzuki, Y. Nakatani, T. Miyazaki, and H. Yoda. "Spin-transfer torque magnetoresistive random-access memory technologies for normally off computing (invited)". In: *J. Appl. Phys.* **115** (2014), p. 172607. DOI: 10.1063/1.4869828.

[And70] O. K. Andersen. "Electronic structure of the fcc transition metals Ir, Rh, Pt, and Pd". In: *Phys. Rev. B* **2** (1970), pp. 883–906. DOI: 10.1103/PhysRevB.2.883.

[Aro89] A. G. Aronov and Y. B. Lyanda-Geller. "Nuclear electric resonance and orientation of carrier spins by an electric field". In: *JETP Lett.* **50** (1989), p. 431.

[Aro91] A. G. Aronov, Y. B. Lyanda-Geller, and G. E. Pikus. "Spin polarization of electrons by an electric current". In: *JETP* **73** (1991), pp. 537–541.

[Art07] N. Artunc, M. D. Bilge, and G. Utlu. "The effects of grain boundary scattering on the electrical resistivity of single-layered silver and double-layered silver/chromium thin films". In: *Surf. Coatings Technol.* **201** (2007), pp. 8377–8381. DOI: 10.1016/j.surfcoat.2006.03.068.

[Art92] N. Artunc, S. Selvi, and Z. Z. Ozttirk. "The effects of surface and interface scattering on the electrical resistivity of Cu/Ag double-layered thin films". In: *Thin Solid Films* **221** (1992), pp. 207–213. DOI: 10.1016/0040-6090(92)90816-T.

[Ash76] N. W. Ashcroft and N. D. Mermin. *Solid State Physics*. Philadelphia: Saunders College, 1976.

[Avc12] C. O. Avci, K. Garello, I. M. Miron, G. Gaudin, S. Auffret, O. Boulle, and P. Gambardella. "Magnetization switching of an MgO/Co/Pt layer by in-plane current injection". In: *Appl. Phys. Lett.* **100** (2012), p. 212404. DOI: 10.1063/1.4719677.

[Aze11] A. Azevedo, L. H. Vilela-Leão, R. L. Rodríguez-Suárez, A. F. Lacerda Santos, and S. M. Rezende. "Spin pumping and anisotropic magnetoresistance voltages in magnetic bilayers: Theory and experiment". In: *Phys. Rev. B* **83** (2011), p. 144402. DOI: 10.1103/PhysRevB.83.144402.

[Bad91] S. Bader. "Smoke". In: *J. Magn. Magn. Mater.* **100** (1991), pp. 440–454. DOI: 10.1016/0304-8853(91)90833-V.

[Bai13a] L. Bai, P. Hyde, Y. S. Gui, C. M. Hu, V. Vlaminck, J. E. Pearson, S. D. Bader, and A. Hoffmann. "Universal method for separating spin pumping from spin rectification voltage of ferromagnetic resonance". In: *Phys. Rev. Lett.* **111** (2013), p. 217602. DOI: 10.1103/PhysRevLett.111.217602.

[Bai13b] M. Bailleul. "Shielding of the electromagnetic field of a coplanar waveguide by a metal film: Implications for broadband ferromagnetic resonance measurements". In: *Appl. Phys. Lett.* **103** (2013), p. 192405. DOI: 10.1063/1.4829367.

[Bai88] M. N. Baibich, J. M. Broto, A. Fert, F. N. Van Dau, F. Petroff, P. Eitenne, G. Creuzet, A. Friederich, and J. Chazelas. "Giant magnetoresistance of (001)Fe/(001)Cr magnetic superlattices". In: *Phys. Rev. Lett.* **61** (1988), pp. 2472–2475. DOI: 10.1103/PhysRevLett.61.2472.

[Bau14] H. Bauer. "Linear and nonlinear magnetization dynamics in thin ferromagnetic films and nanostructures". PhD thesis. Universität Regensburg, 2014.

[Bau17] M. Baumgartner, K. Garello, J. Mendil, C. O. Avci, E. Grimaldi, C. Murer, J. Feng, M. Gabureac, C. Stamm, Y. Acremann, S. Finizio, S. Wintz, J. Raabe, and P. Gambardella. "Spatially and time-resolved magnetization dynamics driven by spin–orbit torques". In: *Nat. Nanotechnol.* **12** (2017), pp. 980–986. DOI: 10.1038/nnano.2017.151.

[Bay06] C Bayer, J. Jorzick, S. O. Demokritov, A. N. Slavin, K. Y. Guslienko, D. Berkov, N. L. Gorn, M. P. Kostylev, and B. Hillebrands. "Spin-Wave Excitations in Finite Rectangular Elements". In: *Spin Dyn. Confin. Magn. Struct. III*. Ed. by B. Hillebrands and A. Thiaville. Vol. 111. Berlin: Springer Berlin Heidelberg, 2006.

[Bed10] D. Bedau, H. Liu, J. Z. Sun, J. A. Katine, E. E. Fullerton, S. Mangin, and A. D. Kent. "Spin-transfer pulse switching: From the dynamic to the thermally activated regime". In: *Appl. Phys. Lett.* **97** (2010), p. 262502. DOI: 10.1063/1.3532960.

[Bel15] M. Belmeguenai, J. P. Adam, Y. Roussigné, S. Eimer, T. Devolder, J. V. Kim, S. M. Cherif, A. Stashkevich, and A. Thiaville. "Interfacial Dzyaloshinskii-Moriya interaction in perpendicularly magnetized Pt/Co/AlOx ultrathin films measured by Brillouin light spectroscopy". In: *Phys. Rev. B* **91** (2015), 180405(R). DOI: 10.1103/PhysRevB.91.180405.

[Ben15] M. J. Benitez, A. Hrabec, A. P. Mihai, T. . A. Moore, G. Burnell, D McGrouther, C. H. Marrows, and S. McVitie. "Magnetic microscopy and topological stability of homochiral Néel domain walls in a Pt/Co/AlOx trilayer." In: *Nat. Commun.* **6** (2015), p. 8957. DOI: 10.1038/ncomms9957.

[Ber09] G. Bertotti, I. D. Mayergoyz, and C. Serpico. *Nonlinear Magnetization Dynamics in Nanostructures*. Elsevier, 2009.

[Bi14] C. Bi, L. Huang, S. Long, Q. Liu, Z. Yao, L. Li, Z. Huo, L. Pan, and M. Liu. "Thermally assisted magnetic switching of a single perpendicularly magnetized layer induced by an in-plane current". In: *Appl. Phys. Lett.* **105** (2014), p. 022407. DOI: 10.1063/1.4890539.

[Bin89] G. Binasch, P. Grünberg, F. Saurenbach, and W. Zinn. "Enhanced magnetoresistance in layered magnetic structures with antiferromagnetic interlayer exchange". In: *Phys. Rev. B* **39** (1989), pp. 4828–4830. DOI: 10.1103/PhysRevB.39.4828.

[Blu01] S. Blundell. *Magnetism in Condensed Matter*. Oxford: Oxford University Press, 2001.

[Boo15] C. T. Boone, J. M. Shaw, H. T. Nembach, and T. J. Silva. "Spin-scattering rates in metallic thin films measured by ferromagnetic resonance damping enhanced by spin-pumping". In: *J. Appl. Phys.* **117** (2015), p. 223910. DOI: 10.1063/1.4922581.

[Bos17] A. Bose, S. Dutta, S. Bhuktare, H. Singh, and A. A. Tulapurkar. "Sensitive measurement of spin-orbit torque driven ferromagnetic resonance detected by planar Hall geometry". In: *Appl. Phys. Lett.* **111** (2017), p. 162405. DOI: 10.1063/1.4999948.

[Bra00] A. Brataas, Y. V. Nazarov, and G. E. W. Bauer. "Finite-Element Theory of Transport in Ferromagnet-Normal Metal Systems". In: *Phys. Rev. Lett.* **84** (2000), pp. 2481–2484. DOI: 10.1103/PhysRevLett.84.2481.

[Bra01] A. Brataas. "Spin-transport in multi-terminal normal metal-ferromagnet systems with non-collinear magnetizations". In: *Eur. Phys. J. B* **22** (2001), pp. 99–110. DOI: 10.1007/PL00011139.

[Bra06] A. Brataas, G. E. W. Bauer, and P. J. Kelly. "Non-collinear magnetoelectronics". In: *Phys. Rep.* **427** (2006), pp. 157–255. DOI: 10.1016/j.physrep.2006.01.001.

[Bru89] P. Bruno. "Tight-binding approach to the orbital magnetic moment and magnetocrystalline of transition-metal monolayers". In: *Phys. Rev. B* **39** (1989), pp. 865–868. DOI: http://dx.doi.org/10.1103/PhysRevB.39.865.

[But00] W. H. Butler, X.-G. Zhang, and J. M. MacLaren. "Semiclassical Theory of Spin-Dependent Transport in Magnetic Multilayers". In: *J. Supercond.* **13** (2000), pp. 221–238. DOI: 10.1023/A:1007799916385.

[Byc84] Y. a. Bychkov and E. I. Rashba. "Properties of a 2D electron gas with uplifted spectral degeneracy". In: *Sov. J. Exp. Theor. Phys. Lett.* **39** (1984), pp. 66–69.

[Cam06] J. M. Camacho and A. I. Oliva. "Surface and grain boundary contributions in the electrical resistivity of metallic nanofilms". In: *Thin Solid Films* **515** (2006), pp. 1881–1885. DOI: 10.1016/j.tsf.2006.07.024.

[Cam16] M. Caminale, A. Ghosh, S. Auffret, U. Ebels, K. Ollefs, F. Wilhelm, A. Rogalev, and W. E. Bailey. "Spin pumping damping and magnetic proximity effect in Pd and Pt spin-sink layers". In: *Phys. Rev. B* **94** (2016), p. 014414. DOI: 10.1103/PhysRevB.94.014414.

[Cas12] V. Castel, N. Vlietstra, J. Ben Youssef, and B. J. Van Wees. "Platinum thickness dependence of the inverse spin-Hall voltage from spin pumping in a hybrid yttrium iron garnet/platinum system". In: *Appl. Phys. Lett.* **101** (2012), p. 132414. DOI: 10.1063/1.4754837.

[Cel97] Z. Celinski, K. B. Urquhart, and B. Heinrich. "Using ferromagnetic resonance to measure magnetic moments of ultrathin films (abstract)". In: *J. Magn. Magn. Mater.* **166** (1997), pp. 6–26. DOI: 10.1063/1.364982.

[Cha07] C. Chappert, A. Fert, and F. N. Van Dau. "The emergence of spin electronics in data storage". In: *Nat. Mater.* **6** (2007), pp. 813–823. DOI: 10.1038/nmat2024.

[Cha14] J. Y. Chauleau, H. G. Bauer, H. S. Körner, J. Stigloher, M. Härtinger, G. Woltersdorf, and C. H. Back. "Self-consistent determination of the key spin-transfer torque parameters from spin-wave Doppler experiments". In: *Phys. Rev. B* **89** (2014), p. 020403. DOI: 10.1103/PhysRevB.89.020403.

[Che15] K. Chen and S. Zhang. "Spin pumping in the presence of spin-orbit coupling". In: *Phys. Rev. Lett.* **114** (2015), p. 126602. DOI: 10.1103/PhysRevLett.114.126602.

[Che16] L. Chen, M. Decker, M. Kronseder, R. Islinger, M. Gmitra, D. Schuh, D. Bougeard, J. Fabian, D. Weiss, and C. H. Back. "Robust spin-orbit torque and spin-galvanic effect at the Fe/GaAs (001) interface at room temperature". In: *Nat. Commun.* **7** (2016), p. 13802. DOI: 10.1038/ncomms13802.

[Chi10] S. Chikazumi. *Physics of Ferromagnetism*. 2nd. Oxford: Oxford University Press, 2010.

[Cho15] J. Cho, N.-H. Kim, S. Lee, J.-S. Kim, R. Lavrijsen, A. Solignac, Y. Yin, D.-S. Han, N. J. J. Van Hoof, H. J. M. Swagten, B. Koopmans, and C.-Y. You. "Thickness dependence of the interfacial Dzyaloshinskii-Moriya interaction in inversion symmetry broken systems". In: *Nat. Commun.* **6** (2015), p. 7635. DOI: 10.1038/ncomms8635.

[Coe10] J. M. D. Coey. *Magnetism and Magnetic Materials*. 1st ed. Cambridge: Cambridge University Press, 2010.

[Cré98] A. Crépieux and C. Lacroix. "Dzyaloshinsky-Moriya interactions induced by symmetry breaking at a surface". In: *J. Magn. Magn. Mater.* **182** (1998), pp. 341–349. DOI: 10.1016/S0304-8853(97)01044-5.

[Cub14] M. Cubukcu, O. Boulle, M. Drouard, K. Garello, C. O. Avci, I. M. Miron, J. Langer, B. Ocker, P. Gambardella, and G. Gaudin. "Spin-orbit torque magnetization switching of a three-terminal perpendicular magnetic tunnel junction". In: *Appl. Phys. Lett.* **104** (2014), p. 042406. DOI: 10.1063/1.4863407.

[Dec12] M. M. Decker. "Spin Hall induced Spin Transfer Torque". Master's Thesis. Universität Regensburg, 2012.

[Dec17] M. M. Decker, M. S. Wörnle, A. Meisinger, M. Vogel, H. S. Körner, G. Y. Shi, C. Song, M. Kronseder, and C. H. Back. "Time Resolved Measurements of the Switching Trajectory of Pt/Co Elements Induced by Spin-Orbit Torques". In: *Phys. Rev. Lett.* **118** (2017), p. 257201. DOI: 10.1103/PhysRevLett.118.257201.

[Dem11a] V. E. Demidov, S. Urazhdin, E. R. J. Edwards, M. D. Stiles, R. D. McMichael, and S. O. Demokritov. "Control of magnetic fluctuations by spin current". In: *Phys. Rev. Lett.* **107** (2011), p. 107204. DOI: 10.1103/PhysRevLett.107.107204.

[Dem11b] V. E. Demidov, S Urazhdin, E. R. J. Edwards, and S. O. Demokritov. "Wide-range control of ferromagnetic resonance by spin Hall effect". In: *Appl. Phys. Lett.* **99** (2011), p. 172501. DOI: 10.1063/1.3655908.

[Dim83] R Dimmich and F Warkusz. "THE ELECTRICAL CONDUCTANCE OF CONTINUOUS THIN METALLIC DOUBLE-LAYER FILMS". In: *Thin Solid Films* **109** (1983), pp. 103–114. DOI: 10.1016/0040-6090(83)90130-X.

[Dre55] G. Dresselhaus. "Spin-Orbit Coupling Effects in Zinc Blende Structures". In: *Phys. Rev.* **100** (1955), pp. 580–586. DOI: 10.1103/PhysRev.100.580.

[Dur16] C. J. Durrant, R. J. Hicken, Q. Hao, and G. Xiao. "Scanning Kerr microscopy study of current-induced switching in Ta/CoFeB/MgO films with perpendicular magnetic anisotropy". In: *Phys. Rev. B* **93** (2016), p. 014414. DOI: 10.1103/PhysRevB.93.014414.

[Dya07] M. I. Dyakonov. "Magnetoresistance due to edge spin accumulation". In: *Phys. Rev. Lett.* **99** (2007), p. 126601. DOI: 10.1103/PhysRevLett.99.126601.

[Dya12] M. I. Dyakonov. "Spin Hall Effect". In: *Proc.SPIE* **7036** (2012), 70360R. DOI: 10.1117/12.798110.

[Dya71a] M. I. Dyakonov and V. I. Perel'. "Current-induced spin orientation of electrons in semiconductors". In: *Phys. Lett. A* **35** (1971), pp. 459–460. DOI: http://dx.doi.org/10.1016/0375-9601(71)90196-4.

[Dya71b] M. I. Dyakonov and V. I. Perel'. "Possibility of Orienting Electron Spins with Current". In: *Sov. J. Exp. Theor. Phys. Lett.* **13** (1971), p. 467.

[Dya71c] M. I. Dyakonov and V. I. Perel'. "Spin Orientation of Electrons Associated With the Interband Absorption of Light in Semiconductors". In: *Sov. Phys. JETP* **33** (1971), p. 1053.

[Dzy58] I. Dzyaloshinsky. "A thermodynamic theory of "weak" ferromagnetism of antiferromagnetics". In: *J. Phys. Chem. Solids* **4** (1958), pp. 241–255. DOI: 10.1016/0022-3697(58)90076-3.

[Ede90] V. M. Edelstein. "SPIN POLARIZATION OF CONDUCTION ELECTRONS INDUCED BY ELECTRIC CURRENT IN TWO-DIMENSIONAL ASYMMETRIC ELECTRON SYSTEMS". In: *Solid State Commun.* **73** (1990), pp. 233–235. DOI: 10.1016/0038-1098(90)90963-C.

[Edw12] E. Edwards. "Study of Spin Waves in In-plane Magnetized Thin Films by means of Brillouin Light Scattering and Magneto-optical Kerr Effect". Ph.D. thesis. Universität Münster, 2012.

[Efr86] B. Efron and R. Tibshirani. "Bootstrap Methods for Standard Errors, Confidence Intervals, and Other Measures of Statistical Accuracy". In: *Stat. Sci.* **1** (1986), pp. 54–77. DOI: 10.1214/ss/1177013817.

[Efr93] B. Efron and R. J. Tibshirani. *Introduction to the Bootstrap World*. 2nd ed. New York: Chapman and Hall, 1993.

[Ell54] R. J. Elliott. "Theory of the effect of spin-Orbit coupling on magnetic resonance in some semiconductors". In: *Phys. Rev.* **96** (1954), pp. 266–279. DOI: 10.1103/PhysRev.96.266.

[Emo13] S. Emori, U. Bauer, S.-M. Ahn, E. Martinez, and G. S. D. Beach. "Current-driven dynamics of chiral ferromagnetic domain walls." In: *Nat. Mater.* **12** (2013), pp. 611–6. DOI: 10.1038/nmat3675.

[Emo14] S. Emori, E. Martinez, K. J. Lee, H. W. Lee, U. Bauer, S. M. Ahn, P. Agrawal, D. C. Bono, and G. S. D. Beach. "Spin Hall torque magnetometry of Dzyaloshinskii domain walls". In: *Phys. Rev. B* **90** (2014), p. 184427. DOI: 10.1103/PhysRevB.90.184427.

[Emo16] S. Emori, T. Nan, A. M. Belkessam, X. Wang, A. D. Matyushov, C. J. Babroski, Y. Gao, H. Lin, and N. X. Sun. "Interfacial spin-orbit torque without bulk spin-orbit coupling". In: *Phys. Rev. B* **93** (2016), 180402(R). DOI: 10.1103/PhysRevB.93.180402.

[Fab07] J. Fabian, A. Matos-Abiague, C. Ertler, P. Stano, and P. Zutic. "SEMICONDUCTOR SPINTRONICS". In: *Acta Phys. Slovaca* **57** (2007), pp. 565–907.

[Fan13] X. Fan, J. Wu, Y. Chen, M. J. Jerry, H. Zhang, and J. Q. Xiao. "Observation of the nonlocal spin-orbital effective field." In: *Nat. Commun.* **4** (2013), p. 1799. DOI: 10.1038/ncomms2709.

[Fan14] X. Fan, H. Celik, J. Wu, C. Ni, K.-j. Lee, V. O. Lorenz, and J. Q. Xiao. "Quantifying interface and bulk contributions to spin-orbit torque in magnetic bilayers." In: *Nat. Commun.* **5** (2014), p. 3042. DOI: 10.1038/ncomms4042.

[Fas95] J. Fassbender, C. Mathieu, B. Hillebrands, G. Güntherodt, R. Jungblut, and M. T. Johnson. "Identification of magnetocrystalline and magnetoelastic anisotropy contributions in ultrathin epitaxial Co(110) films". In: *J. Magn. Magn. Mater.* **148** (1995), pp. 156–157. DOI: 10.1016/0304-8853(95)00189-1.

[Few99] P. F. Fewster. "X-ray analysis of thin films and multilayers". In: *Reports Prog. Phys.* **59** (1999), pp. 1339–1407. DOI: 10.1088/0034-4885/59/11/001.

[Fis79] G. Fischer. "Die geometrische Quantisierung des Elektronen-Energiespektrums in sehr dünnen Platinschichten". PhD thesis. Universität Regensburg, 1979.

[Fis80] G. Fischer, H. Hoffmann, and J. Vancea. "Mean free path and density of conductance electrons in platinum determined by the size effect in extremely thin films". In: *Phys. Rev. B* **22** (1980), pp. 6065–6073. DOI: 10.1103/PhysRevB.22.6065.

[Fre14] F. Freimuth, S. Blügel, and Y. Mokrousov. "Spin-orbit torques in Co/Pt(111) and Mn/W(001) magnetic bilayers from first principles". In: *Phys. Rev. B* **90** (2014), p. 174423. DOI: 10.1103/PhysRevB.90.174423.

[Fuc38] K. Fuchs and N. F. Mott. "The conductivity of thin metallic films according to the electron theory of metals". In: *Math. Proc. Cambridge Philos. Soc.* **34** (1938), p. 100. DOI: 10.1017/S0305004100019952.

[Fuk16] S. Fukami, C. Zhang, S. DuttaGupta, A. Kurenkov, and H. Ohno. "Magnetization switching by spin-orbit torque in an antiferromagnet-ferromagnet bilayer system". In: *Nat. Mater.* **15** (2016), pp. 535–542. DOI: 10.1038/nmat4566.

[Gam03] P. Gambardella, S. Rusponi, M. Veronese, S. S. Dhesi, C. Grazioli, A Dallmeyer, I. Cabria, R. Zeller, P. H. Dederichs, K. Kern, C. Carbone, and H. Brune. "Giant magnetic anisotropy of single cobalt atoms and nanoparticles". In: *Science* **300** (2003), p. 1130. DOI: 10.1126/science.1082857.

[Gam11] P. Gambardella and I. M. Miron. "Current-induced spin-orbit torques". In: *Philos. Trans. R. Soc. A* **369** (2011), pp. 3175–3197. DOI: 10.1098/rsta.2010.0336.

[Gan14] S. D. Ganichev and L. E. Golub. "Interplay of Rashba/Dresselhaus spin splittings probed by photogalvanic spectroscopy - A review". In: *Phys. Status Solidi* **251** (2014), pp. 1801–1823. DOI: 10.1002/pssb.201350261.

[Gan16] S. D. Ganichev, M. Trushin, and J. Schliemann. "Spin polarisation by current". In: *arXiv* **1606.02043** (2016). DOI: http://arxiv.org/abs/1606.02043.

[Gar13] K. Garello, I. M. Miron, C. O. Avci, F. Freimuth, Y. Mokrousov, S. Blügel, S. Auffret, O. Boulle, G. Gaudin, and P. Gambardella. "Symmetry and magnitude of spin-orbit torques in ferromagnetic heterostructures." In: *Nat. Nanotechnol.* **8** (2013), p. 587. DOI: 10.1038/nnano.2013.145.

[Gar14] K. Garello, C. O. Avci, I. M. Miron, M. Baumgartner, A. Ghosh, S. Auffret, O. Boulle, G. Gaudin, and P. Gambardella. "Ultrafast magnetization switching by spin-orbit torques". In: *Appl. Phys. Lett.* **105** (2014), p. 212402. DOI: 10.1063/1.4902443.

[Gil55] T. L. Gilbert. "Abstract". In: *Phys. Rev.* **100** (1955), p. 1243.

[Gre72] D Greig and D Livesey. "The Hall coefficient of dilute palladium and platinum alloys". In: *J. Phys. F Met. Phys* **2** (1972), p. 699. DOI: 10.1088/0305-4608/2/4/014.

[Gri03] G Grinstein and R. H. Koch. "Coarse graining in micromagnetics." In: *Phys. Rev. Lett.* **90** (2003), p. 207201. DOI: 10.1103/PhysRevLett.90.207201.

[Gur63] A. Gurevich. *Ferrites At Microwave Frequencies*. Ed. by A. Gurevich. London: Heywood and Company LTD, 1963.

[Gur93] B. A. Gurney, V. S. Speriosu, J.-P. Nozieres, H. Lefakis, D. R. Wilhoit, and O. U. Need. "Direct Measurement of Spin-Dependent Conduction-Electron Mean Free Paths in Ferromagnetic Metals". In: *Phys. Rev. L* **71** (1993), pp. 4023–4026. DOI: 10.1103/PhysRevLett.71.4023.

[Gur96] A. Gurevich and G. Melkov. *Magnetization Oscillations and Waves*. Ed. by A. Gurevich and G. Melkov. 1st ed. Boca Raton: CRC Press, 1996.

[Han13a] P. M. Haney, H.-W. Lee, K.-J. Lee, A. Manchon, and M. D. Stiles. "Current induced torques and interfacial spin-orbit coupling: Semiclassical modeling". In: *Phys. Rev. B* **87** (2013), p. 174411. DOI: 10.1103/PhysRevB.87.174411.

[Han13b] P. M. Haney, H. W. Lee, K. J. Lee, A. Manchon, and M. D. Stiles. "Current-induced torques and interfacial spin-orbit coupling". In: *Phys. Rev. B* **88** (2013), p. 214417. DOI: 10.1103/PhysRevB.88.214417.

[Han16] D. S. Han, N. H. Kim, J. S. Kim, Y. Yin, J. W. Koo, J. Cho, S. Lee, M. Kläui, H. J. M. Swagten, B. Koopmans, and C. Y. You. "Asymmetric hysteresis for probing Dzyaloshinskii-Moriya interaction". In: *Nano Lett.* **16** (2016), pp. 4438–4446. DOI: 10.1021/acs.nanolett.6b01593.

[Har11] M. Harder, Z. X. Cao, Y. S. Gui, X. L. Fan, and C. M. Hu. "Analysis of the line shape of electrically detected ferromagnetic resonance". In: *Phys. Rev. B* **84** (2011), p. 054423. DOI: 10.1103/PhysRevB.84.054423.

[Har16] M. Harder, Y. Gui, and C. M. Hu. "Electrical detection of magnetization dynamics via spin rectification effects". In: *Phys. Rep.* **661** (2016), pp. 1–59. DOI: 10.1016/j.physrep.2016.10.002.

[Has12] S. Hasegawa. "Reflection High-Energy Electron Diffraction". In: *Charact. Mater.* Ed. by E. N. Kaufmann. John Wiley & Sons, Inc., 2012, pp. 1925–1938. DOI: 10.1002/0471266965.com139.

[Hel17] F. Hellman, M. S. Division, L. Berkeley, A. Hoffmann, G. S. D. Beach, E. E. Fullerton, A. H. Macdonald, and D. C. Ralph. "Interface-Induced Phenomena in Magnetism". In: *Rev. Mod. Phys.* **89** (2017), pp. 1–79. DOI: https://doi.org/10.1103/RevModPhys.89.025006.

[Hen16] Y. Henry, O. Gladii, and M. Bailleul. "Propagating spin-wave normal modes: A dynamic matrix approach using plane-wave demagnetizating tensors". In: *arXiv* **1611.06153** (2016). DOI: http://arxiv.org/abs/1611.06153.

[Her09] R. Hertel. *Micromagnetism - Lecture Notes of the 40th Spring School 2009 - Spintronics : From GMR to Quantum Information*. Ed. by S. Blügel, D. Bürgler, M. Morgenstern, C. M. Schneider, and R. Waser. Jülich: Forschungszentrum Jülich GmbH, Institut für Festkörperforschung, 2009, p. D1.

[Hir99] J. E. Hirsch. "Spin Hall Effect". In: *Phys. Rev. Lett.* **83** (1999), pp. 1834–1837. DOI: 10.1103/PhysRevLett.83.1834.

[Hof10] F. Hoffmann. "Magnetic anisotropies of (Ga,Mn)As fi lms and nanostructures". Ph.D. Thesis. University of Regensburg, 2010.

[Hur72] C. Hurd. *The Hall Effect in Metals and Alloys*. New York: Springer US, 1972.

[Här16] M. O. Härtinger. "Untersuchung magnetischer Materialien mit Methoden der Ferromagnetischen Resonanz". PhD thesis. Universtität Regensburg, 2016.

[Jia13] H. Jiao and G. E. W. Bauer. "Spin backflow and ac voltage generation by spin pumping and the inverse spin hall effect". In: *Phys. Rev. Lett.* **110** (2013), p. 217602. DOI: 10.1103/PhysRevLett.110.217602.

[Jur60] H. J. Juretschke. "Electromagnetic theory of dc effects in ferromagnetic resonance". In: *J. Appl. Phys.* **31** (1960), pp. 1401–1406. DOI: 10.1063/1.1735851.

[Kal86] B. A. Kalinikos and A. N. Slavin. "Theory of dipole-exchange spin wave spectrum for ferromagnetic films with mixed exchange boundary conditions". In: *J. Phys. C Solid State Phys.* **19** (1986), pp. 7013–7033. DOI: 10.1088/0022-3719/19/35/014.

[Kas14] S. Kasai, K. Kondou, H. Sukegawa, S. Mitani, K. Tsukagoshi, and Y. Otani. "Modulation of effective damping constant using spin Hall effect". In: *Appl. Phys. Lett.* **104** (2014), pp. 1–2. DOI: 10.1063/1.4867649.

[Kat04] Y. K. Kato, R. C. Myers, A. C. Gossard, and D. D. Awschalom. "Observation of the Spin Hall Effect in Semiconductors". In: *Science* **306** (2004), pp. 1910–1913. DOI: 10.1126/science.1105514.

[Kim15] N. H. Kim, D. S. Han, J. Jung, J. Cho, J. S. Kim, H. J. M. Swagten, and C. Y. You. "Improvement of the interfacial Dzyaloshinskii-Moriya interaction by introducing a Ta buffer layer". In: *Appl. Phys. Lett.* **107** (2015), p. 142408. DOI: 10.1063/1.4932550.

[Kim17] N.-H. Kim, J. Cho, J. Jung, D.-S. Han, Y. Yin, J.-S. Kim, H. J. M. Swagten, K. Lee, M.-H. Jung, and C.-Y. You. "Role of top and bottom interfaces of a Pt/Co/AlOx system in Dzyaloshinskii-Moriya interaction, interface perpendicular magnetic anisotropy, and magneto-optical Kerr effect". In: *AIP Adv.* **7** (2017), p. 035213. DOI: 10.1063/1.4978867.

[Kit48] C. Kittel. "On the theory of ferromagnetic resonance absorption". In: *Phys. Rev.* **73** (1948), pp. 155–161. DOI: 10.1103/PhysRev.73.155.

[Kit49] C. Kittel. "Physical theory of ferromagnetic domains [37]". In: *Rev. Mod. Phys.* **21** (1949), pp. 541–583. DOI: 10.1103/PhysRev.79.745.2.

[Kob13] A. Kobs. "Magnetogalvanic effects in ferromagnets of reduced dimensions". PhD thesis. Universität Hamburg, 2013.

[Kob16] A. Kobs and H. P. Oepen. "Disentangling interface and bulk contributions to the anisotropic magnetoresistance in Pt/Co/Pt sandwiches". In: *Phys. Rev. B* **93** (2016), p. 014426. DOI: 10.1103/PhysRevB.93.014426.

[Kon16] W. J. Kong, Y. R. Ji, X. Zhang, H. Wu, Q. T. Zhang, Z. H. Yuan, C. H. Wan, X. F. Han, T. Yu, K. Fukuda, H. Naganuma, and M.-J. Tung. "Field-free spin Hall effect driven magnetization switching in Pd/Co/IrMn exchange coupling system". In: *Appl. Phys. Lett.* **109** (2016), p. 132402. DOI: 10.1063/1.4963235.

[Kra15] E. E. Krasovskii. "Spin-orbit coupling at surfaces and 2D materials". In: *J. Phys. C* **27** (2015), p. 493001. DOI: 10.1088/0953-8984/27/49/493001.

[Kru05] O. Krupin, G. Bihlmayer, K. Starke, S. Gorovikov, J. E. Prieto, K. Döbrich, S. Blügel, and G. Kaindl. "Rashba effect at magnetic metal surfaces". In: *Phys. Rev. B* **71** (2005), p. 201403. DOI: 10.1103/PhysRevB.71.201403.

[Kör15] H. S. Körner, J. Stigloher, H. G. Bauer, H. Hata, T. Taniguchi, T. Moriyama, T. Ono, and C. H. Back. "Interfacial Dzyaloshinskii-Moriya interaction studied by time-resolved scanning Kerr microscopy". In: *Phys. Rev. B* **92** (2015), 220413(R). DOI: 10.1103/PhysRevB.92.220413.

[Lai92] B. M. Lairson, M. R. Visokay, R. Sinclair, S. Hagstrom, and B. M. Clemens. "Epitaxial Pt(001), Pt(110), and Pt(111) films on MgO(001), MgO(110), MgO(111), and Al2O3(0001)". In: *Appl. Phys. Lett.* **61** (1992), pp. 1390–1392. DOI: 10.1063/1.107547.

[Led94] M. Lederman, S Schultz, and M Ozaki. "Measurement of the dynamics of the magnetization reversal in individual single-domain Co particles". In: *Phys. Rev. Lett.* **73** (1994), pp. 1986–1989. DOI: 10.1016/0304-8853(95)00405-X.

[Lee13] K.-S. Lee, S.-W. Lee, B.-c. Min, and K.-J. Lee. "Threshold current for switching of a perpendicular magnetic layer induced by spin Hall effect". In: *Appl. Phys. Lett.* **102** (2013), p. 112410. DOI: 10.1063/1.4798288.

[Lee14a] K.-S. Lee, S. W. Lee, B. C. Min, and K. J. Lee. "Thermally activated switching of perpendicular magnet by spin-orbit spin torque". In: *Appl. Phys. Lett.* **104** (2014), p. 072413. DOI: 10.1063/1.4866186.

[Lee14b] O. J. Lee, L. Q. Liu, C. F. Pai, Y. Li, H. W. Tseng, P. G. Gowtham, J. P. Park, D. C. Ralph, and R. A. Buhrman. "Central role of domain wall depinning for perpendicular magnetization switching driven by spin torque from the spin Hall effect". In: *Phys. Rev. B* **89** (2014), p. 024418. DOI: 10.1103/PhysRevB.89.024418.

[Leg15] W. Legrand, R. Ramaswamy, R. Mishra, and H. Yang. "Coherent subnanosecond switching of perpendicular magnetization by the fieldlike spin-orbit torque without an external magnetic field". In: *Phys. Rev. Appl.* **3** (2015), p. 064012. DOI: 10.1103/PhysRevApplied.3.064012.

[Li16] P. Li, T. Liu, H. Chang, A. Kalitsov, W. Zhang, G. Csaba, W. Li, D. Richardson, A. DeMann, G. Rimal, H. Dey, J. S. Jiang, W. Porod, S. B. Field, J. Tang, M. C. Marconi, A. Hoffmann, O. Mryasov, and M. Wu. "Spin-orbit torque-assisted switching in magnetic insulator thin films with perpendicular magnetic anisotropy". In: *Nat. Commun.* **7** (2016), p. 12688. DOI: 10.1038/ncomms12688.

[Lid03] D. R. Lide, ed. *Handbook of Chemistry and Physics*. 84th ed. CRC Press, 2003.

[Liu11] L. Liu, T. Moriyama, D. C. Ralph, and R. A. Buhrman. "Spin-Torque Ferromagnetic Resonance Induced by the Spin Hall Effect". In: *Phys. Rev. Lett.* **106** (2011), p. 036601. DOI: 10.1103/PhysRevLett.106.036601.

[Liu12a] L. Liu, O. J. Lee, T. J. Gudmundsen, D. C. Ralph, and R. A. Buhrman. "Current-induced switching of perpendicularly magnetized magnetic layers using spin torque from the spin hall effect". In: *Phys. Rev. Lett.* **109** (2012), p. 096602. DOI: 10.1103/PhysRevLett.109.096602.

[Liu12b] L. Liu, C. F. Pai, Y. Li, H. W. Tseng, D. C. Ralph, and R. A. Buhrman. "Spin-Torque Switching with the Giant Spin Hall Effect of Tantalum". In: *Science* **336** (2012), pp. 555–558. DOI: 10.1126/science.1218197.

[Liu14] H. Liu, D. Bedau, J. Z. Sun, S. Mangin, E. E. Fullerton, J. A. Katine, and A. D. Kent. "Dynamics of spin torque switching in all-perpendicular spin valve nanopillars". In: *J. Magn. Magn. Mater.* **358-359** (2014), pp. 233–258. DOI: 10.1016/j.jmmm.2014.01.061.

[Luc65] M. S. P. Lucas. "Electrical conductivity of thin metallic films with unlike surfaces". In: *J. Appl. Phys.* **36** (1965), pp. 1632–1635. DOI: 10.1063/1.1703100.

[MA09] A. Matos-Abiague and R. L. Rodríguez-Suárez. "Spin-orbit coupling mediated spin torque in a single ferromagnetic layer". In: *Phys. Rev. B* **80** (2009), p. 094424. DOI: 10.1103/PhysRevB.80.094424.

[Man08a] A. Manchon, C. Ducruet, L. Lombard, S. Auffret, B. Rodmacq, B. Dieny, S. Pizzini, J. Vogel, V. Uhlíř, M. Hochstrasser, and G. Panaccione. "Analysis of oxygen induced anisotropy crossover in Pt/Co/MOx trilayers". In: *J. Appl. Phys.* **104** (2008), p. 043914. DOI: 10.1063/1.2969711.

[Man08b] A. Manchon and S. Zhang. "Theory of nonequilibrium intrinsic spin torque in a single nanomagnet". In: *Phys. Rev. B* **78** (2008), p. 212405. DOI: 10.1103/PhysRevB.78.212405.

[Man09] A. Manchon and S. Zhang. "Theory of spin torque due to spin-orbit coupling". In: *Phys. Rev. B* **79** (2009), p. 94422. DOI: 10.1103/PhysRevB.79.094422.

[Man15] A. Manchon, H. C. Koo, J Nitta, S. M. Frolov, and R. a. Duine. "New perspectives for Rashba spin-orbit coupling". In: *Nat. Mater.* **14** (2015), pp. 871–882. DOI: 10.1038/nmat4360.

[Mar13] E. Martinez, S. Emori, and G. S. D. Beach. "Current-driven domain wall motion along high perpendicular anisotropy multilayers: The role of the Rashba field, the spin Hall effect, and the Dzyaloshinskii-Moriya interaction". In: *Appl. Phys. Lett.* **103** (2013), p. 072406. DOI: 10.1063/1.4818723.

[May70] A. Mayadas and M. Shatzkes. "Electrical-Resistivity Model for Polycristalline Films: The Case of Arbitrary Reflection at External Surfaces". In: *Phys. Rev. B* **1** (1970), pp. 1382–1389. DOI: 10.1103/PhysRevB.1.1382.

[McG75] T. R. McGuire and R. I. Potter. "Anisotropic Magnetoresistance in Ferromagnetic 3d Alloys". In: *IEEE Trans. Magn.* **4** (1975), pp. 1018–1038. DOI: 10.1109/TMAG.1975.1058782.

[McM03] R. D. McMichael, D. J. Twisselmann, and A. Kunz. "Localized Ferromagnetic Resonance in Inhomogeneous Thin Films". In: *Phys. Rev. Lett.* **90** (2003), p. 227601. DOI: 10.1103/PhysRevLett.90.227601.

[Mei14] T. N. G. Meier. "Thermodynamical properties of fluctuating magnetic stripe domains in ultrathin Fe/Ni/Cu(001) and Ni/Fe/Cu(001) films". Masters Thesis. Universtät Regensburg, 2014.

[Mei17] T. N. G. Meier, M. Kronseder, and C. H. Back. "Domain-width model for perpendicularly magnetized systems with Dzyaloshinskii-Moriya interaction". In: *Phys. Rev. B* **96** (2017), p. 144408. DOI: 10.1103/PhysRevB.96.144408.

[Mik15] N. Mikuszeit, O. Boulle, I. M. Miron, K. Garello, P. Gambardella, G. Gaudin, and L. D. Buda-Prejbeanu. "Spin-orbit torque driven chiral magnetization reversal in ultrathin nanostructures". In: *Phys. Rev. B* **92** (2015), p. 144424. DOI: 10.1103/PhysRevB.92.144424.

[Mir10a] I. M. Miron, G. Gaudin, S. Auffret, B. Rodmacq, A. Schuhl, S. Pizzini, J. Vogel, and P. Gambardella. "Current-driven spin torque induced by the Rashba effect in a ferromagnetic metal layer". In: *Nat. Mater.* **9** (2010), pp. 230–234. DOI: 10.1038/nmat2613.

[Mir10b] I. M. Miron, G. Gaudin, S. Auffret, B. Rodmacq, A. Schuhl, S. Pizzini, J. Vogel, and P. Gambardella. "Spin-orbit torques in ultrathin ferromagnetic metal layers". In: *Proc. SPIE* **7760** (2010), 77600Z. DOI: 10.1117/12.862356.

[Mir11] I. M. Miron, K. Garello, G. Gaudin, P.-J. Zermatten, M. V. Costache, S. Auffret, S. Bandiera, B. Rodmacq, A. Schuhl, and P. Gambardella. "Perpendicular switching of a single ferromagnetic layer induced by in-plane current injection." In: *Nature* **476** (2011), pp. 189–193. DOI: 10.1038/nature10309.

[Miz01a] S. Mizukami, Y. Ando, and T. Miyazaki. "Ferromagnetic resonance linewidth for NM/80NiFe/NM Films (NM=Cu, Ta, Pd and Pt)". In: *J. Magn. Magn. Mater.* **226** (2001), pp. 1640–1642. DOI: 10.1016/S0304-8853(00)01097-0.

[Miz01b] S. Mizukami, Y. Ando, and T. Miyazaki. "The Study on Ferromagnetic Resonance Linewidth for NM/80NiFe/NM (NM = Cu, Ta, Pd and Pt) Films". In: *Jpn. J. Appl. Phys.* **40** (2001), pp. 580–585. DOI: 10.1143/JJAP.40.580.

[Miz10] S. Mizukami, E. P. Sajitha, D. Watanabe, F. Wu, T. Miyazaki, H. Naganuma, M. Oogane, and Y. Ando. "Gilbert damping in perpendicularly magnetized Pt/Co/Pt films investigated by all-optical pump-probe technique". In: *Appl. Phys. Lett.* **96** (2010), p. 152502. DOI: 10.1063/1.3396983.

[Mon02] S. Monso, B. Rodmacq, S. Auffret, G. Casali, F. Fettar, B. Gilles, B. Dieny, and P. Boyer. "Crossover from in-plane to perpendicular anisotropy in Pt/CoFe/AlO x sandwiches as a function of Al oxidation: A very accurate control of the oxidation of tunnel barriers". In: *Appl. Phys. Lett.* **80** (2002), pp. 4157–4159. DOI: 10.1063/1.1483122.

[Mor60a] T. Moriya. "Anisotropic Superexchange Interaction and Weak Ferromagnetism". In: *Phys. Rev.* **120** (1960), pp. 91–98. DOI: 10.1103/PhysRev.120.91.

[Mor60b] T. Moriya. "New Mechanism of Anisotropic Superexchange Interaction_Moriya". In: *Phys. Rev. Lett.* **4** (1960), pp. 228–230. DOI: 10.1103/PhysRevLett.4.228.

[Mos10a] O. Mosendz, V Vlaminck, J. E. Pearson, F. Y. Fradin, G. E. W. Bauer, S. D. Bader, and A Hoffmann. "Detection and quantification of inverse spin Hall effect from spin pumping in permalloy/normal metal bilayers". In: *Phys. Rev. B* **82** (2010), p. 214403. DOI: 10.1103/PhysRevB.82.214403.

[Mos10b] O. Mosendz, J. E. Pearson, F. Y. Fradin, G. E. W. Bauer, S. D. Bader, and A Hoffmann. "Quantifying Spin Hall Angles from Spin Pumping: Experiments and Theory". In: *Phys. Rev. Lett.* **104** (2010), p. 46601. DOI: 10.1103/PhysRevLett.104.046601.

[Mow11] M. D. Mower, G. Vignale, and I. V. Tokatly. "Dyakonov-Perel spin relaxation for degenerate electrons in the electron-hole liquid". In: *Phys. Rev. B* **83** (2011), p. 155205. DOI: 10.1103/PhysRevB.83.155205.

[Nag10] N. Nagaosa, J. Sinova, S. Onoda, A. H. MacDonald, and N. P. Ong. "Anomalous Hall effect". In: *Rev. Mod. Phys.* **82** (2010), pp. 1539–1592. DOI: 10.1103/RevModPhys.82.1539.

[Nak98] N. Nakajima, T. Koide, T. Shidara, H. Miyauchi, H. Fukutani, A. Fujimori, K. Iio, T. Katayama, M. Nývlt, and Y. Suzuki. "Perpendicular Magnetic Anisotropy Caused by Interfacial Hybridization via Enhanced Orbital Moment in Co/Pt Multilayers: Magnetic Circular X-Ray Dichroism Study". In: *Phys. Rev. Lett.* **81** (1998), pp. 5229–5232. DOI: 10.1103/PhysRevLett.81.5229.

[Nam70] Y. Namba. "Resistivity and Temperature Coefficient of Thin Metal Films with Rough Surface". In: *Jpn. J. Appl. Phys.* **9** (1970), pp. 1326–1329. DOI: 10.1143/JJAP.9.1326.

[Nan15] T. Nan, S. Emori, C. T. Boone, X. Wang, T. M. Oxholm, J. G. Jones, B. M. Howe, G. J. Brown, and N. X. Sun. "Comparison of spin-orbit torques and spin pumping across NiFe/Pt and NiFe/Cu/Pt interfaces". In: *Phys. Rev. B* **91** (2015), p. 214416. DOI: 10.1103/PhysRevB.91.214416.

[Neu06] I. Neudecker. "Magnetization Dynamics of Confined Ferromagnetic Systems". Ph.D. Thesis. University of Regensburg, 2006.

[Ngu16] M. H. Nguyen, D. C. Ralph, and R. A. Buhrman. "Spin Torque Study of the Spin Hall Conductivity and Spin Diffusion Length in Platinum Thin Films with Varying Resistivity". In: *Phys. Rev. Lett.* **116** (2016), p. 126601. DOI: 10.1103/PhysRevLett.116.126601.

[Obs14] M. Obstbaum, M. Härtinger, H. G. Bauer, T. Meier, F. Swientek, C. H. Back, and G. Woltersdorf. "Inverse spin Hall effect in Ni 81 Fe 19 /normal-metal bilayers". In: *Phys. Rev. B* **89** (2014), 060407(R). DOI: 10.1103/PhysRevB.89.060407.

[Obs15] M. Obstbaum. "Inverse spin Hall effect in metallic heterostructures". PhD thesis. Universität Regensburg, 2015.

[Ole00] I. I. Oleinik, E. Y. Tsymbal, and D. G. Pettifor. "Structural and electronic properties of Co/Al2O3/Co magnetic tunnel junction from first principles". In: *Phys. Rev. B.* **62** (2000), pp. 3952–3959. DOI: 10.1103/PhysRevB.62.3952.

[Osb45] J. A. Osborn. "Demagnetizing factors of the general ellipsoid". In: *Phys. Rev.* **67** (1945), pp. 351–357. DOI: 10.1103/PhysRev.67.351.

[Ou16] Y. Ou, C. F. Pai, S. Shi, D. C. Ralph, and R. A. Buhrman. "Origin of field-like spin-orbit torques in heavy metal/ferromagnet/oxide thin film heterostructures". In: *Phys. Rev. B* **94** (2016), 140414(R). DOI: 10.1103/PhysRevB.94.140414.

[Pai15] C. F. Pai, Y. Ou, L. H. Vilela-Leão, D. C. Ralph, and R. A. Buhrman. "Dependence of the efficiency of spin Hall torque on the transparency of Pt/ferromagnetic layer interfaces". In: *Phys. Rev. B* **92** (2015), p. 064426. DOI: 10.1103/PhysRevB.92.064426.

[Pai16] C. F. Pai, M. Mann, A. J. Tan, and G. S. D. Beach. "Determination of spin torque efficiencies in heterostructures with perpendicular magnetic anisotropy". In: *Phys. Rev. B - Condens. Matter Mater. Phys.* **93** (2016), p. 144409. DOI: 10.1103/PhysRevB.93.144409.

[Per07] K. Perzlmaier. "Propagation and Interference of Spin Waves in Ferromagnetic Thin Films". Ph.D. Thesis. University of Regensburg, 2007.

[Pet07] S. Petit, C. Baraduc, C. Thirion, U. Ebels, Y. Liu, M. Li, P. Wang, and B. Dieny. "Spin-torque influence on the high-frequency magnetization fluctuations in magnetic tunnel junctions". In: *Phys. Rev. Lett.* **98** (2007), p. 077203. DOI: 10.1103/PhysRevLett.98.077203.

[Pfe99] P Pfeffer and W Zawadzki. "Spin splitting of conduction subbands in III-V heterostructures due to inversion asymmetry". In: *Phys. Rev. B* **59** (1999), p. 5312. DOI: 10.1103/PhysRevB.59.R5312.

[Phi11] M. Philipp. "Electrical Transport and Scattering Mechanisms in Thin Silver Films for Thermally Insulating Glazing". Ph.D. Thesis. Technischen Universität Dresden, 2011.

[Piz14] S. Pizzini, J. Vogel, S. Rohart, L. D. Buda-Prejbeanu, E. Jué, O. Boulle, I. M. Miron, C. K. Safeer, S. Auffret, G. Gaudin, and A. Thiaville. "Chirality-induced asymmetric magnetic nucleation in Pt/Co/AlOx ultrathin microstructures". In: *Phys. Rev. Lett.* **113** (2014), p. 047203. DOI: 10.1103/PhysRevLett.113.047203.

[Pla98] W. Platow, A. Anisimov, G. Dunifer, M. Farle, and K. Baberschke. "Correlations between ferromagnetic-resonance linewidths and sample quality in the study of metallic ultrathin films". In: *Phys. Rev. B* **58** (1998), pp. 5611–5621. DOI: 10.1103/PhysRevB.58.5611.

[RS14] J. C. Rojas-Sánchez, N. Reyren, P. Laczkowski, W. Savero, J. P. Attané, C. Deranlot, M. Jamet, J. M. George, L. Vila, and H. Jaffrès. "Spin pumping and inverse spin hall effect in platinum: The essential role of spin-memory loss at metallic interfaces". In: *Phys. Rev. Lett.* **112** (2014), p. 106602. DOI: 10.1103/PhysRevLett.112.106602.

[Ras60] E. Rashba. "Properties of semiconductors with an extremum loop. I. Cyclotron and combinational resonance in a magnetic field perpendicular to the plane of the loop". In: *Sov. Phys. Solid State* **2** (1960), p. 1109.

[Rau14] I. G. Rau, S. Baumann, S. Rusponi, F. Donati, S. Stepanow, L. Gragnaniello, J. Dreiser, C. Piamonteze, F. Nolting, S. Gangopadhyay, O. R. Albertini, R. M. Macfarlane, C. P. Lutz, B. A. Jones, P. Gambardella, A. J. Heinrich, and H. Brune. "Reaching the magnetic anisotropy limit of a 3d metal atom". In: *Science* **344** (2014), pp. 988–992. DOI: 10.1126/science.1252841.

[Rea07] J. C. Read, P. G. Mather, and R. A. Buhrman. "X-ray photoemission study of CoFeB/MgO thin film bilayers". In: *Appl. Phys. Lett.* **90** (2007), p. 132503. DOI: 10.1063/1.2717091.

[Sag16] E. Sagasta, Y. Omori, M. Isasa, M. Gradhand, L. E. Hueso, Y. Niimi, Y. Otani, and F. Casanova. "Tuning the spin Hall effect of Pt from the moderately dirty to the superclean regime". In: *Phys. Rev. B* **94** (2016), 060412(R). DOI: 10.1103/PhysRevB.94.060412.

[Sam83] J. R. Sambles. “THE RESISTIVITY OF THIN METAL FILMS-SOME CRITICAL REMARKS”. In: *Thin Solid Films* **106** (1983), pp. 321–331. DOI: 10.1016/0040-6090(83)90344-9.

[Sas09] W. M. Saslow. “Landau-Lifshitz or Gilbert damping? That is the question”. In: *J. Appl. Phys.* **105** (2009). DOI: 10.1063/1.3077204.

[Sch13] K. Schultheiß. “Spinwellentransport in zweidimensionalen Mikrostrukturen”. PhD thesis. Technische Universität Kaiserslautern, 2013.

[Sch15] M. A. W. Schoen, J. M. Shaw, H. T. Nembach, M. Weiler, and T. J. Silva. “Radiative damping in waveguide-based ferromagnetic resonance measured via analysis of perpendicular standing spin waves in sputtered permalloy films”. In: *Phys. Rev. B* **92** (2015), p. 184417. DOI: 10.1103/PhysRevB.92.184417.

[Sha09] J. M. Shaw, T. J. Silva, M. L. Schneider, and R. D. McMichael. “Spin dynamics and mode structure in nanomagnet arrays: Effects of size and thickness on linewidth and damping”. In: *Phys. Rev. B* **79** (2009), p. 184404. DOI: 10.1103/PhysRevB.79.184404.

[Sin15] J. Sinova, S. O. Valenzuela, J. Wunderlich, C. H. Back, and T. Jungwirth. “Spin Hall effects”. In: *Rev. Mod. Phys.* **87** (2015), pp. 1213–1260. DOI: 10.1103/RevModPhys.87.1213.

[Ski14] T. D. Skinner, M. Wang, a. T. Hindmarch, a. W. Rushforth, a. C. Irvine, D. Heiss, H. Kurebayashi, and a. J. Ferguson. “Spin-orbit torque opposing the Oersted torque in ultrathin Co/Pt bilayers”. In: *Appl. Phys. Lett.* **104** (2014), p. 062401. DOI: 10.1063/1.4864399.

[Sof67] S. B. Soffer. “Statistical model for the size effect in electrical conduction”. In: *J. Appl. Phys.* **38** (1967), pp. 1710–1715. DOI: 10.1063/1.1709746.

[Son52] E. Sondheimer. “The mean free path of electrons in metals”. In: *Adv. Phys.* **1** (1952), pp. 1–42. DOI: 10.1080/00018735200101151.

[Sta09] D. D. Stancil and A. Prabhakar. *Spin Waves - Theory and Applications*. Ed. by D. D. Stancil and A. Prabhakar. New York: Springer, 2009.

[Sta17] C. Stamm, C. Murer, M. Berritta, J. Feng, M. Gabureac, P. M. Oppeneer, and P. Gambardella. “Magneto-Optical Detection of the Spin Hall Effect in Pt and W Thin Films”. In: *Phys. Rev. Lett.* **119** (2017), p. 087203. DOI: 10.1103/PhysRevLett.119.087203.

[Ste05] W. Steinhögl, G. Schindler, G. Steinlesberger, M. Traving, and M. Engelhardt. “Comprehensive study of the resistivity of copper wires with lateral dimensions of 100 nm and smaller”. In: *J. Appl. Phys.* **97** (2005), p. 023706. DOI: 10.1063/1.1834982.

[Sti02] M. D. Stiles and A. Zangwill. "Anatomy of spin-transfer torque". In: *Phys. Rev. B* **66** (2002), pp. 144071–1440714. DOI: 10.1103/PhysRevB.66.014407.

[Sti16] J. Stigloher, M. Decker, H. S. Körner, K. Tanabe, T. Moriyama, T. Taniguchi, H. Hata, M. Madami, G. Gubbiotti, K. Kobayashi, T. Ono, and C. H. Back. "Snell's Law for Spin Waves". In: *Phys. Rev. Lett.* **117** (2016), p. 037204. DOI: 10.1103/PhysRevLett.117.037204.

[Sto06] J. Stoehr and H. C. Siegmann. *Magnetism - From fundamentals To Nanoscale Dynamics*. Heidelberg: Springer Verlag Berlin Heidelberg, 2006.

[Sto98] I. Stone. "On the electrical resistance of thin films". In: *Phys. Rev. (Series I)* **6** (1898), pp. 1–16. DOI: 10.1103/PhysRevSeriesI.6.1.

[Suh55] H. Suhl. "Ferromagnetic Resonance in Nickel Ferrite Between One and Two Kilomegacycles". In: *Phys. Rev.* **97** (1955), pp. 555–557. DOI: 10.1103/PhysRev.97.555.2.

[Suz94] T. Suzuki, D. Weller, C. A. Chang, R. Savoy, T. Huang, B. A. Gurney, and V. Speriosu. "Magnetic and magneto-optic properties of thick face-centered-cubic Co single-crystal films". In: *Appl. Phys. Lett.* **64** (1994), pp. 2736–2738. DOI: 10.1063/1.111946.

[Thi12] A. Thiaville, S. Rohart, É. Jué, V. Cros, and A. Fert. "Dynamics of Dzyaloshinskii domain walls in ultrathin magnetic films". In: *Europhys. Lett.* **100** (2012), p. 57002. DOI: 10.1209/0295-5075/100/57002.

[Tor15] J. Torrejon, F. Garcia-Sanchez, T. Taniguchi, J. Sinha, S. Mitani, J. V. Kim, and M. Hayashi. "Current-driven asymmetric magnetization switching in perpendicularly magnetized CoFeB/MgO heterostructures". In: *Phys. Rev. B* **91** (2015), p. 214434. DOI: 10.1103/PhysRevB.91.214434.

[Tse02a] Y. Tserkovnyak, A. Brataas, and G. E. W. Bauer. "Enhanced Gilbert Damping in Thin Ferromagnetic Films". In: *Phys. Rev. Lett.* **88** (2002), p. 117601. DOI: 10.1103/PhysRevLett.88.117601.

[Tse02b] Y. Tserkovnyak, A. Brataas, and G. E. W. Bauer. "Spin pumping and magnetization dynamics in metallic multilayers". In: *Phys. Rev. B* **66** (2002), p. 224403. DOI: 10.1103/PhysRevB.66.224403.

[Tse05] Y. Tserkovnyak, A. Brataas, G. E. W. Bauer, and B. I. Halperin. "Nonlocal Magnetization Dynamics in Ferromagnetic Hybrid Nanostructures". In: *Rev. Mod. Phys.* **77** (2005), pp. 1375–1421. DOI: 10.1002/chin.200506230.

[Tse14] Y. Tserkovnyak and S. A. Bender. "Spin Hall phenomenology of magnetic dynamics". In: *Phys. Rev. B* . **90** (2014), p. 014428. DOI: 10.1103/PhysRevB.90.014428.

[Tsy12] E. Y. Tsymbal and I. Zutic, eds. *Handbook of Spin Transport and Magnetism*. Boca Raton: CRC Press, 2012.

[Urb01] R. Urban, G. Woltersdorf, and B. Heinrich. "Gilbert Damping in Single and Multilayer Ultrathin Films : Role of Interfaces in Nonlocal Spin Dynamics". In: *Phys. Rev. Lett.* **87** (2001), p. 217204. DOI: 10.1103/PhysRevLett.87.217204.

[Val93] T. Valet and A. Fert. "Theory of the perpendicular magnetoresistance in magnetic multilayers". In: *Phys. Rev. B* **48** (1993), pp. 7099–7113. DOI: 10.1103/PhysRevB.48.7099.

[Van14] A. Vansteenkiste, J. Leliaert, M. Dvornik, M. Helsen, F. Garcia-Sanchez, and B. Van Waeyenberge. "The design and verification of MuMax3". In: *AIP Adv.* **4** (2014), p. 107133. DOI: 10.1063/1.4899186.

[Vas79] F. T. Vas'ko. "." In: *Sov. Phys. Solid State* **21** (1979), p. 994.

[Wad91] B. C. Wadell. *Transmission Line Design Handbook*. Artech House, Inc., 1991.

[Wan14] Y. Wang, P. Deorani, X. Qiu, J. H. Kwon, and H. Yang. "Determination of intrinsic spin Hall angle in Pt". In: *Appl. Phys. Lett.* **105** (2014), p. 152412. DOI: 10.1063/1.4898593.

[Wan16] L. Wang, R. J. H. Wesselink, Y. Liu, Z. Yuan, K. Xia, and P. J. Kelly. "Giant Room Temperature Interface Spin Hall and Inverse Spin Hall Effects". In: *Phys. Rev. Lett.* **116** (2016), p. 196602. DOI: 10.1103/PhysRevLett.116.196602.

[Was05] G. Wastlbauer and J. a. C. Bland. "Structural and magnetic properties of ultrathin epitaxial Fe films on GaAs(001) and related semiconductor substrates". In: *Adv. Phys.* **54** (2005), pp. 137–219. DOI: 10.1080/00018730500112000.

[Wei14] D. Wei, M. Obstbaum, M. Ribow, C. H. Back, and G. Woltersdorf. "Spin Hall voltages from a.c. and d.c. spin currents". In: *Nat Commun* **5** (2014), p. 3768. DOI: 10.1038/ncomms4768.

[Wel01] D. Weller, L. Folks, M. Best, E. E. Fullerton, B. D. Terris, G. J. Kusinski, K. M. Krishnan, and G. Thomas. "Growth, structural, and magnetic properties of high coercivity Co/Pt multilayers". In: *J. Appl. Phys.* **89** (2001), pp. 7525–7527. DOI: 10.1063/1.1363602.

[Wel94] D. Weller, . Wu, J. Stöhr, M. Samant, B. Hermsmeier, and C. Chappert. "Orbital magnetic moments of Co in multilayers with perpendicular magnetic anisotropy". In: *Phys. Rev. B* **49** (1994), pp. 888–896. DOI: DOI:https://doi.org/10.1103/PhysRevB.49.12888.

[Wel95] D. Weller, J. Stöhr, R. Nakajima, A. Carl, M. G. Samant, C. Chappert, R. Megy, P. Beauvillain, P. Veillet, and G. A. Held. "Microscopic origin of magnetic anisotropy in Au/Co/Au probed with X-ray magnetic circular dichroism". In: *Phys. Rev. Lett.* **75** (1995), pp. 3752–3755. DOI: 10.1103/PhysRevLett.75.3752.

[Wil00] F. Wilhelm, P. Poulopoulos, G. Ceballos, H. Wende, and K. Baberschke. "Layer-Resolved Magnetic Moments in Ni/Pt Multilayers". In: *Phys. Rev. Lett.* **85** (2000), pp. 413–416. DOI: 10.1103/PhysRevLett.85.413.

[Wol01] S. A. Wolf, D. D. Awschalom, R. A. Buhrman, J. M. Daughton, S. Von Molnar, M. L. Roukes, A. Y. Chtchelkanova, and D. M. Treger. "Spintronics: A Spin-Based Electronics Vision for the Future". In: *Science* **294** (2001), pp. 1488–1495. DOI: 10.1126/science.1065389.

[Wol04] G. Woltersdorf. "SPIN-PUMPING AND TWO-MAGNON SCATTERING IN MAGNETIC MULTILAYERS". PhD thesis. Simon Fraser University, 2004.

[Wol13] G. Woltersdorf, F. Hoffmann, H. G. Bauer, and C. H. Back. "Magnetic homogeneity of the dynamic properties of (Ga,Mn)As films from the submicrometer to millimeter length scale". In: *Phys. Rev. B* **87** (2013), p. 054422. DOI: 10.1103/PhysRevB.87.054422.

[Wu16] D. Wu, G. Yu, Q. Shao, X. Li, H. Wu, K. L. Wong, Z. Zhang, X. Han, P. Khalili Amiri, and K. L. Wang. "In-plane current-driven spin-orbit torque switching in perpendicularly magnetized films with enhanced thermal tolerance". In: *Appl. Phys. Lett.* **108** (2016), p. 212406. DOI: 10.1063/1.4952771.

[Wun05] J. Wunderlich, B. Kaestner, J. Sinova, and T. Jungwirth. "Experimental observation of the spin-hall effect in a two-dimensional spin-orbit coupled semiconductor system". In: *Phys. Rev. Lett.* **94** (2005), p. 047204. DOI: 10.1103/PhysRevLett.94.047204.

[Yaf63] Y. Yafet. "G Factors and Spin-Lattice Relaxation of Conduction Electrons". In: *Solid State Phys.* **14** (1963), p. 1. DOI: https://doi.org/10.1016/S0081-1947(08)60259-3.

[Yin06] L. F. Yin, D. H. Wei, N. Lei, L. H. Zhou, C. S. Tian, G. S. Dong, X. F. Jin, L. P. Guo, Q. J. Jia, and R. Q. Wu. "Magnetocrystalline anisotropy in permalloy revisited". In: *Phys. Rev. Lett.* **97** (2006), p. 067203. DOI: 10.1103/PhysRevLett.97.067203.

[Yu14a] G. Yu, P. Upadhyaya, K. L. Wong, W. Jiang, J. G. Alzate, J. Tang, P. K. Amiri, and K. L. Wang. "Magnetization switching through spin-Hall-effect-induced chiral domain wall propagation". In: *Phys. Rev. B* **89** (2014), p. 104421. DOI: 10.1103/PhysRevB.89.104421.

[Yu14b] G. Yu, P. Upadhyaya, Y. Fan, J. G. Alzate, W. Jiang, K. L. Wong, S. Takei, S. A. Bender, L.-T. Chang, Y. Jiang, M. Lang, J. Tang, Y. Wang, Y. Tserkovnyak, P. K. Amiri, and K. L. Wang. "Switching of perpendicular magnetization by spin-orbit torques in the absence of external magnetic fields." In: *Nat. Nanotechnol.* **9** (2014), p. 548. DOI: 10.1038/nnano.2014.94.

[Zha00] S. Zhang. "Spin Hall effect in the presence of spin diffusion". In: *Phys. Rev. Lett.* **85** (2000), pp. 393–396. DOI: 10.1103/PhysRevLett.85.393.

[Zha06] Q. G. Zhang, X. Zhang, B. Y. Cao, M. Fujii, K. Takahashi, and T. Ikuta. "Influence of grain boundary scattering on the electrical properties of platinum nanofilms". In: *Appl. Phys. Lett.* **89** (2006), p. 114102. DOI: 10.1063/1.2338885.

[Zha15a] C Zhang, S Fukami, H Sato, F Matsukura, and H Ohno. "Spin-orbit torque induced magnetization switching in nano-scale Ta / CoFeB / MgO". In: *Appl. Phys. Lett.* **107** (2015), p. 012401. DOI: 10.1063/1.4926371.

[Zha15b] W. Zhang, W. Han, X. Jiang, S. H. Yang, and S. P. Parkin. "Role of transparency of platinum-ferromagnet interfaces in determining the intrinsic magnitude of the spin Hall effect". In: *Nat. Phys.* **11** (2015), pp. 496–502. DOI: 10.1038/nphys3304.

[Zim60] J. Ziman. *Electrons and Phonons*. Oxford: OUP Oxford, 1960.

[Zwi05] M. Zwierzycki, Y. Tserkovnyak, P. J. Kelly, A. Brataas, and G. E. W. Bauer. "First-principles study of magnetization relaxation enhancement and spin transfer in thin magnetic films". In: *Phys. Rev. B* **71** (2005), p. 06442. DOI: 10.1103/PhysRevB.71.064420.

[Van84] P. M. T. M. Van Attekum, P. H. Woerlee, G. C. Verkade, and A. A. M. Hoeben. "Influence of grain boundaries and surface Debye temperature on the electrical resistance of thin gold films". In: *Phys. Rev. B* **29** (1984), pp. 645–650. DOI: 10.1103/PhysRevB.29.645.

List of Publications

J. Stigloher, T. Taniguchi, M. Madami, **M. Decker**, H. S. Koerner, T. Moriyama, G. Gubbiotti, T. Ono and C. H. Back:
Spin-wave wavelength down-conversion at thickness steps
in: Appl. Phys. Express **11**, 053002 (2018)

M. Zimmermann, T. N. G. Meier, F. Dirnberger, A. Kákay, **M. Decker**, S. Wintz, S. Finizio, E. Josten, J. Raabe, M. Kronseder, D. Bougeard, J. Lindner and C. H. Back
Origin and Manipulation of Stable Vortex Ground States in Permalloy Nanotubes
in: Nano Lett., Article ASAP, https://doi.org/10.1021/acs.nanolett.7b05222

H. S. Koerner, M. A. W. Schoen, T. Mayer, **M. M. Decker**, J. Stigloher, T. Weindler, T. N. G. Meier, M. Kronseder and C. H. Back:
Magnetic damping in poly-crystalline $Co_{25}Fe_{75}$: Ferromagnetic resonance vs. spin wave propagation experiments
in: Appl. Phys. Lett. **111**, 132406 (2017)

M. M. Decker, M. S. Woernle, A. Meisinger, M. Vogel, H. S. Koerner, G. Y. Shi, C. Song, M. Kronseder and C. H. Back:
Time Resolved Measurements of the Switching Trajectory of Pt/Co Elements Induced by Spin-Orbit Torques
in: Phys. Rev. Lett. **118**, 257201 (2017)

A. Talalaevskij, **M. Decker**, J. Stigloher, A. Mitra, H. S. KoernerH. S. Cespedes, C. H. Back and B. Hickey:
Magnetic properties of spin waves in thin yttrium iron garnet films
in: Phys. Rev. B. **95**, 064409 (2017)

L. Chen, **M. Decker**, M. Kronseder, R. Islinger, M. Gmitra, D. Schuh, D. Bougeard, J. Fabian, J. D. Weiss, and C. H. Back:
Robust spin-orbit torque and spin-galvanic effect at the Fe/GaAs(001) interface at room temperature
in: Nat. Comm. **7**, 13802 (2016)

M. Obstbaum, **M. Decker** A. K. Greitner, M. Haertinger, T. N. G. Meier, M. Kronseder, K. Chadova, S. Wimmer, D. Koedderitzsch, H. Ebert and C. H. Back
Tuning Spin Hall Angles by Alloying
in: Phys. Rev. Lett. **117**, 167204 (2016)

J. Stigloher, **M. Decker**, H. S. Koerner, K. Tanabe, T. Moriyama, T. Taniguchi, H. Hata, M. Madami, G. Gubbiotti, K. Kobayashi, T. Ono and C. H. Back
Snell's Law for Spin Waves
in: Phys. Rev. Lett. **117**, 037204 (2016)

Acknowledgement

Als erstes bedanke ich mich bei Prof. Christian H. Back und Prof. Georg Woltersdorf für die Möglichkeit, meine Doktorarbeit am Lst. Back in Regensburg durchzuführen. Insbesondere bedanke ich mich bei Christian Back, mich nach dem Wechsel von Georg Woltersdorf aus Regensburg nach Halle als Doktoranden zu übernehmen. Beide hatten immer ein offenes Ohr für mich und haben mir sehr viel geholfen, bei physikalischen wie auch bei nicht-physikalischen Problemen.
Ich danke Prof. Dieter Weiss für die Möglichkeit, die Gerätschaften seines Lehrstuhls zur Probenpräparation und Charakterisierung zu nutzen. Insbesondere geht mein Dank in diesem Kontext auch an Dr. Jonathan Eroms, der mir des Öfteren beim Lösen von technischen Problemen behilflich war. Weiterer Dank für die Hilfe bei der Probenherstellung richtet sich an Prof. Rupert Huber und Imke Gronwald.
Des Weiteren möchte ich mich bei Prof. Mark Stiles und Dr. Amin Vivek für die ausführlichen Erklärungen zur Spin Mixing Conductivity bedanken.
Im Zuge der Recherchen zur inhomogenen Leitfähigkeit haben folgende Personen durch hilfreiche Diskussionen zu meinem Verständnis beigetragen, wofür ich an dieser Stelle meinen Dank aussprechen möchte: Prof. Bret Heinrich, Prof. Klaus Richter, Prof. Jaroslav Fabian and Prof. Bryan Hickey. Insbesondere danke ich Georgios Stefanou aus Prof. Hickeys Arbeitsgruppe für die XRD- und Leitfähigkeitsmessungen an Pt Schichten.
Ich möchte mich auch bei Prof. Ganichev für ein erhellendes Gespräch bezüglich des Rashba-Edelstein Effekts (Spin Galvanischen Effekts) bedanken.
Ich danke Dr. Matthias Kronseder für den immensen Einsatz von Mensch und Material, um die metallischen Schichten herzustellen, die in dieser Arbeit verwendet wurden. Alle hier präsentierten Ergebnisse wurden an Schichten aus der Cluster-MBE (der Fakultät für Physik zugehörig) oder der PEEM-MBE (am Lst. Back) gemessen. Außerdem danke ich ihm besonders für das Korrekturlesen besonders zäher Teile dieser Arbeit.
Für das Bereitstellen von Schichtsystemen, die, wenngleich sie nicht direkten Eingang in die Arbeit gefunden haben, dennoch zum Lernprozess beigetragen haben,

danke ich: Mohammad Tarequzzaman und Dr. Ricardo Ferreira, Dr. See-Hun Yang und Prof. Stuart Parkin und Guoyi Shi und Cheng Song.
Ich möchte mich auch bei Johannes Wild und Prof. Joseph Zweck für TEM Untersuchungen an Querschnittspräparaten danken, die von Olga Ganicheva hergestellt wurden.
Im Zuge meiner Doktorarbeit haben mir zahlreiche Mit-Doktoranden bei diversen Problemen geholfen und verschiedene Messungen für mich durchgeführt:
Markus Härtinger verdanke ich viel von meinem Wissen über die FMR und Labview. Außerdem hat er mir manches Mal schnell eine Probe per Full Film FMR charakterisiert.
Martin Obstbaum hat mir in zahlreichen Diskussion zur Theorie und Praxis des ISHE die Grundlagen dieses Experiments und der dafür nötigen Tools, z.B. der Software Sonnet vermittelt. Der ISHE Teil dieser Arbeit baut auf dem Grundgerüst auf, das von Martin Obstbaum errichtet wurde.
Hans Bauer möchte ich für seine Erklärungen zur Theorie des Mikromagnetismus und der LLG danken. Des Weiteren hat er mir oft bei Programmier-Problemen aller Art geholfen. Das Programm für das Lösen der stehenden Spinwellen in magnetischen Streifen stammt von ihm und viele weitere Algorithmen, die ich zur Datenauswertung benutzt habe, sind von seinen Tipps geprägt. In gleicher Weise möchte ich Johannes Stigloher danken, der mir mit einigen Python-Problemen und Mumax geholfen hat, ganz zu Schweigen von diversen Laser-Cleaning Aktionen.
Helmut Körner hat immer wieder SQUID Messungen für mich durchgeführt und hatte immer Zeit für eine Diskussion über physikalische und nicht-Physik-bezogene Probleme.
Martin Wörnle war mir im Zuge seiner Masterarbeit (und schon vorher als Bachelorand) eine sehr große Hilfe, ohne ihn wäre das Switchen nicht zustandegekommen.
Alois Meisinger hat viel Arbeit in die Simulationen zum Switching gesteckt, wofür ich ihm sehr dankbar bin. Michael Vogel danke ich für das Comsol-Modell für die Temperaturrechungen zum Switchen.
Thomas N. G. Meier danke ich für einige XPS Messungen und für das sehr kontrollierte Plasma-Ätzen einiger Proben; des weiteren für ein sehr sorgfältiges Korrekturlesen des Theorieteils dieser Arbeit. Für weitere Korrekturen möchte ich mich bei Michael Zimmermann bedanken.
Bei Oleksandr Talalaevskyy und Anatoly Shestakov bedanke ich mich für diverse Diskussionen. Ich danke Anatoly für die Konstuktion eines 1 T oop Magneten und einer ip Feld-Überhöhung auf auch ca. 1 T für meinen Aufbau, die die Grenzen des

Machbaren bedeutend erweitert haben.
Dr. Lin Chen danke ich für zahlreiche harte Diskussionen über SOTs und die LLG. Insbesondere danke ich für das Überlassen von unveröffentlichten Daten.
Ein besondere Dank geht auch an unseren Lehrstuhltechniker, Markus Hollnberger, der mir so manches Ding gedreht hat (und auch gefräst...), und das viel schneller als es die Mechanikwerkstatt erlaubt. Ebenso möchte ich unserem Sekreteriat, bestehend aus Magdalena Pfleger, Claudia Zange, Sylvia Hrdina und Doris Meier, herzlich für die Unterstützung bei allerlei bürokratischem Ärger danken.
Ich danke Robert Islinger und Martin Buchner für die gemeinsame Zeit und viele Diskussionen.
Bei Tobias Weindler (und Familie) möchte ich mich an dieser Stelle für alles bedanken was er seit Beginn des Studiums für mich getan hat, allerdings ohne die Möglichekeit dem Anlass gerecht werden zu können.
Bei allen Mitarbeitern des Lehrstuhls möchte ich mich für die wirklich tolle Atmosphäre und die ständige Unterstützung bedanken. Ohne den Rückhalt von euch allen wäre diese Arbeit so nicht möglich gewesen.
Schlussendlich möchte ich meinen Eltern und meiner Schwester Rosa-Maria für ihre unermüdliche Unterstützung danken. Insbesondere möchte ich mich bei meiner Schwester für die Gestaltung des Covers dieser Arbeit bedanken. Der größte Dank allerdings geht an meine kleinen Familie, Andrea und Jan, dafür, dass ich immer - auch zu Zeiten schlechter Datenlage - guten Mutes sein konnte. Ohne die akribische Korrektur der Arbeit auf Rechtschreibung und Grammatik durch meine Frau wären zudem viele Fehler unentdeckt geblieben, wofür ich ihr hier auch nochmals meinen Dank aussprechen will.

Vielen Dank!